Declassified and Approved For Release 2013/09/24 : CIA-RDP10-02196R000700010005-2

Volume 18, Number 5

May, 1965

SOVIET ATOMIC ENERGY

АТОМНАЯ ЭНЕРГИЯ
(ATOMNAYA ÉNERGIYA)

TRANSLATED FROM RUSSIAN

c/b CONSULTANTS BUREAU

Declassified and Approved For Release 2013/09/24 : CIA-RDP10-02196R000700010005-2

Declassified and Approved For Release 2013/09/24 : CIA-RDP10-02196R000700010005-2

NUCLEAR SCIENCE

MÖSSBAUER EFFECT METHODOLOGY
Volume 1

Erwin J. Gruverman, Editor

Proceedings of the First Symposium on Mössbauer Effect Methodology, held in New York City on January 26, 1965

The editor, a well-known and prolific writer in the Mössbauer field, briefly reviews applications, then clearly and accurately discusses the previously inaccessible methodology of Mössbauer-effect studies.

Because the book carefully examines the complexities of required equipment for velocity modulation, measurements of effects, and modification of external environments, the reader can find information not only for evaluating the potential of Mössbauer-effect studies, but also for estimating the merits of alternative means of applying the techniques. The comprehensive reviews by Herber and Spijkerman describe new techniques for absolute standardization of isomer shifts, using sodium nitroprusside standard absorbers. This will make possible adoption of a standard to eliminate the now-prevalent confusion in comparing work performed at different laboratories.

Chemical-process industrialists, physicists, biologists, chemists, and educators working in the Mössbauer field should find this book of immeasurable help. For example, it will aid readers in selecting a transducer system, building it, or writing specifications for its purchase; in assessing the merits of the Mössbauer technique; and in constructing and specifying measurements, calibration and environmental control systems. The excellent coverage of research and problems in this methodology includes nine carefully labeled diagrams of the apparatus and five pertinent graphs, together with legend.

CONTENTS: Mössbauer spectroscopy: some recent applications to chemical problems, *Rolfe H. Herber* • Review of advances in physics, *S. L. Ruby* • Application of the Mössbauer effect to biological systems, *U. Gonser and R. W. Grant* • Feedback in electrochemical drive systems, *E. Kankeleit* • Cam driven, constant acceleration Mössbauer spectrometer, *Alan J. Bearden, M. G. Hauser, and P. L. Mattern* • Constant velocity Mössbauer drive system, *P. Flinn* • Measurements by scattering techniques—I, *J. K. Major* • Measurements by scattering techniques—II, *P. Debrunner* • f measurement with black absorbers, *J. G. Dash* • Standardization of the differential chemical shift for Fe^{57}, *J. J. Spijkerman, F. C. Ruegg, and J. R. DeVoe* • Computation of Mössbauer spectra, *J. R. Gabriel* • Superconducting magnets — applications to the Mössbauer effect, *Paul P. Craig* • Mössbauer techniques using high field water-cooled solenoids, *Norman A. Blum* • Low temperature cryostats for Mössbauer experiments, *Michael Kalvius* • High pressure techniques, *R. Ingalls*.

200 pages PP 1965 $12.50

THEORY AND METHODS OF NUCLEAR REACTOR CALCULATIONS

G. I. Marchuk, Editor

Six of the 18 papers in the collection are concerned with transport theory. The first two papers (by Marchuk *et al.*) deal with the properties and application of even-order P_n approximations, applying the difference equation factorization method. These papers consider the distribution of neutrons from a point source; it is shown that the techniques of renormalization, extrapolation and overrelaxation applied to S_n equations accelerate pointwise convergence. Three fundamental papers on resonance absorption are concerned with improving the treatment of deviations from the basic narrow resonance formulas, including computation of the departure of the collision density from the narrow-resonance shape. The paper (Shikhov and Abagyan) on a method for constructing multigroup constants in the resonance region, taking heterogeneous effects into account, has fundamental interest to engineering physicists. Three papers report original work on fast neutron cross sections, and six are concerned with reactor calculation methods. The papers in the collection employ unified methods of analysis based on a strict mathematical approach, with subsequent application of the results to concrete practical solutions. A Special Research Report translated from Russian.

208 pages CB 1964 $40.00

EFFECTS OF RADIATION ON SEMICONDUCTORS

By V. S. Vavilov

Devoted to the effects of electromagnetic and corpuscular radiations on semiconductors, this new volume deals with the processes of absorption of electromagnetic radiation, photoionization and ionization by charged high-energy particles and the principal types of recombination processes by which an excited crystal returns to its original equilibrium state. Translated from Russian.

CONTENTS: Absorption of light by semiconductors • Photoionization and photoconductivity in semiconductors • Ionization of semiconductors by charged high-energy particles • Radiative recombination in semiconductors; possibility of the amplification and generation of light using semiconductors • Changes in the properties of semiconductors due to bombardment with fast electrons, gamma rays, neutrons, and heavy charged particles • Literature cited • Index.

238 pages CB 1965 $15.00

(c/b) CONSULTANTS BUREAU / PLENUM PRESS
227 West 17th Street, New York, New York 10011

Declassified and Approved For Release 2013/09/24 : CIA-RDP10-02196R000700010005-2

Declassified and Approved For Release 2013/09/24 : CIA-RDP10-02196R000700010005-2

ATOMNAYA ÉNERGIYA
EDITORIAL BOARD

A. I. Alikhanov
A. A. Bochvar
N. A. Dollezhal'
V. S. Fursov
I. N. Golovin
V. F. Kalinin
N. A. Kolokol'tsov *(Assistant Editor)*
A. K. Krasin
A. I. Leipunskii
V. V. Matveev
M. G. Meshcheryakov
M. D. Millionshchikov *(Editor-in-Chief)*
P. N. Palei
V. B. Shevchenko
D. L. Simonenko
V. I. Smirnov
A. P. Vinogradov
N. A. Vlasov *(Assistant Editor)*

SOVIET ATOMIC ENERGY

A translation of **ATOMNAYA ÉNERGIYA,**
a publication of the Academy of Sciences of the USSR

© 1966 CONSULTANTS BUREAU, A DIVISION OF PLENUM PUBLISHING CORPORATION, 227 West 17th Street, New York, N. Y. 10011

Volume 18, Number 5 May, 1965

CONTENTS

	PAGE	RUSS. PAGE
Equilibrium of a Spatial Plasma Pinch in a Longitudinal Magnetic Field Under Steady-State Conditions—V. D. Shafranov	575	443
Properties of a Thermionic Diode Placed in an Autonomous-Discharge Plasma —N. D. Morgulis and Yu. P. Korchevoi	580	447
Coherent Effects During the Interaction of Slow Neutrons with Liquids—V. P. Vertebnyi, I. P. Dzyub, A. N. Maistrenko, and M. V. Pasechnik	585	452
Total and Differential Fission Cross Sections of Uranium and Thorium for Low Energy Deuterons—Yu. A. Nemilov, V. V. Pavlov, Yu. A. Selitskii, S. M. Solov'ev, and V. P. Éismont	590	456
An Exact General Solution in Spherical Harmonics of the Boltzmann Equation —G. Ya. Rumyantsev	594	459
Calculation of Weak Self-Oscillatory Conditions in Nuclear Reactors—B. Z. Torlin	600	463
Propagation of Neutrons in Iron—V. I. Golubev, A. V. Zvonarev, M. N. Nikolaev, M. Yu. Orlov, V. V. Penenko, and O. P. Uznadze	608	469
Investigation of Power Effects of the BR-5 Reactor. N. V. Krasnoyarov, R. V. Nikol'skii, and I. A. Efimov	613	474
Development of a Fabrication Technology for Organic-Coolant Purifying Filters, and the Study of Their Hydraulic Resistance—Yu. I. Tokarev, F. F. Bogdanov, E. I. Pavlovskaya, and A. P. Chernopyatova	617	478
Internal Stresses Caused by Non-Uniform Swelling of Fissionable Material —Yu. I. Likhachev, V. P. Zvonarev, and V. Ya. Pupko	623	483
Extraction of Radium from Liquid Waste by Sorption on Manganese Dioxide —A. P. Tyutrina, B. P. Zhagin, and V. G. Bakhurov	628	487
Reaction Kinetics and the Equilibrium State in the System CO_2—CO—C Under the Action of Fast Electrons—G. P. Zhitneva, S. Ya. Pshezhetskii, N. A. Slavinskaya, and S. A. Kamenetskaya	632	492
Sr^{90} Content of Radioactive Fallout in Western Slovakia—Sh. Chupka, M. Petrashova, and I. Tsarakh	637	496
Use of the Autoradiographic Technique for Studying Radioactive Aerosols—V. N. Lavrenchik	640	499
Pb^{210} in the Atmosphere and in Fallout—V. I. Baranov and V. D. Vilenskii	645	503
ABSTRACTS OF DEPOSITED ARTICLES		
Investigation of the Phonon Spectrum in the Copper Lattice by Using the Method of Inelastic Neutron Scattering—E. Z. Vintaikin, V. V. Gorbachev, and P. L. Gruzin	649	507

Annual Subscription: $95 **Single Issue: $30** **Single Article: $15**

All rights reserved. No article contained herein may be reproduced for any purpose whatsoever without permission of the publisher. Permission may be obtained from Consultants Bureau, A Division of Plenum Publishing Corporation, 227 West 17th Street, New York, N. Y. 10011, U.S.A.

Declassified and Approved For Release 2013/09/24 : CIA-RDP10-02196R000700010005-2

Declassified and Approved For Release 2013/09/24 : CIA-RDP10-02196R000700010005-2

CONTENTS (continued)

	PAGE	RUSS. PAGE
Turbulent Couette Flow—V. D. Vilenskii and V. P. Smirnov	650	508
REVIEWS OF GENEVA 1964 PAPERS		
Nuclear Power Plants for Civilian Maritime Use—N. S. Khlopkin	653	510
Science and Engineering Exhibits at the Third Geneva Conference—B. A. Kuvshinnikov and V. V. Frolov	656	511
LETTERS TO THE EDITOR		
Multibeam Radio-Interferometer Determines Plasma Parameters—V. Ya. Balakhanov, V. D. Rusanov, and A. R. Striganov	660	515
Bremsstrahlung and Characteristic Radiation Spectra of Zirconium-Tritium Sources —Yu. P. Betin	663	516
Determination of the Relative Fission Reaction Rates for Different Isotopes by Recording the γ-Radiation of La^{140} Fission Fragments—L. N. Yurova and A. V. Bushuev	665	518
Energy Distribution of α Particles Emerging from a Thick Source—É. B. Ershov, A. A. Karan, and V. P. Shamov	667	519
Parabolic Approximation of the Total Attenuation Coefficients of γ-Quanta in the Energy Range from 0.03 to 10 MeV—O. S. Marenkov and R. S. Derzhimanov	669	520
The Effect of Boron-Containing Blocking on the Yield of Capture γ-Radiation —S. A. Kozlovskii, V. S. Kyz'yurov, K. K. Popkov, and D. N. Lebedev	672	522
Pulsations of the Pipe Wall Temperature Under Conditions of Intensive Convective Heat Exchange—V. I. Subbotin, M. Kh. Ibragimov, V. I. Merkulov, E. V. Nomofilov, and N. A. Tychinskii	676	525
Experimental Investigation of the Thermal Conditions of Fuel Elements in the VVR-M Reactor—I. F. Barchuk, M. M. Nazarchuk, S. S. Ogorodnik, D. T. Pilipets, and S. O. Slesarevskii	679	528
Attenuation by Iron and Polyethylene of Tissue Dose of Neutrons Incident Obliquely on the Shielding—G. V. Miroshnikov	681	529
Attenuation of Neutron Tissue Dose by Thin Layers of Hydrogenous Materials —G. V. Miroshnikov	685	532
Fractionation of Radioactive Isotopes in Hot Particles—Ya. I. Gaziev, S. G. Malakhov, and L. E. Nazarov	689	535
SCIENCE AND ENGINEERING NEWS		
Dubna August 1964 International Conference on High Energy Physics	692	538
II Colloquium on Inelastic Scattering of Slow Neutrons in Crystals and Liquids —V. V. Golikov	699	543
NEWS		
The Beta-2: New Isotope Electric Power Source—G. M. Fradkin, V. M. Kodyukov, and A. I. Rogozinskii	702	545
General-Purpose Gamma-Ray Device Designed for Pilot-Plant Radiation-Chemical Processes with Displacement of Radioactive Co^{60} Preparations by Compressed Air —V. I. Volgin, V. E. Drozdov, M. E. Eroshov, G. I. Lisov, A. N. Neprokin, and Yu. S. Ryabukhin	704	546

The Russian press date (podpisano k pechati) of this issue was 5/8/1965. Publication therefore did not occur prior to this date, but must be assumed to have taken place reasonably soon thereafter.

Declassified and Approved For Release 2013/09/24 : CIA-RDP10-02196R000700010005-2

Declassified and Approved For Release 2013/09/24 : CIA-RDP10-02196R000700010005-2

EQUILIBRIUM OF A SPATIAL PLASMA PINCH IN A LONGITUDINAL MAGNETIC FIELD UNDER STEADY-STATE CONDITIONS

(UDC 533.9.07)

V. D. Shafranov

Translated from Atomnaya Énergiya, Vol. 18, No. 5,
pp. 443-446, May, 1965
Original article submitted September 5, 1964

The equilibrium conditions of plasma in toroidal chambers of the figure-of-eight type are determined for the case in which the plasma is preserved for longer than the magnetic field takes to pass through the windings of the solenoid. In this case, some of the magnetic lines of force pass through the solenoid windings, closing outside it. Hence, the radius of the cross section of the extreme toroidal magnetic surface lying as a whole inside the chamber is always smaller than the radius of cross section of the solenoid. For a plasma pressure exceeding a certain critical value, toroidal magnetic surfaces are absent, and containment of the plasma is in principle impossible.

The simplest system for containing a dense plasma in an external magnetic field created earlier is a closed solenoid having the form of a space curve (for example, a figure of eight). This sytems was proposed by Spitzer [1], who also made a qualitative estimate of the equilibrium conditions of plasma in a solenoid in the shape of a figure eight. A more precise derivation of the equilibrium conditions, based on a calculation of the equilibrium position of a plasma pinch inside a solenoid of given form, was made in [2, 3]. In these papers, however, it was assumed that the surface of the solenoid (chamber) was an ideal conductor and, hence, coincided with the extreme toroidal magnetic surface of the equilibrium configuration. In this case equilibrium is in principle possible for any values of the parameter $\beta = 8\pi p/B^2$; this follows, for example, from [4]. In practice, however, the severe distortion of the magnetic surfaces arising for relatively large values of β is undesirable. From the requirement that the distortion of the magnetic surfaces should be small we may define an arbitrary critical value β_{cr} for plasma equilibrium in the ideal solenoid. This arbitrary criterion was also determined in [2, 3].

The condition that a solenoid made of ordinary (nonsuperconducting) materials should be ideal is only satisfied for periods small compared with the time of penetration of the magnetic field through the walls of the solenoid, which in experiment is some hundredth parts of a second. Hence, if the plasma containment time is of the order of, or greater than, 10 msec (such orders of containment time are already met with in experiments), the equilibrium conditions obtained on the assumption that the chamber is ideally conducting become inoperative.

The aim of this paper is to find the equilibrium conditions for a fairly large containment time, when the configuration of the magnetic field is determined not by the position of the conducting surfaces but by the assigned current distribution on these surfaces (steady-state conditions). This is formally expressed by the fact that the condition that the normal component of magnetic field on the surface of the solenoid should vanish is replaced by a condition expressing the difference between the tangential components of the magnetic field in terms of the given value of surface current density in the solenoid (the thickness of the solenoid windings being neglected), and the condition that the normal component of magnetic field should be continuous.

If the coils of the solenoid are disposed in planes perpendicular to its axis, then, as we know, for a toroidal axially-symmetric solenoid, all the magnetic lines of force pass inside the solenoid. In a solenoid having its axis in the form of a space curve, however, under steady-state conditions some of the lines of force penetrate the surface and close outside. The process of establishing a magnetic field in such a solenoid takes place as follows. When the

Declassified and Approved For Release 2013/09/24 : CIA-RDP10-02196R000700010005-2

Declassified and Approved For Release 2013/09/24 : CIA-RDP10-02196R000700010005-2

current is rapidly switched on, a magnetic field is set up in the solenoid with the same configuration as if the solenoid had ideal conductivity. Then the magnetic field partly diffuses through the windings of the solenoid, so that the outer toroidal magnetic surfaces in the solenoid are disrupted. If plasma is placed in such a magnetic field, then, as plasma pressure increases, the magnetic surfaces are not pressed to the walls of the chamber, as would be the case for ideal conductivity, but unimpededly pass through the surface of the chamber (solenoid). For a fairly large plasma pressure the toroidal magnetic surfaces vanish completely, when the magnetic axis shifts to the surface of the solenoid. Thus, in steady-state conditions, in contrast to the case of an ideally-conducting chamber, where equilibrium is possible for any plasma pressure, there is a certain critical value β_{cr} above which equilibrium is in principle impossible (magnetic toroidal surfaces absent).

A method of calculating plasma equilibria in spatial solenoids is described in [2, 3]. This is based on the use of a quasi-cylindrical orthogonal system of coordinates Q, s, ω, [5] in which Q is distance reckoned from the axis of the solenoid, s is the axis arc length, and ω is the azimuthal angle reckoned on the surface Q = const from a line perpendicular to the sections s = const. The toroidal corrections to all the quantities are expanded in Fourier series:

$$\mathbf{B}^{(1)} = Re \sum_{n=-\infty}^{\infty} \mathbf{B}_n(\varrho)\, e^{i(\omega-\varkappa_0 s)+i\frac{2\pi}{L}ns}. \tag{1}$$

The equation of a magnetic surface with cross-sectional radius Q' has the form

$$\begin{aligned} \varrho &= \varrho' + \xi(\varrho', \omega, s) \\ &= \varrho' + Re \sum_{n=-\infty}^{\infty} \xi_n(\varrho')\, e^{i(\omega-\varkappa_0 s)+i\frac{2\pi}{L}ns}, \end{aligned} \tag{2}$$

where $\varkappa_0$ is the mean value of the rotation angle $\alpha(s)$ of the principal normal to the axis of the solenoid, relative to the line ω = const.

$$\varkappa_0 = \frac{\alpha(L)}{L}, \tag{3}$$

where L is the total length of the axis.

An equation for determining $\xi_n(Q)$ was obtained in [3], together with expressions for the Fourier components of the toroidal corrections to the magnetic field, plasma pressure, and plasma current density in terms of $\xi_n(Q)$ and $d\xi_n/dQ$. All these formulas appear simplest when the curvature k(s) and the rotation angle of the principal normal $\alpha(s)$ are smooth functions of arc s. Let us consider just this case. For a figure-of-eight consisting of circular arcs, the results given below are valid everywhere except for a circle of points where the arcs join over a length roughly equal to the diameter of the solenoid ($\Delta s \approx 2b$). In the approximation indicated, the equation for $\xi_n(Q)$, in the absence of longitudinal current, is obtained from Eq. (102) of [3] in the form

$$\frac{d\xi_n(\varrho)}{d\varrho} = \frac{k_n}{\varkappa_n^2 \varrho} \cdot \frac{8\pi[\langle p\rangle_\varrho - p_0(\varrho)]}{B_{s0}^2} - \frac{3}{4} k_n \varrho. \tag{4}$$

Here $\langle p\rangle_\rho$ is the pressure averaged over the cross section of radius Q; the quantity $\varkappa_n$ is connected with $\varkappa_0$ [see Eq. (3)] by the relation

$$\varkappa_n = \varkappa_0 - \frac{2\pi}{L} n. \tag{5}$$

The condition (mentioned above) that the functions k(s) and $\alpha(s)$ should be smooth corresponds to the limitation

$$\varkappa_n \varrho \ll 1. \tag{6}$$

The Fourier components of the toroidal corrections to the magnetic field, current density, and plasma pressure are expressed by the formulas:

$$B_{\rho n} = -i\varkappa_n \xi_n B_{s0}; \tag{7}$$

Declassified and Approved For Release 2013/09/24 : CIA-RDP10-02196R000700010005-2

Declassified and Approved For Release 2013/09/24 : CIA-RDP10-02196R000700010005-2

$$B_{\omega n} = \left[k_n \varkappa_n \varrho^2 + \varkappa_n \left(\xi_n + \varrho \frac{d\xi_n}{d\varrho} \right) \right] B_{s0}; \tag{8}$$

$$B_{sn} = \frac{4\pi}{c} \xi_n j_{\omega 0} + k_n \varrho B_{s0}; \tag{9}$$

$$j_{\rho n} = i \frac{\xi_n}{\varrho} j_{\omega 0}; \tag{10}$$

$$j_{\omega n} = -\frac{dj_{\omega 0}}{d\varrho} \xi_n - j_{\omega 0} \left(\frac{d\xi_n}{d\varrho} + k_n \varrho \right); \tag{11}$$

$$j_{sn} = -2 \frac{k_n}{\varkappa_n} j_{\omega 0}; \tag{12}$$

$$p_n = -\xi_n \frac{dp_0}{d\varrho}. \tag{13}$$

Here k_n is the Fourier component of the relative curvature K(s)

$$k_n = \frac{1}{L} \int_0^L K(s) e^{-i \frac{2\pi}{L} ns} ds; \tag{14}$$

$$K(s) = k(s) e^{i[\varkappa_0 s - \alpha(s)]}, \tag{15}$$

which is easily calculated from the known functions k(s) and $\alpha(s)$ [3].

Let us denote by a the radius of the plasma pinch, i.e., the radius of the cross section of some magnetic surface on which the current density and pressure gradient are negligibly small. Then for $Q \geq a$ the mean pressure in formula (4) is

$$\langle p \rangle_\rho = \langle p \rangle_a \frac{a^2}{\varrho^2}; \tag{16}$$

the displacement of the plasma pinch of radius a in an ideally-conducting solenoid of radius b, determined by integrating expression (4) from b to a, takes the form [3]:

$$\xi_n(a) = \frac{3}{8} k_n (b^2 - a^2) - \frac{k_n}{2\varkappa_n^2} \beta \left(1 - \frac{a^2}{b^2} \right), \tag{17}$$

where

$$\beta = \frac{8\pi \langle p \rangle_a}{B_{s0}^2}. \tag{18}$$

In the case of our poorly-conducting solenoid, however, where the extreme toroidal magnetic surface has a cross-sectional radius smaller than that of the solenoid, in order to determine the equilibrium position of the plasma pinch we must solve the problem of the magnetic field under the following conditions:

1) on the surface of the plasma pinch, in accordance with the definition of this surface, the normal component of magnetic field vanishes;

2) the tangential components of magnetic field on the surface of the plasma pinch are determined by the values (8) and (9) obtained from solution of the internal problem;

3) on the surface of the solenoid the normal component of magnetic field is continuous;

4) the jump in the tangential component is determined by the given distribution of currents on the surface of the solenoid.

Declassified and Approved For Release 2013/09/24 : CIA-RDP10-02196R000700010005-2

Declassified and Approved For Release 2013/09/24 : CIA-RDP10-02196R000700010005-2

Since the solution procedure is extremely simple, we shall confine ourselves to giving the results obtained. The expression for the magnetic-field components between the pinch and the solenoid may be taken from [2]:

$$B_{\rho n} = -i\frac{k_n}{\varkappa_n} B_{s0} + A_n I_1'(\varkappa_n \varrho) + B_n K_1'(\varkappa_n \varrho); \tag{19}$$

$$B_{\omega n} = \frac{k_n}{\varkappa_n} B_{s0} + \frac{i}{\varkappa_n \varrho}[A_n I_1(\varkappa_n \varrho) + B_n K_1(\varkappa_n \varrho)]; \tag{20}$$

$$B_{sn} = -i[A_n I_1(\varkappa_n \varrho) + B_n K_1(\varkappa_n \varrho)], \tag{21}$$

where I_1 and K_1 are Bessel functions of imaginary argument. Outside the solenoid:

$$B_{\rho n} = C_n K_1'(\varkappa_n \varrho);$$

$$B_{\omega n} = \frac{i}{\varkappa_n \varrho} C_n K_1(\varkappa_n \varrho); \tag{22}$$

$$B_{sn} = -iC_n K_1(\varkappa_n \varrho).$$

The constants A_n and B_n are obtained from the first two conditions with the allowance for relations (4), (8), and (9), taken for Q = a, in the form:

$$A_n = -i\varkappa_n^2 a^2 B_{s0}\left(\varkappa_n \xi_n - \frac{k_n}{\varkappa_n}\right) K_2(\varkappa_n a) + ik_n \varkappa_n a^2 K_1'(\varkappa_n a)\frac{8\pi\langle p\rangle_a - \frac{3}{2}\varkappa_n^2 a^2 B_{s0}^2}{B_{s0}}; \tag{23}$$

$$B_n = -i\varkappa_n^2 a^2 B_{s0}\left(\varkappa_n \xi_n - \frac{k_n}{\varkappa_n}\right) I_2(\varkappa_n a) - ik_n \varkappa_n a^2 I_1'(\varkappa_n a)\frac{8\pi\langle p\rangle_a - \frac{3}{2}\varkappa_n^2 a^2 B_{s0}^2}{B_{s0}}. \tag{24}$$

Since relations (4), (8), and (9) were obtained on the assumption that $\varkappa_n Q \ll 1$, for determining A_n and B_n we must also use the expansion of the modified Bessel functions in terms of $\varkappa_n a$. From the third and fourth conditions we find C_n and ξ_n. Let us suppose that, in addition to the current created by the main magnetic field, the surface of the solenoid also bears a longitudinal current of the dipole type, by means of which the position of the magnetic surfaces can be regulated:

$$i_s = Re\sum_{n=-\infty}^{\infty} i_{sn} e^{i(\omega - \varkappa_n s) + i\frac{2\pi}{L}ns}. \tag{25}$$

Then the expression for C_n takes the form

$$C_n = i\left\{\frac{k_n \varkappa_n^3 b^4}{8} B_{s0} - \frac{k_n \varkappa_n a^2}{2}\beta B_{s0} + \frac{2\pi}{c} i_{sn} \varkappa_n^2 b^2\right\}, \tag{26}$$

and the unknown Fourier component of displacement is

$$\xi_n = \frac{k_n b^2}{4}\left(1 - \frac{3}{2}\cdot\frac{a^2}{b^2}\right) - \frac{k_n}{2\varkappa_n^2}\beta + \frac{2\pi}{c}\cdot\frac{b}{\varkappa_n}\cdot\frac{i_{sn}}{B_{s0}}. \tag{27}$$

A characteristic feature of equilibrium in the conditions of a poorly-conducting solenoid considered is that the displacement due to the plasma pressure (second term in the expression for ξ_n) is independent of the radius of the plasma pinch. For a certain critical value of parameter β the displacement becomes comparable with the cross-sectional radius of the solenoid. Hereupon, the cross-sectional radius of the extreme toroidal magnetic surface touching the walls of the solenoid vanishes, and equilibrium becomes impossible in principle. By comparing expressions (27) and (17) we see that the displacement connected with the pressure in an ideally-conducting sheath differs from that in a poorly-conducting solenoid by the coefficient $1 - a^2/b^2$. This means that there is no need to make a numerical

Declassified and Approved For Release 2013/09/24 : CIA-RDP10-02196R000700010005-2

Declassified and Approved For Release 2013/09/24 : CIA-RDP10-02196R000700010005-2

calculation for the displacement ξ (a, ω, s) in a poorly-conducting solenoid, since we may use the results for the ideal sheath given for certain configurations in [3].

Another characteristic feature of equilibrium in a poorly-conducting solenoid is the possibility in principle of experimentally determining the energy of the plasma from measurement of the magnetic field outside the solenoid. This field (dipole type) is determined by the formulas

$$B_{\rho n} = -\frac{C_n}{\varkappa_n^2 \varrho^2}; \quad B_{\omega n} = i\frac{C_n}{\varkappa_n^2 \varrho^2}, \tag{28}$$

i.e., according to Eq. (1),

$$\frac{B_\omega(\varrho, \omega, s)}{B_{s0}} = \frac{b^2}{\varrho^2}\sum_{n=-\infty}^{\infty}\left(-\frac{k_n \varkappa_n b^2}{8} + \beta\frac{a^2}{b^2}\cdot\frac{k_n}{2\varkappa_n}\right)\cos\left(\omega - \varkappa_0 s + \frac{2\pi}{L}ns\right); \tag{29}$$

$$\frac{B_\rho(\varrho, \omega, s)}{B_{s0}} = \frac{b^2}{\varrho^2}\sum_{n=-\infty}^{\infty}\left(-\frac{k_n \varkappa_n b^2}{8} + \beta\frac{a^2}{b^2}\cdot\frac{k_n}{2\varkappa_n}\right)\sin\left(\omega - \varkappa_0 s + \frac{2\pi}{L}ns\right). \tag{30}$$

In order of magnitude $k_0/\varkappa_0 \approx 1$. Hence, this dipole field close to the surface of the solenoid is approximately a fraction β of the main field in the solenoid and should be easy to measure. Moreover from formula (29) or (30) we may find the value of βa^2, proportional to the thermal energy of the plasma. A detailed calculation of the external field [associated with the summation of the series in Eqs. (29) and (30)] can easily be made in any specific case by analogy with the calculation of displacement made in [3].

In conclusion we note that, when the plasma contains a longitudinal current J and an associated field $B_\omega^0(Q) = 2J/cQ$, the formula for the displacement is more complicated. For reference we give this without derivation

$$\xi_n = \frac{2\pi}{c}\cdot\frac{b}{\varkappa_n}\cdot\frac{i_{sn}}{B_{s0}} + \frac{k_n b^2}{4}\left(1 - \frac{3}{2}\cdot\frac{a^2}{b^2}\right) + \frac{k_n a}{2\varkappa_n}\cdot\frac{B_\omega^0(a)}{B_{s0}}\left(\ln\frac{b}{a} - 1\right) - \frac{k_n a\left[8\pi\langle p\rangle_a + \langle B_\omega^2\rangle_a/2 + \langle \varkappa_n \varrho B_\omega B_s\rangle_a - \frac{3}{4}\varkappa_n a B_\omega^0(a) B_{s0}\right]}{2\varkappa_n B_{s0}\left[\varkappa_n a B_{s0} - B_\omega^0(a)\right]}. \tag{31}$$

This formula, like (27), is obtained on condition that

$$\varkappa_n b \ll 1 \text{ and } \varkappa_n a B_\omega^0 \ll B_{s0}.$$

LITERATURE CITED

1. L. Spitzer, In the book "Transactions of the Second International Conference on the Peaceful Use of Atomic Energy (Geneva, 1958)" [Russian translation], collected contributions of foreign scientists, 1, Moscow, Atomizdat (1959), p. 505.
2. V. D. Shafranov, "Yadernyi sintez," 4, 114 (1964).
3. V. D. Shafranov, Ibid., p. 232.
4. M. Krupska and R. Kul'srud, See [1], p. 221.
5. C. Mercier, "Yadernyi sintez," 3, 89 (1963).

Declassified and Approved For Release 2013/09/24 : CIA-RDP10-02196R000700010005-2

Declassified and Approved For Release 2013/09/24 : CIA-RDP10-02196R000700010005-2

PROPERTIES OF A THERMIONIC DIODE PLACED IN AN AUTONOMOUS-DISCHARGE PLASMA

(UDC 533.9)

N. D. Morgulis and Yu. P. Korchevoi

Translated from Atomnaya Énergiya, Vol. 18, No. 5,
pp. 447-451, May, 1965
Original article submitted May 27, 1964, and in final form November 14, 1964

The physical properties of a thermionic diode introduced into an autonomous-discharge plasma in cesium and mercury vapors are considered. In this way, it is possible to obtain increased values of emf and output voltage of the diode, depending mainly on the temperature of the plasma electrons. The distribution of the parameters of the mercury plasma in the interelectrode space of such a diode are measured. Certain conclusions are drawn from the results.

In our previous papers [1, 2] we considered certain features in the behavior of a thermionic diode introduced at "floating" potential into an autonomous cesium-discharge plasma (i.e., plasma capable of independent creation and control). It was established here in particular that such a diode had a comparatively high emf ε and output voltage V, even when the contact potential difference between its electrodes (cathode–anode) $\Delta V_c = 0$, and the temperature difference between them ($T_c - T_a$) was not very great. The results obtained were explained in terms of the electron temperature of the plasma, on which the potential jumps arising near the electrodes (cathode jump V_c and especially anode jump V_a) in the diode depend. For example, in the case of a plane-parallel system of electrodes with equal areas ($S_c = S_a$), when the density of the disordered Maxwellian current of the plasma electrodes, J_e, is greater than the thermionic cathode saturation current J_c, and when $\Delta K_c = 0$, the expression for emf introduced in [1] has the form

$$\varepsilon = (V_a - V_c) = \frac{kT_e}{e} \ln \frac{J_c + J_p}{J_a + J_p} \approx \frac{kT_e}{e} \ln \frac{J_c}{J_p} . \tag{1}$$

Here T_e and n_e are respectively the temperature and concentration of the electrons in the plasma, $J_p = J_e \sqrt{m/M}$; J_a = thermionic anode saturation current. Thus, the value of ε is essentially determined by T_e; the dependence of this emf on the electrode temperatures T_c and T_a is expressed in terms of currents J_c and J_a in Eq. (1). A corresponding equation for the emf may also be obtained for the less important case in which $J_e < J_c$ [1].

A method of deriving a computing formula for the output voltage of the diode, i.e., its volt/ampere characteristic $V = f(J)$, was also indicated in [1]. Taking account of the conditions indicated in deriving formula (1), this relationship may approximately be written in the form

$$V = (V_a - V_c) = \frac{kT_e}{e} \ln \frac{J_c + J_p - J}{J_a + J_p + J} \approx \approx \frac{kT_e}{e} \ln \frac{2J_0 - J}{J} , \tag{2}$$

where $J_0 = 1/2 J_c$ is the short-circuit current of the diode for which V = 0; for J = 0, formula (2) naturally passes into formula (1).

By considering Eq. (2) we obtain an approximate expression for the optimum output power obtainable from the diode in an external circuit:

$$W_m = J_m V_m \approx 0.6 \cdot J_0 \frac{kT_e}{e} . \tag{3}$$

Declassified and Approved For Release 2013/09/24 : CIA-RDP10-02196R000700010005-2

Declassified and Approved For Release 2013/09/24 : CIA-RDP10-02196R000700010005-2

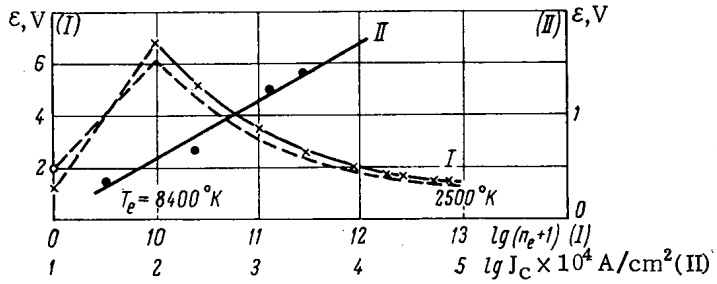

Fig. 1. Variation of the ε of the diode in cesium plasma with: I) concentration n_e and temperature T_e of the plasma electrons for T_c = 1100°K (———— experiment, ——— calculated); II) cathode saturation thermionic current density J_c for $n_e = 2 \cdot 10^{12}$ cm^{-3}, T_e = 2900°K, and T = 510 to 1100°K.

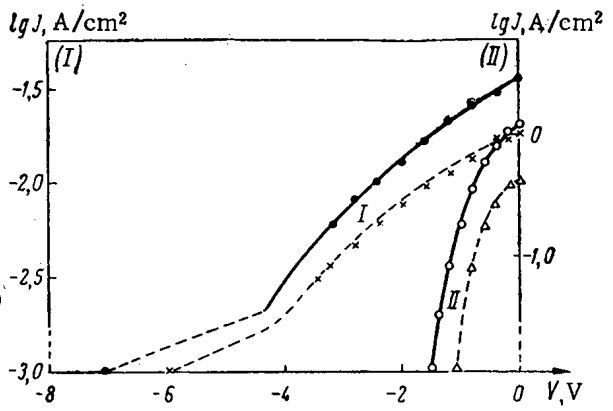

Fig. 2. Volt/ampere characteristics of diode current in cesium plasma for the cases: I) $n_e = 10^{10}$ cm^{-3} and T_e = 8400°K; II) $n_e = 8 \cdot 10^{12}$ cm^{-3} and T_e = 2500°K; cathode temperature 1450 (————) and 800°K (— — —).

This power is determined by two factors: 1) the output current $J_m \sim 0.44 J_0$, which is determined by the thermionic-emission current of the cathode, and 2) the output voltage $V_m \approx 1.3\ kT_e/e$, which is determined by the electron temperature. Expression (3) is analogous to the well-known expression for the vacuum diode, where $W_m = 0.37 J_0\ kT_c/e$.

Hence, for an all-around increase in the values of ε and V we must use an autonomous plasma with as high an electron temperature as possible, the values of this being given, for example, in [3]. For this purpose we may use the well-known [4] method of increasing the anode potential jump V_a by enlarging the relative surface of the anode ($S_a \gg S_c$). On the other hand, for an all-around increase in the diode current, we must have a cathode with a large emitting power and also ensure that the electron space charge near the cathode is effectively neutralized [5]. For this, we need a corresponding concentration of charges in the autonomous plasma, since the flux of electrons from the cathode does not normally give any marked additional ionization. For this kind of neutralization we must clearly satisfy the condition

$$J_p' = 0.4 e n_p \sqrt{\frac{2kT_e}{M}} \geqslant J_c \sqrt{\frac{m}{M}}, \text{ i.e. } J_e = e n_e \sqrt{\frac{kT_e}{2\pi m}} \geqslant 0.7 J_c, \tag{4}$$

which characterizes the degree of ionization of the plasma necessary for the operation of the diode. Here we must remember the effect of J_e and J_p on ε and V [formulas (1) and (2)].

We thus see how important it is to make a systematic experimental investigation of the properties of such diodes as a physical model of the "thermionic-plasma" energy converter. In the first stage of our work on this subject (reported in [1, 2]), we studied the properties of a diode placed in an autonomous discharge plasma in cesium vapor. This plasma is of special interest in connection with its wide use mainly in the ordinary kind of thermionic energy converter. It should be noted that the parameters of the cesium plasma obtained in the latter case are determined by the operating conditions of the diode system as a whole, and, hence, it is practically impossible to control them independently. Moreover, the electron temperature for operating conditions typical of these converters is extremely low (order of 3000°K) [6]. Hence, the output voltage of the ordinary type of converter is insignificant, even for $\Delta V_c \neq 0$ (order of 1 to 2 V).

In our paper on the diode in an autonomous cesium discharge plasma [1, 2] for $\Delta V_c \approx 0$, we gave some experimental data which enabled us to estimate the degree of accuracy of the considerations underlying formulas (1) and (2).

Figure 1 (curve I) shows the relationships $\varepsilon = f(n_e, T_e)$ as obtained experimentally and by calculation from formula (1). As we see from Fig. 1, these curves are in close agreement. In the same figure (curve II) we have the relationship $\varepsilon = f(\log J_c)$ plotted from experimental data; in accordance with formula (1), in this case we obtain a straight line, the slope of which gives the value of $T_e \sim 3000$°K, which agrees closely with the true value.

Declassified and Approved For Release 2013/09/24 : CIA-RDP10-02196R000700010005-2

Declassified and Approved For Release 2013/09/24 : CIA-RDP10-02196R000700010005-2

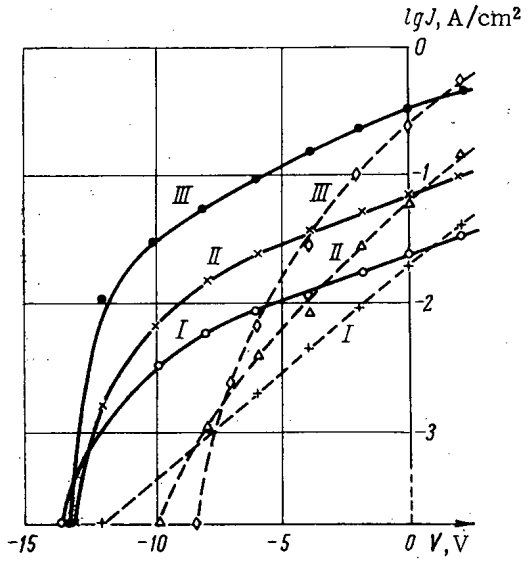

Fig. 3. Volt/ampere characteristics of the current of a plane-parallel diode in mercury plasma for the cases: ——— T_e = 30,000°K; I) $n_e = 8 \cdot 10^9$ cm^{-3}; II) $n_e = 4 \cdot 10^{10}$ cm^{-3}; III) $n_e = 4 \cdot 10^{11}$ cm^{-3}; — — — — — — T_e = 15,000°K; I) $n_e = 3 \cdot 10^9$ cm^{-3}; II) $n_e = 2 \cdot 10^{10}$ cm^{-3}; III) $n_e = 1 \cdot 10^{11}$ cm^{-3}.

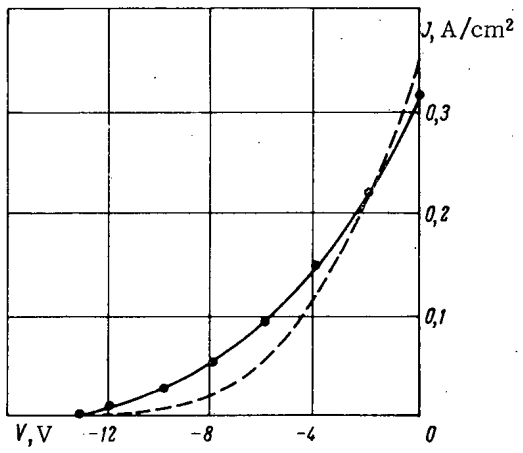

Fig. 4. Volt/ampere characteristics of the current of a plane-parallel diode in mercury plasma for the case $n_e = 4 \cdot 10^{11}$ cm^{-3} and T_e = 30,000°K: ——— experiment; — — — — — — calculated from formula (2).

Figure 2 shows the experimental volt/ampere characteristics on a semilogarithmic scale for various values of n_e, T_e, T_c. Under these conditions the emf (represented in the figure by the intercept on the axis of abscissa) may reach considerable values (~ 7 V). Comparison shows satisfactory agreement between the experimental and computed data obtained for various values of T_e and T_c, i.e., J_c.

In the second stage of the work it seemed natural to study plasma in which the electron temperature was much greater than that in the cesium plasma. This holds for a discharge plasma in inert gases or mercury vapor [3]. We found it convenient to use the plasma of a mercury-vapor arc discharge, which had a fairly high T_e, easily regulated by the mercury-vapor pressure. Diode systems of two types were introduced into this kind of plasma: 1) a plane-parallel system ($S_a = S_c$) consisting of a small barium-impregnated disk cathode, a disk anode, and a stationary probe set alongside them in the plasma; 2) a cylindrical system consisting of an ordinary heated oxide cathode, a wide corrugated anode ($S_a \gg S_c$) and a stationary probe introduced inside this system. In all cases $\Delta V_c = 0$, since the anode was doubtless covered with an active layer of evaporation products from the cathode.

Figure 3 presents volt/ampere characteristics obtained with the plane-parallel diode for various values of n_e and electron temperature 30,000 and 15,000°K. We see that as T_e rises there is a considerable increase in the emf and the optimum output voltage of the diode V_m. On raising the value of n_e, i.e., J_e and J_p, the short-circuit current J_0 rises and ε falls. All this agrees with formulas (1) and (2). In order to make this comparison perfectly clear, the experimental and theoretical volt/ampere characteristics for certain values of n_e and T_e are shown in Fig. 4. The two curves, reduced to the same value of short-circuit current, agree closely with one another. Finally, we note that the experimental curve gives extremely high values of ε and V_m (~ 14 V and ~ 5 V, respectively).

A comparison between the volt/ampere characteristics for the plane-parallel and cylindrical diodes for the same plasma parameters is shown in Fig. 5 (curves I and II). On passing from the first system to the second there is a certain increase in ε and V_m. It is interesting to note that, when the value of T_e for the cylindrical diode was raised from 30,000 to 50,000°K for the same value of n_e, curve III was obtained; this gives still larger values of ε and V_m (~ 20 and ~ 8 V, respectively), as would be expected. In comparison with these, the emf of the ordinary diode $\varepsilon' \approx [\Delta V_c + 2k/e\,(T_c - T_a)]$ is insignificant.

After elucidating these features, we passed on to a more detailed consideration of the phenomena in the interelectrode space of the diode in the mercury discharge plasma. For this we used an apparatus in which the diode system to be studied was situated at floating potential in the mercury-arc discharge plasma (apparatus shown schematically in Fig. 6). The cathode of the diode was a chain of seven heated oxide cathodes in parallel on the surface of a 5-mm diameter cylinder; the anode was an ordinary molybdenum cylinder 7 mm in diameter and 18 mm in length. On both sides of the diode (close to it) lay two stationary probes, enabling the potential drop ΔV_g in the plasma in

Declassified and Approved For Release 2013/09/24 : CIA-RDP10-02196R000700010005-2

Declassified and Approved For Release 2013/09/24 : CIA-RDP10-02196R000700010005-2

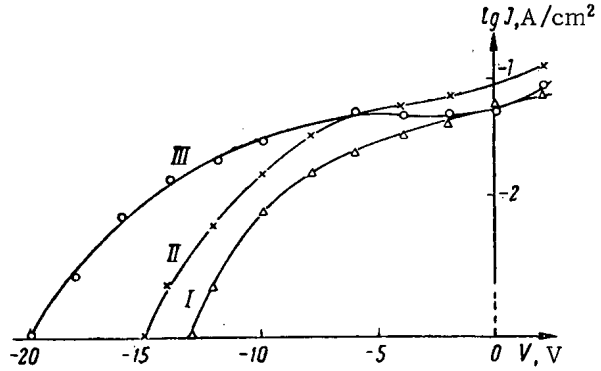

Fig. 5. Volt/ampere characteristics of the current of a diode in mercury plasma for the case $n_e = 10^{10}$ cm^{-3}; T_e = 30,000°K and short-circuit current $J_0 = 0.1$ A/cm^2: I) plane-parallel diode; II) corrugated cylindrical diode; III) the same cylindrical diode at T_e = 50,000°K.

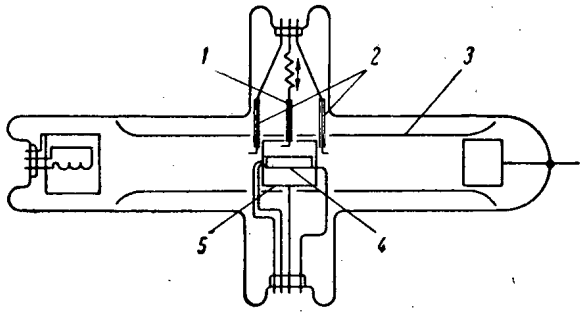

Fig. 6. Experimental apparatus for studying mercury-plasma parameters inside the cylindrical diode: 1) internal movable probe; 2) two external stationary probes; 3) guiding glass tube; 4) cathode; 5) anode of the diode.

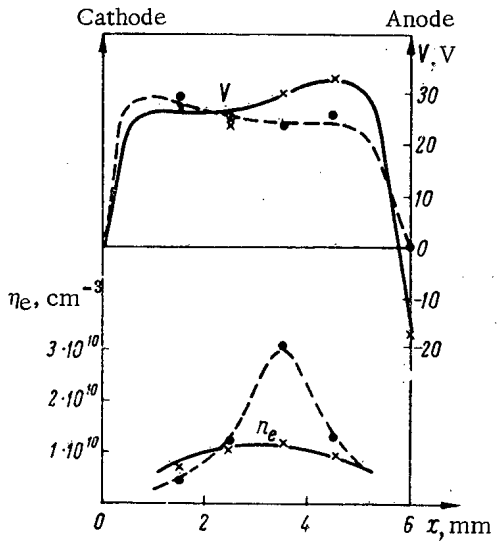

Fig. 7. Distribution of potential V and electron concentration n_e inside the diode for discharge current 0.1 A in the plasma and $T_e \sim$ 80,000°K for the emf (————) and short-circuit (— — —) conditions.

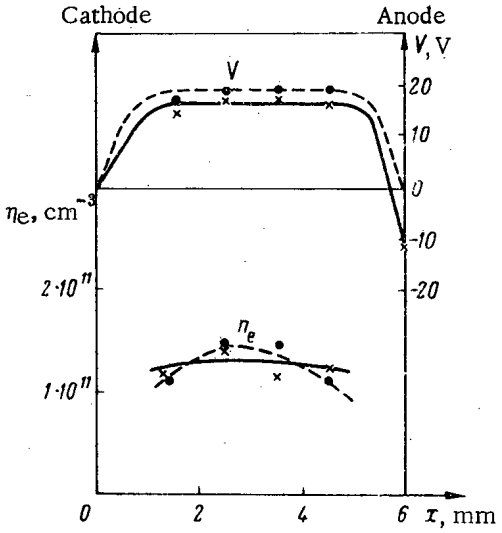

Fig. 8. Distribution of potential V and electron concentration n_e inside the diode for discharge current 1.0 A in the plasma and $T_e \sim$ 50,000°K for the emf (————) and short-circuit (— — —) conditions.

this section to be determined. Inside the diode system, a third probe was introduced through a small hole in the anode; this could be moved over the radius. The probe in the interelectrode (cathode–anode) space was used to determine the distribution of potential V and the temperature T_e and concentration n_e of the plasma electrons. Measurements of this kind were made for the emf and short-circuit ($\Delta V_c = 0$) conditions of the diode.

Figure 7 gives the distributions of potential and electron concentration obtained for the case in which the discharge current in the plasma i = 0.1 A; here, it was found that $T_e \sim$ 80,000°K = const, and ΔV_g = 8 V. On the other hand, measurement of the volt/ampere characteristics showed that in this case ε = 17 V and the optimum output voltage V_m = 7 V. Figure 8 shows results obtained for the case in which the discharge current in the plasma i = 1.0 A. For this $T_e \sim$ 50,000°K = const, ΔV_g = 5 V, ε = 12 V and V_m = 5 V.

Declassified and Approved For Release 2013/09/24 : CIA-RDP10-02196R000700010005-2

Declassified and Approved For Release 2013/09/24 : CIA-RDP10-02196R000700010005-2

From the data presented in these figures we may draw the following conclusions.

1. The distribution of potential in the interelectrode space of the diode $V = f(x)$ shows that, first, in accordance with formulas (1) and (2), the large values of ε and V_m (agreeing with T_e) are due mainly to the large negative potential jump V_a at the anode [4] (for example, in these experiments V_a reached 30 to 50 V in the emf condition); secondly, within the diode there is a considerable and smooth rise in potential, and, hence, a substantial cathode potential jump; as a result of the latter, electrons coming straight from the cathode may play some part in the formation of charge in the plasma.

2. The electron concentration n_e measured inside the diode is considerably smaller, and the electron temperature T_e and longitudinal electric field $E = \Delta V_g/d$ considerably larger, than under the same conditions in "free" plasma (according to the results of [3] and of the measurements indicated above). This is connected with the additional increased recombination of plasma charges at the electrodes of the diode, similar to the well-known conditions in a plasma pinch.

Finally, we should mention some further experiments confirming that a slight longitudinal and transverse magnetic field may have a considerable effect on the parameters of the diode shown in Fig. 6. For example, for a discharge current of $i = 0.1$ A in the plasma and a magnetic field of ~ 150 Oe, the value of V_m reaches ~ 10 V for the longitudinal and ~ 16 V for the transverse field, while the value of ε in both cases is ~ 30 V.

The results of our experiments indicate the interesting physical properties of such diodes and also show that increased emf and output voltages can be obtained and controlled with them. We shall continue to study this problem.

In conclusion we must make two comments.

1. This kind of diode, as a physical model of a "thermionic-plasma" energy converter, can have nothing in common with a converter using an auxiliary discharge as a source of the ions required for increasing the electron current [7]. On the other hand, certain features of this diode are probably similar to those of the well-known converter using an ionized-gas flow without a magnetic field [8]. The operating principle of our diode to a certain extent reflects the recent widespread tendency to use nonequilibrium plasma systems with "hot" electrons, as, for example, in questions of the conductivity and electron emission of semiconductors, the conductivity of magnetohydrodynamic energy converters, and so forth.

2. After all our cesium-plasma work had been completed and [1, 2] had been published, a brief, independent article [9] appeared. This contained arguments similar to ours (though without experimental foundation) and also the results of certain experiments directly demonstrating the genuine possibility of converting energy by means of this kind of diode. Values showing the practical applicability of this method were obtained for an argon plasma created by an hf discharge: $\varepsilon \approx 10$ V, $V_m \sim 5.3$ V, and (according to the estimate of [9]) a conversion efficiency of $\sim 36\%$.

LITERATURE CITED

1. N. Morgulis and Yu. Korchevoi, ZhTF, 32, 1487 (1962).
2. N. Morgulis, "Ukr. fiz. zh.," 7, 1131 (1962).
3. B. Klyarfel'd, in the coll.: "Electron and Ion Apparatus" [in Russian], Moscow-Leningrad, Gosénergoizdat (1940), p. 165; J. Phys., 5, 155 (1941).
4. B. Klyarfel'd and N. Neretina, ZhTF, 28, 296 (1958); 29, 15 (1959); 30, 186 (1960).
5. P. Marchuk, "Trudy IF AN USSR," No. 7, 17 (1956).
6. N. Morgulis and Yu. Korchevoi, "Radiotekhnika i élektronika," 6, 2073 (1961).
7. D. Gabor, Nature, 189, 868 (1961); W. Bloss, Z. angew. Phys., 14, 1 (1962).
8. S. Klein, Proceedings of Fifth International Conference Ioniz. Phenomena in Gases, 5, 1 (1962), p. 806.
9. J. Waymouth, J. Instn. Electr. Engrs., 8, 380 (1962).

Declassified and Approved For Release 2013/09/24 : CIA-RDP10-02196R000700010005-2

Declassified and Approved For Release 2013/09/24 : CIA-RDP10-02196R000700010005-2

COHERENT EFFECTS DURING THE INTERACTION OF SLOW NEUTRONS WITH LIQUIDS

(UDC 539.17.02)

V. P. Vertebnyi, I. P. Dzyub, A. N. Maistrenko, and M. V. Pasechnik

Translated from Atomnaya Énergiya, Vol. 18, No. 5, pp. 452-455, May, 1965
Original article submitted May 18, 1964

The total cross sections of liquid nitrogen and oxygen and the total cross section of gaseous nitrogen for neutrons with wavelengths in the 4 to 15-A range were determined in the VVR-M reactor of the Institute of Physics, Academy of Sciences, Ukr.SSR. The cross sections of gaseous oxygen and nitrogen rise monotonically with increasing wavelength, while those of the liquids begin to fall at $\lambda \approx 5\text{-}5.5$ A. Apparently this effect is connected with the existence of short-range order in the liquids; in nature, it is similar to the scattering of neutrons in polycrystalline material for wavelengths close to $\lambda = 2d_{max}$. The existence of coherent effects in the total cross section of heavy water is considered.

The total cross section for the interaction of neutrons with a liquid may in general be written in the form

$$\sigma_{tot} = \sigma_{scat} + \sigma_{react.} \tag{1}$$

The question of the energy dependence of σ_{react} is practically solved. The energy dependence of σ_{scat} may be found if we know the correlation function $G(r, t)$ [1], since

$$\frac{d^2\sigma_{scat}}{d\Omega\, d\varepsilon} = \frac{a^2 k}{2\pi\hbar k_0} \int \exp\left[i(\bar{k}\bar{r} - \omega t)\right] G(\bar{r}, t)\, dr\, dt. \tag{2}$$

In reality, however, the function $G(\bar{r}, t)$ is unknown. If we put the total scattering cross section in the form

$$\sigma_{scat} = \sigma_{elas}^{coh} + \sigma_{elas}^{incoh} + \sigma_{inelas}, \tag{3}$$

and suppose that the term σ_{elas}^{coh} is the greatest (this assumption is apparently valid for liquids at low temperatures with a large coherent cross section, for example, for liquid oxygen and nitrogen), then in the static approximation (without allowing for loss of energy in scattering) we may obtain some information on the variation of σ_{coh}^{elas} with neutron wavelength. In fact

$$\frac{d\sigma_{coh}}{d\Omega} = a_{coh}^2 4\pi Q_0 \int_0^\infty [g(r) - 1] \frac{\sin sr}{sr} r^2\, dr \equiv a_{coh}^2 i(s), \tag{4}$$

where a_{coh} is the amplitude of coherent scattering, $g(r)$ is the binary correlation function, Q_0 the density of the nuclei, $s = 4\pi/\lambda \sin \theta/2$ (here θ is the neutron-scattering angle). It follows from (4) that

Declassified and Approved For Release 2013/09/24 : CIA-RDP10-02196R000700010005-2

Declassified and Approved For Release 2013/09/24 : CIA-RDP10-02196R000700010005-2

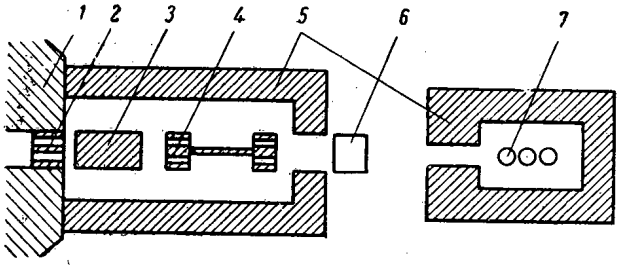

Fig. 1. Arrangement of experiment to determine the total neutron cross sections of nitrogen and oxygen: 1) reactor shielding; 2) collimator; 3) beryllium filter cooled with nitrogen; 4) mechanical monochromator (or interrupter); 5) radiation shielding; 6) cryostat for gas container; 7) Born counters SNMO-5.

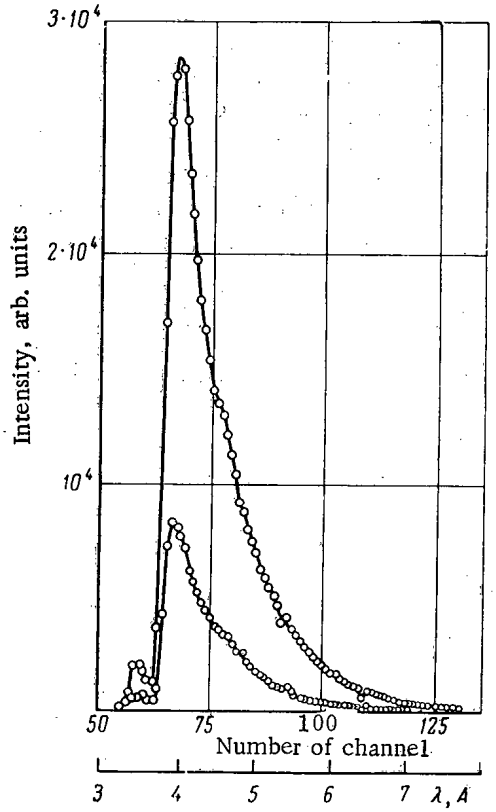

Fig. 2. Neutron spectrum measured by means of a mechanical neutron interruptor with resolution 16 μsec/m, after passing through the beryllium filter. The upper curve relates to cooled beryllium.

$$\sigma_{\text{elas}}^{\text{coh}}(\lambda) = \int \left(\frac{d\sigma}{d\Omega}\right)_{\text{coh}} d\Omega = \\ = 4\pi a_{\text{coh}}^2 \left(\frac{\lambda}{4\pi}\right)^2 \int_0^{s_{\text{lim}} \equiv \frac{4\pi}{\lambda}} si(s)\, ds. \qquad (5)$$

Similar expressions may also be obtained in the approximation of [2], where the quasi-elastic character of the elastic scattering is taken into account. The quantity i(s), the Fourier transform of the binary correlation function, may be obtained directly from x-ray or neutron-diffraction data [3, 4]. The general character of i(s) is this: for small s, i(s) is small; as s rises, the value of i(s) passes through a sharp maximum connected with the existence of short-range order in liquids; as s rises further, i(s) falls once more and smoothly with s. Hence, for large neutron wavelengths the integral $\int_0^{s_{\text{lim}} \equiv \frac{4\pi}{\lambda}}$ is small and so is the coherent-scattering cross section. As the wavelength decreases, there comes a moment when s_{lim} falls in the neighborhood of the maximum of i(s). Here the cross section increases quite sharply. Finally, after passing the i(s) maximum and continuing to shorter wavelengths, there is a slight increase in the integral $\int_0^{s_{\text{lim}}} i(s)\, s\, ds$; the variation in the factor λ^2 in front of the integral in (5) may be more substantial, so that the coherent-scattering cross section will again diminish.

It is interesting to note that i(s) may be determined from measured values of the coherent-scatttering cross section. In fact, if we introduce the notation $\xi = 4\pi/\lambda$, it follows from (5) that

$$i(\xi) = \frac{1}{4\pi a_{\text{coh}}^2} \frac{1}{\xi} \frac{d}{d\xi} [\xi^2 \sigma_{\text{tot}}^{\text{coh}}(\xi)]. \qquad (6)$$

Declassified and Approved For Release 2013/09/24 : CIA-RDP10-02196R000700010005-2

Declassified and Approved For Release 2013/09/24 : CIA-RDP10-02196R000700010005-2

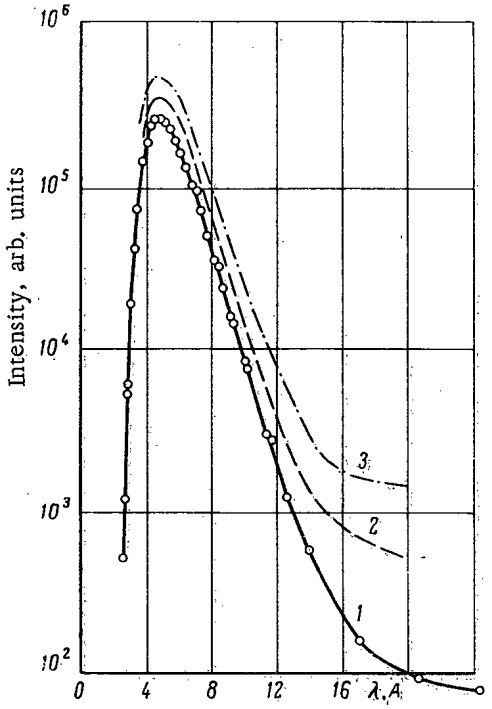

Fig. 3. Neutron spectrum measured by means of a mechanical monochromator after passing through the beryllium filter: 1) immediate results of measurements; 2) with the introduction of a correction for attenuation of the neutrons in the air on the way from the channel exit to the counter; 3) with further allowance for the attenuation of the neutrons in the air channel of the reactor.

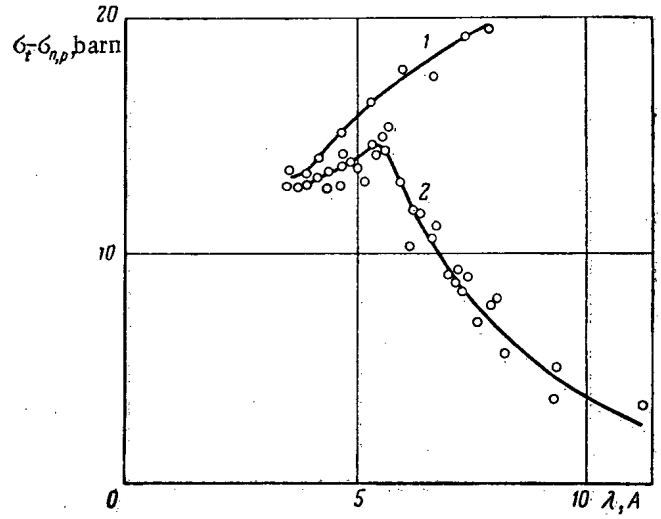

Fig. 4. Variation of the total scattering cross section of liquid nitrogen with wavelength (measured by means of the mechanical neutron interruptor with resolution 16 μsec/m and the mechanical neutron monochromator): 1) gaseous nitrogen at pressure 8.5 atm; 2) liquid, sample thickness 7.5, 10, and 29 mm. Cross section of (n, p) reaction reckoned on 1/v law.

We note once more that all these considerations have a qualitative character, since we cannot in reality separate out a part of the neutron cross section corresponding to scattering without energy transfer.

The effects described above were first observed experimentally in sulfur, lead, and bismuth by Chamberlain and a little later in helium by Somers et al. [4]. Coherent processes in the scattering of neutrons in liquids without energy exchange were first discussed in detail in [5].

Below, we present some results of measuring the total neutron cross sections of liquid oxygen and nitrogen and gaseous nitrogen as a function of neutron wavelength in the VVR-M reactor of the Institute of Physics, Academy of Sciences, UkrSSR. Nitrogen and oxygen have large coherent cross sections (11.0 and 4.2 barn respectively) and are, therefore extremely suitable for observing coherent effects in the scattering of slow neutrons.

EXPERIMENT

The total neutron cross sections were determined from the transparencies T of the samples:

$$\sigma_t = -\frac{1}{nx} \ln T. \tag{7}$$

The liquid nitrogen was at the boiling point of 77°K. To determine its cross section, samples 7.4, 10, and 29 mm thick were used. Measurements without sample were made by replacing the nitrogen with aluminum containers. The liquid oxygen was at its boiling point; the sample thickness was 29 mm.

For measuring the cross section of gaseous nitrogen, two cylindrical containers with Duralumin tops were made. The length of these was 50 cm and the diameter 60 mm. One of the containers was filled with nitrogen up to a pressure of 8.5 atm, the second was pumped out to 10^{-1} mm Hg. For determining the transparency of the nitrogen, these containers were placed in turn in the neutron beam.

Declassified and Approved For Release 2013/09/24 : CIA-RDP10-02196R000700010005-2

Declassified and Approved For Release 2013/09/24 : CIA-RDP10-02196R000700010005-2

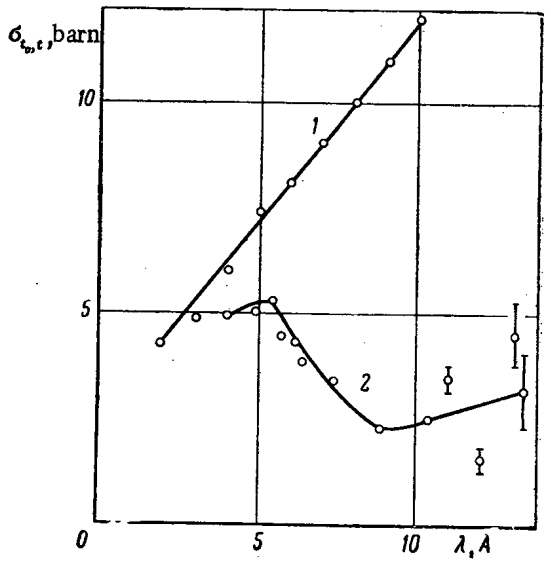

Fig. 5. Total cross section of oxygen: 1) gas [7]; 2) liquid; measured by means of the mechanical monochromator.

The arrangement of the experiment is indicated in Fig. 1. For reducing the background of fast neutrons a liquid-nitrogen-cooled beryllium filter 9 cm in diameter and 25 cm thick was used. The variation of the cross section of liquid nitrogen with wavelength was determined by the time-of-flight method by means of a mechanical neutron interruptor and a mechanical neutron monochromator with a longitudinal axis of rotation. The neutrons were controlled by a battery of ten Born counters SNMO-5 set at 3 m from the sample. The maximum height of the counting space was 18.5 cm, the breadth 10 cm, and the depth 12 cm. The flight time was measured with a multichannel analyzer with ferrite memory. In order to indicate the resolution of the systems, Figs. 2 and 3 show neutron spectra after passing through the beryllium filter. The wavelength graduation for the mechanical monochromator was effected with respect to gold. The cross sections of liquid nitrogen were determined for various dimensions of the counting surface and with samples of various thickness (T = 0.2 to 0.75). Various methods of monochromatizing the neutrons were used. The results are in mutual agreement.

The cross sections of liquid oxygen and gaseous nitrogen were only measured by means of the mechanical monochromator.

RESULTS OF MEASUREMENTS AND DISCUSSION

The results of determining the cross sections are shown in Figs. 4 and 5. By comparing the graphs we see a sharp difference between the behavior of the cross sections for the gases and liquids. For the liquids there is quite a sharp fall in cross section after $\lambda \approx 5.5$ A. This effect may naturally be ascribed to the existence of short-range order in the liquids. The angular distribution of scattered neutrons with $\lambda = 1.08$ A in liquid oxygen and nitrogen was studied in [6]. In principle the value of $i(s) = \frac{I(s)-I_\infty}{I_\infty}$, where $I(s)$ is the observed scattering intensity, and $I_\infty = \lim_{s \to \infty} I(s)$ could be obtained from these data. There are difficulties, however, in determining I_∞. These were aggravated by the fact that we only had graphs taken from a journal article at our disposal. The inaccuracies in determining I_∞ are increased on using formula [5] owing to the factor λ^2. We should therefore not expect any quantitative agreement between the transformed results of [6] and our measured total cross sections. We made a transformation of the data for nitrogen [6] in accordance with Eq. (5). In order to make the cross section positive, a constant quantity differing from the constant determined from the graph of [6] had to be added at each point. The variation of the elastic-scattering cross sections so obtained with wavelength is shown in Fig. 6. This is noticeably similar to the experimental curves. The maxima for nitrogen in both cases lie at $\lambda \approx 5.5$ A. In general, the effect of the fall in cross section for waves corresponding to the position of the maximum in i(s) must be expected for all liquids in which the coherent scattering cross section is comparable with or much larger than the incoherent and reaction cross sections. The fall in the neutron cross sections of D_2O [7] at 0.002 eV may also be connected with the effect of coherent scattering. In fact, using the angular distribution of neutrons with $\lambda = 1.12$ A scattered in heavy water measured in [8], together with relation (5), we can show that σ_{elas}^{coh} varies sharply for $E_{neut} \sim 0.002$ eV ($\lambda = 6.26$ A).

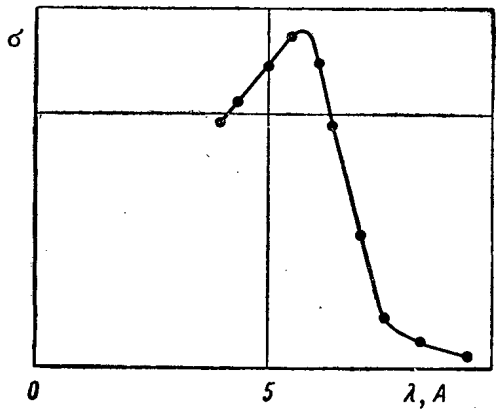

Fig. 6. Variation of the total elastic coherent neutron-scattering cross section in liquid nitrogen with wavelength, as obtained from neutron-diffraction data [4].

From the energy dependence of the neutron cross sections in the liquid phase, we can estimate the upper limit of the

Declassified and Approved For Release 2013/09/24 : CIA-RDP10-02196R000700010005-2

Declassified and Approved For Release 2013/09/24 : CIA-RDP10-02196R000700010005-2

inelastic-scattering cross section. This is smaller than that predicted by the Nelkin-Krieger model. The discrepancies are to a certain extent connected with the inaccuracy of this model. They may also be connected, however, with the retardation of molecular rotation (x-ray and neutron-diffraction data indicate that oxygen and at any rate nitrogen are molecular liquids [3, 6]). Hence, the measurement of total neutron cross sections over a wide temperature and pressure range may enable us to follow the process of the retardation of molecular rotation on approaching the condensed state.

In conclusion the authors consider it their duty to thank V. A. Gul'ko, V. F. Razbudei, V. L. Nechitailo, and V. A Medvedev for help in the work.

LITERATURE CITED

1. L. Van Hove, Phys. Rev., 95, 249 (1954).
2. G. Vineyard, Phys. Rev., 110, 999 (1958).
3. N. Gingrich, Rev. Mod. Phys., 15, 90 (1943).
4. O. Chamberlain, Phys. Rev., 77, 305 (1950).
5. H. Sommers et al., Phys. Rev., 97, 855 (1955); L. Goldstein, Phys. Rev., 84, 466 (1951).
6. D. Hershaw et al., Phys. Rev., 92, 1226 (1958).
7. J. Hughes, Neutron cross sections, BNL-325 (1958).
8. B. Brockhou, Nuovo cimento, 9, 45 (1958).

Declassified and Approved For Release 2013/09/24 : CIA-RDP10-02196R000700010005-2

Declassified and Approved For Release 2013/09/24 : CIA-RDP10-02196R000700010005-2

TOTAL AND DIFFERENTIAL FISSION CROSS SECTIONS OF URANIUM AND THORIUM FOR LOW ENERGY DEUTERONS

(UDC 539.172.13 + 539.17.015)

Yu. A. Nemilov, V. V. Pavlov, Yu. A. Selitskii,
S. M. Solov'ev, and V. P. Éismont

Translated from Atomnaya Énergiya, Vol. 18, No. 5,
pp. 456-459, May, 1965
Original article submitted June 23, 1964

A method of recording fission fragments with glasses is used for determining the total and differential fission cross sections of Th^{232}, U^{233}, U^{235}, and U^{238} for deuterons with energy considerably below the Coulomb barrier – 6.6 MeV and less. The results are compared with data from published papers in which the same quantities were studied by means of semiconductor detectors in the region of high-energy deuterons. New facts are noted, which indicate that for nuclei with different neutron fission thresholds, as a result of irradition with sub-barrier deuterons, the reactions preceding fission may differ considerably.

In recent years, due to the development of techniques for recording fission fragments (especially semiconductor detectors and mica [1] and glass [2] methods) the study of the fission of heavy nuclei by charged particles with energy below the Coulomb barrier has been made possible. Thus, by means of semiconductor detectors, in [3] the fission cross sections for Th^{232}, U^{233}, U^{235} and U^{238} were determined for deuterons with energies of 5.8-6.6 MeV, in [4]—the fission cross sections of Th^{232} and U^{238} for protons and deuterons with energies 3-12 and 6-12 MeV respectively, and in [5]—the cross sections and angular anisotropy were measured for the fission of Th^{232}, U^{233} and U^{235} by deuterons with energy 8-20 MeV.

In the present project a method of recording fission fragments with glass plates was used, which enabled the total as well as the differential cross sections to be measured at even lower deuteron energies. Investigations with sub-barrier deuterons are of particular interest since it was established earlier in [3] that different reactions precede fission in different nuclei: in the even-even nuclei Th^{232} and U^{238}, which have a high deuteron fission threshold, fission is originated mainly by the complete merging of the deuterons with the target nucleus, while with nuclei with odd number of neutrons U^{233}, and U^{235}, which are fissioned by thermal neutrons, fission takes place principally as a result of capture of a neutron in a stripping reaction. In the first case, a nucleus with high excitation but small angular momentum is formed, since for sub-barrier deuterons central collisions are the most effective. In the second case, on the contrary, excitation of the nucleus due to the transfer of energy to the stripping proton may turn out to be very low, close to the fission threshold, but the moment may be relatively high [6]. The differences in parity of the number of nucleons, the energy of excitation and the angular momentum of the fissioning nucleus should be reflected in the probability of fission and in the angular distribution of the fission fragments.

PROCEDURE FOR THE INVESTIGATION

The principal complexity in investigating the fission of nuclei by charged particles consists in the fact that such fission fragment detectors as ionization chambers, scintillation counters, semiconductor detectors, photoemulsions can be overloaded by background from particles which are scattered by the target. The method of capture by foils also has considerable disadvantages which are associated with the unavoidable reduction of the recording efficiency by the complexity and uncertainty of the chemical separation of the elements.

It was reported in [1, 2] that in the surface layer of mica or glass, fission fragments produce such significant damage that subsequent etching by fluoric acid forms craters, easily visible under the microscope even at low magnification. In the present paper, glasses were used as the most simple and most convenient method of recording fission fragments.

Declassified and Approved For Release 2013/09/24 : CIA-RDP10-02196R000700010005-2

Declassified and Approved For Release 2013/09/24 : CIA-RDP10-02196R000700010005-2

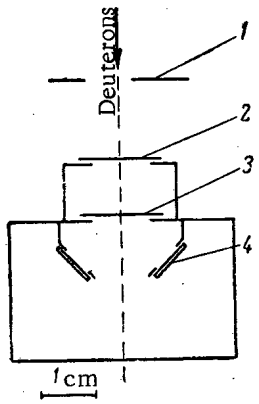

Fig. 1. Diagram of the fission cross section measurement: 1) diaphragm; 2) foil for varying the deuteron energy; 3) target; 4) glass plate for recording fission fragments of nuclei.

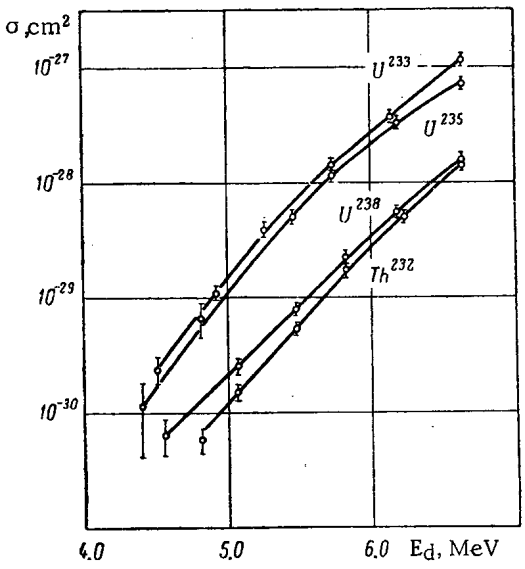

Fig. 2. Relationship between the fission cross section σ and the deuteron energy E_d.

It is desirable that there should be the smallest possible structural damage and nonuniformities on the surface of the glass. Normal photographic plates are completely suitable for this, protected from damage by a layer of emulsion, which has been carefully stripped from the functional surface with a 3% solution of fluoric acid. The exposed plates were etched in acid of the same concentration and were examined under the microscope at ×200 magnification. The irradiation geometry ensured an almost perpendicular path for the fission fragments into the glass surface (in this case, the recording efficiency is 100%). The glasses were put on metallic holders with openings 7 × 7 mm for fission cross section measurements and 6 × 16 mm in the case of measurements of the fission fragment angular distribution.

Targets of uranium and thorium, with a thickness of ~ 200 μg/cm², were prepared by evaporation in vacuo of the fluorides [7] on thin silver backings 2 × 2 cm and with a weight of ~ 500 μg/cm², stuck to the framework of a copper foil. The silver films were quite stable and did not change under the action of the beam of charged particles, absorbing only a small fraction of the fission fragment energy.

The accuracy of determining the energy of the deuterons, which were accelerated in a cyclotron, was 0.1 MeV. In order not to worsen the geometrical resolving power, in the experiments for measuring the angular distribution of the fission fragments, the energy of the deuterons was varied within small limits in the cyclotron itself, and in the case of cross section measurements reduction of energy from the primary value (6.6 MeV) was carried out by retardation in platinum foils. The maximum half-width of the deuterons in the energy spectrum, due to the retardation, did not exceed 2%. The deutron current passing through the target, equal to ~ 0.5 μa, was measured with a current integrator.

FISSION CROSS SECTIONS

A diagram of the experiment for measuring the fission cross sections is shown in Fig. 1. In order to eliminate the distortions in measuring the deuteron current, on the last collimating diaphragm, located outside the influence of the direct beam, a potential of 200 V was applied which prevented the escape of secondary electrons from the surface of the filter. In the measurements undertaken in this project, primary consideration was given to the relative nature of the dependence of the cross section on the deuteron energy; absolute values were obtained which were normalized with respect to previous data for E_d = 6.6 MeV [3], and which for Th^{232} and U^{238} agree with the results of [4]. As the experimental results showed, the measurement of a fission cross section of ~ 10^{-32} cm² by means of glasses is not very complex, but in the case of deuteron irradiation of nuclei the background of neutrons formed by light nuclei as a result of (d, n) reactions is a hindrance.

The effect of the neutrons from fluorine was estimated by comparing a number of targets of different weight. The background determination in this case was based on the fact that the number of nuclear fissions by the deuterons is proportional to the target weight, but the number of fissions by neutrons from the fluorine is proportional to the square of the target weight. The fission cross sections of nuclei, with the background taken into account, is shown in Fig. 2. The steeper decrease of σ_f for U^{235} and U^{233} in the region of small deuteron energies may be connected with

Declassified and Approved For Release 2013/09/24 : CIA-RDP10-02196R000700010005-2

Declassified and Approved For Release 2013/09/24 : CIA-RDP10-02196R000700010005-2

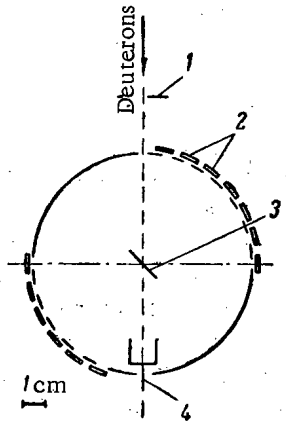

Fig. 3. Arrangement for measuring the angular distribution of the fission fragments: 1) diaphragm; 2) glass plate, for recording fission fragments from nuclei; 3) target; 4) Faraday cylinder.

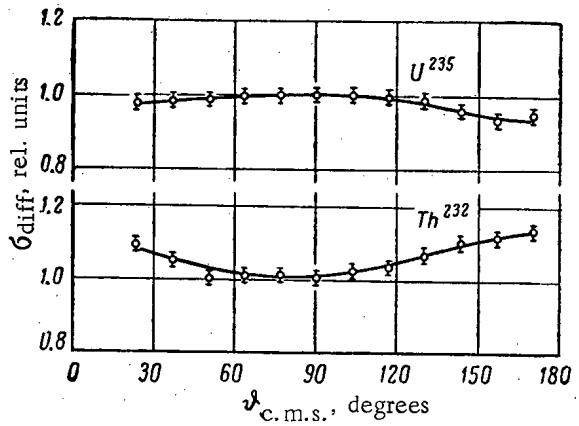

Fig. 4. Relationship between the differential fission cross section and the angle in the center of mass system (c.m.s.) relative to the direction of the neutron beam for Th^{232} and U^{235}.

the gradual reduction of the fraction of fissions after the (d, p) reaction because of insufficient excitation of the nuclei for subsequent fission. It follows from the data given below that the angular anisotropy of the fission fragments is of low magnitude, and, consequently, the corresponding corrections were not introduced into the cross section.

The cross section curve for U^{233} (see Fig. 2) falls somewhat more abruptly in comparison with the previous measurements [3], which is explained, probably, by taking a more accurate account of the background of fission neutrons formed in the target.

ANGULAR ANISOTROPY

In preparing the experiment, the fact was taken into account that the anisotropy of the angular distribution of the fission fragments may be small, and, consequently, the geometrical resolving power must be combined with high statistical accuracy.

The structure and dimensions of the chamber used for measuring the angular distribution of the fission fragments are shown in Fig. 3. Thirteen glass plates allowed the fission fragments to be recorded simultaneously at 12 angles over the range from 23° to 170° relative to the direction of motion of the deuterons with an aperture of angle on each of the plates equal to 7°. Central passage of the beam of deuterons through the target was ensured by collimators and was controlled by adjusting the chamber and by coincidence of the number of recorded fission fragments on pairs of glasses located at an angle of 90° to the direction of the beam. The number of fission fragments recorded by a single plate was 2000-4000.

It was established that for all nuclei the differential fission cross sections over the range of deuteron energies investigated vary smoothly within small limits, and, therefore, we have limited ourselves to showing the groups corrected for the effect of motion of the center of mass,* only for Th^{232} and U^{235} for E_d = 6.6 MeV (Fig. 4), and the remaining results are given in the table. Two facts should be noted: 1) the small anisotropy value in all cases; 2) the "anomalous" nature of the anisotropy for U^{235}, consisting in the fact that in contrast to other nuclei, the angular distribution of the fission fragments has a maximum not at 0°but at 90°. Both the facts noted are due to the nature of the interactions leading to fission and in the new aspect they confirm the conclusions reached in [3]. The low anisotropy value for Th^{232} and U^{238} is associated with the fact that fission of these nuclei by sub-barrier deuterons takes place because of the complete coalescence of the deuteron with the target, leading to a compound nucleus with a high energy of excitation but with a small angular momentum. Fission of U^{233} and U^{235} takes place primarily as a result of a (d, p) stripping reaction; in this case, the anisotropy is found to be small, obviously, because the orbital momentum of the neutron entering the nucleus (at such low deuteron energies) is also small and there is no sharp orientation relative to the beam of deuterons. Even the excitation of the nucleus, fissioning after stripping, must be

*A correction to the impulse of fissioning nucleus was introduced in all cases on the assumption of total coalescence of the deuteron with the target nucleus. It can be seen from Fig. 4 that for U^{235}, the cross section at an angle of 10° to the deuteron beam was found to be somewhat larger than the cross section at an angle of 170°, which is possibly associated with the momentum produced by the proton from the stripping recoiling backwards.

Declassified and Approved For Release 2013/09/24 : CIA-RDP10-02196R000700010005-2

Declassified and Approved For Release 2013/09/24 : CIA-RDP10-02196R000700010005-2

Magnitude of Fission Anisotropy, More Precisely $\frac{\sigma(10°)+\sigma(170°)}{2\sigma(90°)}$ for Various Nuclei and Neutron Energies

E_d, MeV	$_{159}U^{233}$	U^{235}	U^{238}	Th^{232}
6.6	1.05± 0.03	0.95± 0.03	1.05± 0.03	1.10± 0.03
6.0	1.08± 0.03	0.95± 0.03	1.00± 0.04	1.10± 0.04

small. The anomalous anisotropy of U^{235} also confirms this, since the latter is possible only for a small number of open fission channels [9-11].

On the basis of the concepts developed, it is possible to give a first opinion on the strange fact noted in [5]: despite the normal dependence of fission anisotropy of strongly excited nuclei on the parameter Z^2/A, in the region of sub-barrier deuteron energies the anisotropy for U^{233} was found to be not less but greater in comparison with U^{238} This relationship is not surprising if one takes into account that because of the difference in the reactions, excitation of the U^{238} nucleus is considerably less than excitation of the U^{233} nucleus. Further, when fission takes place by an identical route, for example, in the case of irradiation by sub-barrier deuterons of Th^{232} and U^{238}, the anisotropy for the nucleus with the lowest parameter Z^2/A, i.e., Th^{232}, is found to be the greater (see table), which also should be expected.

From comparison of our data on U^{235} with the results of [5], it can be seen that the increase of anisotropy reported for E_d = 7 MeV is associated with statistical deviations.

In conclusion, the authors express their thanks to the group of staff responsible for operation of the cyclotron.

LITERATURE CITED

1. P. Price and R. Walker, Phys. Rev. Letters, 3, 113 (1962).
2. V. P. Perelygin, S. P. Tret'yakova, and I. Zvara, Preprint OIYaI P-1323 [in Russian], Dubna (1963).
3. G. I. Marov et al., ZhÉTF, 44, 1445 (1963).
4. G. Choppin, J. Meriwether, and J. Fox, Phys. Rev., 131, 2149 (1963).
5. G. Bate, R. Chaudhry, and J. Huizenga, Phys. Rev., 131, 722 (1963).
6. H. Britt et al., Bull. Amer. Phys. Soc., S2, 8, 525 (1963).
7. A. I. Baranov et al., Pribory i tekhnika éksperimenta, No. 5, 173 (1962).
8. V. Elmor and M. Sands, Electronics in Nuclear Physics [Russian translation], Izd-vo, IL, Moscow (1953).
9. O. Bor, in the book: "Data from the International Conference on the Peaceful Uses of Atomic Energy (Geneva, 1955)" 2, [in Russian], Fizmatgiz, Moscow (1958), p. 175.
10. V. M. Strutinskii, ZhÉTF, 30, 606 (1956).
11. L. Welets and D. Chase, Phys. Rev., 103, 1296 (1956).

All abbreviations of periodicals in the above bibliography are letter-by-letter transliterations of the abbreviations as given in the original Russian journal. *Some or all of this periodical literature may well be available in English translation.* A complete list of the cover-to-cover English translations appears at the back of this issue.

Declassified and Approved For Release 2013/09/24 : CIA-RDP10-02196R000700010005-2

Declassified and Approved For Release 2013/09/24 : CIA-RDP10-02196R000700010005-2

AN EXACT GENERAL SOLUTION IN SPHERICAL HARMONICS OF THE BOLTZMANN EQUATION

(UDC 621.039.51)

G. Ya. Rumyantsev

Translated from Atomnaya Énergiya, Vol. 18, No. 5,
pp. 459-463, May, 1965
Original article submitted May 18, 1964

A solution of the one-velocity kinetic Boltzmann equation is obtained as a series of spherical harmonics. General expressions are obtained for the terms of the series, derived without any approximately valid assumptions. As particular cases of this solution, we obtain formulas for the known P_N-approximations for the spherical-harmonic method.

The exact general solution of the kinetic equation in the form of a series of spherical harmonics contains arbitrary functions which must depend on the formulation of boundary conditions. The general determination of the boundary conditions and the arbitrary functions is not considered. All the results of [4] remain valid for P_N-approximations.

The well-known and usually very effective spherical-harmonic method [1-6], by which the integro-differential Boltzmann equation is reduced to an infinite system of differential equations, is always applied in a P_N-approximation. In this approximation only the first N + 1 equations of the system are solved under the artificial condition that the spherical harmonic of number N + 1 be identically zero. In some cases, however, this condition is too rough, and for small values of N the spherical-harmonic method, in the form in which it is at present used, leads to large errors.

In the present work, we give an exact solution of the infinite system of equations obtained by the spherical-harmonic method; this solution is essentially equivalent to an exact solution of the Boltzmann equation. Our solution is general, i.e., it is not subject to any boundary conditions, and so it is determined with a precision up to certain arbitrary functions. We do not consider the formulation of boundary conditions and the solution of concrete physical problems in the present work. Different approximate approaches to this problem are possible, the use of which would obviously considerably broaden the range of applicability of the spherical-harmonic method. The ordinary P_N-approximations together with the appropriate boundary conditions are easily obtained as special cases of the general solution.

Harmonic Polynomials and Vector Operators

We seek the solution of the one-velocity kinetic Boltzmann equation in the form

$$F(\mathbf{r}, \Omega) = \frac{1}{4\pi} \sum_{n=0}^{\infty} (2n+1)\, Y_n(\mathbf{r}, \Omega). \tag{1}$$

All the notation is the same as in [4] except when differences are specifically mentioned. Each spherical harmonic Y_n corresponds to a homogeneous harmonic field U_n:

$$U_n(\mathbf{r}, \mu) = \mu^n Y_n(\mathbf{r}, \Omega). \tag{2}$$

We note that U_n, being a polynomial in μ_x, μ_y and μ_z, satisfies in the space μ the Laplace equation

$$\dot{\nabla}^2 U_n = 0. \tag{3}$$

Declassified and Approved For Release 2013/09/24 : CIA-RDP10-02196R000700010005-2

Declassified and Approved For Release 2013/09/24 : CIA-RDP10-02196R000700010005-2

The coefficients of the polynomial are functions of r. We consider those polynomial satisfying the equation

$$\nabla^2 U_n = \varkappa^2 U_n, \tag{4}$$

in the space r, where $\varkappa^2$ is a constant, for the moment arbitrary.

Let the operator $(\mu\nabla)^l$ denote the l-tuple application of the operator $(\mu\nabla)$. Polynomials in $(\mu\nabla)$ introduced below will have their obvious meaning. We now demonstrate the theorem that enables us to obtain an exact expression for any term of the series (1).

Theorem. If f_k is a harmonic polynomial of degree k satisfying

$$(\dot{\nabla}\dot{\nabla}) f_k = 0; \quad \nabla^2 f_k = \varkappa^2 f_k, \tag{5}$$

then the operator $\mu^{n-k} P_n^{(k)}\left(\frac{\mu\nabla}{\mu\varkappa}\right)$ converts it into a harmonic polynomial of degree n. Here and below $P_n^{(k)}(t) = d^k/dt^k P_n(t)$, where $P_n(t)$ is a Legendre polynomial.

Proof. The operator $\mu^{n-k} P_n^{(k)}\left(\frac{\mu\nabla}{\mu\varkappa}\right)$ is a homogeneous polynomial of degree n−k in μ_x, μ_y, and μ_z, since it is a linear combination of expressions of the type

$$\mu^{2q}\left(\frac{\mu\nabla}{\varkappa}\right)^{n-k-2q} \quad \text{or} \quad (\mu_x^2 + \mu_y^2 + \mu_z^2)^q \left(\frac{\mu\nabla}{\varkappa}\right)^{n-k-2q},$$

where $0 \leq q \leq n-k/2$. Hence $\mu^{n-k} P_n^{(k)}\left(\frac{\mu\nabla}{\mu\varkappa}\right) f_k$ is a homogeneous polynomial of degree n. It remains to prove that this polynomial satisfies the Laplace equation:

$$\dot{\nabla}^2 \mu^{n-k} P_n^{(k)}\left(\frac{\mu\nabla}{\mu\varkappa}\right) f_k = 0, \tag{6}$$

i.e., that it is harmonic.

This is proved by induction. We first show that Eq. (6), for a fixed k, is satisfied for any value of n if it holds for n−1 and n−2.

The operational relations needed for the proof are the following:

$$\dot{\nabla}^2 (\mu\nabla) = (\mu\nabla)\dot{\nabla}^2 + 2(\nabla\dot{\nabla}); \tag{7}$$

$$\dot{\nabla}^2 \mu^2 = \mu^2 \dot{\nabla}^2 + 4(\mu\dot{\nabla}) + 6; \tag{8}$$

$$(\nabla\dot{\nabla})\,\mu^{2k}(\mu\nabla)^l = \mu^{2k}(\mu\nabla)^l(\nabla\dot{\nabla}) + \frac{(\mu\nabla)}{\mu}\frac{\partial[\mu^{2k}(\mu\nabla)^l]}{\partial\mu} + \nabla^2\frac{\partial[\mu^{2k}(\mu\nabla)^l]}{\partial(\mu\nabla)}. \tag{9}$$

We also need the following recurrence relations for derivatives of the Legendre polynomials*:

$$(n-k)P_n^{(k)}(t) = (2n-1)tP_{n-1}^{(k)}(t) - (n+k-1)P_{n-2}^{(k)}(t); \tag{10}$$

$$(n-k-1)tP_{n-1}^{(k)}(t) + (1-t^2)P_{n-1}^{(k+1)}(t) = (n+k-1)P_{n-2}^{(k)}(t). \tag{11}$$

For brevity we use the notation

$$P_n^{(k)}\left(\frac{\mu\nabla}{\mu\varkappa}\right) \equiv P_n^{(k)}\left(\frac{\Omega\nabla}{\varkappa}\right) \equiv \hat{\mathbf{P}}_n^{(k)}. \tag{12}$$

Using (10), we write

$$\mu^{n-k}\hat{\mathbf{P}}_n^{(k)} = \frac{1}{n-k}\left[(2n-1)\frac{\mu\nabla}{\varkappa}\mu^{n-k-1}\hat{\mathbf{P}}_{n-1}^{(k)} - (n+k-1)\mu^2\mu^{n-k-2}\hat{\mathbf{P}}_{n-2}^{(k)}\right]. \tag{13}$$

*It is possible that (11) is not in the literature. It can be derived from other known recurrence relations.

Declassified and Approved For Release 2013/09/24 : CIA-RDP10-02196R000700010005-2

Declassified and Approved For Release 2013/09/24 : CIA-RDP10-02196R000700010005-2

Now using (7) and (8) and assuming that (6) holds for n − 1 and n − 2, we obtain

$$\dot{\nabla}^2\mu^{n-k}\hat{\mathbf{P}}_n^{(k)}f_k=\frac{1}{n-k}\left\{(2n-1)\,2\,\frac{(\dot{\nabla}\dot{\nabla})}{\varkappa}\,\mu^{n-k-1}\hat{\mathbf{P}}_{n-1}^{(k)}-(n+k-1)\,[4\,(\mu\dot{\nabla})+6]\,\mu^{n-k-2}\hat{\mathbf{P}}_{n-2}^{(k)}\right\}f_k. \quad (14)$$

To an operator of the form $\frac{(\dot{\nabla}\dot{\nabla})}{\varkappa}\,\mu^{n-k-1}\hat{\mathbf{P}}_{n-1}^{(k)}$ we apply the formula (9) and, using (5), we have

$$\frac{(\dot{\nabla}\dot{\nabla})}{\varkappa}\,\mu^{n-k-1}\hat{\mathbf{P}}_{n-1}^{(k)'}f_k=\mu^{n-k-2}\times\left\{(n-k-1)\,\frac{(\mu\nabla)}{\mu\varkappa}\,\hat{\mathbf{P}}_{n-1}^{(k)}+\left[1-\left(\frac{\mu\nabla}{\mu\varkappa}\right)^2\right]\hat{\mathbf{P}}_{n-1}^{(k+1)}\right\}f_k \quad (15)$$

or, from (11),

$$\frac{(\nabla\dot{\nabla})}{\varkappa}\,\mu^{n-k-1}\hat{\mathbf{P}}_{n-1}^{(k)}f_k=(n+k-1)\,\mu^{n-k-2}\hat{\mathbf{P}}_{n-2}^{(k)}f_k. \quad (16)$$

We substitute the last expression in the right-hand side of (14) and eliminate the operator $(\mu\dot{\nabla})$ by using the Euler identity:

$$(\mu\dot{\nabla})\mu^{n-k-2}\hat{\mathbf{P}}_{n-2}^{(k)}f_k=(n-2)\,\mu^{n-k-2}\hat{\mathbf{P}}_{n-2}^{(k)}f_k. \quad (17)$$

(17)

The relation (17) is a consequence of the fact that the expression $\mu^{n-k-2}\hat{\mathbf{P}}_{n-2}^{(k)}f_k$ is a homogeneous polynomial of degree n − 2.

Using (16) and (17), we find that

$$\dot{\nabla}^2\mu^{n-k}\hat{\mathbf{P}}_n^{(k)}f_k=0. \quad (18)$$

Hence, for the above assumptions a homogeneous polynomial of degree n of the form $\mu^{n-k}\hat{\mathbf{P}}_n^{(k)}f_k$ is harmonic.

We have n ≥ k in all expressions, and so for the completion of the proof, it is sufficient to prove that (18) is satisfied for n = k and n = k + 1. This is done directly:

for n = k

$$\dot{\nabla}^2\hat{\mathbf{P}}_k^{(k)}f_k=\text{const}\,\dot{\nabla}^2f_k=0;$$

for n = k + 1

$$\dot{\nabla}^2\mu\hat{\mathbf{P}}_{k+1}^{(k)}f_k=\text{const}\,\dot{\nabla}^2\,(\mu\nabla)\,f_k=\text{const}\,[(\mu\nabla)\,\dot{\nabla}^2+2\,(\nabla\dot{\nabla})]\,f_k=0.$$

Consequences of the theorem. Every harmonic polynomial U_n, satisfying the equation

$$\nabla^2U_n=\varkappa^2U_n, \quad (19)$$

Can be written as a sum:

$$U_n=\sum_{k=0}^{n}\mu^{n-k}\hat{\mathbf{P}}_n^{(k)}f_k. \quad (20)$$

It is easily shown that the terms of this sum cannot be linearly dependent, and that the sum is a harmonic polynomial of general type.

Setting $\mu = 1$ in (20), we obtain an expression for the spherical harmonic Y_n:

$$Y_n=\sum_{k=0}^{n}\hat{\mathbf{P}}_n^{(k)}y_k, \quad (21)$$

where $y_k = [f_k]_{\mu=1}$ is a spherical harmonic of order k.

Declassified and Approved For Release 2013/09/24 : CIA-RDP10-02196R000700010005-2

Declassified and Approved For Release 2013/09/24 : CIA-RDP10-02196R000700010005-2

The Solution of the Kinetic Equation

The solution of the homogeneous equation is of special interest and so, because of the brevity of this article, we will consider the one-velocity kinetic Boltzmann equation only for a source-free medium:

$$(\Omega\nabla) F(\mathbf{r}, \Omega) + \Sigma F(\mathbf{r}, \Omega) - \Sigma_s \int_{4\pi} F(\mathbf{r}, \Omega') W(\Omega', \Omega)\, d\Omega' = 0. \tag{22}$$

Substituting the function $F(\mathbf{r}, \Omega)$ in the form (1) into Eq. (22), we obtain

$$\sum_{n=0}^{\infty} (2n+1)\left[(\Omega\nabla) Y_n + \Sigma_n Y_n\right] = 0, \tag{23}$$

where $\Sigma_n = \Sigma - \Sigma_s c_n$ and the c_n are the coefficients in the expansion of the scattering indicatrix (for more details see [4])*.

We now express Y_n in the form (21) and use (10). In order not to mix functions y_k belonging to different harmonics Y_n, we use for them the notation y_{nk}, and remember in the following that the order of the spherical harmonics $y_{nk}(\mathbf{r}, \Omega)$ is determined only by the second subscript. Then (23) becomes

$$\sum_{n=0}^{\infty} \sum_{k=0}^{n} \{\varkappa\left[(n-k+1)\hat{\mathbf{P}}_{n+1}^{(k)} + (n+k)\hat{\mathbf{P}}_{n-1}^{(k)}\right] y_{nk} + (2n+1)\Sigma_n \hat{\mathbf{P}}_n^{(k)} y_{nk}\} = 0. \tag{24}$$

If the linearly independent terms of the expression in (24) are equated to zero, we obtain

$$\varkappa\left[(n-k)\, y_{n-1,k} + (n+k+1)_{n+1,k}\right] + (2n+1)\Sigma_n y_{nk} = 0. \tag{25}$$

This relation enables us to express all the functions y_{nk} in terms of y_{kk}. We assume that

$$y_{nk} = (-1)^{n-k} M_{nk} y_{kk}, \tag{26}$$

where we obviously have $M_{kk} = 1$.

We now introduce the notation $\nu = \Sigma/\varkappa$ and $\varepsilon_n = \Sigma_n/\Sigma$. The relation (25) now yields the recurrence relation

$$(n+k+1) M_{n+1,k} = (2n+1)\nu\varepsilon_n M_{nk} - (n-k) M_{n-1,k}, \tag{27}$$

for the coefficients M_{nk}, and so these coefficients are polynomials of degree $n-k$ in ν, where each of these polynomials contain either purely even or purely odd powers of ν.

In (25) and (27) there are quantities with the same subscripts k, and so for each k there is an independent infinite sequence of functions y_{nk} beginning with the function y_{kk}. In the general solution the functions y_{kk} are arbitrary except for the fact that, from the assumption, they must satisfy the equations

$$(\nabla\dot{\nabla})\,\mu^k y_{kk} = 0; \tag{28}$$

$$\nabla^2 y_{kk} = \left(\frac{\Sigma}{\nu}\right)^2 y_{kk}. \tag{29}$$

In concrete problems, the form of the functions y_{kk} is determined by the geometry of the medium and the boundary conditions. Substituting (26) in (21), we obtain

$$Y_n(\mathbf{r}, \Omega, \nu) = \sum_{k=0}^{n} (-1)^{n-k} M_{nk}(\nu)\, \hat{\mathbf{P}}_n^{(k)} y_{kk}(\mathbf{r}, \Omega, \nu). \tag{30}$$

*In [4] $\Sigma_n = (2n+1)(\Sigma - \Sigma_s c_n)$.

Declassified and Approved For Release 2013/09/24 : CIA-RDP10-02196R000700010005-2

Declassified and Approved For Release 2013/09/24 : CIA-RDP10-02196R000700010005-2

All real angular distributions are such that the functions Y_n in the expansion (1) cannot increase indefinitely with increasing n. We require that the coefficients $M_{nk}(\nu)$ also satisfy this condition. An investigation of the relation (27) shows that the functions $M_{nk}(\nu)$ are bounded for all real ν in the region $\nu | < 1$ and for certain values $\nu = \pm \nu_k$ in $| \nu . | > 1$. Hence, the general expression for the spherical harmonic of order n must be

$$Y_n(\mathbf{r}, \Omega) = \sum_{k=0}^{n} (-1)^{n-k} \left\{ M_{nk}(\nu_k) \hat{P}_n^{(k)} y_{kk}(\mathbf{r}, \Omega, \nu_k) + \int_0^1 M_{nk}(\nu) \hat{P}_n^{(k)} y_{kk}(\mathbf{r}, \Omega, \nu)\, d\nu \right\}. \quad (31)$$

The integration here is only for positive values of ν, since the general form of the functions y_{kk} for the complete solution in the large is independent of the sign of ν. The numbers ν_k can always be given a plus sign. The values of the ν_k depend only on the physical properties of the medium. In each concrete case, the ν_k can in principle be calculated with any desired degree of accuracy.

P_N-Approximations of the Spherical-Harmonic Method

As a special case of (31), we can obtain formulas for the P_N-approximations of the spherical-harmonic method, if, without worrying about the convergence of the $M_{nk}(\nu)$ when $n \to \infty$, we specify the conditions

$$M_{N+1,k}(\nu) = 0, \quad 0 \leqslant k \leqslant N \quad (32)$$

and $y_{N+1} \equiv 0$, which clearly agree with the assumption $Y_{N+1} \equiv 0$. Then the set of permissible values of ν reduces to the set of roots ν_{ki} of Eq. (32).

The roots ν_{0i} correspond to those numbers $\varkappa_{0i}$ which in [4] were called fundamental numbers, and the roots ν_{ki} for $k > 0$ correspond to the supplementary numbers $\varkappa_{ki}$. In one-dimensional, plane, or spherical geometry, the functions y_{kk} for $k > 0$ must be identically zero, since otherwise it is impossible to satisfy the condition (28), i.e., the supplementary roots take no part in the solution of such problems.

In the general case, among the roots ν_{ki} there will also be zero roots of the odd polynomials $M_{N+1,\,k}$. The corresponding functions $y_{kk}(\mathbf{r}, \Omega, 0)$, if they are defined to be

$$y_{kk}(\mathbf{r}, \Omega, 0) = \lim_{\nu \to 0} y_{kk}(\mathbf{r}, \Omega, \nu),$$

have an infinitely small relaxation distance, and their contribution to the general solution is in the form of finite discontinuities on the boundaries. It can be seen that for even N the discontinuities (or jumps) will occur in even harmonics, and for odd N in odd harmonics; the component of the first harmonic which can be interpreted as the normal component of the diffusion current, however, is always continuous.

The existence of zero roots was also noted in [3, 6], but these roots and the corresponding special solution were discarded. In [4], where the P_N-approximations of the spherical-harmonic method are described in their most general form, the zero roots are also not taken into account, but in this work the discontinuity of certain spherical harmonics follows from the boundary conditions. When zero roots are taken into account, the requirement that all the spherical harmonics be separately coupled becomes formally realizable. It can be shown that in the P_N-approximation, because of the above-mentioned properties of the functions $y_{kk}(\mathbf{r}, \Omega, 0)$, the formal coupling of all harmonics is actually equivalent to the satisfaction of the boundary conditions given in [4].

CONCLUSIONS

The exact general expression for harmonics of any number on the one hand simplifies the analytical transition to P_N-approximations of the spherical-harmonic method. This simplification is particularly important in multidimensional problems. As is clear from the preceding, P_N-approximations are obtained by approximating the infinite set of characteristic numbers ν and functions $y_{kk}(\mathbf{r}, \Omega, \nu)$ by a finite set of numbers ν_{ki} and the corresponding functions $y_{kk}(\mathbf{r}, \Omega, \nu_{ki})$. The boundary conditions derived in [4] remain in force, but they have a new mathematical interpretation.

On the other hand the assumption $Y_{N+1} = 0$, which lies at the basis of the usually employed P_N-approximations, is not obligatory here. It is thus possible that new approximate forms of the spherical-harmonic method may

Declassified and Approved For Release 2013/09/24 : CIA-RDP10-02196R000700010005-2

Declassified and Approved For Release 2013/09/24 : CIA-RDP10-02196R000700010005-2

CALCULATION OF WEAK SELF-OSCILLATORY CONDITIONS IN NUCLEAR REACTORS

(UDC 621.039.51)

B. Z. Torlin

Translated from Atomnaya Énergiya, Vol. 18, No. 5,
pp. 463-468, May, 1965
Original article submitted February 24, 1964; final revision submitted July 17, 1964

A method for the approximate calculation of the parameters of self-oscillatory conditions in nuclear reactors with small power oscillation amplitudes is presented. An equation is derived, which, within the framework of the assumptions made, can be used for determining the frequencies of the reactor's possible self-oscillatory states as well as the amplitudes of reactivity and power fluctuations and the phase difference between these fluctuations.

The first problem that is ordinarily encountered in investigating the dynamics of reactors with feedback is the problem of the system's stability. If sufficiently small deviations from the equilibrium state are considered, the solution can be obtained in a relatively simple manner by using the known methods of linear analysis. If the system is stable, its deviation or the amplitude of its deviation from the equilibrium state will asymptotically tend to zero after any sufficiently small disturbance. If the system is unstable, linear analysis cannot yield any information on its asymptotic behavior. At the same time, beyond the limits of the linear stability region, a reactor can actually have very interesting stable self-oscillatory states with very small amplitudes. Actually, if the oscillation amplitude does not exceed, for instance, the noise level in the system, this implies a broader stability region, and, consequently, a wider range of the reactor's operating conditions.

The above apparently does not constitute all the useful information that can be obtained as a result of solving the problem of stable self-oscillatory conditions with a small oscillation amplitude in a reactor.

We shall use equations of the following types for considering the mean neutron density N throughout the reactor's volume for the mean concentrations c_j of sources of all the m groups of delayed neutrons.

$$\begin{aligned} \frac{dN}{dt} &= \beta\,\frac{\varrho-1}{T}N+\sum_{j=1}^{m}\lambda_j c_j;\\ \frac{dc_j}{dt} &= \frac{\beta_j}{T}N-\lambda_j c_j;\quad j=1,\ 2,\ \ldots,\ m, \end{aligned} \tag{1}$$

where ρ is the system's reactivity in dollars. T is the mean lifetime of neutrons, β_j and λ_j are the yield and the decay constant of the j-th delayed neutron group, respectively, and $\beta=\sum_{j=1}^{m}\beta_j$. For the investigation of small deviations of the neutron density from a certain theoretical value N_0, we shall introduce the notation

$$N=\overline{N}(1+n) \tag{2}$$

($\overline{N}$ is the mean value of the neutron density, which is generally different from N_0), and we shall reduce system (1) to the following form

$$w_1(p)\,n=\varrho\,(1+n), \tag{3}$$

Declassified and Approved For Release 2013/09/24 : CIA-RDP10-02196R000700010005-2

Declassified and Approved For Release 2013/09/24 : CIA-RDP10-02196R000700010005-2

where p = d/dt is the differentiating operator, while $w_1(p) = p\left(\frac{T}{\beta} + \sum_{j=1}^{m} \frac{\alpha_j}{p+\lambda_j}\right)$ is the linear operator, (4)

where $\alpha_j = \frac{\beta_j}{\beta}$.

For the sake of simplicity, we shall subsequently investigate a system with linear feedback* :

$$w_2(p)\, n \frac{\overline{N}}{N_0} = \varrho, \tag{5}$$

where $w_2(p)$ is the linear operator; the N/N_0 coefficient appears as a result of the fact that $w_2(p)$ is determined for the theoretical neutron density N_0, while n pertains to the mean neutron density $\overline{N}$.

Since we are interested only in the periodic solutions of the system, the problem can be divided into two parts:

1. Finding of the periodic solutions $n(\omega t)$ of the nonlinear Eq. (3) for the assigned periodic action $Q(\omega t)$. It is found in this case that the $Q(\omega t)$ function must satisfy certain requirements if Eq. (3) is to have periodic solutions n (wt).

2. Determination of such $q(\omega t)$ values for which the corresponding functions $n(\omega t)$ would yield the $w_2(p)$ function after the $Q(\omega t)$ operator is applied to them.

The solution of the first problem for $|n| < 1$ can readily be obtained by using the method of successive approximations [1]. If the $Q(\omega t)$ function is given by

$$\varrho(\omega t) = a_0 + \sum_{-\infty}^{\infty} a_k e^{ik\omega t}; \quad k \neq 0 \tag{6}$$

and $n(\omega t)$ is sought in the following form:

$$n(\omega t) = \sum_{-\infty}^{\infty} A_l e^{il\omega t}; \; l \neq 0, \tag{7}$$

the expression $A_l^{\nu+1}$ for every subsequent $(\nu + 1)$ approximation in terms of the preceding (ν) approximation is given by

$$A_l^{(\nu+1)} = \frac{a_l + \sum_{-\infty}^{\infty} a_k A_{k-l}^{(\nu)}}{w_1(i\omega l)}. \tag{8}$$

In order to secure a periodic solution of Eq. (3), it is necessary to satisfy the condition

$$a_0 = -2\mathrm{Re} \sum_{l=1}^{\infty} a_l A_{-l} \tag{9}$$

or, when using the method of successive approximations

$$a_0^{(n+1)} = -2\mathrm{Re} \sum_{l=1}^{\infty} a_l A_{-l}^{(\nu)}. \tag{10}$$

* The same method can also be used in the case where the feedback equations contain nonlinear terms.

Declassified and Approved For Release 2013/09/24 : CIA-RDP10-02196R000700010005-2

Declassified and Approved For Release 2013/09/24 : CIA-RDP10-02196R000700010005-2

The linear approximation is used as the zero approximation.

The second part of the problem can also be solved by using the method of successive approximations. In this case, it is natural to use expression (6) for the first approximation, retaining in it only the first harmonic. The subsequent approximations for $Q(\omega t)$ can be obtained by substituting the corresponding solutions $n(\omega t)$ of Eq. (3) in expression (5).

It should be remembered that, in order to secure a negative reactivity shift a_0, the mean neutron density $\overline{N}$ in the reactor must deviate from the calculated steady-state value N_0. The relationship between these values is given by

$$\overline{N} = N_0(1 - \varkappa_0 a_0), \tag{11}$$

where $\varkappa_0$ is the negative feedback gain at the "zero frequency."

By using (8) and (10), we readily obtain the following expressions in the second approximation:

$$A_1^{(2)} = a_1 w_1^{-1}(i\omega)\{1 + |a_1|^2 w_1^{-1}(i\omega)[w_1^{-1}(2i\omega) - 2\,\mathrm{Re}\, w_1^{-1}(i\omega)] + |a_1|^4 O_1(i\omega)\}; \tag{12}$$

$$A_2^{(2)} = a_1^2 w_1^{-1}(i\omega)\, w_1^{-1}(2i\omega)[1 + |a_1|^2 O_2(i\omega)]. \tag{13}$$

Expression (13) indicates that oscillations with a frequency twice as high as the frequency of the basic disturbance arise in the system. Through feedback (5), the oscillations with this frequency will begin to act on n in Eq. (3). The contribution of this effect to the expression $A_1^{(2)}$ is

$$w_1^{-1}(i\omega)\, w_2^{-2}(2i\omega)\, w_2(2i\omega)\, a_1 |a_1|^2. \tag{14}$$

If the value of this term is of the same order as the rejected terms, it can be neglected. In practice, this can be done if $|w_2(2i\omega)| \ll 1$. Subsequently, we shall neglect the term only in order to simplify the presentation of the method.

The expression for $a_0^{(2)}$ in the second approximation is given by

$$a_0^{(2)} = -2|a_1|^2\,\mathrm{Re}\, w_1^{-1}(i\omega). \tag{15}$$

By using expressions (5), (11), and (15) for the ratio of the complex amplitudes of the basic harmonics of the Q and n functions, we obtain

$$\frac{a_1}{A_1} = w_2(i\omega)[1 + \varkappa_0 \cdot 2|a_1|^2\,\mathrm{Re}\, w_1^{-1}(i\omega)]. \tag{16}$$

By substituting (12) in (16) and solving the expression obtained with respect to $|a_1|^2$, we arrive at the following expression:

$$|a_1|^2 = \frac{1 - \dfrac{w_2(i\omega)}{w_1(i\omega)}}{\dfrac{w_2(i\omega)}{w_1(i\omega)}\left[\dfrac{w_1^{-1}(2i\omega) - 2\,\mathrm{Re}\, w_1^{-1}(i\omega)}{w_1(i\omega)} + 2\varkappa_0 \cdot \mathrm{Re}\, w_1^{-1}(i\omega)\right]}. \tag{17}$$

By setting the imaginary part of the expression (17) equal to zero, we obtain an algebraic equation for determining the frequency of the self-oscillatory conditions. The real part of expression (17) determines the amplitude of the basic harmonic of reactivity fluctuations.

The amplitude of neutron density fluctuations and the phase shift between the reactivity fluctuations and the neutron density oscillations can be determined by means of expressions (12) and (16).

It is readily seen from expressions (12), (13), and (16) that the approximation used in deriving Eq. (17) holds only if the condition $|a_1|^2 \ll 1$ is satisfied. It follows from expression (8) that the use of the method of successive approximations is justified if at least $|A_1| < 1$. Therefore, from the totality of all solutions of Eq. (17), only those solutions which satisfy the above requirements must have a physical significance.

Declassified and Approved For Release 2013/09/24 : CIA-RDP10-02196R000700010005-2

Declassified and Approved For Release 2013/09/24 : CIA-RDP10-02196R000700010005-2

As an illustration of the above method, we shall investigate weak self-oscillatory conditions in a boiling homogeneous reactor with a single effective delayed neutron group while neglecting the mechanical inertia of water.

As follows from [2], with an allowance for the overheating of the liquid phase and without taking into account its mechanical inertia, the frequency characteristic of the feedback system of a boiling homogeneous reactor is given by

$$w_2(i\omega) = -\frac{K}{1-\vartheta\theta\omega^2+i\vartheta\omega}. \tag{18}$$

It was shown in [2] that the time constant θ of the overheat of the liquid phase is related to its heat capacity C, the steady-state overheat t_0, and the reactor's steady-state power level N_0, by the following relationships:

$$\theta = \frac{Ct_0}{N_0}. \tag{19}$$

The time constant ϑ of the vapor phase yield is almost independent of the parameters in relationship (19). The steam reactivity coefficient K is proportional to the steady-state power:

$$K = K_0 N_0. \tag{20}$$

By substituting (18) in (17), we obtain equations which determine the frequency ω and the amplitude $|a_1|$ of reactivity fluctuations under the self-oscillatory conditions in question:

$$|a_1|^2 = -\frac{1}{K}\frac{1+K-\vartheta\theta\omega^2+i\left(\vartheta\omega-K\frac{\lambda}{\omega}\right)}{2K-1+i\left(\frac{\lambda^3}{2\omega^3}+\frac{3}{2}\frac{\lambda}{\omega}-2K\frac{\lambda}{\omega}\right)}. \tag{21}$$

Expression (21) was analyzed in the region of the variables (K; θ), as well as in the regions of the variables (N_0; t_0) for different ϑ values.

The boundary of the linear stability region is determined on the basis of expression (21) for $|a_1| = 0$; it is given by

$$\theta\lambda - 1 = \frac{1}{K} \tag{22}$$

in a (K; $\theta\lambda$) plot or by

$$K_0 N_0 + 1 = K_0 \lambda C t_0 \tag{23}$$

in a (N_0; t_0) plot.

Expression (21) can also be used for determining the amplitude $|a_1|$ and the frequency ω of reactivity fluctuations under weak self-oscillatory conditions:

$$|a_1|^2 = -\frac{1}{K}\cdot\frac{1-\vartheta\theta\omega^2+K}{2K-1} \tag{24}$$

or

$$|a_1|^2 = -\frac{2}{K}\cdot\frac{\vartheta\lambda-Kx}{x^2-(4k-3)x}, \tag{25}$$

where

$$x = \frac{\lambda^2}{\omega^2} = -\frac{1}{2}\frac{3(1-K)-\lambda^2\vartheta\theta}{1+K} \pm \sqrt{\left[\frac{1}{2}\frac{3(1-K)-\lambda^2\theta\vartheta}{1+K}\right]^2 - \vartheta\lambda\frac{2-4K-3\lambda\theta+4K\lambda\theta}{1+K}}. \tag{26}$$

Declassified and Approved For Release 2013/09/24 : CIA-RDP10-02196R000700010005-2

Declassified and Approved For Release 2013/09/24 : CIA-RDP10-02196R000700010005-2

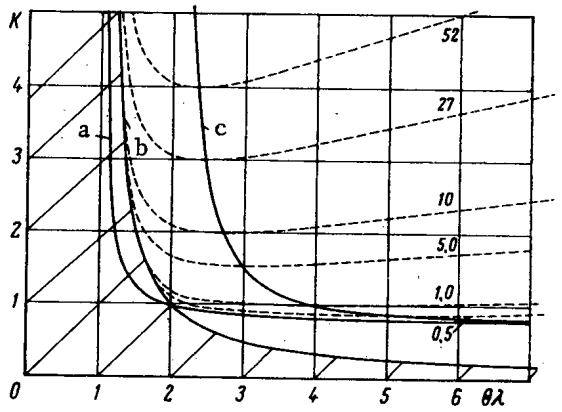

Fig. 1. Linear stability region (shaded area) and the characteristic curves in a K−λθ plot. a) Boundary of the region of self-oscillatory states with small amplitudes; b) boundary of the linear stability region; c) curve passing through the minimums of the dashed curves of equal roots x (see Eq. (33)) for different λθ values, which are indicated on each curve.

First of all, it follows from expressions (24)-(26), that, for fixed parameter values in this approximation, the system of equations under investigation can have not more than two periodic solutions, one of which must be stable. Consequently, there may be cases with one or two periodic solutions or none at all. Let us define in a [K; θλ) plot the regions where such situations can arise. For this purpose, we shall plot the characteristic curves, using the above coordinate system.

Assuming that $|a_1| = 0$, we obtain the equation of the curve $1/K_{crit} = \theta\lambda - 1$, which constitutes the boundary of the linear stability region (curve b in Fig. 1). In terms of nonlinear analysis, the boundary of the linear stability region is characterized by the fact that at least one of the possible self-oscillatory conditions (stable or unstable) has a zero amplitude at this boundary. The two x values corresponding to the boundary of the linear stability region are equal to

$$x_1 = \frac{\vartheta\lambda}{K_{crit}} \tag{27}$$

and

$$x_2 = 3\frac{K_{crit} - 1}{K_{crit} + 1}, \tag{28}$$

where x_1 corresponds to $|a_1| = 0$, while x_2 corresponds to

$$|a_1|^2 = \theta\lambda \cdot \frac{\frac{x_1}{x_2} - 1}{2K - 1}. \tag{29}$$

Since x is larger than zero by definition, the x_2 quantity is devoid of physical meaning if $K < 1$. The second condition for the existence of x_2 is also obvious: $x_1 > x_2$.

Useful information on the behavior of the amplitude of the periodic solution near the boundary of the linear stability region can be obtained by means of the expression

$$\frac{d|a_1|^2}{d\theta} = \frac{2K}{K+1}\frac{1}{x_1 - x_2} \tag{30}$$

for $\theta = K + 1/K$, whence, it follows that, if $x_1 > x_2$, i.e., if $K < K_1$ is determined from the relationship

$$\vartheta\lambda = 3K_1 \cdot \frac{K_1 - 1}{K_1 + 1}, \tag{31}$$

the amplitude of the self-oscillatory conditions must gradually increase beyond the boundaries of the linear stability region at increasingly greater distances from the boundary (the so-called soft operating conditions). In the opposite case, the so-called hard operating conditions prevail. In this, within the boundaries of the linear stability region, the probability of self-oscillatory conditions with an already considerable amplitude increases as the distance to the boundary diminishes.

The other characteristic curve in Fig. 1 is the curve a, which corresponds to $\omega \to \infty$. In this case, $|a_1| \to \infty$ also holds. The equation of this curve is given by

$$\theta_b\lambda = \frac{4K - 2}{4K - 3}; \quad K \geqslant \frac{3}{4}. \tag{32}$$

Region II (see Fig. 3), which is enclosed between the curves a and b, is characterized by the fact that only a single oscillatory state with a small amplitude is possible at every point within this region. To the left of this region I (see Figs. 1 and 2), in which self-oscillatory conditions with small amplitudes do not exist at all.

Declassified and Approved For Release 2013/09/24 : CIA-RDP10-02196R000700010005-2

Declassified and Approved For Release 2013/09/24 : CIA-RDP10-02196R000700010005-2

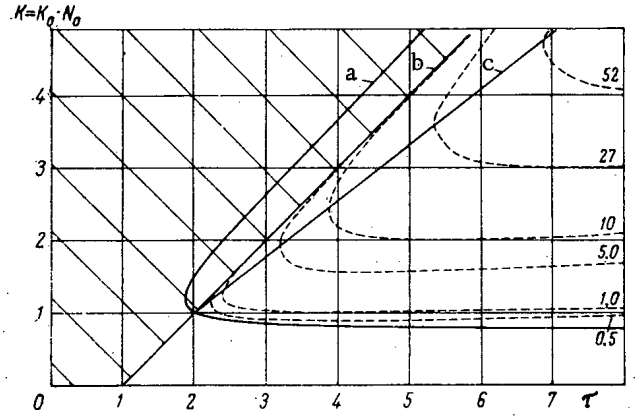

Fig. 2. Linear stability region (shaded area) and the characteristic curves in a K–τ plot. a) Boundary of the region of self-oscillatory states with small amplitudes; b) boundary of the linear stability region; c) straight line passing through the minimum τ values of the curves of equal roots (similar to the dashed curves in Fig. 1).

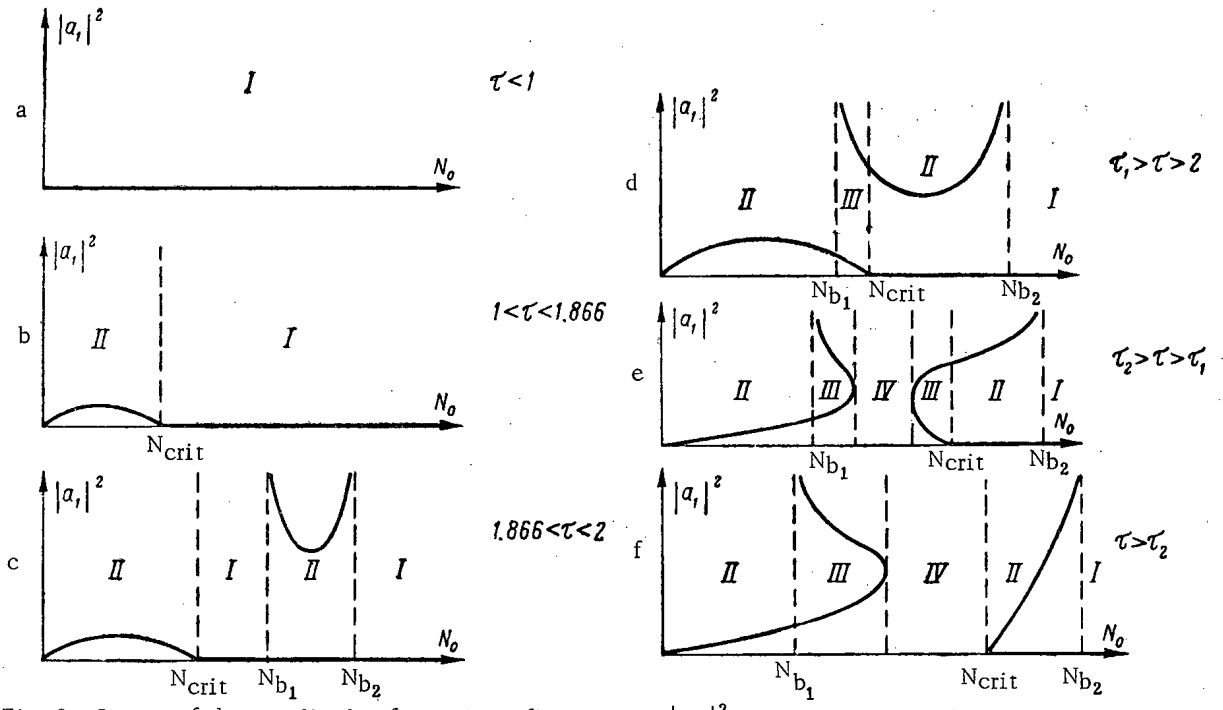

Fig. 3. Square of the amplitude of reactivity fluctuations $|a_1|^2$ in dependence on the reactor's steady-state power level N_0 for different τ values. The Romans figures denote the reactor's different stability regions: N_{crit} is the boundary of the linear stability region; N_{b_1} and N_{b_2} are the boundaries of the regions of self-oscillatory states with small amplitudes.

A family of curves along which both x values are equal (these curves are shown by dashed lines for different $\vartheta\lambda$ values in Fig. 1) are tangent to the curve b at the points $K_{crit} = K_1$. The equation of this family of curves is given by

$$\vartheta\lambda\theta\lambda = (8K^2 - K - 3) \pm \sqrt{8(K+1)(2K-1)[K(4K-3) - \vartheta\lambda]}. \quad (33)$$

Declassified and Approved For Release 2013/09/24 : CIA-RDP10-02196R000700010005-2

Declassified and Approved For Release 2013/09/24 : CIA-RDP10-02196R000700010005-2

It is obvious that, for $K = K_y$ (K_y satisfies the equation $\theta\lambda = K_y(4K_y - 3)$, both θ values determined by expression (33) coincide, while, for $K < K_y$, expression (33) does not have real solutions. Curve c connects the minimums of the curves described by expression (33). Region III, at every point of which there are two positive $|a_1|^2$ values, is located between the region limited by curves a and b and the curve described by Eq. (33) (for a concrete $\lambda\theta$ value).

Region IV, which does not have real $|a_1|$ values, is located above the curve described by Eq. (33). This region is characterized by an absence of either stable or self-oscillatory conditions.

It is readily seen from expressions (24)-(26) that, for $\theta \to \infty$, the $|a_1|$ value corresponding to a larger x tends to zero. The second $|a_1|$ value exists only if $K > 3/4$, and it increases unboundedly with an increase in θ.

As follows from Eq. (23), the reactor is unstable at low power levels and $t_0 > t_0(0) = 1/K_0\lambda C$. The inconvenience connected with this consists in the fact that, if the t_0 value of the system exceeds $t_0(0)$, it would be necessary to pass through the linear instability region as the reactor's power level is raised to the rated value. Let us investigate this region while increasing the reactor's power level for $t_0 = \text{const}$. It is readily seen that, in a (K, $\theta\lambda$) plot, the $t_0 = \text{const}$ curves represent hyperbolas given by

$$K = \frac{\tau}{\theta\lambda},$$

where $\tau = t_0/t_0(0)$, while, in a ($K - \tau$) plot (see Fig. 2), they represent vertical lines.

The characteristic curves in Fig. 2 are the straight line $K = K_0N_0 = \tau - 1$, which constitutes the boundary of the linear stability region; the curve along which $x = 0$, $|a_1| \to \infty$, which is described by the equation

$$\tau_b = K \cdot \frac{4K-2}{4K-3};$$

the dashed curves of equal roots x for $\lambda\vartheta = 0.5;\ 1;\ 5;\ 10;\ 27;\ 52$, which are tangent to the straight line b at the points τ_2 given by the relationship

$$\lambda\vartheta = 3\frac{(\tau_2-1)(\tau_2-2)}{\tau_2};$$

and the straight line c, which passes through the minimum τ values of the curves of equal roots. For every θ value, there are single values of τ_1 and τ_2. The dependence of $|a_1|^2$ on the reactor's power level N_0 for different values is shown in Fig. 3. For $\tau \leq 1$ (graph a), the reactor is within the stability region for all N_0 values. For $1 < \tau < \tau_1$ (graphs b, c, and d), there exist such stable self-oscillatory conditions which make it possible to pass to the region of stable reactor operation without fear that runaway conditions will arise. For $\tau > \tau_1$ (graphs e and f), there is a region of N_0 values where self-oscillatory conditions with small amplitudes are absent. Besides, for $\tau > \tau_2$, dangerous hard operating conditions exist at the boundary of linear stability.

Thus, by using our method of approximate calculation of the parameters of weak self-oscillatory conditions within the framework of the hydrodynamic model of boiling [2], we arrive at the following conclusions:

1. For sufficiently large K values $K \geq K_2 = \frac{3 + \vartheta\lambda + \sqrt{9 + 18\lambda\vartheta + \vartheta^2\lambda^2}}{6}$, hard operating conditions exist at the boundary of linear stability (which limits the linear stability region on the side of low power values).

2. For steam reactivity coefficient values $K < K_2$, the region of the reactor's stable operation may prove to be somewhat larger than its linear stability region.

3. For steady-state overheat t_0 values which exceed $t_0(0)$, but are lower than $t_1 = \tau_1 t_0(0)$, the raising of the reactor's power level to the rated value* should take place in an entirely safe manner.

4. In the case of sufficiently large steady-state overheat values $t_0 > t_1$, the raising of the reactor's power level may cause dangerous pulsations, while, at $t_0 > t_2 = \tau_2 t_0(0)$, there is danger in approaching the boundary of linear stability because hard operating conditions may set in.

*It is assumed that the reactor is in the linear stability region at the rated power level.

Declassified and Approved For Release 2013/09/24 : CIA-RDP10-02196R000700010005-2

Declassified and Approved For Release 2013/09/24 : CIA-RDP10-02196R000700010005-2

The author is grateful to B. R. Bergel'son, P. P. Blagovolin, A. D. Galanin, E. F. Sabaev, S. M. Fainberg, and Ya. V. Shevelev for their discussion of the paper and valuable remarks.

LITERATURE CITED

1. H. Sandmeier, Nucl. Sci. Engng., 6, 85 (1959).
2. B. V. Érshler, B. Z. Torlin, and L. A. Suvorov, Atomnaya Énergiya, 9, 5 (1960).

All abbreviations of periodicals in the above bibliography are letter-by-letter transliterations of the abbreviations as given in the original Russian journal. *Some or all of this periodical literature may well be available in English translation.* A complete list of the cover-to-cover English translations appears at the back of this issue.

Declassified and Approved For Release 2013/09/24 : CIA-RDP10-02196R000700010005-2

Declassified and Approved For Release 2013/09/24 : CIA-RDP10-02196R000700010005-2

PROPAGATION OF NEUTRONS IN IRON

(UDC 539.125.52)

V. I. Golubev, A. V. Zvonarev, M. N. Nikolaev,
M. Yu. Orlov, V. V. Penenko, and O. P. Uznadze

Translated from Atomnaya Énergiya, Vol. 18, No. 5,
pp. 469-473, May, 1965
Original article submitted March 16, 1964

Results of a theoretical and experimental study of the space-energy distribution of neutrons in the iron screen of the BR-1 reactor are presented.

The experimental results are compared with multigroup calculations in the P_3-approximation (one-dimensional geometry) and the P_1-approximation (two-dimensional geometry). The effect of allowing for resonance blocking of the cross sections on the exactness of the description of neutron propagation in the medium is demonstrated.

This paper relates to a series of macroscopic experiments on the propagation of neutrons in various media, carried out in order to check and improve the system of constants used in multigroup calculations of fast reactors, and also in order to determine some integral characteristics of the media.

Results of studying the propagation of neutrons in uranium, uranium carbide, copper, and nickel were published in [1-3]. In this paper, we present results of studying the propagation of neutrons in the iron screen of the BR-1 reactor.

Iron is of special interest, since it is widely used in reactor construction. Moreover, a detailed study of the propagation of neutrons in iron enables us to explain the general laws governing the passage of neutrons through matter (for example, the effect of the resonance structure of the cross sections on the slowing-down of the neutrons).

Among the isotopes of iron, the most widespread (92%) is the even-even isotope Fe^{56}. Hence, all the resonance characteristics of the cross section of Fe^{56} (in particular, the deep interference minimum in front of the s resonance at 29 keV) appear sharply in the cross section of a natural mixture of iron isotopes. The presence of the deep minimum in the cross section of iron means that, on slowing the neutrons down from the energy of the source (assumed fairly high), there is a great probability that the neutrons will fall into the region of very long free paths. At some distance from the source a leading group of neutrons with energy around 27 keV is formed; this has a decisive influence on the propagated distribution of neutrons in iron. Hence, the accuracy of describing the neutron distribution depends substantially on the correctness with which the constants are averaged in the group containing the cross-section minimum. The behavior of the cross section of iron in this region and in the region of other interference minima at higher energies is known fairly well, so that verification of the group constants for iron is of particular interest.

COMPARISON OF EXPERIMENTAL AND CALCULATED DATA

The construction of the BR-1 reactor was given in detail in [1]. The neutron distribution was determined in the iron screen of the reactor; the height of the screen was 70 cm. The thickness of the screen was increased to ~ 90 cm as a result of an attachment on one side (Fig. 1). All the movable parts of the screen lying close to the active zone were made of iron. Experiments performed with this relatively simply geometry made it easy to compare calculated data with experiment.

The space-energy distributions of the neutrons were determined in the plane of the center of the reactor in vertical experimental channels of the active zone and the screen by means of fission chambers containing layers of Pu^{239}, U^{235}, Th^{232}, and activation detectors using the reactions $Au^{197}(n, \gamma)$, $Mn^{55}(n, \gamma)$, $La^{139}(n, \gamma)$, $Na^{23}(n, \gamma)$, $In^{115}(n, \gamma)$, $Cu^{63}(n, \gamma)$, $P^{31}(n, p)$, $Si^{28}(n, p)$. The measuring technique was described in [1, 4].

Declassified and Approved For Release 2013/09/24 : CIA-RDP10-02196R000700010005-2

Declassified and Approved For Release 2013/09/24 : CIA-RDP10-02196R000700010005-2

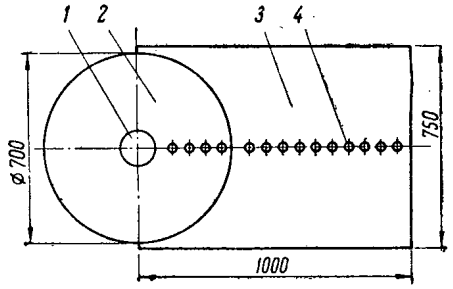

Fig. 1. Arrangement of the BR-1 reactor: 1) active zone; 2) main reflector; 3) attachment; 4) experimental channels.

A 26-group system of constants was used in the calculations [5]. The computing programs provided for the use of a system of constants with a smaller number of groups (18 and 21), so that some energy groups had to be combined. Combination was effected in energy ranges where the spectra had no substantial peculiarities, i.e., in the range below 10 keV. The constants were subsequently prepared for the calculation in accordance with the recommendations of [5]. Calculations were made both in one-dimensional spherical geometry and in two-dimensional geometry. In the latter case it was assumed that the screen had the form of a cylinder 82 cm in diameter and with a height equal to the actual height of the screen (140 cm). The cylindrical active zone was set at 30 cm from the end of the screen. In the one-dimensional calculation the anisotropy of the neutron flux was considered in the P_3-approximation. The transitions of neutrons from group to group were considered isotropic. The anisotropy of these transitions was taken into account indirectly: in order to describe the anisotropy of the scattering, the so-called "corrected transport approximation" was used [5]. In this approximation, a value of $(\mu\sigma_s)$ averaged over all neutrons scattered in a given group is used in calculating the transport cross section (not only over the neutrons left in the given group as a result of scattering, as in the simple transport approximation with isotropic transitions). Calculation in two-dimensional geometry was effected in the P_1-approximation; the scattering anisotropy was taken into account in the same way as in the P_3-approximation. The computing program in spherical geometry provided for a determination of the radius of the critical active zone. The two-dimensional calculation was effected for the actual dimensions and composition of the active zone, but in view of the inaccuracy of the P_1-approximation K_{eff} proved to be less than unity. Critical conditions were achieved by an artificial change in the value of ν.

Figure 2 shows the results of a one-dimensional calculation of the distributions of the number of different reactions over the radius of the screen in the P_3-approximation (spherical geometry using the constants of [5]. The dot-dash curves give the results of the two-dimensional calculation in the P_1-approximation; the dashed curves give the calculated results for a spherical reactor in the P_3-approximation from the constants of [5] without introducing the correction for resonance blocking of the cross sections. The points show experimental results (measuring errors not greater than 5%). All the experimental and computed data are normalized in the total number of fissions of Pu^{239} in the active zone. We see from Fig. 2, that in the active-zone region all the distributions calculated in the P_3-approximation (continuous curves) lie below the experimental points. This is because the computed critical radius (8.38 cm) proved to be considerably larger than the experimental (6.94 cm, i.e., 0.95 of the radius of a sphere with a volume equal to that of the active zone). This discrepancy was due to two causes: the first was that, in the P_3-approximation (radius of active zone ~ 1.5 free paths), the leakage of neutrons from the active zone was substantially overestimated. The second was that the effects of resonance blocking, taken into account in accordance with the recommendations of [5], actually only occur on an average over the whole screen. In the first layers of the screen the neutron spectrum in the resonance region depends substantially on distance. The self-screening coefficients vary accordingly. In the ordinary multigroup calculation, however, this variation cannot be taken into account. Hence, the cross sections of iron in the layers adjacent to the active zone are underestimated as a result of the overestimation of the blocking, which must lead in turn to a considerable worsening of the albedo characteristics of the screen and to an overestimate of the critical mass. For an iron screen the second of these aspects is decisive. In fact, the computed critical radius of a reactor with cupronickel control units and a nickel screen [2] (where the effect of the second aspect is insignificant) exceeds the experimental value by only 6%.

The example given shows that the ordinary multigroup calculation of systems, with large neutron leakages from the active zone and strong resonance self-screening of the cross sections of the screen material, can lead to serious errors. In order to remove these errors, we need a more exact estimate of self-screening than that which is possible in the ordinary multigroup calculation. This in turn, requires more detailed information on the structure of the cross section to be introduced into the calculation, which may be done, for example, by means of the method proposed in [6]. In the two-dimensional calculation the effect of these causes of discrepancy was effectively compensated by varying the properties of the active-zone material (see above).

Declassified and Approved For Release 2013/09/24 : CIA-RDP10-02196R000700010005-2

Declassified and Approved For Release 2013/09/24 : CIA-RDP10-02196R000700010005-2

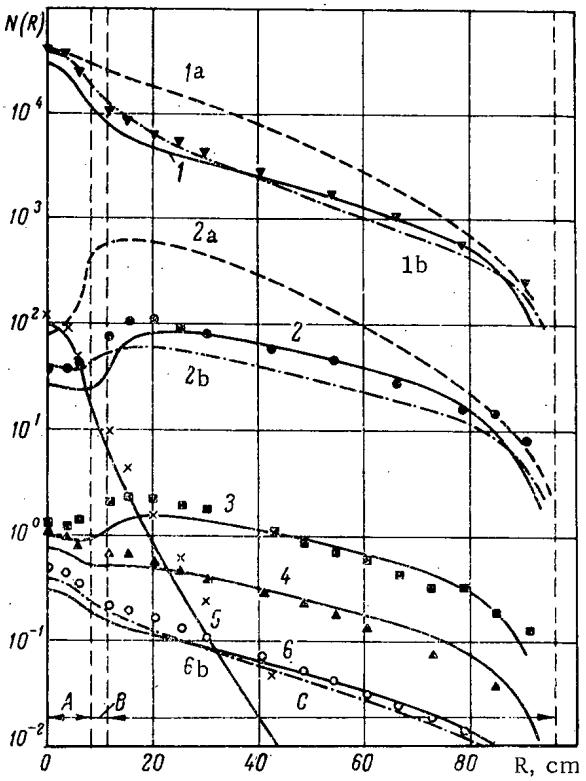

Fig. 2. Distribution of the numbers of different reactions in the iron screen of the BR-1 reactor: 1) 1) (▼)—$Pu^{239}(n,f)$; 2) (●)—$Au^{197}(n,\gamma)$; 3)(■)—$Mn^{55}(n,\gamma)$; 4)(▲)—$Na^{23}(n,\gamma)$; 5)(×)—$Th^{232}(n,f)$, 6)(○)—$Cu^{63}(n,\gamma)$. A, active zone; B, control units; C, iron screen.

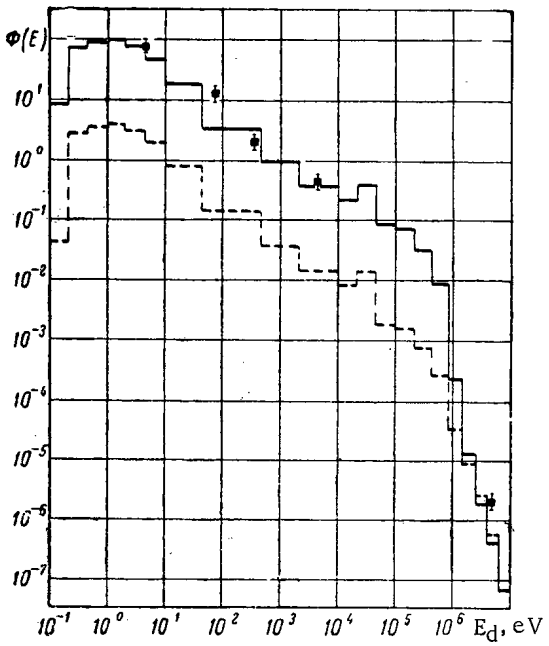

Fig. 3. Neutron spectra in iron: ———) calculation of spectrum in the P_3-approximation; ------) equilibrium spectrum; ■) experimental points.

A long way from the active zone, the averaging of the constants of iron recommended in [5] is valid, and, hence, discrepancies in the space-energy distributions are caused mainly by inaccuracy in the cross sections of the iron. On comparing the results of the calculation on the P_3-approximation with experimental data in this region, satisfactory agreement is obtained. To a certain extent, however, this agreement is fortuitous, since in the one-dimensional calculation the neutron leakage through the sides of the prism cannot be taken into account. Allowing for this loss in the two-dimensional calculation led to a difference between the calculated and experimental data. The leakage has an especially marked effect on the distribution of low-energy neutrons, which are mainly responsible for the reaction $Au^{197}(n,\gamma)$. As we see from Fig. 2, on allowing for leakage the flux of these neutrons changed by a factor of almost 2. As we know, the estimate for large leakages in the P_1-approximation is inexact; it leads to an overestimate of the leakage. Estimates show that in this case, the determination of leakage in the P_1-approximation leads to its overestimation by a factor of 1.5. Thus, a more correct calculation of neutron leakage would improve agreement between calculated and experimental data. Even in this case, however, the discrepancies would not be eliminated altogether. The nature of these discrepancies indicates a certain overestimate of the role of resonance self-screening in calculating the transport cross sections of iron [5]. Apparently, this inaccuracy relates mainly to the group containing the above-mentioned interference minimum at 27 keV. Qualitatively this conclusion confirms the results of [7], in which the neutron spectra in iron were measured in detail by the time-of-flight method. Unfortunately, we cannot draw quantitative conclusions regarding the inaccuracy of the constants from available computed material.

The discrepancy between calculation and experiment at the outer boundary is probably caused by the influence of neutrons reflected from the walls of the chamber. The existence of these neutrons was not considered in the calculation. Thus, we may say that the differences between calculation and experiment are due both to the inaccuracy in the constants of iron and the defects in the computing method, and in certain cases also to incomplete knowledge of the constants of the indicators [see Fig. 2, curves for $Mn^{55}(n,\gamma)$ and $Na^{23}(n,\gamma)$].

Let us now discuss the characteristics of the neutron spectra in iron. Figure 3 shows the equilibrium spectrum [1] of neutrons in iron and the calculated neutron spectrum at a point of the screen 54.2 cm from the center of the active zone. As we see, these curves are quite similar in form in the region below the first strong s resonance of iron at 29 keV. At the same time, the forms of the hard parts of the spectra differ.

Declassified and Approved For Release 2013/09/24 : CIA-RDP10-02196R000700010005-2

Declassified and Approved For Release 2013/09/24 : CIA-RDP10-02196R000700010005-2

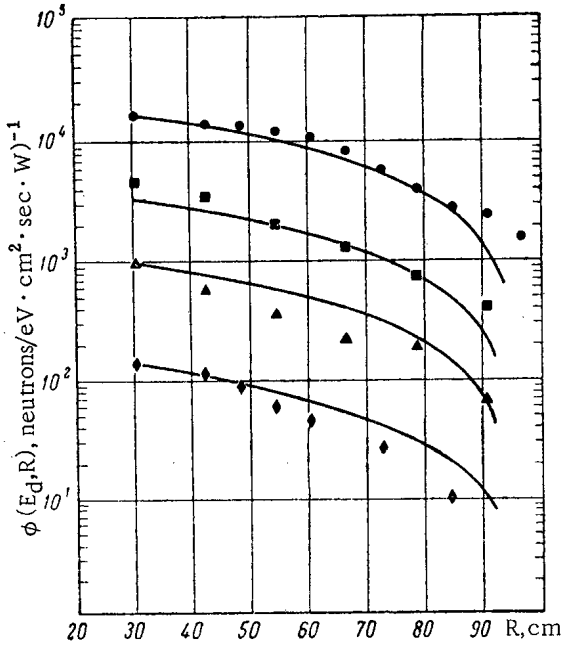

Fig. 4. Spatial distribution of neutron fluxes of certain energies over the iron screen of the BR-1 reactor: ●—4.9 eV; ■—73.5 eV; ▲—337 eV; ◆—2850 eV.

TABLE 2. Ratio of the Cross Sections σ_i of Various Reactions to that of Pu^{239} Fission (σ_{239})

Reaction	σ_i/σ_{239} in equilibrium spectrum	
	experiment	calculated
Pu^{239} (n, f)	1.000	1.000
U^{235} (n, f)	0.95 ± 0.10	0.77 ± 0.04
Au^{197} (n, γ)	2.6 ± 0.2	2.6 ± 0.2
In^{115} (n, γ)	1.8 ± 0.2	1.9 ± 0.2
Mn^{55} (n, γ)	0.040 ± 0.004	0.046 ± 0.003
Na^{23} (n, γ)	0.0010 ± 0.0001	0.00095 ± 0.00009
Cu^{63} (n, γ)	0.023 ± 0.002	0.020 ± 0.002
Si^{28} (n, p)	0.000024 ± 0.000003	0.000017 ± 0.000002
P^{31} (n, p)	0.000079 ± 0.000008	0.000063 ± 0.000006
Th^{232} (n, f)	0.00019 ± 0.00002	0.00018 ± 0.00002

TABLE 1. Carrying-Off Cross Sections of Neutrons under the Threshold of the Reactions Th^{232} (n,f), Si^{28} (n, p) and P^{31} (n, p) for Iron

Reaction	Carrying-off cross sections, barn	
	experiment	calculation
Th^{232} (n, f)	0.90 ± 0.20	0.81
P^{31} (n, p)	0.95 ± 0.20	1.05
Si^{28} (n, p)	1.10 ± 0.20	1.38

The agreement between the neutron spectra in the energy range below 27 keV is easily explicable. The relaxation length of the leading group of neutrons, lying in the region of 27 keV is considerably greater than the migration length of the neutrons leaving this group, so that after the formation of the leading group an asymptotic equilibrium of the neutron spectrum should arise in the region below the energy of this group. Since the gradient of the flux of the leading group is small, this asymptotic spectrum should be close to the equilibrium spectrum (spectrum of an infinite medium).

On the curve of the calculated spectrum (see Fig. 3) we have placed the values of neutron fluxes for certain energies obtained experimentally by the method of resonance indicators (Au^{197}, La^{139}, Mn^{55} and Na^{23}) set out in [4] and the flux of neutrons with energies over 1.5 MeV. The experimental and calculated data are normalized to the plutonium-fission integral in the active zone. The agreement between calculation and experiment in the soft part of the spectrum is quite satisfactory. The calculated fast-neutron flux, however, proved too low. Analysis shows that this was due to an overestimate of the neutrons carried off under the Th^{232} fission threshold in the calculated active zone, larger in size than the true active zone (Table 1). The spatial relationships of the neutron fluxes for the energies of the indicators used are given in Fig. 4.

It is interesting to compare the ratio of the cross sections of various reactions in the equilibrium spectrum in iron with experimental data. This comparison can easily be made for reactions mainly sensitive to slow neutrons, since, in view of the establishment of the neutron spectrum in the low-energy range, the neutron leakage has no effect on the ratio of the cross sections of these reactions.

It is not hard to calculate the ratios of the cross sections of the threshold reactions: for these the influence of neutron leakage is practically absent, so that the ratios of the cross sections in the spectrum of the screen are equal to those in the equilibrium spectrum. In order to determine the ratios of the cross sections of the threshold reactions to those of nonthreshold reactions, however, the effect of neutron leakage must be taken into account; this may be done with the aid of multigroup-calculation data. Unfortunately, in the case in question the correction for neutron leakage is extremely large (~ 50%); this seriously reduced the accuracy of the experimental ratios for the cross sections of threshold and nonthreshold reactions. The results of the comparison are shown in Table 2. (The errors indicated in the table do not allow for errors in introducing corrections for neutron leakage, which may reach ~15%). We see from the table that the computed data agree satisfactorily with experiment.

Declassified and Approved For Release 2013/09/24 : CIA-RDP10-02196R000700010005-2

Declassified and Approved For Release 2013/09/24 : CIA-RDP10-02196R000700010005-2

In order to demonstrate the effect of allowing for resonance blocking of the cross sections, we calculated the reactor in the P_3-approximation from the system of constants given in [5], without allowing for resonance blocking (see Fig. 2, broken lines). These results are very close to the data obtained by using the earlier 21-group system of constants [8].

CONCLUSIONS

Use of the system of constants given for iron in [5] enables us to obtain satisfactory agreement between experiment and correctly-applied theory. We see from the data presented that this can only be done if the resonance self-screening of the cross sections is allowed for. Although this system of constants still requires some correction of the coefficients of resonance blocking, the corrections needed are not large. On calculating the space-energy distributions of neutrons at the boundaries of iron with other media, use of the constants from [5] may lead to substantial errors, since in such cases the use of resonance-media "constants" which are constant over space is in general not justified. At the same time, it should be noted that for calculations of neutron distributions in media where the iron is diluted by traces of other elements (for example, in stainless steel) the influence of resonance effects is considerably lessened, and so are the inaccuracies in question [7].

The authors are grateful to I. I. Bondarenko for interest in the work and useful discussions. The authors also thank all the staff of the BR-1 reactor for assistance, and K. I. Nesterov for constant help in formulating the results.

LITERATURE CITED

1. A. I. Leipunskii et al., Atomnaya énergiya, 5, 277 (1958).
2. M. N. Nikolaev et al., Physics of Fast and Intermediate Reactors, Vienna, IAEA (1962), p. 403.
3. I. I. Bondarenko et al., Atomnaya énergiya, 17, 113 (1964).
4. V. I. Golubev et al., Atomnaya énergiya, 11, 522 (1961).
5. L. P. Abagyan et al., Group Constants of Fast and Intermediate Neutrons for Calculating Nuclear Reactors [in Russian], Moscow, Atomizdat (1964).
6. M. N. Nikolaev and V. V. Filippov, Atomnaya énergiya, 15, 493 (1963).
7. I. I. Bondarenko et al., Atomnaya énergiya, 18, No. 6 (1965).
8. G. I. Marchuk, Methods of Calculating Nuclear Reactors [in Russian], Moscow, Gosatomizdat (1961).

All abbreviations of periodicals in the above bibliography are letter-by-letter transliterations of the abbreviations as given in the original Russian journal. *Some or all of this periodical literature may well be available in English translation.* A complete list of the cover-to-cover English translations appears at the back of this issue.

Declassified and Approved For Release 2013/09/24 : CIA-RDP10-02196R000700010005-2

Declassified and Approved For Release 2013/09/24 : CIA-RDP10-02196R000700010005-2

INVESTIGATION OF POWER EFFECTS OF THE BR-5 REACTOR

(UDC 621.039.51)

N. V. Krasnoyarov, R. V. Nikol'skii, and I. A. Efimov

Translated from Atomnaya Énergiya, Vol. 18, No. 5,
pp. 474-477, May, 1965
Original article submitted April 10, 1964

The results of experiments in the study of power effects of the BR-5 reactor are discussed for various coolant feeds. A method is described for determining the components of the power effect associated with heating up of the core fuel elements.

The study of the power effects of reactivity is necessary for knowledge of the behavior of a reactor under conditions of self-regulation as well as under normal operating conditions. The effect of power changes on the reactivity is a feedback which leads to stable or unstable behavior of the reactor or which contributes to it.

It is shown in [1-4] that the most rapid component in the change of reactivity accompanying change of power is particularly important for stability. Consequently, in order to study power effects, it is important to determine this fast component. The experiment should be so organized that safety is ensured even in the case when reactor investigations are carried out in unstable regimes.

Nonstationary processes in the unit, which has input and output parameters, can be studied by pulse as well as by harmonic properties, i.e., the law of variation of the output parameter can be observed as a result of a stepwise or harmonic change of the input parameter. Examples of the use of these methods for fast reactors are given, for example, in [1, 2]. In these experiments, changes were carried out with the automatic control system disconnected. From the point of view of safety it is advantageous that the automatic control system should be connected. One of the procedures which satisfies this requirement is the introduction into the automatic control system of a harmonic electrical signal and observation of the amplitude of the principal harmonic in the oscillations of the automatic control rods and of the power. The ratio of the amplitudes and the phase difference enables the transfer function of the reactor $k(j\omega)$ to be determined. Another method is the injection into the automatic control system of a stepwise electrical signal and observation of the time-behavior of the autocontrol rod and of the power. Technically this leads to a quite rapid change of position of the controller.

The autocontrol rod performs a movement which tends to change the power from one constant value to another. As a result of a good quality automatic control system this change of power can be considered as stepwise and the behavior of the automatic control rod can be identified with the transient characteristic $r(\tau)$ of the reactor, for which the power is assumed to be the input parameter and the reactivity the output parameter. This route of investigation was used on the BR-5 reactor.

A third method is completely unassociated with any external effect on the reactor and leads to observation of correlations of reactivity and power fluctuations originating by the effect of various fluctuations in the reactor[5].

In Fig. 1 (curve 1), the change of power is shown which should be attained on the BR-5 reactor by the injection of a stepwise signal into the autocontrol system. Curves 2 and 3 represent the behavior of the autoncontrol rod for small and large reactor powers respectively. Since an identical reactivity change corresponds to an identical nature of the power change, then the difference in the behavior of the autocontrol rods $r(\tau)$ (curve 4) is the result of the effect of a power change on the reactivity. In order to eliminate possible errors, the relative power changes in cases 2 and 3 were defined by identical conditions and they were carried out at one and the same temperature and positions of the other control rods. Experiments with the object of estimating and averaging the effects of various random processes on the measurement results were repeated frequently. In particular, the comparability of the

Declassified and Approved For Release 2013/09/24 : CIA-RDP10-02196R000700010005-2

Declassified and Approved For Release 2013/09/24 : CIA-RDP10-02196R000700010005-2

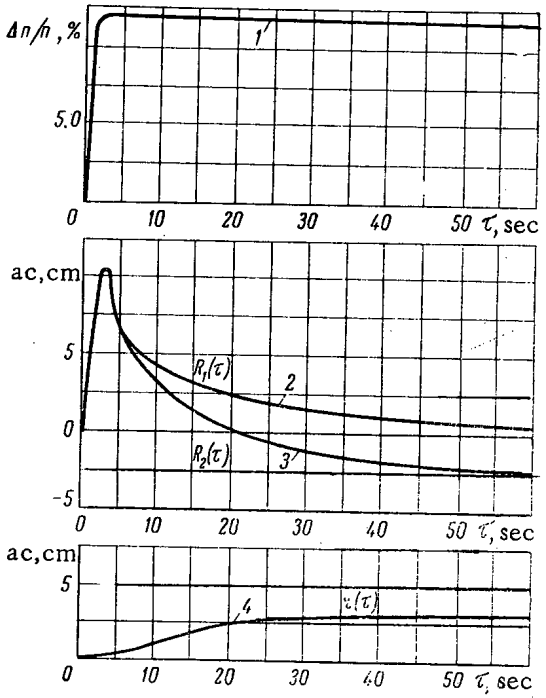

Fig. 1. Transient processes as a result of introducing a stepwise signal into the self-regulating system.

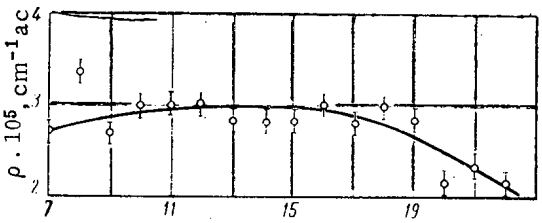

Fig. 2. Normalized graph of autocontrol rod.

measurement results as a result of power jumps indicates that the kinematics of the mechanism between the rod and its position detector does not noticeably distort the record of the reactivity transient behavior after 2 to 3 sec. There is no distortion also in the system for recording the position of the rod over this time interval.

For convenience of converting changes of rod position into change of reactivity all measurements were undertaken mainly in the linear portion of the autocontrol rod. The normalized curve of rod efficiency at the operating temperature of the measurements is shown in Fig. 2. In isolated cases errors were introduced by deviation from linearity.

In assessing the feasibility of this method, it can be stated that it allows the transient characteristics to be obtained for the reactor feedback chain (effect of power on the reactivity) for relatively slow processes. Fast processes (~ 1 sec) will give only their asymptotic value. During the first 2-3 sec, the measurement accuracy deteriorates also because the autocontrol rod as a result of this is deflected strongly at a high rate and the final result is the difference of these deflections. In addition, the difference in the nature of the change of power may be expressed.

In the BR-5 reactor [6-8], the change of reactivity after a power jump occurs by three groups of processes:

1) by nonuniform heating of the core components (over 1-5 sec), which leads to its expansion and to some buckling of the fuel elements and bundles;

2) by heating up of the central tube from the core by the sodium (over 2-20 sec), causing a relative displacement of the core and the reflector elements;

3) by uniform heating up of all the core components as a result of the sodium entering at high temperature into the reactor inlet (over ~ 20 sec).

In the first stage of operation of the BR-5 reactor it was observed that the total effect of heating up of the core components and of the central tube causes a zero change of reactivity [9].

By achieving a 2% fuel burnup and even greater burnups, this effect became positive and reached a value of $(2\text{-}4) \cdot 10^{-4}$ MW^{-1}. This phenomenon, obviously, is associated with a gradual increase in the dimensions of the plutonium dioxide briquets in the fuel elements of the BR-5 reactor and their adhesion to the cladding. As a result of this, expansion of the core in the axial direction was reduced significantly, since the extension of the plutonium dioxide columns exceeds by several times the cladding extension.

In 1963, after replacing part of the fuel elements, the measurements were repeated and carried out for various coolant feed rates. One of the problems in this experiment was the separation of the power effect component which is associated with heating up of the fuel.

Preliminary calculations of the nature of the change of temperature of the fuel, cladding sodium and walls of the bundle showed that the first group of processes takes place quite rapidly for all values of the sodium feed rate, and over an interval of 6-20 sec, the asymptotic value of the reactivity pertaining to this group of processes can be observed in the experiment. The asymptotic value is reached after 20 sec.

Declassified and Approved For Release 2013/09/24 : CIA-RDP10-02196R000700010005-2

Declassified and Approved For Release 2013/09/24 : CIA-RDP10-02196R000700010005-2

Experimental Conditions for Determining the Components of the Power Effect Caused by Fuel Heating

No. of expt.	Sodium feed rate, m^3/h	Power, kW	Sodium temperature rise	Change of power, kW	
1	245	2000	30°C	+200	—150
2	145	1600	40	+225	—100
3	83	1350	60	+225	—225
4	44	875	76	+100	—100
5	25	430	70	+50	—50
6	10	140	50	+20	—20

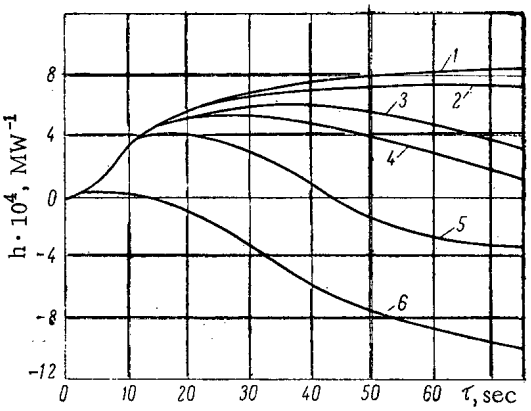

Fig. 3. Change of reactivity caused by change of power, for various coolant feed rates.

Characteristic data for the experimental conditions are given in the table.

The results of measuring $r(\tau)$, normalized to a power jump which corresponds to constant change of coolant temperature (70°C) are shown in Fig. 3 (the curve number corresponds to the experiment number in the table).

Each curve can be divided into three sections:

1) Over the interval 0-3 sec the stated method does not give sufficiently reliable data concerning the transient characteristics. Over 5-6 sec an almost zero reactivity is observed. This indicates that the fast processes taking place in the core, integrated for the power rise, introduce a zero contribution.

2) Over a lapse of ~ 6 sec, a smooth rise of reactivity is observed up to a certain maximum value. The rise time of the reactivity for this depends on the coolant feed rate. For example, for curves 5 and 6 corresponding to the smallest feed rates, it amounts to more than 60 sec. Since all processes in the core over this interval of time have already ceased, this rise is explained by the slower effect of extension of the central reactor tube.

3) After reaching a certain maximum value, the reactivity commences to fall more rapidly the greater is the coolant feed rate. This is explained by the re-entry of the heated sodium into the reactor inlet.

Uniform heating of the core components leads to a negative reactivity effect which is confirmed by experiments carried out earlier to measure the temperature effect, which is equal to

$$k_T = 3.3 \cdot 10^{-5}\ °C^{-1}.$$

Thus, the transient characteristics $r(\tau)$ which are being considered for various coolant feed rates can be separated into fast and slow processes of reactivity change.

The asymptotic or limiting value of the reactivity observed in the second section of each curve is not constant. This is explained by the different contribution to the reactivity from heating up of the core fuel elements.

The dependence of the reactivity value on the quantity which is the reciprocal of the feed rate (G) is linear. Its extension for infinitely large coolant feed rates ($1/G \to 0$) gives the value of the effect associated only with the fuel heating. This fact is illustrated in Fig. 4a. Reactivity data are scaled here to a constant power rise of 1 MW. The value of the effect associated with the fuel heating for the BR-5 reactor, obtained by the method of least squares, is found to be equal to

$$\varrho = -(1.5 \pm 0.3) \cdot 10^{-4}\ MW^{-1}.$$

Thus, in this experiment, without direct observation of process development in the first 4-5 sec, the value of the fastest component of the power effect is determined.

Declassified and Approved For Release 2013/09/24 : CIA-RDP10-02196R000700010005-2

Declassified and Approved For Release 2013/09/24 : CIA-RDP10-02196R000700010005-2

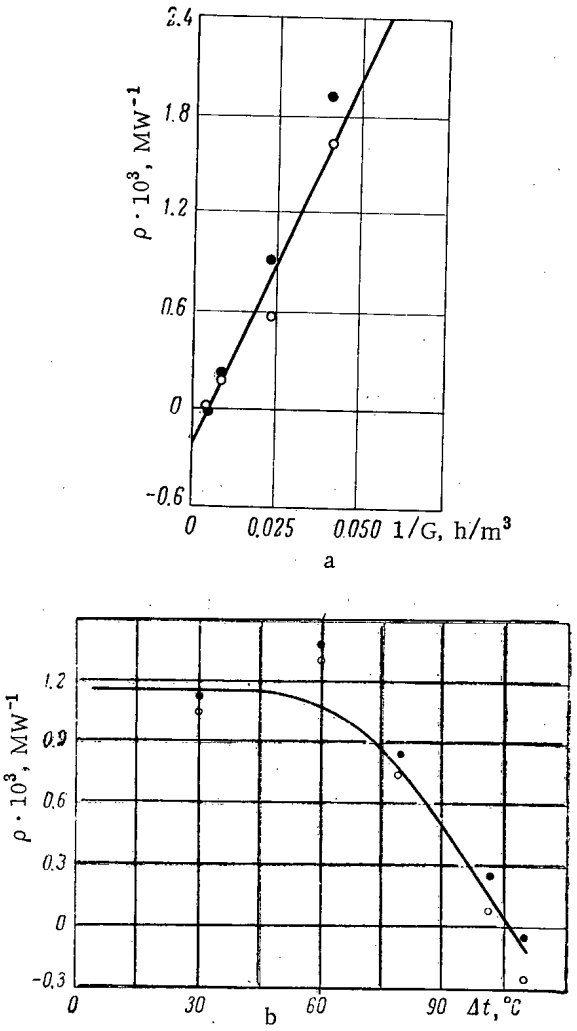

Fig. 4. Asymptotic value of the change of reactivity caused by heating up of the core components and of the central tube, for various feed rates (a) and various coolant temperatures rises (b). ○—positive power rise; ●—negative power rise.

The negative effect from the fuel and the positive effect from the components whose temperature is associated with the sodium feed rate, should lead to the fact that for a feed rate of 245 m^3/h, a negative value of $r(\tau)$ should be observed over the first few seconds, then transition almost to zero value (because of extension of the central tube) and again to a negative value after return of the sodium into the reactor inlet. However, measurements with G = 245 m^3/h do not give this picture directly, obviously because of the measurement inaccuracy during the first few seconds.

Conversion of the experimental data to constant values of cooling temperature rise or power changes can be valid only for a linear change of reactivity, depending on the change of power. The assumption requires experimental verification, since the effects associated with change of reactor geometry depend on clearances which vanish for certain conditions. A special experiment was carried out with a sodium feed rate of 28 m^3/h and at a constant sodium inlet temperature, and at powers corresponding to coolant temperature rises of 30, 60, 80 and 100°C. This experiment showed (see Fig. 4b) that in the range of interest to us (0-70°C) the linearity practically exists. At the same time, a definite deviation from linearity was found with sodium temperature rises exceeding 70°C.

A complete investigation of the behavior of $r(\tau)$ by an oscillator method in the first few seconds, the investigation of the relationship between the limit of loss of linearity and the magnitude of the coolant feed, and also an investigation of the origin of nonlinear effects are staged for future tasks on the BR-5 reactor.

LITERATURE CITED

1. V. N. Andreev, O. D. Kazachkovskii, and N. V. Krasnoyarov, Atomnaya Énergiya, 7, 363 (1959).
2. F. Télgott et al., in the book: "Proceedings of the Second International Conference on the Peaceful Uses of Atomic Energy." Selection of reports by foreign scientists [in Russian], 5, Moscow, Atomizdat (1959), p. 600.
3. R. Acroud and G. Kinchin, Report No. 1462, presented by Great Britain at the Second International Conference on the Peaceful Uses of Atomic Energy [Russian translation], Geneva (1958).
4. K. Henry and D. Smith, Nucl. Energy Soc., 1, No. 3 (1962).
5. A. I. Mogil'ner, Physics of Fast and Intermediate Reactors, Pt. 3, Vienna, IAEA (1962), p. 33.
6. A. I. Leipunskii et al., Physics of Fast and Intermediate Reactors, Pt. 3, Vienna, IAEA (1962), p. 328.
7. A. I. Leipunskii, O. D. Kazachkovskii, and M. S. Pinkhasik, Atomnaya Énergiya, 7, 370 (1961).
8. A. I. Leipunskii et al., Physics of Fast and Intermediate Reactors, Pt. 3, Vienna, IAEA (1962), p. 318.
9. N. V. Krasnoyarov, Reactor Safety and Hazards Evaluation Techniques. SM 24/81, Vienna, IAEA (1962).

Declassified and Approved For Release 2013/09/24 : CIA-RDP10-02196R000700010005-2

Declassified and Approved For Release 2013/09/24 : CIA-RDP10-02196R000700010005-2

DEVELOPMENT OF A FABRICATION TECHNOLOGY FOR ORGANIC-COOLANT PURIFYING FILTERS, AND THE STUDY OF THEIR HYDRAULIC RESISTANCE

(UDC 621.039.5)

Yu. I. Tokarev, F. F. Bogdanov, E. I. Pavlovskaya, and A. P. Chernopyatova

Translated from Atomnaya Énergiya, Vol. 18, No. 5, pp. 478-483, May, 1965
Original article submitted April 28, 1964; final editing completed September 5, 1964

Results of an experimental investigation of the hydraulic resistances of cermet disk filters designed to filter organic coolants under operating conditions are reported. A method of fabricating these filters is described, as well as experience acquired in their use under operating conditions. It is shown that the relationship $\zeta = f(\mathrm{Re})$ in the capillaries of the filters investigated here is described by the empirical formula $\zeta = C/\mathrm{Re}^n$.

It was established that the filters investigated may be regenerated (their filtering power may be restored) by a backflow of the required amount of coolant (5 to 8 liters) and by dumping the contaminated coolant into a drainage tank vented to the atmosphere.

The primary-loop piping and ancillary equipment in nuclear electric power generating stations based on organic-cooled reactors are usually made of carbon steels and may be used without biological shielding because of the absence of induced activity in the coolant (provided the requisite purity of the coolant is maintained). One of the fundamental requirements imposed on the coolant is, therefore, the absence of activating impurities in the coolant.

In operating experience with organic-cooled reactors in the USA (the OMRE) and in the USSR (the ARBUS), the persistent accumulation of small quantities of inorganic contaminants has been noted in the primary-loop coolant, despite stringent measures to purify the coolant prior to startup. These impurities are magnetite crystals in the primary-loop coolant (hydrogenation–stabilized gas oil coolant) of the ARBUS facility. Inorganic inclusions found in the OMRE reactor (using a polyphenyl mixture as coolant fluid) consist mainly of iron percarbide $Fe_{20}C_9$, though even here a slight quantity of magnetite contaminant was detected. The dry residue of the OMRE reactor coolant consists of iron percarbide or ferric oxide crystals (sized from several microns to fractions of a micron) surrounded by an insoluble highly polymerized organic film. The composition of the film is characterized by the high ratio of carbon atoms to hydrogen atoms. It was found that oxygen catalyzes the thermal decomposition of the polyphenyls, and that this is accompanied by the formation of resins and sludges.

The sources of the formation of inorganic contaminants in the coolant may be any of these:

1) metal filings, shavings, chips, gaining access to the loop from the exterior environment during assembly or overhaul operations;

2) products of corrosion of carbon steel formed as a result of water or oxygen getting into the loop in small quantities, as a result of the coolant coming into contact with atmospheric air when the loop is opened up for repair and overhaul. A direct relationship between the content of inorganic impurities in the coolant and the time spend in contact with atmospheric air has been observed on more than one occasion in the case of the OMRE reactor [1]. But it is not possible to completely preclude such contact at the existing state of technology in refueling operations. The high coolant temperature contributes to rapid descaling of the primary-loop walls by the coolant;

Declassified and Approved For Release 2013/09/24 : CIA-RDP10-02196R000700010005-2

Declassified and Approved For Release 2013/09/24 : CIA-RDP10-02196R000700010005-2

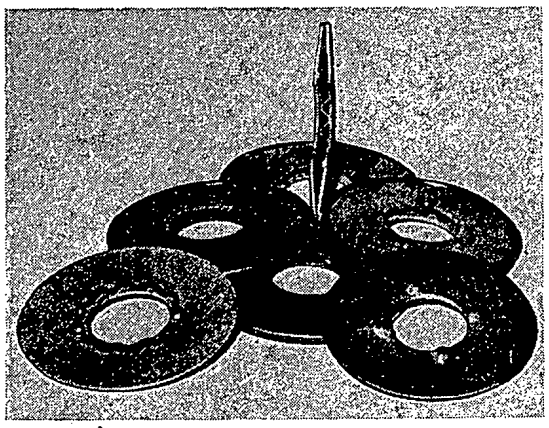

Fig. 1. Cermet filtering elements.

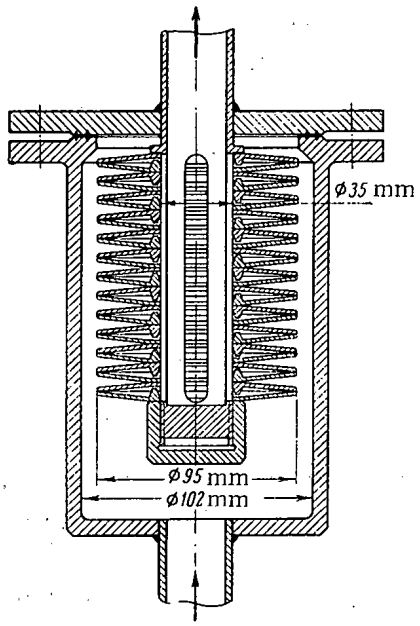

Fig. 2. Stack of filtering elements in place for testing.

3. corrosion products of carbon steel contacted with hot coolant. The corrosion rate in this case is insignificant, coming to ~ 0.05 mg/cm^2 at 315°C in the course of a month in the case of terphenyl, or ~ 0.15 mg/cm^2 in a month in the case of gas oil. Moreover, the corrosion is produced by the water present in trace amounts (several hundredths of a percent) in the organic coolant.

The purifying filters (porous stainless steel, pores sized from 5 to 40μ) installed in the auxiliary loop of the OMRE facility operated below expectations, clogging rapidly, so that more complicated techniques had to be invoked to purify the coolant: electrostatic and electromagnetic separations, cyclone separation, and centrifugation [1]. The clogging of the porous filters appears to be due to settling out of inorganic particulates entrained in the coolant and encapsulated in organic matter.

Coking deposits were formed in lesser amounts in the coolant (hydrogenation–stabilized gas oil) of the ARBUS facility primary loop. Ferric oxide particles present in the coolant did not become coated with organic film. This made it possible to do without more complicated purification procedures and to rely on the simplest available method, that of mechanical clean-up by the use of cermet filters.

Cermet filters are widely used in the machine-tool industry, in chemical processing, and in other branches of industry, since they: 1) exhibit improved retention of fine solid particulates thanks to the tortuosity and multilayered pore network, and the rigid fixed arrangement of the matrix of metal particles; 2) possess adequate mechanical strength; 3) are capable of withstanding sharp temperature fluctuations; 4) do not contaminate the filtrate with filter particles; 5) are distinguished by the simple fabrication technology and simple regeneration method (flushing the filtering surface with chemical solvents, baking the filter, ultrasonic cleaning).

The filter design must be as compact as possible as a result of precipitation of inorganic particulates on the filtering components, in order to reduce the γ background from the filter housing. With this object in mind, the design of the filtering component was selected as that of lenticular disks 95 by 36 mm in diameter (Fig. 1). This shaping rendered possible an increased ratio of filtration surface to volume occupied, reaching a figure of 1.54.

The fabrication technology of the filtering components was developed to consist of the following steps: production of the powder, preparation of the powder for compacting, sintering, chrome-plating, and expanding by rolling.

Spherical low-carbon steel pellets were produced from MSt. 1 and MSt. 2 steel wire on an EM-6 electric metallizer. The principle underlying the powder fabrication process is as follows: two wire electrodes are melted down

TABLE 1. Properties of Filter Elements

Powder fraction, mm	Compacting pressure, tons/cm^2	Air throughput, (p = 600 mm H_2O), m^3/min	Gas oil throughput (p = 1 atm), liters/min	Filtration fineness, μ	Crushing pressure, atm
0.063	2	0.20	10	15	18
0.1	2	0.25	16	20	16
0.2	2	0.35	20	25	10
0.3	2	0.50	24	30	8

Declassified and Approved For Release 2013/09/24 : CIA-RDP10-02196R000700010005-2

Declassified and Approved For Release 2013/09/24 : CIA-RDP10-02196R000700010005-2

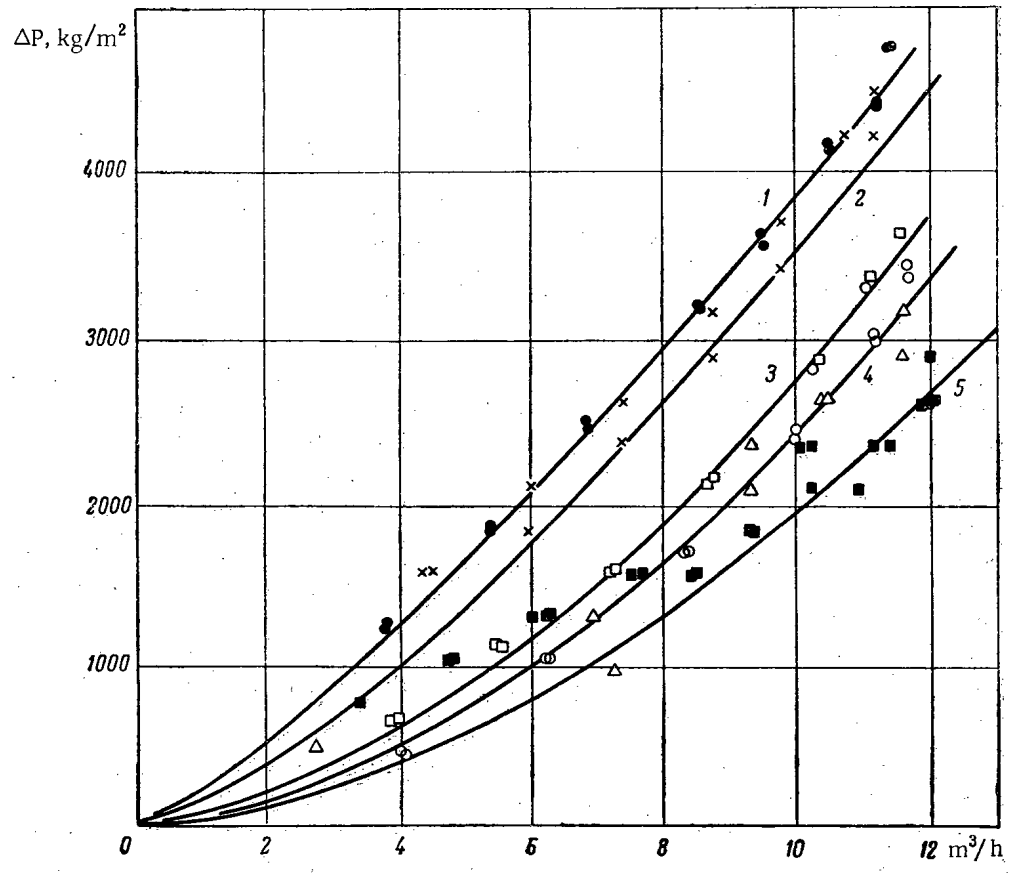

Fig. 3. Graph of $\Delta p = f(Q)$ for cermet filtering elements: 1) ●)– 0.063 mm fraction, t = 170°C; 2) × –0.2 mm fraction, t = 100°C; 3) □– 0.1 mm, fraction t = 180°C; 4) ○ –0.063 mm fraction, t = 300°C; 5) ■–0.2 mm fraction, t = 300°C; 6) △–0.2 mm fraction, t = 170°C.

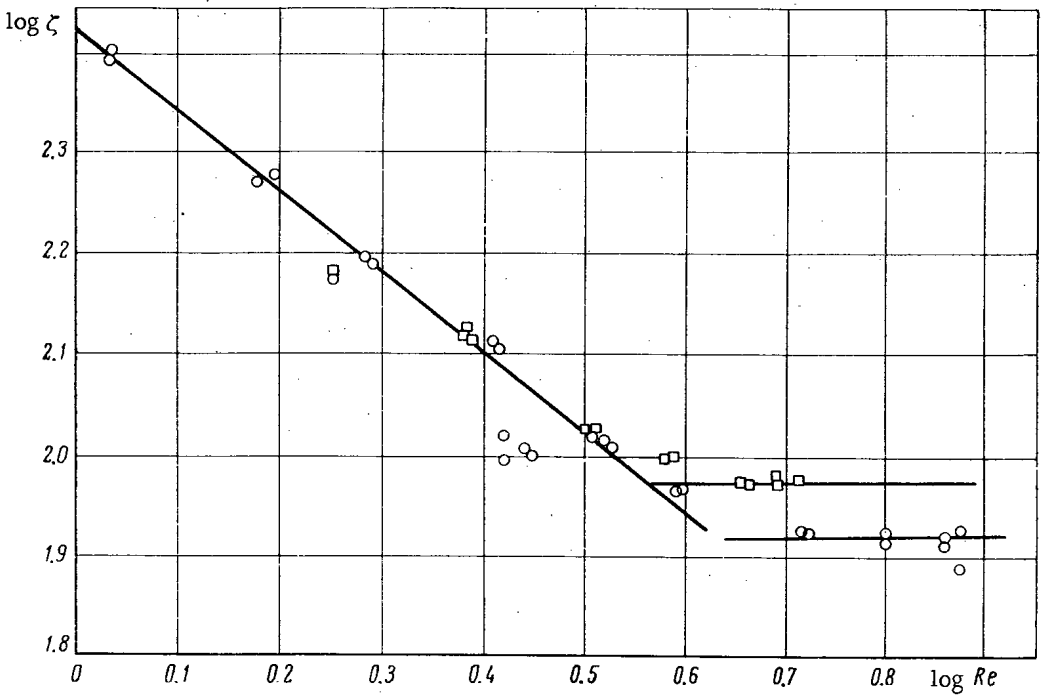

Fig. 4. Generalized graph of $\zeta = f(\mathrm{Re})$ for cermet filtering elements: ○, □–experimentally derived data for fractions 0.063 mm and 0.1 mm, respectively.

Declassified and Approved For Release 2013/09/24 : CIA-RDP10-02196R000700010005-2

Declassified and Approved For Release 2013/09/24 : CIA-RDP10-02196R000700010005-2

by the electric arc formed between them, whereupon the molten metal is sprayed into water by a compressed air jet. Since the powder is produced in oxidized form, it is reduced at 800°C in a 2 h operation. The reduced powder is broken down into segregated fractions in a device designed to effect mesh grading. Powders of mesh 0.063 mm, 0.1 mm, 0.2 mm, and 0.3 mm are employed in fabricating the filtering elements. The powders are mixed with filler material, to improve compacting behavior and contribute to enlarged open pores. Paraffin in amounts of 3 wt.% of the powder is used as filler. The mixture is then cold-pressed on a hydraulic press. The compacting pressure is 2 tons per square centimeter. The pressed filter disks are then sintered in special boxes in sintering ovens at 1200°C for 3 h. The sintering is performed in a reducing (hydrogen) atmosphere.

The filtering elements made of low-carbon steel powder are then diffusion chrome-plated in order to enhance their mechanical strength and their resistance to corrosive attack.

The diffusion gaseous chrome-plating process in a solid charge proceeds as follows. The filter disks are charged into a chrome-plated mix consisting of ferrochrome, aluminum oxide, and ammonium chloride. The chrome-plating step is carried out in an electric furnace at 1000°C for 10 h. The filter disks, after being chrome-plated, are then joined by rolling with the aid of 0.5 mm thick aluminum sheet. The basic properties of these filtering elements are listed in Table 1.

Special experiments involving the use of monoisopropyldiphenyl were carried out at 300°C in order to assess the filtering power and hydraulic resistances of cermet filtering elements so designed. Four stacks each containing 12 or 13 disk elements made of a specified powder mesh fraction (Fig. 2) were tested: d_1 = 0.063 mm (12 elements), d_2 = 0.1 mm, d_3 = 0.2 mm, and d_4 = 0.3 mm (13 filtering elements). The experiments were carried out on an experimental test assembly comprising a closed loop with forced circulation and electric heating of the coolant on the economizer section of the loop.

The following parameters were measured in the experiment: pressure drop across the filter; liquid flowrate through the filter, measured by a flowrate diaphragm and a mercury-filled differential manometer (error not exceeding 4% in either case); temperature of working fluid upstream of the filter (using chromel–alumel thermocouples and a PPTV potentiometer); breakdown of slurry by fractions before and after filtering in each run of experiments (using a medical microscope).

The experimentally derived data on hydraulic drag was processed in the form

$$\Delta p = f(Q);\ \zeta = f(Re),$$

where Δp is the pressure drop across the filters, in kg/m^2; Q is the coolant flow rate in m^3/h; $\zeta = 2g\Delta p/\gamma w^2$ is the local drag coefficient; Re = wd eq/ν. The coolant flowspeed in the filter capillary pores was determined from the ratio

$$w = \frac{Q}{F_1},$$

where F_1 is the filter flow area in m^2. In the case of a checkerboard arrangement of spherical particles in the layer F_1 = 0.0931 F, where F is the total filter area, in m^2.

In calculating the Re number as the decisive dimension, we made use of the hydraulic diameter $d_{eq} = 0.423\ \varepsilon^{1.25}/1-\varepsilon$ [2, 3]. In the case of the checkerboard arrangement of spherical particles, ε = 0.256, so that $d_{eq} = 0.0066 \cdot 10^{-3}$ for a filter of particles d = 0.063 mm, and $d_{eq} = 0.0105 \cdot 10^{-3}$ m for a filter of particles d = 0.1 mm.

Figure 3 shows a graph plotted for $\Delta p = f(Q)$ in the case of filters fabricated of powders of fractions 0.063 mm, 0.1 mm, 0.2 mm. Figure 4 shows a graph of $\zeta = f(Re)$ for filters fabricated of powders of fractions 0.063 and 0.1 mm with a total filtration area F = 0.1074 m^2 presented by 12 filtering elements. The experimental data points fit approximately on the straight line described by the formula

$$\zeta = 262 Re^{-0.785}. \qquad (1)$$

[plotted in log–log coordinates]. We see from Fig. 4, that the generalized formula is valid when Re < 4; but when Re > 4 the drag coefficient ζ hardly changes at all, in any of the filters tested, as Re increases; ζ = 84.0 for the filter fabricated with the 0.063 mm powder fraction, and ζ = 94.5 for the filter of the 0.1 mm powder fraction. Formula (1) deviates substantially from expressions published earlier, in both the value of the coefficient and in the exponential expression attached to the Re number. This means that the data published in references [2-6] are not suitable for use in design calculations for this type of purifying filters.

Declassified and Approved For Release 2013/09/24 : CIA-RDP10-02196R000700010005-2

Declassified and Approved For Release 2013/09/24 : CIA-RDP10-02196R000700010005-2

TABLE 2. Breakdown of Suspended Solids by Fraction

Particulate size, μ	Number particulates
$20 < \delta < 30$	To 35
$15 < \delta < 20$	To 35
$10 < \delta < 15$	To 140
$5 < \delta < 10$	To 315
$\delta < 5$	To 7200

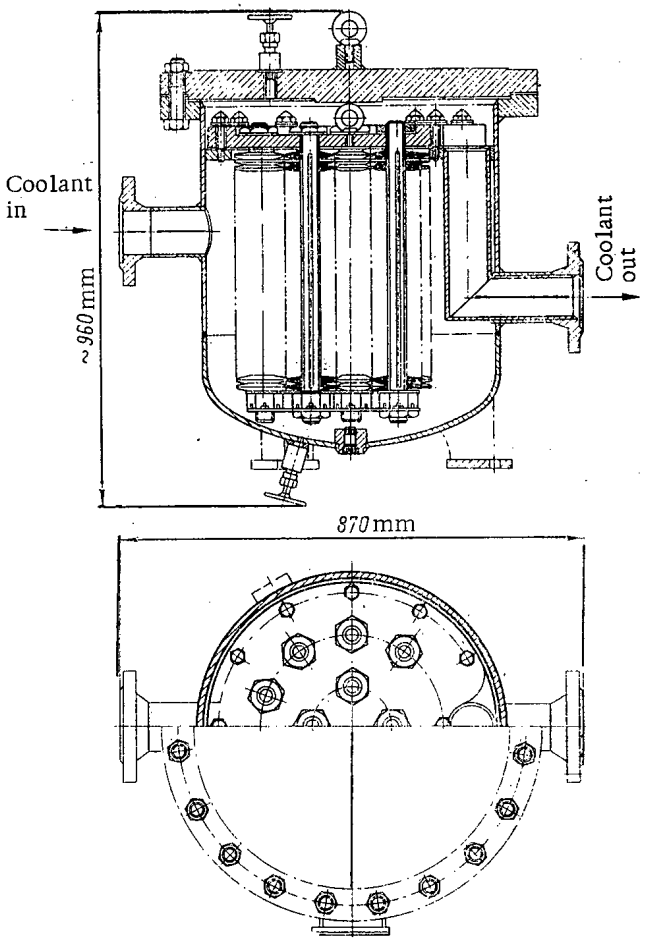

Fig. 5. Filter unit of the ARBUS facility.

Coolant samples were taken during the experiments prior to and after filtration, for microscopic analysis of the composition of suspended solids in the coolant. Table 2 lists the breakdown of these suspended solids by fractions, as found in a coolant sample (1 cm^3) tapped from the circulation loop upstream of the filter. 1380 particulates of up to 5μ in size were detected downstream of the filter. At the fraction composition of contaminants listed above, filters made of 0.3 mm, 0.1 mm, and 0.063 mm powder fractions and installed in the operating portion of the loop operated satisfactorily (without regeneration) for several tens of hours with no appreciable reduction in the flowrate of the filtered fluid at the specified pressure drop.

The experiments carried out and the analysis of the fraction composition of the suspended solids showed that particulates sized below 5μ are not completely retained by cermet filters fabricated with the 0.1 mm powder fraction (as operating experience was to reveal, these particulates are retained almost completely after a layer of retained fine-dispersion particulates is allowed to form on the filtering surface), and that cermet filter elements made of the 0.3 mm and 0.2 mm powder fractions fail to completely retain particulates sized from 10 to 15 μ unless the above-mentioned layer has already caked on the filtering surface.

It did not seem possible to account for the efficiency of the filtering elements during the preliminary tests in the face of a heightened content of polymers and unsaturated compounds formed via radiolysis of the coolant and entrained in the coolant. But a rise in the content of these compounds to 9-10% (permissible concentration limit) during experimental operation still had no discernible effect on the efficiency and capability of the filters.

Suspended solid particulates retained by the cermet filtering elements piled up on the filter surface and in the pores of the filters, thereby augmenting the hydraulic drag, so that the rate of coolant flow elements was restored almost completely by a regenerative backflow of the fluid through the filtering bed (the pressure drop across the filtering bed must exceed the operating pressure drop across the filter as a whole by 1-2 atm to achieve this.

A design of a filter unit (Fig. 5) was worked out to facilitate industrial-scale tests on the ARBUS plant. The housing of the filter unit was divided into top and bottom parts by a flange. The bottom communicates with the inlet, the top with the outlet connecting pipe. Twelve filter cartridges are mounted on the flange. Each cartridge consists of a rod on which 48 to 50 lenticular filtering elements 95 by 36 mm are fitted. The contaminated fluid enters the bottom of the filter housing, then on passing through the filtering elements becomes purified and is returned to the system via the knee-bend outlet connection. The housing is covered on top by a cover plate. Two such filter units are installed in parallel on the bypass line of the primary-loop main circulating pumps in the ARBUS facility. The rate of coolant flow through the filter units is 10% of the total flowrate.

Only two filtering cartridges were mounted in the housing of one of the filtering units in order to shorten the test duration. Tests carried out during experimental operations showed the filters to retain suspended particulates with satisfactory reliability. The iron concentration in the coolant does not exceed 0.4 mg/liter, assuring thereby a sufficiently low level of gamma-ray activity in the primary loop.

Declassified and Approved For Release 2013/09/24 : CIA-RDP10-02196R000700010005-2

Declassified and Approved For Release 2013/09/24 : CIA-RDP10-02196R000700010005-2

The requisite conditions for the successful performance of cermet filters designed to purify organic coolants in nuclear electric power generating stations are:

a) efficient precleaning of the coolant;

b) use of coolants recalcitrant to the formation of coking films;

c) taking all measures necessary to keep oxygen and water out of the coolant.

LITERATURE CITED

1. C. A. Trilling, Nucl. Engng., 6, No. 67 (1961).
2. R. S. Bernshtein, S. L. Shagalova, and V. V. Pomerantsev, Aerodynamics and heat transfer problems in boilers and furnaces. Symposium, edited by Knorre [in Russian], Moscow, State power press (1958).
3. I. E. Idel'chik, Handbook on hydraulic resistances [in Russian], Moscow, State power press (1960).
4. T. M. Bashta, Calculations and designs of aircraft hydraulic devices [in Russian], Moscow, Nat'l defense press, Oborongiz (1961).
5. G. F. Denisenko, Byulleten' "Kislorod," No. 6 (1962).
6. N. P. Ishkin and M. G. Kaganer, Byulleten' "Kislorod," No. 3 (1952).

All abbreviations of periodicals in the above bibliography are letter-by-letter transliterations of the abbreviations as given in the original Russian journal. *Some or all of this periodical literature may well be available in English translation.* A complete list of the cover-to-cover English translations appears at the back of this issue.

Declassified and Approved For Release 2013/09/24 : CIA-RDP10-02196R000700010005-2

Declassified and Approved For Release 2013/09/24 : CIA-RDP10-02196R000700010005-2

INTERNAL STRESSES CAUSED BY NON-UNIFORM SWELLING OF FISSIONABLE MATERIAL

Yu. I. Likhachev, V. P. Zvonarev and V. Ya. Pupko

Translated from Atomnaya Énergiya, Vol. 18, No. 5,
pp. 483-487, May, 1965
Original article submitted May 25, 1964

This paper examines a new cause of macro-stresses of the first kind in fuel elements—namely, non-uniform swelling of the fissionable material, caused by the fact that, owing to "corrosion" of the neutron flux, the amount of fission products formed is not uniform across-section of the fuel element. The authors give methods of calculating the magnitudes of the stresses. They note cases in which the stresses have an appreciable effect on the efficiency of the fuel element.

As is well known, internal stresses in solids can be caused by various factors—mechanical loading, non-uniform heating, the action of electromagnetic fields, and so on. However, in the fuel elements of nuclear reactors, internal stresses can also be caused by non-uniform swelling of the fissionable composition, due to the formation of fission products.

In heterogeneous reactors with slow neutrons, the neutron flux due to fission decreases from the surface to the center of the fuel element, so that the number of nuclei undergoing fission, and thus the amount of fission products formed, will also decrease from the surface to the center. The variation in fission density over the cross section of the fuel element depends essentially on the reactor parameters (moderator type, enrichment of the fissionable material, composition of fissionable substances, etc.), and can be determined either experimentally or by sufficiently precise calculations [1].

It has been experimentally and theoretically shown [2, 3] that the total volume of the fissioning uranium, and this leads to an increase in volume of the fissionable composition, known as "swelling." The varying number of fissions must therefore lead to non-uniform swelling over the volume of the fuel element, and this may lead to macro-stresses of the first kind, similar to those caused by non-uniform heating.

As the swelling in a small volume can be regarded as isotropic, we can use the Duhamel-Neumann principle [4] to find the amount of swelling by methods alreads fully developed for thermal stresses. For this purpose, in the expressions for thermal stress, the linear expansion αt must be replaced by the linear swelling deformation β_s (obtained by comparing V, the volume after swelling, with V_0, the initial volume):

$$\beta_s = \sqrt[3]{1+S} - 1, \tag{1}$$

where

$$S = \frac{V - V_0}{V_0}.$$

For small burnup (S of order of a few percent) we can put

$$\beta_s \approx \frac{1}{3} S.$$

To estimate the swelling caused by U^{235} burnup in various compositions, we make the following assumptions: The volume of the solid fission products in the composition lattice is equal to that in the pure state: the gaseous

Declassified and Approved For Release 2013/09/24 : CIA-RDP10-02196R000700010005-2

Declassified and Approved For Release 2013/09/24 : CIA-RDP10-02196R000700010005-2

fragments accumulating in the composition's micropores obey the Van der Weals gas equation; and the swelling depends linearly on the burnup. We then get

$$\left.\begin{aligned} S_{\mathrm{U}}(r) &= \left(3.1 + 1.8\frac{T}{p}\right) a_{\mathrm{U}} \frac{Q(r)\tau}{\varrho_{\mathrm{U}}}; \\ S_{\mathrm{UO_2}}(r) &= \left(1.6 + 0.9\frac{T}{p}\right) a_{\mathrm{UO_2}} \frac{Q(r)\tau}{\varrho_{\mathrm{U}}}; \\ S_{\mathrm{UN}}(r) &= \left(2.2 + 1.2\frac{T}{p}\right) a_{\mathrm{UN}} \frac{Q(r)\tau}{\varrho_{\mathrm{U}}}; \\ S_{\mathrm{UAl_3}}(r) &= \left(1.7 + \frac{T}{p}\right) a_{\mathrm{UAl_3}} \frac{Q(r)\tau}{\varrho_{\mathrm{U}}}, \end{aligned}\right\} \quad (2)$$

where T, p = temperature in °K and equilibrium pressure in kg/cm², respectively, of the gaseous fission products accumulating in the micropores; τ = irradiation time in sec; Q(r) = fission density in fissions/cm³·sec; ρ_{U} = concentration of fuel nuclei in composition; and a_j = volume fraction of fissionable material.

The first terms in the brackets represent the excess of the total fragment volume over the volume of fissioned uranium (the so-called "cold" swelling). (We note that the theoretical values for cold swelling agree satisfactorily with the experimental data—see [2] for pure uranium, [5] for uranium carbide, and [6] for uranium dioxide.)

The second terms represent "gaseous" (hot) swelling, caused by increase in the micropore volume due to gaseous fission products accumulating in the pores.

Hot swelling can be determined on the basis of a model of the gas pores [2, 3].

At high temperatures, the macrostress* in the fuel elements will be due to the inhomogeneous distribution of fission density and also of temperature (the temperature governs the pressure of the gaseous fission products and the creep resistance of the composition material [2]). Account must be taken of relaxation of the stresses during the working of the fuel element.

If the swelling deformation β_s is constant over the cross section of the fuel element, or changes according to a linear law (in rectangular coordinates), the swelling stresses will be zero for simply or doubly connected bodies, as in the case of thermal stresses [4]. With only cold, uniform swelling (β_s = const), the stresses in the fissionable material will be zero for any porosity, i.e., small volumes swell freely and the pores grow in size but remain geometrically similar (there should be no "corrosion" of the pores).

As an example, let us consider the stresses due to uniform cold swelling in a fuel element shaped as a long solid cylindrical rod. In this case,

$$Q(\varrho) = Q_0 I_0(c\varrho), \quad (3)$$

where Q_0 = fission density at center of fuel slug; $\rho = r/b$ = dimensionless radius, b being the outer radius of the slug; c = parameter depending on the composition and enrichment of the fissionable composition.

For a rod with free ends, the stresses due to non-uniform swelling are determined as follows [5]:

$$\sigma_\theta^s = \frac{E}{1-\mu}\left[\int_0^1 \beta_s(\varrho)\,\varrho\,d\varrho + \frac{1}{\varrho^2}\int_0^\varrho \beta_s(\varrho)\,\varrho\,d\varrho - \beta_s(\varrho)\right];$$

$$\sigma_r^s = \frac{E}{1-\mu}\left[\int_0^1 \beta_s(\varrho)\,\varrho\,d\varrho - \frac{1}{\varrho^2}\int_0^\varrho \beta_s(\varrho)\,\varrho\,d\varrho\right];$$

$$\sigma_z^s = \frac{E}{1-\mu}\left[2\int_0^1 \beta_s(\varrho)\,\varrho\,d\varrho - \beta_s(\varrho)\right],$$

where E = modulus of elasticity of the first kind, and μ = Poisson coefficient. For a low degree of burnup (a few percent),

*In calculating the macrostresses, we assume that small volumes contain enough micropores for their swelling to be considered isotropic.

Declassified and Approved For Release 2013/09/24 : CIA-RDP10-02196R000700010005-2

Declassified and Approved For Release 2013/09/24 : CIA-RDP10-02196R000700010005-2

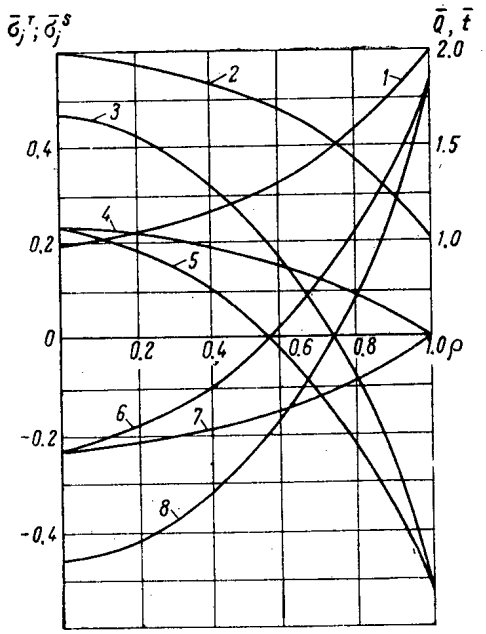

Fig. 1. Distribution curves of dimensionless components over cross section of cylindrical slug. 1) Fission density Q; 2) Temperature t; 3, 4, 5) Stresses $\bar{\sigma}_z^s, \bar{\sigma}_r^s, \bar{\sigma}_\theta^s$, respectively, caused by inhomogeneity of fission; 6, 7, 8) thermal stresses, $\bar{\sigma}_\theta^T$, $\bar{\sigma}_r^T$, $\bar{\sigma}_z^T$ respectively.

$$\left.\begin{aligned}
\sigma_\theta^s &= \frac{Q_0 \tau a}{\varrho U} G \frac{E}{1-\mu} \\
&\times \left[\frac{1}{c} I_1(c) + \frac{1}{c\varrho} I_1(c\varrho) - I_0(c\varrho)\right]; \\
\sigma_r^s &= \frac{Q_0 \tau a}{\varrho U} G \frac{E}{1-\mu}\left[\frac{1}{c} I_1(c) - \frac{1}{c\varrho} I_1(c\varrho)\right]; \\
\sigma_z^s &= \frac{Q_0 \tau a}{\varrho U} G \frac{E}{1-\mu}\left[\frac{2}{c} I_1(c) - I_0(c\varrho)\right],
\end{aligned}\right\}$$

where a_G = volume fraction of fissionable material.

For heat sources distribured according to (3), the thermal field is represented by the equation

$$t(\varrho) - t(1) = \frac{q_{V_0}}{\lambda c^2}\left[I_0(c) - I_0(c\varrho)\right],$$

where λ = coefficient of thermal conductivity of composition, q_{V_0} = density of thermal flux at center of slug. Then the thermal stresses [5] are

$$\left.\begin{aligned}
\sigma_\theta^T &= \frac{\alpha q_{V_0}}{\lambda c^2} \frac{E}{1-\mu} \\
&\times \left[I_0(c\varrho) - \frac{1}{c\varrho} I_1(c\varrho) - \frac{1}{c} I_1(c)\right]; \\
\sigma_r^T &= \frac{\alpha q_{V_0}}{\lambda c^2} \frac{E}{1-\mu}\left[\frac{1}{c\varrho} I_1(c\varrho) - \frac{1}{c} I_1(c)\right]; \\
\sigma_z^T &= \frac{\alpha q_{V_0}}{\lambda c^2} \frac{E}{1-\mu}\left[I_0(c\varrho) - \frac{2}{c} I_1(c)\right],
\end{aligned}\right\} \quad (5)$$

where α = thermal expansion coefficient of material of fuel element. Figure 1 gives the distribution curves for certain parameters across the cross section of a slug made of UO_2 with 10% enrichment by U^{235} (so that $c \approx 1.8$). The parameters given are the relative fission density $\bar{Q} = Q(\rho)/Q_0$, the relative temperature $\bar{t} = [t(\rho) - t(1)]\frac{\lambda c^2}{q_{V^0}}$ and the dimensionless stress

$$\bar{\sigma}_j^s = \sigma_j^s \frac{1-\mu}{E} \frac{\varrho U}{Q_0 \tau a_r}; \quad \bar{\sigma}_j^T = \sigma_j^T \frac{1-\mu}{E} \frac{\lambda c^2}{\alpha q_{V_0}},$$

where $j = \theta, r, z$.

From (4) and (5) we see that $\bar{\sigma}_j^s = -\bar{\sigma}_j^T$.

If the burnup at the center of the slug is 10% in U^{235}, then, for $E = 2 \cdot 10^4$ kg/mm^2 and $\mu = 0.3$, we get

$$\varrho = 0; \quad \sigma_z^s = 2\sigma_\theta^s = 2\sigma_r^s = 66 \text{ kg/mm}^2;$$
$$\varrho = 1, \quad \sigma_\theta^s = \sigma_z^s = -74 \text{ kg/mm}^2; \quad \sigma_r^s = 0.$$

The absolute value of the thermal stresses will be equal to the stresses from non-uniform swelling at 10% burnup, if the temperature difference across the slug cross section is $\Delta t = 420°C$.

Let us examine the joint action of stresses from non-uniform swelling and of thermal stresses for various cases.

Case 1. Brittle material with negligible creep rate (ceramic slug, medium temperature). Thermal stresses attain their full value when the reactor goes on power. The stresses due to non-uniform swelling are then zero. As the fuel is burnt up, they increase, reducing the thermal stresses.

Declassified and Approved For Release 2013/09/24 : CIA-RDP10-02196R000700010005-2

Declassified and Approved For Release 2013/09/24 : CIA-RDP10-02196R000700010005-2

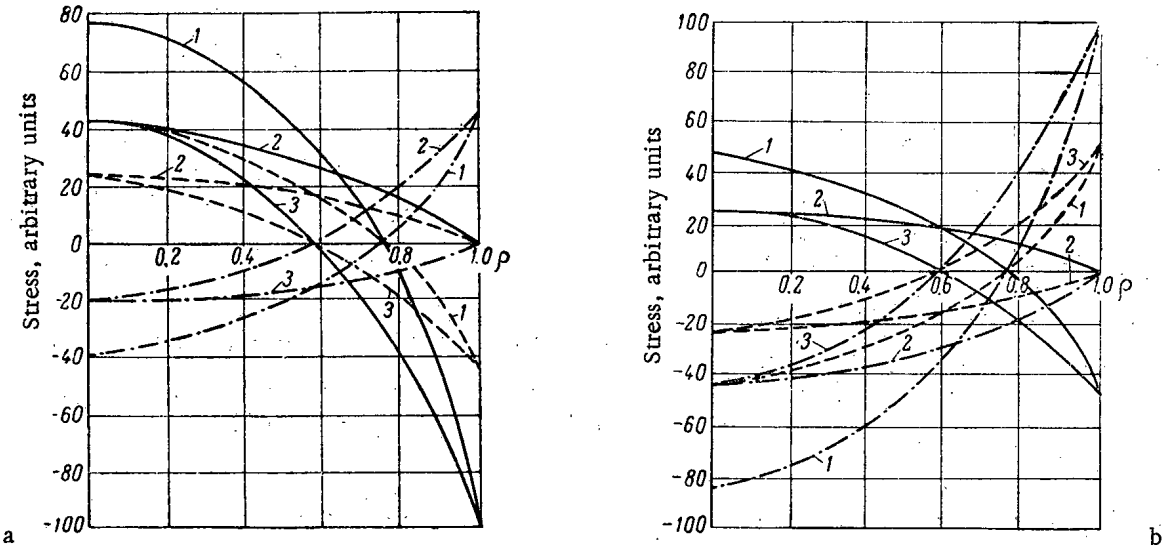

Fig. 2. Curves of stress due to non-uniform swelling, thermal stress, and total stress in cylindrical slug. (a) Initial stage with $\frac{\alpha q_{V_0}}{\lambda c^2} > \frac{Q_0 \tau a_G}{\varrho U}$; (b) With burnup such that $\frac{\alpha q_{V_0}}{\lambda c^2} < \frac{Q_0 \tau a_G}{\varrho U}$: (1, 2, 3) Stresses σ_z, σ_r, σ_θ respectively. ———— Stresses due to non-uniform swelling, σ_j^s; —·—·—·— Thermal stresses, σ_j^T; σ_j^s; – – – – Total stresses σ_j^Σ.

Fig. 2 shows the thermal stresses, due to non-uniform swelling and total stresses, $\sigma_j^\Sigma = \sigma_j^T + \sigma_j^s$, for the case when

$$\frac{\alpha q_{V_0}}{\lambda c^2} > \frac{Q_0 \tau a_G}{\varrho U}. \tag{6}$$

As the burnup increases, the total stress decreases; when the equation

$$\frac{\alpha q_{V_0}}{\lambda c^2} = \frac{Q_0 \tau a_G}{\varrho U} \tag{7}$$

is satisfied, the stress due to non-uniform swelling equals the thermal stress in absolute value, so that the total stress vanished and consequently the heated fuel element is completely free from load.

After further burnup, when

$$\frac{\alpha q_{V_0}}{\lambda c^2} < \frac{Q_0 \tau a_G}{\varrho U}, \tag{8}$$

the stress due to non-uniform swelling becomes greater than the thermal stress, and the total stress changes sign and smoothly rises (see Fig. 2b).

When the reactor is shut down the thermal stresses vanish, but the stresses due to non-uniform swelling remain and are greater than in the element when working, so that the fuel element is more likely to break down when the reactor is shut off.

From the above it follows that, when calculating the fuel element durability in this case, it is necessary to take account of both types of stress working together.

Case 2. Plastic material with negligible creep rate (metal slug, relatively low temperature). If the thermal stresses do not cause plastic deformation, then, for the degree of burnup at which (6) and (7) hold, the slug remains elastic and the stresses are determined in the same way as for Case 1. For relatively high degrees of burnup, when (8) holds, the stresses in a shut-down reactor may be appreciably more than the thermal stresses (see Fig. 2b), and thus plastic deformation may occur (at the slug surface) on shutting down the reactor.

Declassified and Approved For Release 2013/09/24 : CIA-RDP10-02196R000700010005-2

Declassified and Approved For Release 2013/09/24 : CIA-RDP10-02196R000700010005-2

It should be noted that, when the reactor is shut down, the residual stresses due to non-uniform swelling cause triaxial stretching, which may result in brittle fracture of the plastic slug material, especially as radiation damage may convert the material to a brittle state.

In this case, estimates of the strength must also take account of stresses due to swelling.

Case 3. Material with appreciable creep rate (relatively high temperature). As stresses due to non-uniform swelling increase only slowly, they will be largely relaxed by the creep. In estimating the strength of a fuel element at considerable thermal loadings, thermal stresses play the most important part.

On cooling a slug in which the termal and non-uniform swelling stresses have almost vanished during working owing to relaxation, considerable residual thermal stresses will appear owing to the sharp fall in creep rate when the temperature is reduced. These stresses may result in the fracture of slugs made of ceramic materials.

LITERATURE CITED

1. G. I. Marchuk, Numerical methods for calculations on nuclear reactors [in Russian], Moscow, Gosatomizdat, (1961).
2. Benns et al., in book "Proc. of Second International Conference on the Peaceful Uses of Atomic Energy." Reports of non-Soviet scientists. 6, Atomizdat, (1959), p. 325.
3. V. M. Agranovich, É. Ya. Mikhlin, and L. P. Semenov, Atomnaya Énergiya , 15, 393 (1963).
4. B. Boley and J. Weiner, Theory of Thermal Stresses. N. Y.—London, Columbia University (1960).
5. F. Rough and R. Dickerson, Nucleonics, 18, 70 (1960).
6. J. Ainscough, Nucl. Engng, No. 87, 272 (1963).
7. Symposium, "Strength and deformation in non-uniform temperature fields", ed. by Ya. B. Fridman, Moscow., Gosatomizdat (1962).

All abbreviations of periodicals in the above bibliography are letter-by-letter transliterations of the abbreviations as given in the original Russian journal. *Some or all of this periodical literature may well be available in English translation.* A complete list of the cover-to-cover English translations appears at the back of this issue.

Declassified and Approved For Release 2013/09/24 : CIA-RDP10-02196R000700010005-2

Declassified and Approved For Release 2013/09/24 : CIA-RDP10-02196R000700010005-2

EXTRACTION OF RADIUM FROM LIQUID WASTE BY SORPTION ON MANGANESE DIOXIDE

(UDC 621.039.714 : 546.432)

A. P. Tyutrina, B. P. Zhagin and V. G. Bakhurov

Translated from Atomnaya Énergiya, Vol. 18, No. 5,
pp. 487-491, May, 1965
Original article submitted May 13, 1964

The authors study the feasibility of using amorphous manganese dioxide and pyrolusite to extract radium from the effluent of uranium production. The recommended sorbent is synthetic manganese dioxide deposited on sawdust, or alternatively pyrolusite, used in columns with a fluidized bed. The spent pyrolusite can economically be used to oxidize uranium at the stage of stripping the ore.

The liquid waste formed in the hydrometallurgical treatment of uranium ores contains a considerable amount of toxic impurities. For example, the radium concentration is often one or two orders of magnitude greater than the permitted level; the latter is $5 \cdot 10^{-11}$ curie/liter (PDK maximum permissible concentration) [1].

Amorphous manganese dioxide is well known as a good sorbent for the alkaline earth metals [2]. Ebler [3] showed that active dioxide effectively sorbs radium, even in the presence of high barium concentrations. The present authors have used amorphous manganese dioxide and pyrolusite to extract radium from effluent.

For carrying out the process continuously in dynamic conditions, a suitable sorbent can be obtained by distributing amorphous dioxide on the developed surface of a solid coarsely-dispersed filler which effectively retains the precipitate. The base used to carry the dioxide was sawdust.

To prepare the sorbent, air-dried sawdust was impregnated with 0.1 M potassium permanganate solution. The amount taken up was 70-80 mg/g sawdust. In some cases the sawdust was additionally treated with manganous chloride solution. The sorbent was loaded into columns of diameter 20-35 mm and washed free from potassium and chlorine ions with distilled water. The weight of the sawdust was 7-30 g. We studied the sorption of radium from solutions of a mixture of salts, corresponding to industrial effluent. The average solution composition is given in Table 1. The linear filtration rate was 0.5-1.2 m/h. The solution was in contact with the sorbent for 7-16 min.

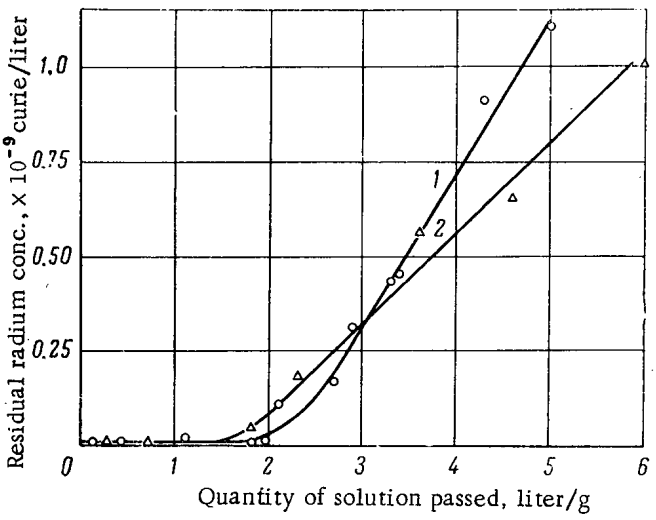

Fig. 1. Dynamic sorption of radium on amorphous manganese dioxide at pH = 7.3. (1) Sawdust treated with 0.1 M $KMnO_4$; (2) Sawdust treated with 0.1 M $KMnO_4$ and 0.25 M $MnCl_2$.

When solution 1 interacted with amorphous manganese dioxide on sawdust, radium was efficiently sorbed. The residual radium concentration dropped to the maximum permissible level after the filtrate had traversed 6 liter/g sawdust. The dioxide's sorptive capacity was thus $1.4 \cdot 10^{-7}$ curie/liter, equivalent to $1.1 \cdot 10^{-9}$ curie/g sawdust. The full capacity was not attained owing to lack of time.

Radium was also efficiently sorbed from Solution 2 at pH = 7.3. Fig. 1 gives the results of this series of experiments: curves 1 and 2 are practically

Declassified and Approved For Release 2013/09/24 : CIA-RDP10-02196R000700010005-2

Declassified and Approved For Release 2013/09/24 : CIA-RDP10-02196R000700010005-2

TABLE 1. Solution Compositions, g/liter

Soln.	pH	Ra	U	Ca	Mg	Fe	F	SO_4	NO_3	Cl	Dry residue
1	10.5	$2 \cdot 10^{-10}$	$5 \cdot 10^{-5}$	1.19	—	$3 \cdot 10^{-4}$	—	2.5	3.0	$6.4 \cdot 10^{-2}$	9.2
2	7.3	$1.5 \cdot 10^{-9}$	$6 \cdot 10^{-5}$	1.10	1.55	$9.8 \cdot 10^{-3}$	$5.6 \cdot 10^{-2}$	8.0	—	—	17.1

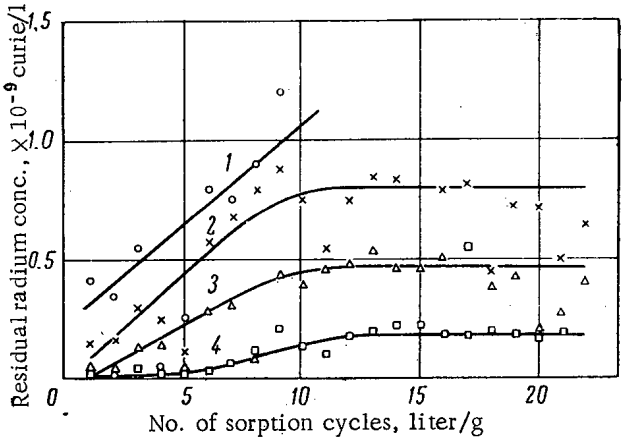

Fig. 2. Sorption of radium by pyrolusite in static conditions at pH = 10.3. 1) Fraction 0.63–1 mm; 2) fraction 0.4–0.63 mm; 3) fraction 0.05–0.3 mm; 4) fraction < 0.05 mm.

TABLE 2. Sorptive Capacity of Pyrolusite in Static Conditions at pH = 7.3 and 10.3

Sorptive fraction	pH	Quantity of solution treated, liter	Sorptive capacity, curie/liter	Remarks
0.63—1.0	7.3	5	$1.27 \cdot 10^{-9}$	
	10.3	9	$2.72 \cdot 10^{-9}$	
	7.3	6	$0.88 \cdot 10^{-9}$	
0.4—0.63	10.3	22	$1.4 \cdot 10^{-8}$	
	7.3	27	$1.48 \cdot 10^{-9}$	Full sorptive capacity not attained
0.05—0.3	10.3	22	$1.76 \cdot 10^{-8}$	
	7.3	27	$2.18 \cdot 10^{-8}$	
<0.05	10.3	22	$2.18 \cdot 10^{-8}$	

identical, so it was unnecessary to treat the sawdust with any more manganous chloride.

When the residual radium concentration in the filtrate is less than the permitted level, the sorptive capacity of the dioxide is $2.8 \cdot 10^{-7}$ curie/liter, or $2.2 \cdot 10^{-9}$ curie/g sawdust, which, when converted to volume of solution passing through, is 1.9 liter/g. In the same conditions the total sorptive capacity was $5 \cdot 10^{-7}$ curie/g MnO_2, i.e., $4.9 \cdot 10^{-9}$ curie/g sawdust.

We also studied the sorption of radium from industrial solutions on natural pyrolusite containing 63% MnO_2. The mineral specimens used did not swell and retained their original degree of dispersion on wetting. The following pyrolusite fractions were studied: 0.63–1.0 mm; 0.4–0.63 mm; 0.05–0.3 mm and < 0.05 mm. Sorption was performed both in static and dynamic conditions.

In static conditions, 1 g of crushed mineral was weighed into a beaker and agitated with 1 liter of solution 2 (see Table 1) for 30 min until equilibrium was attained. After being left to stand for a day, the precipitate was filtered off. The filtrate was analyzed for radium content, and the precipitate was again transferred to a beaker and agitated with a fresh portion of solution.

Two series of experiments were performed with solutions of pH 7.3 and 10.3. The latter solution was prepared by treating solution 2 with calcium hydroxide suspension and separating the precipitate.

In each of these two series of experiments, the sorptive capacity depended on the surface area of the precipitate, and increased regularly with decreasing sorbent particle radius. The most characteristic curves were obtained by sorption of radium from alkaline solution (Fig. 2). The scatter of the points on the graph is due to unavoidable fluctuations of the radium concentrion in solution 2. For the same degree of fineness, the sorptive capacity in the alkaline medium was greater than in the neutral medium. At pH = 10.3, after 22 stages of sorption the total sorptive capacity was not attained, and the solid phase was a long way from being saturated. The sorptive capacities of various pyrolusite fractions are given in Table 2.

In dynamic conditions, the sorptive capacity was determined for the three fractions 0.63–1.0 mm; 0.4–0.63 mm; 0.3–0.4 mm. With finer fractions, owing to the high degree of compaction when acted on by the current, industrially usable filtration rates were not achieved. The sorptive capacity was found by analyzing the solid phase and filtrate. As with static conditions, the sorptive capacity of the sorbent increases with its specific surface, and for the 0.63–1.0 mm fraction was $0.73 \cdot 10^{-9}$ curie/g, for 0.4–0.63 mm, $1.41 \cdot 10^{-9}$ curie/g, and for 0.3–0.4 mm, $2.53 \cdot 10^{-9}$ curie/g.

Declassified and Approved For Release 2013/09/24 : CIA-RDP10-02196R000700010005-2

Declassified and Approved For Release 2013/09/24 : CIA-RDP10-02196R000700010005-2

TABLE 3. Parameters of Filtration Columns Containing Mixture of Pyrolusite and Sawdust

Column No.	Pyrolusite fraction, mm	Height of sorbent layer, cm	Linear velocity, m/hr	Duration of interaction of solution and sorbent, min.
1	0.05—1.0	22	1.0—2.4	6—11
2	<0.25	17	1.2	9
3	<0.05	12	1.2	6

The use of an inert filler, which imparts a greater porosity to the sorbent layer, enables finer fractions to be employed. The filler used was sawdust. A well-regulated flow rate with satisfactory permeability was obtained when the ratio by weight of pyrolusite to sawdust was 5 : 1 or less. Table 3 gives the parameters of the filtration columns containing filler; the column cross section was 4.15 cm^2. Fig. 3 plots the sorption dynamics of radium versus the particle radius.

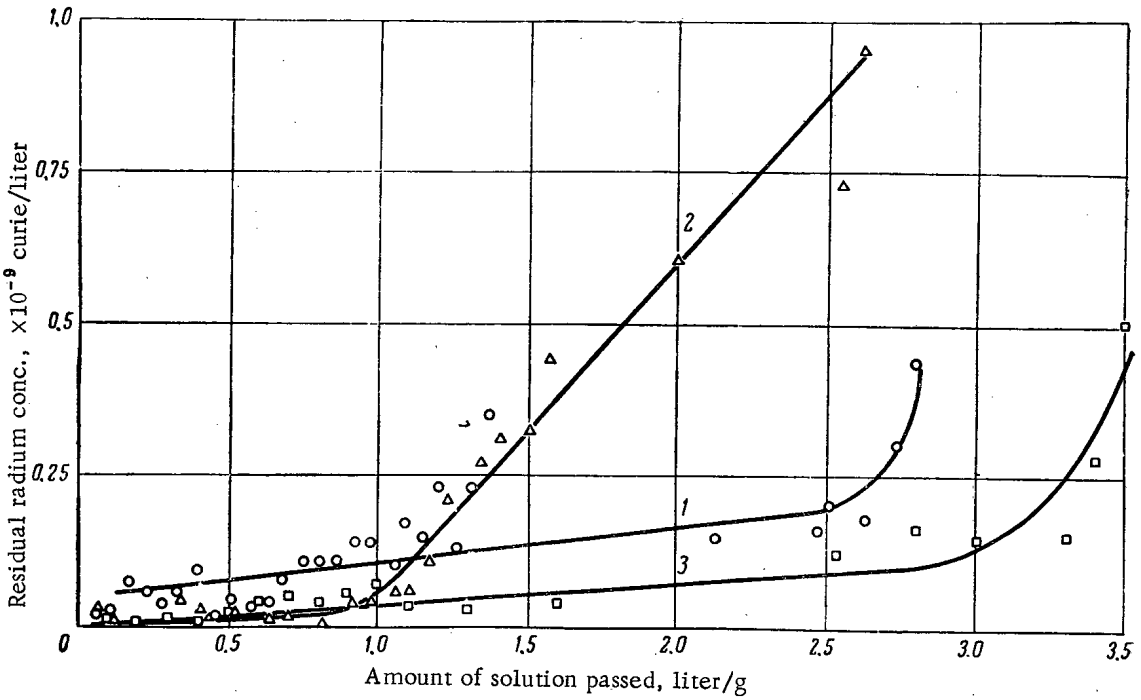

Fig. 3. Sorption dynamics on pyrolusite with filler. (1) Fraction 0.05-1 mm; (2) fraction < 0.25 mm; (3) fraction < 0.05 mm.

The high density of natural pyrolusite makes it possible to carry out sorption in a fluidized bed with a limited liquid flow rate. For a given fraction, the amount of sorbent carried away by the flow depends on the rate of filtration, the column parameters and the degree of inhomogeneity of the particles. With particles < 0.25 mm and flow rate 5 m/h, the weight loss of sorbent is 25-28%. As the flow rate is decreased, the amount of entrainment sharply falls, and at 3 m/h is 4-5% or less. Table 4 and Fig. 4 give the column parameters and sorption dynamics for pyrolusite in a fluidized bed. The sorption columns with the pyrolusite were connected in series with columns containing sawdust to catch the pyrolusite entrained by the flow.

It has been shown [3] that the interaction of radium with manganese dioxide is due to a chemical process taking place at the surface of the solid phase. The strong adhesion of radium to the precipitate may be explained by the formation of an adsorbed compound of the manganite or pyromanganite type, less soluble than the corresponding salts of the other alkaline earths.

The use of amorphous manganese dioxide spread on the surface of sawdust will effect the sorption of radium from solutions containing up to 20 g/liter of salts, yielding solutions with radium concentrations below the sorbent carrier is attractive, because, by burning it after a sorption cycle, we can get a solid with a relatively high radium concentration. The sorbent weight is then decreased by a factor of 20-50, depending on the salt composition of the solution treated; the total sorptive capacity of manganese dioxide is $5 \cdot 10^{-7}$ curie/g.

Declassified and Approved For Release 2013/09/24 : CIA-RDP10-02196R000700010005-2

Declassified and Approved For Release 2013/09/24 : CIA-RDP10-02196R000700010005-2

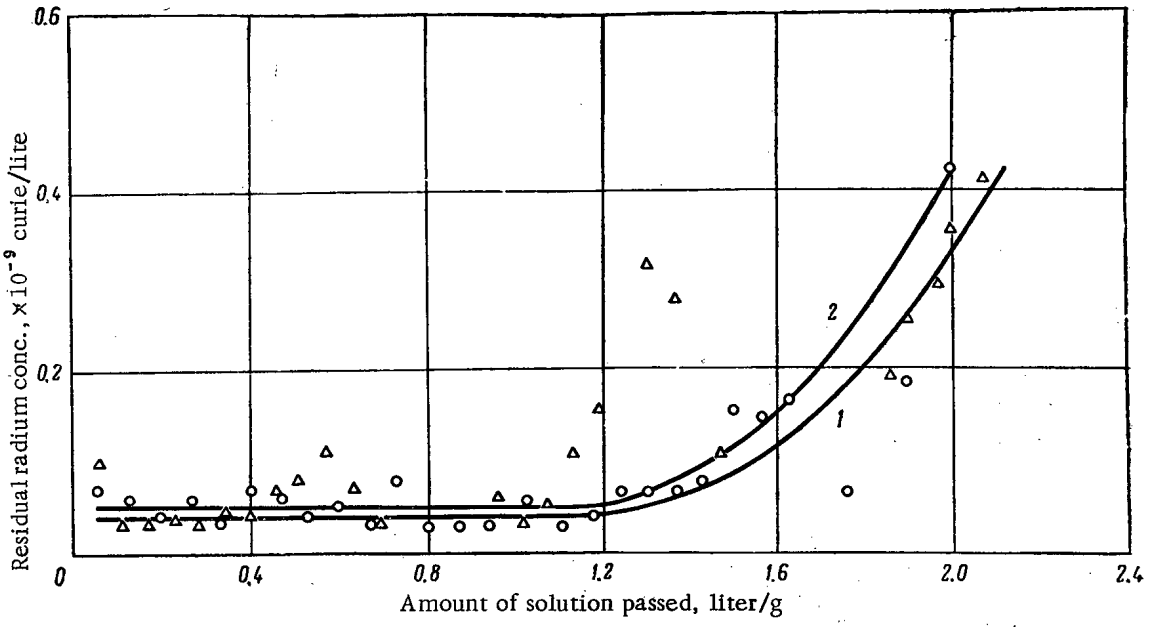

Fig. 4. Sorption of radium in fluidized bed of pyrolusite. Linear velocities: (1) 1.6 m/hr; (2) 3.3 m/h.

TABLE 4. Column Parameters for Pyrolusite in Fluidized Bed

Column no.	Pyrolusite particle size, mm	Column diameter, cm	Weight of pyrolusite, g	Height of pyrolusite layer, cm	Weight of sawdust, g	Height of sawdust layer, cm	Ratio of pyrolusite weight to sawdust weight	Linear velocity of flow, m/hr.
1	<0.25	1.4	30	18	10	42	3 : 1	3.3
2	<0.25	2.0	35	10.7	7	15	5 : 1	1.6

When fine fractions of natural pyrolusite are used (mixed with sawdust to get industrial filtration velocities) the component ratio should not exceed 5 : 1. In the sorption of radium under dynamic conditions with flow rates of 5 m/h or less, equilibrium is attained as rapidly as in static conditions. It was found that the sorptive capacity for both conditions is of the same order, and increases with rising pH.

Pyrolusite can be used for purifying solutions in simple apparatus at high flow rates. Effective utilization of the working volume of the column (when filtering from above downwards) can be attained by using pyrolusite without filler. However, in this case the degree of dispersion of the sorbent limits its permeability.

It is preferable to use pyrolusite in a fluidized bed, as this makes it possible to sorb radium from a liquid containing considerable quantities of solid impurities. The intense mixing of the sorbent particles in a fluidized bed brings the sorption close to the static state.

The process efficiency can be increased by using a system of adsorbers and filters to capture solid particles entrained by the flow. Sawdust is recommended as a cheap and easily available material for the filters.

In the sulfuric-acid stripping of ores, pyrolusite is used as an oxidant. It is therefore economical to combine radium sorption with subsequent use of the spent sorbent in ore stripping.

The authors wish to thank S. V. Golovin, V. A. Gorinov and A. I. Shustova for help in the work.

LITERATURE CITED

1. Health rules for work with radioactive substances and sources of ionizing radiation. Moscow., Gosatomizdat, [in Russian], (1960).
2. E. V. Alekseevskii, Active Manganese Dioxide [in Russian], L., ONTI-Khimteoretizdat, (1937).
3. E. Ebler and W. Bender, Z. anorgan. chem., 84, 77 (1913); Z. angew. chem., 28, 1042 (1915).

Declassified and Approved For Release 2013/09/24 : CIA-RDP10-02196R000700010005-2

Declassified and Approved For Release 2013/09/24 : CIA-RDP10-02196R000700010005-2

REACTION KINETICS AND THE EQUILIBRIUM STATE IN THE SYSTEM $CO_2 - CO - C$ UNDER THE ACTION OF FAST ELECTRONS

(UDC 541.15)

G. P. Zhitneva, S. Ya. Pshezhetskii, N. A. Slavinskaya, and S. A. Kamenetskaya

Translated from Atomnaya Énergiya, Vol. 18, No. 5, pp. 492-496, May, 1965
Original article submitted May 13, 1964

The kinetics of reactions occurring in the system CO_2-CO-C under the action of fast electrons (200 keV) were studied under standard conditions. The temperature was varied within the range 25-400°C; pressure 200-600 mm Hg. The absorbed energy was equal to $3.0 \cdot 10^{15}$ eV /(cm^3 · sec) at a current strength of 100 μA. The decomposition of CO_2 in the presence of carbon is a zero order reaction, while the decomposition of CO is a first order reaction. The activation energies of both reactions are close to zero. The rate of decomposition of CO_2 and CO is a linear function of the radiation intensity. The steady-state concentration of CO, established in the system after prolonged irradiation, is independent of the radiation intensity, temperature of the reaction zone, and depends on the magnitude of the carbon surface.

A study of the kinetic of the reaction of carbon dioxide with carbon dioxide with carbon under the action of ionizing radiations is interesting in view of the use of CO_2 as a coolant in uranium-graphite reactors. The published data concerning this reaction are very incomplete [1]. Its kinetics have been little studied; there are practically no kinetic characteristics.

This article presents data characterizing the kinetics of the forward and reverse reactions, as well as the basic principles determining the establishment of an equilibrium state in the system $CO_2 + C \rightleftharpoons 2CO$. The radiation was simulated by fast electrons with an energy of about 200 keV, the chemical effects of which, just as those of other types of nuclear radiation, were chiefly due to interaction with molecules of secondary electrons.

INVESTIGATION PROCEDURE

An electron accelerator with extracted beam was used. The voltage of the accelerating field was equal to 200 kV. The electron beam entered the reaction vessel through a membrane of aluminum foil 20 μ thick. The reaction vessel, with a volume of 1.4 liters, was made of molybdenum glass. The energy absorbed by the gas was measured with the aid of the dosimetric reaction of decomposition of nitric oxide. The absorbed energy comprised $3.0 \cdot 10^{15}$ eV /(cm^3 · sec), at a current strength of 100 μA. The reaction vessel was heated by an electric furnace.

TABLE 1. Rate of the Forward Reaction for Various CO_2 Concentrations.

$[CO_2]_0$, $\times 10^2$ Moles/liter	t, min	$[CO_2]_0 - [CO_2]$, $\times 10^5$	w_{for}, $\times 10^7$, moles/liter · min
0.50	30	1.2	4.0
0.77	30	0.9	3.0
0.97	30	0.9	3.0
0.99	30	3.5	3.9
1.20	90	3.5	3.9
1.43	30	1.2	4.0

The temperature was measured with a chromel-copel thermocouple. Before the experiment, CO_2 and CO were thoroughly purified and dried. Carbon was used in the form of graphite bars (2.5 · 10 · 0.5 cm), and a powder applied on glass wool. The reaction rate was measured according to the change in the composition of the gas mixture with time. The composition of the mixture was determined

Declassified and Approved For Release 2013/09/24 : CIA-RDP10-02196R000700010005-2

Declassified and Approved For Release 2013/09/24 : CIA-RDP10-02196R000700010005-2

TABLE 2. Rate Constant of the Forward Reaction

$[CO_2]_0$, $\times 10^2$ mole/liter	t, min	$[CO_2]_0 - [CO_2]$, $\times 10^6$	k^*_{for}, $\times 10^7$ mole/liter · min
0.50	10	4.0	4.0
	15	6.2	4.1
	20	8.0	4.0
	25	10.0	4.0
	30	12.0	4.0
1.43	10	3.9	3.9
	20	7.8	3.9
	30	12.3	4.1
	40	16.4	4.1
	50	20.0	4.0

* $k_{av} = 4.0 \cdot 10^{-7}$

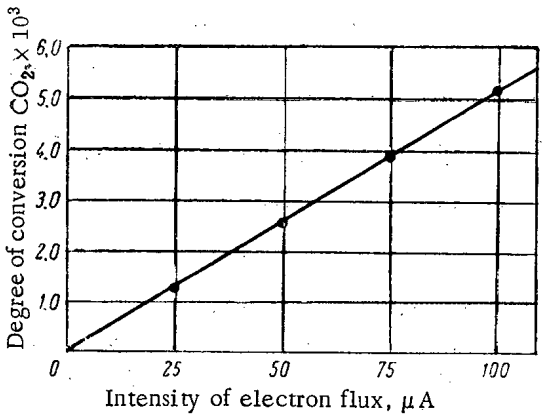

Fig. 1. Dependence of the degree of conversion of CO_2 on the irradiation intensity.

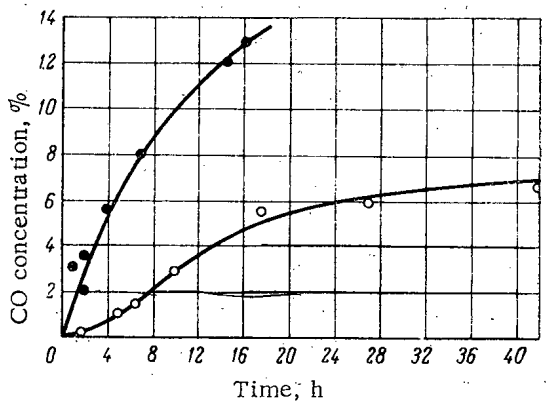

Fig. 2. Variation of the CO concentration with time of irradiation of various samples of graphite: ●) powder; ○) bars.

by a chromatographic method with an error of up to 0.1%.

KINETICS OF THE FORWARD REACTION $CO_2 + C \rightarrow 2CO$

We determined the order of the reaction by investigating its rate as a function of the CO_2 concentration. Conditions of experiment: T = 400°C; current strength 100 μA; surface of graphite bars 370 cm^2; CO_2 concentration varied within the range $(0.50\text{-}1.43) \cdot 10^{-2}$ mole/liter.

The average reaction rate w_{for} was determined according to the formula

$$w_{for} = \frac{[CO_2]_0 - [CO_2]}{t},$$

where $[CO_2]_0$ is the initial concentration; $[CO_2]$ is the CO_2 concentration at the moment of time t, moles/liter. The reaction rate was determined on the linear portions of the composition versus time curves.

The data obtained (Table 1) show that within the investigated range of concentrations, the reaction rate is independent of the CO_2 concentration:

$$w_{for} = -\frac{d[CO_2]}{dt} = k_{for} \qquad (1)$$

Table 2 presents the value of the rate constants k_4, calculated from the time dependence of the concentration for two values of the initial CO_2 concentration ($0.50 \cdot 10^{-2}$ and $1.43 \cdot 10^{-2}$ mole/liter). As can be seen from the data, the zero order constant for different times is constant. The zero order of the reaction is evidently due to the fact that at the irradiation intensities used, the maximum possible number of active particles is four to five order of magnitude lower than the total number of molecules, and consequently is independent of it. It may also be determined to some degree by the peculiarities of the heterogeneous reaction.

Figure 1 presents the dependence of the degree of CO_2 ($\alpha = \frac{[CO_2]_0 - [CO_2]}{[CO_2]_0}$) on the intensity of the electron flux. Conditions of experiment: p = 600 mm Hg; t = 400°C; outer surface of the graphite bars 370 cm^2; exposure for 2.5 h; flux intensity varied from 25 to 100 μA. As is evident from Fig. 1, the degree of conversion of CO_2 to CO is proportional to the irradiation intensity.

The curves presented in Fig. 2 characterize the dependence of the CO concentration of the time for experiments in which graphite possessed various surfaces. Conditions of experiment: T = 400°C; p = 600 mm Hg; electron

Declassified and Approved For Release 2013/09/24 : CIA-RDP10-02196R000700010005-2

Declassified and Approved For Release 2013/09/24 : CIA-RDP10-02196R000700010005-2

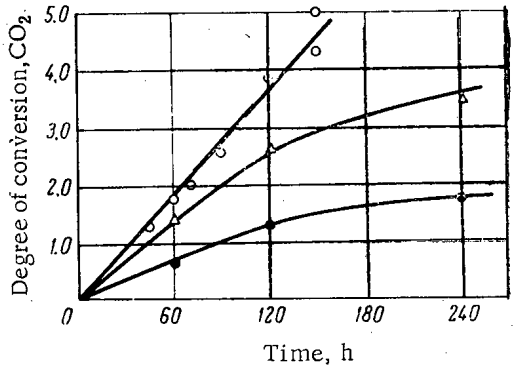

Fig. 3. Dependence of the degree of conversion of CO_2 on the time of irradiation at a temperature, °C: ●) 25; △) 200; ○) 400.

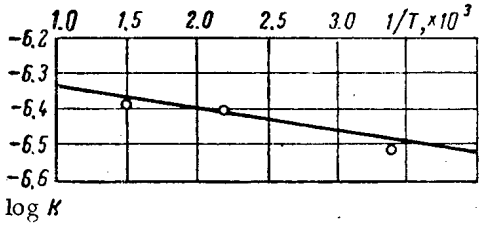

Fig. 4. Dependence of log k on 1/T.

TABLE 3. Rate Constant of the Reverse Reaction, Calculated According to Equation (2)

$[CO]_0$, × 10² Moles/liter	$[CO]_0 - [CO]$, × 10⁴	$[CO]_2$, × 10²	K_{rev}, ×10⁴ min⁻¹
0.41	0.83	0.40	3.34
0.49	1.10	0.48	3.45
0.76	1.65	0.74	3.76
0.83	1.72	0.82	3.45
1.13	2.30	1.11	3.45
1.43	2.99	1.40	3.53

TABLE 4. Values of the Steady State Concentration of CO, Calculated According to Equation (4)

Form of graphite	k_4, moles/(liter · min)	k_{rev}, min^{-1}	Calculated steady state concentration of CO	
			Moles/liter	vol. %
Powder	$1.8 \cdot 10^{-6}$	$7.2 \cdot 10^{-4}$	$2.5 \cdot 10^{-3}$	16.
Bars	$4.0 \cdot 10^{-7}$	$3.5 \cdot 10^{-4}$	$1.14 \cdot 10^{-3}$	7.7

flux 100 μA. From a comparison of the curves it was evident that the reaction rate is substantially higher in the case of graphite powder, which possesses a greater surface. The reaction rate constant on graphite powder is 4.5 times as great as the reaction rate constant on graphite bars; on powder $k_{for} = 1.8 \cdot 10^{-6}$ mole/(liter · min).

Figure 3 presents the dependence of the degree of conversion of CO_2 on the time of irradiation at 25, 200, and 400°C. Conditions of experiment: p = 600 mm Hg; current strength 100 μA; outer surface of graphite 370 cm^2. Figure 4 presents the Arrhenius dependence calculated according to these data. The activation energy of the reaction, determined from the slope of the straight line, was about 0.3 kcal. For the temperatures 200 and 400°C, the values of the rate constant coincide. Thus, the activation energy is practically equal to zero. From this it follows that particles for which there is no potential barrier to the reaction interact with graphite. The reacting particles are found in direct proximity to graphite. Otherwise, the rate of the process would be limited by diffusion of the active particles to the surface, and the activation energy would correspond to the temperature dependence of the coefficient of molecular diffusion. Such particles may be CO_2^+ ions, or excited CO_2 molecules, formed during electronic impact in direct proximity to the graphite surface.

KINETICS OF THE REVERSE REACTION $2CO \rightarrow CO_2 + C$

The interaction of carbon dioxide with graphite is a reversible reaction. Hence, for a complete characterization of the processes that occur after the action of radiation in the system CO_2–CO–carbon, it is also necessary to know the kinetics of the reverse reaction. It is known that the decomposition of CO under the action of radiations represents a complex reaction, which leads, in particular, to the formation of suboxides of the general formula $C_{n+1}O_n$. However, since it is a matter of the equilibrium state of the system CO_2–CO–C, we measured only the rate of the process of formation of CO_2 in the reaction $2CO \rightarrow CO_2 + C$.

The formation of suboxides was observed according to the formation of a reddish incrustation of the cold portions of the reaction vessel. We should mention that at 400°C, suboxides are unstable and decompose, forming CO and carbon. Consequently, the formation of CO_2 in the irradiation of CO may be considered as a process that takes place independent of suboxide formation.

Figure 5 presents the dependence of the degree of conversion of CO $\left(\alpha = \frac{[CO]_0 - [CO]}{[CO]_0}\right)$ on the irradiation

Declassified and Approved For Release 2013/09/24 : CIA-RDP10-02196R000700010005-2

Declassified and Approved For Release 2013/09/24 : CIA-RDP10-02196R000700010005-2

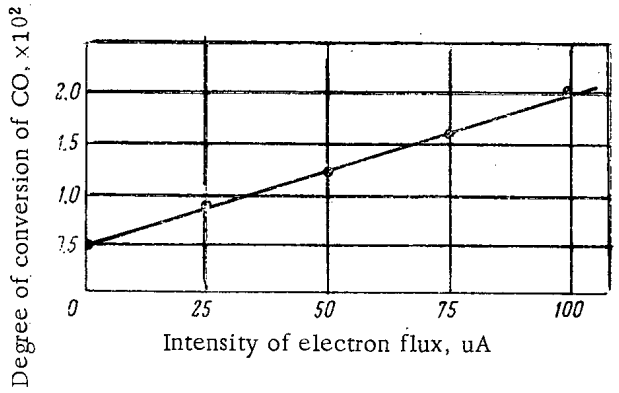

Fig. 5. Dependence of the degree of conversion of CO on the irradiation intensity.

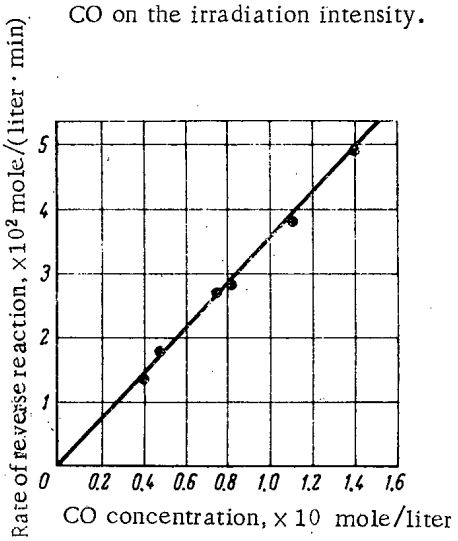

Fig. 6. Dependence of the rate of the reverse reaction on the CO concentration.

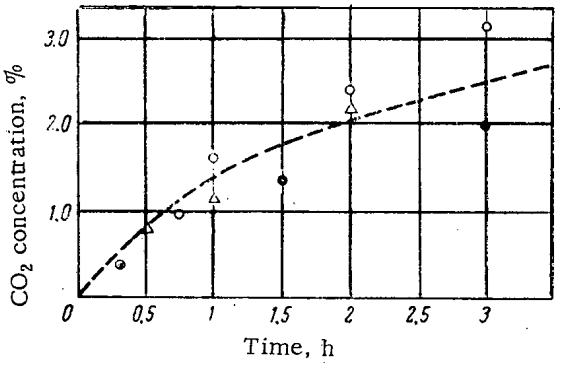

Fig. 7. Variation of the CO_2 concentration with time at a temperature, °C: ●) 25; △) 200; ○) 400.

intensity. Conditions of experiment: CO pressure equal to 600 mm Hg; T = 400°C; exposure for one hour. The degree of conversion of CO to CO_2, just as in the case of the forward reaction, is proportional to the radiation intensity.

To determine the reaction order with respect to CO, we investigated the dependence of the rate of formation of CO_2 on the CO concentration. The initial CO concentration was varied within the range (0.41-1.43) · $\cdot 10^{-2}$ mole/liter. Conditions of the experiment: T = 400°C; radiation intensity 100 μA; outer surface of graphite 370 cm^2. From Fig. 6 it is evident that the reaction rate w_{rev} is proportional to the CO concentration, i.e.,

$$w_{rev} = k_{rev}[CO]. \quad (2)$$

The rate constants calculated according to equation (2) are cited in Table 3; $k_{av} = 3.5 \cdot 10^{-4}$.

As the measurements showed, the reaction rate is independent of the external surface of the graphite within the range of values studied (0.370 cm^2). From this it follows that the reaction is homogeneous. However, in the case of a very large carbon surface, the reaction rate increases somewhat. Partial oxidation of CO by oxygen adsorbed on the graphite surface may occur. Since the reaction is bimolecular, it might have been expected that it would follow a second order. However, at the irradiation intensity used, the number of active molecules is practically independent of the pressure, and, consequently, the reaction may be first order.

Figure 7 presents the dependence of the concentration of CO_2 formed on the duration of irradiation within the interval 25-400°C. Conditions of experiment: p = = 600 mm Hg; electron flux 100 μA; graphite surface 370 cm^2. From the equality of the quantities for different temperatures, it follows that the activation energy of this reaction is practically equal to zero.

The absence of an activation energy makes it probable that CO_2 is formed according to an ionic-molecular reaction:

$$CO^+ + CO \longrightarrow CO_2 + C^+.$$

The reaction

$$CO^+ + CO \rightarrow C_2O^+ + O.$$

was observed in a mass sprectrometer [2].

EQUILIBRIUM STATE OF THE SYSTEM $CO_2 - CO - C$

In the case of sufficiently long irradiation, an equilibrium state is established in the system. Figure 8 shows the establishment of the steady-state concentration of CO. Curve 1 characterizes the achievement of an equilibrium state in the irradiation of CO_2, curve 3 in the irradiation of a mixture of CO_2 (80%) + CO (20%). As we can see,

Declassified and Approved For Release 2013/09/24 : CIA-RDP10-02196R000700010005-2

Declassified and Approved For Release 2013/09/24 : CIA-RDP10-02196R000700010005-2

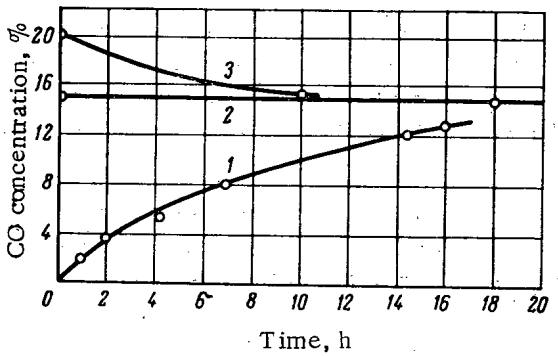

Fig. 8. Establishment of an equilibrium state on graphite powder.

the CO content in both cases approaches a limiting value of ~ 15%. Irradiation of a mixture containing 15% CO is characterized by Eq. (2). From Fig. 8 it is evident that the composition of the gas mixture is unchanged in this case.

It is of interest to compare the values of the steady state concentration of CO, calculated from the condition of equilibrium according to kinetic data, with the experimental values.

The condition of equilibrium is equality of the rates of the forward and reverse processes:

$$w_{for} = w_{rev}. \quad (3)$$

The steady state concentration of CO is determined by the ratio of the rate constant of the forward and reverse reactions:

$$[CO]_{st} = \frac{k_{for}}{k_{rev}}. \quad (4)$$

Table 4 presents the initial data and the results of calculations according to equation (4). The calculated values are in good agreement with the experimental values: ~ 15% for graphite powder and ~ 7% for graphite bars (see the lower curve in Fig. 2).

The nature of the dependence of the rate constants of the forward and reverse reactions on the radiation intensity, temperature, and surface established indicates that the steady state concentration of CO is independent of the radiation intensity and the temperature and depends on the carbon surface.

Thus, the reaction kinetics were studied in the system CO_2-CO-C under the action of fast electrons, and the basic principles of the establishment of an equilibrium state in this system were determined.

LITERATURE CITED

1. S. Lind, Radiation Chemistry of Gases, Reinhold Publishing Corporation, New York, (1961), p. 117.
2. V. Cermak and Z. Herman, Chemical Effects of Nuclear Transformations, Vienna, IAEA, No. 1, (1961), p. 99.

Declassified and Approved For Release 2013/09/24 : CIA-RDP10-02196R000700010005-2

Declassified and Approved For Release 2013/09/24 : CIA-RDP10-02196R000700010005-2

Sr^{90} CONTENT OF RADIOACTIVE FALLOUT IN WESTERN SLOVAKIA

(UDC 551.577.7)

Sh. Chupka, M. Petrashova, and I. Tsarakh

Regional Health Office, Bratislava, Czechoslovak SSR

Translated from Atomnaya Énergiya, Vol. 18, No. 5,
pp. 496-499, May, 1965
Original article submitted July 22, 1964

The absolute and relative content of Sr^{90} in radioactive fallout was investigated at four points in western Slovakia during 1962-1963. A significant increase in the Sr^{90} content of fallout was found in 1963, particularly in November and December (to 12%). The conclusion was reached that, at the present time, radioactive fallout results from long-lived isotopes of stratospheric origin.

At the present time, the basic constituents of atmospheric radioactive contamination are long-lived emitters which have been produced by nuclear explosions. These radioactive isotopes are the fission fragments of uranium and plutonium nuclei. In addition, they arise from the interaction of neutrons with the stable nuclei of atmospheric elements.

TABLE 1. Sr^{90} Activity (nCi/m^2) in atmospheric fallout, 1962-1963

Time of collection	Collection point			
	Bratislava	Yaslovske Bogunitse	Piestyany	Trnava
1962				
January	0.41	0,47	0.31	0.14
February	0.41	—	0.41	—
March	0.13	0,33	0.72	0.30
April	0.51	0,25	0.57	0.56
May	2.68	1,64	0.99	1.35
June	0.56	1,15	0.76	0.27
July	1.05	0,90	1.77	1.43
August	0.99	1,30	1.93	1.42
September	5.23	1,97	0.81	3.82
October	0.56	0,55	0.32	0.41
November	1.24	1,87	1.57	1.72
December	0.76	1,13	0.93	1.21
Yearly total	14.53	11.56	11.09	12.63
January	1.00	0.94	1.18	0.92
February	0.36	0.31	0.40	0.56
March	0.41	1.03	0.96	1.44
April	3.08	1.40	5.28	0.63
May	4.67	2.15	3.55	3.55
June	3.27	3.19	3.03	2.76
July	0.98	1.13	1.29	1.17
August	2.23	2.74	2.36	2.62
September	1.10	0.34	2.46	1.27
October	0.83	0.79	0.95	0.32
November	1.23	7.56	1.00	8.96
December	0.39	0.66	0.12	1.71
Yearly total	19.55	22.24	22.28	25.91

Of the long-lived radioactive elements, Sr^{90} and Cs^{137} attract the most attention. The continuing interest in Sr^{90} is explained by the biological consequences which may arise because of the accumulation of this isotope in the human organism. The metabolism of Sr^{90} is almost the same as that of calcium; through the atmosphere-soil-vegetation-foodstuff chain, Sr^{90} can get into the human organism and become incorporated in the skeleton.

The rate and range of stratospheric mixing and tropospheric fallout have been studied in part [1-3]. The main questions which must be answered are the

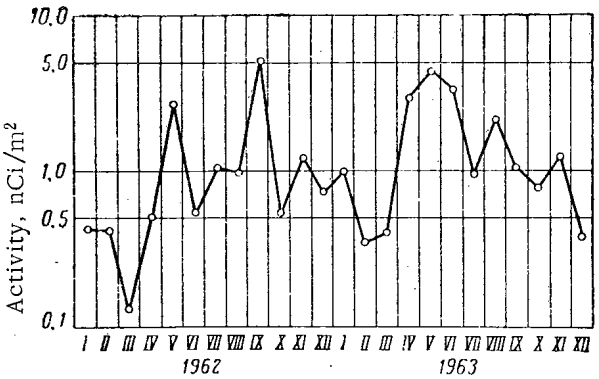

Sr^{90} activity in atmospheric fallout at Bratislava, 1962-1963

Declassified and Approved For Release 2013/09/24 : CIA-RDP10-02196R000700010005-2

Declassified and Approved For Release 2013/09/24 : CIA-RDP10-02196R000700010005-2

TABLE 2. Comparison of Sr^{90} Activity with Total Fallout Activity and with Amount of Precipitation

Time of collection	Precipitation, mm	Total β activity, nCi/m²	Sr^{90} activity, nCi/m²	Sr^{90} fraction, %
1962				
January	18	61.7	0.33	0.53
February	46	62.3	0.41	0.66
March	48	82.0	0.37	0.45
April	34	77.4	0.47	0.61
May	67	156.5	1.67	1.07
June	16	45.6	0.68	1.49
July	50	74.3	1.29	1.74
August	28	37.2	1.41	3.79
September	23	47.5	2.96	6.23
October	47	18.5	0.46	2.49
November	152	247.1	1.60	0.65
December	54	110.8	1.01	0.91
Average for 1962		85.07	1.05	1.23
1963				
January	34	71.5	1.01	1.41
February	24	24.8	0.41	1.65
March	58	114.2	0.96	0.84
April	10	109.0	2.60	2.39
May	52	157.7	3.48	2.21
June	101	164.0	3.06	1.87
July	22	64.0	1.14	1.78
August	95	62.7	2.49	3.97
September	65	64.1	1.22	1.90
October	31	25.4	0.72	2.83
November	53	38.0	4.69	12.34
December	13	5.7	0.72	12.63
Average for 1963		75.1	1.88	2.50

increased cumulative Sr^{90} fallout in the middle latitudes of the northern hemisphere and the annual spring maximum in the Sr^{90} content of atmospheric fallout [1]. At the present time, because of the Moscow agreement forbidding the testing of nuclear weapons in three media, the total β activity of radioactive fallout exhibits a tendency toward continuing reduction. Thus, because of the prohibition of nuclear testing, it appears feasible to determine fission fragment hold-up time in the stratospheric reservoir of the atmosphere, the transfer from the stratosphere to the lower layers of the atmosphere, and fallout on the surface of the Earth.

The present work was carried out in 1962-1963 in order to determine the radioactive background in the construction area for an atomic power station before reactor startup. To collect samples of atmospheric radioactive fallout, pots 20 cm in diameter were used which were installed at a height of 2 m above the ground. The sample collectors were located at four localities in Western Slovakia (Bratislava, Yaslovske Bogunitse, Pieshtyany, and Trnava) at points with grassy cover which are sufficiently removed from large sources of industrial fumes. To fix deposited atmospheric aerosols, a thin layer of distilled water was maintained in the bottom of the pots; in winter, a mixture of distilled water and ethyl alcohol was used. After a month's exposure, the samples of atmospheric deposits were processed.

The Sr^{90} content was determined by a modification of Bryant's method [4, 5] in which the separation of strontium from calcium was not performed; therefore, nitric acid was not used. The Sr^{90} activity was determined from the activity of Y^{90} β radiation which was recorded with NZQ 612 laboratory-type counting equipment using a Tesla 30/30 A/B end-window Geiger-Muller counter (mica window thickness, 1.6 mg/cm²).

The Sr^{90} content in monthly fallout collected in Bratislava during the period January 1, 1962, to January 1, 1964, is shown in the figure; clearly visible are the spring and fall maxima in 1962 which correlate with the increased total β fallout activity, the fall maximum considerably exceeding the spring maximum. A subsequent noticeable increase in Sr^{90} fallout was observed in the spring of 1963 when the Sr^{90} content was almost three times as great as that for the same period of 1962. One can assume that the strontium activity which was measured in 1963 was of resent origin and resulted from the last nuclear tests, which were carried out in the summer of 1962. at the individual collection points (Yaslovske Bogunitse, Pieshtyany, Trnava, and Bratislava). It is clear from the table that approximately the same amount of Sr^{90} is contained in fallout samples collected during the same time period at the different points. The average cumulative activity from the four sample-collection points reaching the ground in 1962 was 11-15 nCi/m² and 19-26 nCi/m² in 1963. During the period 1962-1963, 30-41 nCi/m² accumulated in the region under study.

Mean values are given in Table 2 for monthly precipitation, total β activity in the monthly fallout, Sr^{90} content in the fallout, and the Sr^{90} fraction of the total β activity for the four collection points during 1962-1963.

Declassified and Approved For Release 2013/09/24 : CIA-RDP10-02196R000700010005-2

Declassified and Approved For Release 2013/09/24 : CIA-RDP10-02196R000700010005-2

TABLE 3. Comparison of Sr^{90} Activity with Total Fallout Activity and with Amount of Precipitation

Collection point	Jan.	Feb.	March	April	May	June	Average
				1962			
Yaslovske Bogunitse	0.47	—	0.33	0.25	1.64	1.15	0.77
Pieshtyany	0.31	0.41	0.72	0.57	0.99	0.76	0.63
Trnava	0.14	—	0.30	0.56	1.35	0.27	0.52
Bratislava	0.41	0.41	0.13	0.51	2.68	0.56	0.78
Columbia	2.62	0.88	1.10	1.07	2.25	0.69	1.43
Los Angeles	0.46	3.29	0.53	0.07	0.07	0.05	0.75
New York	0.36	1.22	0.56	0.85	0.88	1.49	0.89
Pittsburg	0.56	0.80	0.92	1.65	1.55	0.67	1.02
Salt Lake City	0.45	1.74	2.15	2.61	4.12	0.13	1.86
				1963			
Yaslovske Bogunitse	0.94	0.31	1.03	1.40	2.15	3.19	0.92
Pieshtyany	1.18	0.40	0.96	5.28	3.55	3.03	1.95
Trnava	0.92	0.56	1.44	0.63	3.55	2.74	0.89
Bratislava	1.00	0.36	0.41	3.08	4.67	3.27	1.21
Calgary	0.25	0.13	0.23	1.10			0.43
Montreal	0.25	0.87	1.42	2.98			1.63
Sheerwater	0.51	—	—	1.98			—
Vancouver	0.47	1.80	1.38	2.54			1.55
Winnipeg	0.19	0.51	0.22	2.84			0.94

The total β activity, particularly in the last months of 1963, shows a tendency to fall, and reaches a minimum in December while the average cumulative value of Sr^{90} content (5.7 nCi/m^2) remains practically unchanged. This point to the stratospheric origin of the Sr^{90} which being deposited on the ground at the present time.

In 1962, the average cumulative value for the β activity in montly fallout at the four points was 85.07 nCi/m^2, the Sr^{90} activity was 1.05 nCi/m^2, and the Sr^{90} fraction reached 1.23%. In 1963, the corresponding values were 75, 10, and 1.88 nCi/m^2 (2.5%). This indicates that the atmospheric fallout of Sr^{90} shows no tendency toward reduction and that the principal part of the Sr^{90} resulting from the nuclear tests in 1961-1962 was deposited during 1963. The ratio of the total fallout β activity in 1963 to the total fallout β activity in 1962 is 0.88 while the ratio of the Sr^{90} activities which fell out in the same periods is 1.79. Thus the amount of Sr^{90} which was deposited on the surface of the Earth in 1963 was almost twice as much as that deposited in 1962. A similar conclusion can be reached by a comparison of the fractions of Sr^{90} in the total β activity (1.23% in 1962, and 2.5% in 1963). This factor increased mainly in the last months of 1963 when the Sr^{90} fraction reached 12%. At the present time, the predominant portion of total β activity in montly radioactive fallout consists of long-lived isotopes.

A comparison of our data on Sr^{90} content in atmospheric fallout with results obtained at a number of places in Canada and the United States [6] is shown in Table 3. Excellent agreement is observed for the values given; this indicates that the Sr^{90} content in atmospheric fallout in the northern hemisphere is approximately constant.

LITERATURE CITED

1. E. Martell, Science, 129, 3357 (1959).
2. V. Santholser and V. Havlovic, Jaderna energie, 8, 422 (1962).
3. M. Eisenbad, Science, 130, 3367 (1959).
4. F. Bryant, A. Morgan, and G. Spicer, AERE R-3030, (1959).
5. W. Haussermann and W. Morgenstern, Atompraxis, 2, 37 (1962).
6. Radiological Health Data, Monthly Report, U. S. Department of Health, Education and Welfare. Public Health Service. IV. No. 8, 9 (1963).

Declassified and Approved For Release 2013/09/24 : CIA-RDP10-02196R000700010005-2

Declassified and Approved For Release 2013/09/24 : CIA-RDP10-02196R000700010005-2

USE OF THE AUTORADIOGRAPHIC TECHNIQUE FOR STUDYING RADIOACTIVE AEROSOLS

(UDC 551.577.7:621.386.8)

V. N. Lavrenchik

Translated from Atomnaya Énergiya, Vol. 18, No. 5,
pp. 499-503, May, 1965
Original article submitted January 31, 1964; in revised form April 15, 1964

The process in which black spots are produced in nuclear emulsions by β and γ emitters with dimensions from 10μ down to hundredths of microns is discussed. A calibration curve is presented which relates activity to spot size for locally produced type XX film after 10-day exposures. By means of the technique which was developed, a spot size distribution was obtained for fallout samples collected in the northern hemisphere in December 1962 and May 1963. It is shown that the distribution is of a hyberbolic type with a tendency toward increased slope with the passage of time after the instant of aerosol injection into the stratosphere.

The autoradiographic method makes it possible to determine the activity and location of individual radioactive particles contained in a sample. Systematic observations of particle activity in stratospheric fallout can give important information on activity distribution at the time of formation and about the migration of radioactive aerosols in the Earth's atmosphere. Recently appearing work [1] concerning the application of radiography to the study of radioactive aerosols, however, did not contain information about the application of this method to the study of fission fragments. The purpose of the present paper is to remedy this deficiency to some extent.

From the data of previous investigations [2, 3], the sensitivity of a photoemulsion to electrons and γ-quanta falls rapidly with decreasing size of the silver halide grains. In this respect, most suitable for determining the activity of aerosols containing β and γ emitters is coarse-grained x-ray film with emulsion whose grain size is several microns. Among locally produced types, the most suitable for exposure without intensifying screens is type XX x-ray film. The emulsion thickness of such a film is about 30μ. In Fig. 1 is shown the location of the sample 1, the protective foil 2, the x-ray film 3, the holder 4, the light-tight cover 5, and the metal backing 6 in the process of producing an autoradiograph. The smooth metal backing is necessary to improve the contact between sample and emulsion. The protective covering of aluminum foil (of thickness δ = 10μ) prevents loss of particles from the sample during various manipulations.

The sample and film were placed in contact in absolute darkness because even very weak red light in the room produce a noticeable fogging of the emulsion. It was also determined that the pressure exerted by the holder must not exceed 100 g/cm^2 since otherwise fogging will appear and, in localized areas, blackening of the film. An easily controlled pressure is produced by placing spiral springs under the bolt heads.

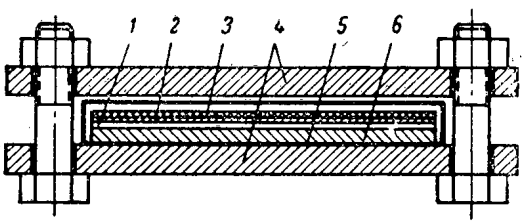

Fig. 1. Assembly for producing audioradiographs.

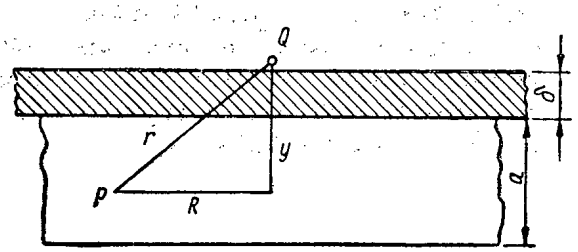

Fig. 2. Diagram of black spot formation in emulsion.

Declassified and Approved For Release 2013/09/24 : CIA-RDP10-02196R000700010005-2

Declassified and Approved For Release 2013/09/24 : CIA-RDP10-02196R000700010005-2

The exposure time, depending on the problem at hand, varied from several hours to several weeks. After development, fixing, washing, and drying, the film underwent scanning which was performed with a microphotometer. Since the black spots have a diffuse edge, their dimension was determined by the points where the blackening was 50% of the blackening at the center of the spot.

A diagram is shown in Fig. 2 which illustrates the formation of a black spot in an emulsion of thickness a by a particle with activity $Q = Q_\beta + Q_\gamma$. The electron flux n at the point p which is a distance r from the particle is determined by the total effect produced by electrons which are emitted by the particle with β activity Q_β, and by electrons which are created by the interactions of γ-quanta which are emitted by the same particle (γ activity, Q_γ) with material in the emulsion. If the absorbing and scattering characteristics of the medium for electrons and γ-quanta are indicated by μ_β and μ_γ, respectively, the flux at the point p can be determined from the relation

$$n = \frac{Q_\beta e^{-\mu_\beta r}}{4\pi r^2} + \frac{\theta Q_\gamma e^{-\mu_\gamma r}}{4\pi r^2}, \tag{1}$$

where θ is a constant determining the number of electrons in the emulsion per γ-quantum.

Striking a silver halide grain, the electrons cause an activation which, in the subsequent photographic treatment, leads to the formation of metallic silver (blackening). The number of grains dN which appear in a strip dy (where $0 < y < a$) of an emulsion having a photographic sensitivity $\varkappa$ for electrons after an exposure time t is

$$dN = n\varkappa t\, dy. \tag{2}$$

If we call the intensity of the light incident on the film and that of the light penetrating it I_0 and I, respectively, density can be defined in the following manner:

$$D = \ln I_0/I. \tag{3}$$

In accordance with the Lambert-Bouger law

$$I = I_0 \exp\left(-b\int_0^a dN\right), \tag{4}$$

where b is the average size of an opaque emulsion grain. Substituting (4) into (3), we obtain

$$D = b\int_0^a dN. \tag{5}$$

This expression is valid for N not too large. Substituting (1) and (2) into (5), we have

$$D = \frac{Q_\beta \varkappa b t}{4\pi}\int_0^a \frac{e^{-\mu_\beta dy}}{(y+\delta)^2 + R^2} + \frac{Q_\gamma \varkappa \theta b t}{4\pi}\int_0^a \frac{e^{-\mu_\gamma r}\, dy}{(y+\delta)^2 + R^2}; \tag{6}$$

$$r^2 = (y+\delta)^2 + R^2;$$

μ_β can be determined from the well-known empirical relation

$$\mu_\beta = 22\, d/E^{1.33}, \tag{7}$$

where d is the density of emulsion and aluminum foil ($d \approx 2.7$ g/cm^3); E is the average maximum energy of the electrons emitted by fission fragments 30-200 days old. ($\bar{E} = 1.0$ MeV with an accuracy of 10% [4]). On the basis of this data, we obtain a value of $\mu_\beta = 60$ cm^{-1}.

For the average energy of the γ-quanta (0.7 MeV) emitted by fission fragments of the same age, μ_γ is 0.2 cm^{-1}, the basic mechanism for interaction of the γ-quanta in the energy range under consideration with the medium being Compton scattering.

Declassified and Approved For Release 2013/09/24 : CIA-RDP10-02196R000700010005-2

Declassified and Approved For Release 2013/09/24 : CIA-RDP10-02196R000700010005-2

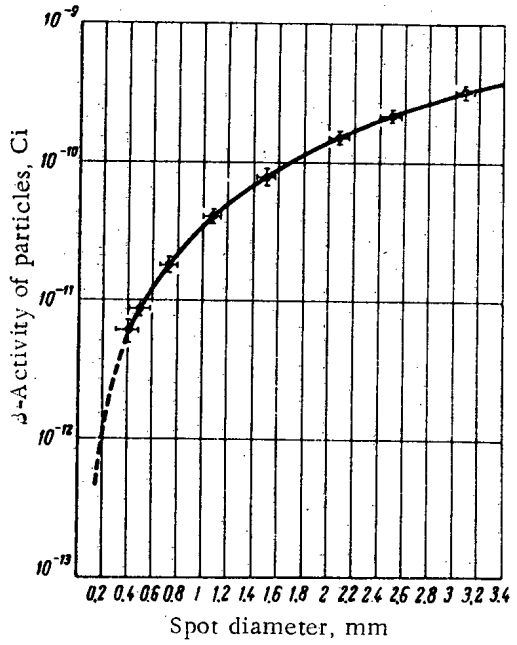

Fig. 3. Calibration curve showing the relation between spot diameter and β activity of the particles.

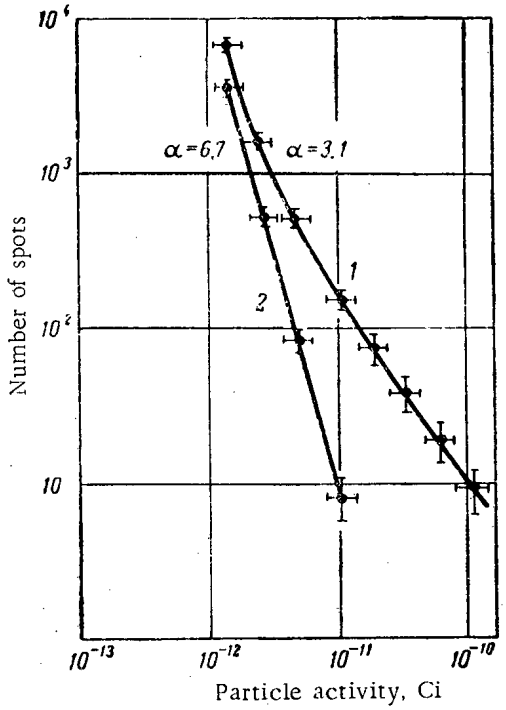

Fig. 4. Distribution of spot sizes for samples of atmospheric fallout in the northern hemisphere: 1) December 1962; 2) May 1963.

Within 20% accuracy, the ratio Q_β and Q_γ for fission fragments of the age mentioned is 1.9. An approximate integration of (6) taking into account the closeness of the limits of integration and the fact that $\mu_\gamma r \ll 1$, permits a determination of D in the following form:

$$D = \frac{Q_\beta e^{-\mu_\beta R} b \varkappa t a}{8\pi R^2} + \frac{Q_\gamma b \varkappa \theta t a}{4\pi R^2}. \qquad (8)$$

An evaluation indicates that approximately equal contributions to the blackening will be contributed by electrons and γ quanta when R ≈ 0.04 cm (first term in expression (8) equal to the second). For R < 0.04 cm, the main part of the blackening results from the first term in expression (8), and when R > 0.04 cm, it arises chiefly from the γ quanta (second term in (8)).

Expression (8) allows one to compare the activities Q_1 and Q_2 of two particles which give black spots with dimensions R_1 and R_2 for the same exposure t, or to determine the change of R_1 and R_2 for black spots from particles of the same activity with different exposure times t_1 and t_2.

For small black spots, produced mainly by electrons (0.001 < R < 0.04), the following relations are valid

$$\frac{Q_1}{Q_2} = \left(\frac{R_1}{R_2}\right)^2 e^{\mu_\beta (R_1 - R_2)} \quad \text{for} \quad t = \text{const}; \qquad (9a)$$

$$\frac{t_1}{t_2} = \left(\frac{R_1}{R_2}\right)^2 e^{\mu_\beta (R_1 - R_2)} \quad \text{for} \quad Q = \text{const}. \qquad (9b)$$

For large spots, where the blackening results from the interaction of γ quanta with material in the emulsion (R > 0.04), and for small spots where one can neglect the variation in electron absorption (R < 0.001 cm), the following relations are valid

$$\frac{Q_1}{Q_2} = \left(\frac{R_1}{R_2}\right)^2 \quad \text{for} \quad t = \text{const}; \qquad (10a)$$

$$\frac{t_1}{t_2} = \left(\frac{R_1}{R_2}\right)^2 \quad \text{for} \quad Q = \text{const}. \qquad (10b)$$

On the basis of expression (8), one can compare the activities of particles, or study the effect of exposure length on sizes of spots, in the case of substantially different dimensions, neglecting the second term in the case of small spots and the first term for large spots. The respective relations for $R_1 > 0.04$ cm and $R_2 < 0.04$ take the form

$$\frac{Q_1}{Q_2} = \left(\frac{R_1}{R_2}\right)^2 \frac{e^{-\mu_\beta R_2}}{20} \quad \text{for} \quad t = \text{const}; \qquad (11a)$$

$$\frac{t_1}{t_2} = \left(\frac{R_1}{R_2}\right)^2 \frac{e^{-\mu_\beta R_2}}{20} \quad \text{for} \quad Q = \text{const}. \qquad (11b)$$

Declassified and Approved For Release 2013/09/24 : CIA-RDP10-02196R000700010005-2

Declassified and Approved For Release 2013/09/24 : CIA-RDP10-02196R000700010005-2

Of the computing formulas given (10a) and (10b) are the most exact. The other formulas, which contain the parameter μ_β, cannot pretend to great accuracy since the true average maximum energy of the electrons emitted by a mixture of fission fragments 30-200 days old is insufficiently well-known. Therefore, the formulas containing μ_β can be recommended for obtaining estimates in that spot size range where ordinary radiometric equipment is useless because of the low activity of the particles.

In all the calculations, it was assumed that the β and γ spectra of the active particles were the same. However, isotopic fractionation in the process of radioactive aerosol formation leads to significant differences in the composition of the β and γ emitters which are contained in particles of differing activity. Spectral measurements have shown that, despite a considerable difference in γ spectra, the average energy of the γ-quanta differed little from that assumed above while the average energy of the electrons emitted by the most active particles (10^{-8} Ci) was noticeably less than the average energy assumed above for electrons which were emitted by particles with activities of 10^{-10}-10^{-13} Ci.

The computational difficulties demanded creation of the corresponding calibration curve. In order to construct it, small portions (~ 4 mm^2) were removed from sampling filters, to which there corresponded definite spot sizes on the autoradiograms. The activity of the particles thus removed was measured with a "low-background" counter having a known efficiency. Particles giving spots with $R < 200\mu$ (for a 10-day exposure) were not measured on the β counter because the activity was too weak. The portion of the calibration curve where $R < 200\mu$ was constructed by extrapolation using relation (9a).

The dependence of spot size on particle activity is shown in Fig. 3 for the following experimental conditions: length of exposure, 10 days; emulsion thickness of the type XX film, 30μ; thickness of the protective aluminum foil, 10μ; samples were aerosols on a type FPA-15A filter. The experimental points on the calibration curve were plotted as the average values of the activities of several tens of active particles about 100 days old. The dashed line was drawn on the basis of calculations in accordance with expression (9a).

One of the main problems facing autoradiography of active aerosols is the obtaining of spot-size distributions.

In the analysis of autoradiograms, the entire range of spot sizes is broken down into a sufficiently large number of equal intervals in each of which spots of definite dimensions fall.

Figure 4 shows the distribution of spot sizes for the northern hemisphere at the end of 1962 and in May 1963. In December 1962, particles with activities of 10^{-10}-10^{-12} Ci gave about 60% of the total β activity, but in May 1963, they gave about 5%.

The distribution shown in Fig. 4 is most easily represented as a hyperbolic function of the form

$$\frac{dM}{dR} = \frac{A}{R^{\alpha}}, \qquad (12)$$

where dM is the number of spots falling in the interval from R to R + dR; A and α are constants.

From December 1962 to May 1963, the exponent α changed from 3.1 to 6.7. In other words, there is observed with the passage of time a gradual shift from a polydisperse spot distribution to a monodisperse distribution. Apparently, this is associated with the predominant yield of heavier (and, therefore, also more active) aerosols from the stratosphere.

The experimentally observed dependence of α on t, and consideration of the decay of particles with the activities being considered, make it possible to determine the particle activity distribution at the time of formation.

The autoradiographic method has its threshold which can be changed if there is a possibility of changing the length of exposure. For a 10-day exposure, the threshold is approximately $5 \cdot 10^{-13}$ Ci, which corresponds to $3 \cdot 10^7$ electrons per square centimeter of emulsion.

LITERATURE CITED

1. J. Sisefsky, Science, 133, 735 (1961).
2. W. Chang, Phys. Rev., 69, 60 (1946).

Declassified and Approved For Release 2013/09/24 : CIA-RDP10-02196R000700010005-2

Declassified and Approved For Release 2013/09/24 : CIA-RDP10-02196R000700010005-2

3. Z. Elektrochem., 36, 750 (1930).
4. A. Bykov et al., Atomnaya énergiya., 10, 362 (1961).

All abbreviations of periodicals in the above bibliography are letter-by-letter transliterations of the abbreviations as given in the original Russian journal. *Some or all of this periodical literature may well be available in English translation.* A complete list of the cover-to-cover English translations appears at the back of this issue.

Declassified and Approved For Release 2013/09/24 : CIA-RDP10-02196R000700010005-2

Declassified and Approved For Release 2013/09/24 : CIA-RDP10-02196R000700010005-2

Pb^{210} IN THE ATMOSPHERE AND IN FALLOUT

(UDC 551.577.7)

V. I. Baranov and V. D. Vilenskii

Translated from Atomnaya Énergiya, Vol. 18, No. 5,
pp. 503-506, May, 1965
Original article submitted August 14, 1963; in revised form, June 22, 1964

Data are given for the intensity of Pb^{210} fallout in the Moscow area during 1961-1963. The intensity of Pb^{210} fallout ordinarily increases with increasing amounts of precipitation. The average Pb^{210} concentration in fallout is not related to the amount of precipitation, and rises sharply only in dry periods. The intensity of Pb^{210} fallout is practically constant in the spring, summer, and fall, and decreases in the winter only by a factor of 2-2.5. The average concentration of Pb^{210} in fallout is practically independent of season. The mean annual intensity of Pb^{210} fallout in the Moscow area is ~ 2.8 nCi/m^2. The Pb^{210} concentration in the surface layer of the atmosphere above the Pacific and Indian Oceans varies within wide limits ($(0.1\text{-}1.60)\cdot 10^{-3}$ nCi/m^3), and, apparently is chiefly determined by meteorological factors. The Pb^{210} content in the troposphere above the oceans is probably only slightly less than the content in the troposphere above dry land. The variations in Pb^{210} concentration in the surface layer of the atmosphere above land and ocean can evidently be used for studying the meteorological factors responsible for the transport of radioactive isotopes within the troposphere and for their deposition on the surface of the earth.

The possibility of using Pb^{210} as a natural tracer for the meteorological processes which are responsible for the distribution of radioactive isotopes within the atmosphere and for their deposition on the surface of the Earth is attracting the attention of many investigators at the present time [1-4]. However, data on the distribution of Pb^{210} in the atmosphere and on its deposition on the surface of the Earth is still sparse, and it mainly deals with singly collected samples making it difficult to uncover the over-all regularities in the distribution of Pb^{210} in the atmosphere.

A complete representation of the global distribution of Pb^{210} in the troposphere can only be obtained by a study of its distribution above both dry land, the source of radon, and above the oceans also. As is well known, radon inflow into the atmosphere above the ocean is negligibly small. However, there is no data on Pb^{210} content in the troposphere above the oceans except for a few values which were obtained for heights of 3-15 km in the troposphere above the ocean [2]. In this connection, it is of interest to refine the average value for the intensity of Pb^{210} fallout at ground level and to determine the seasonal variations of this quantity on the basis of data which was obtained over an extended period of time, and also to estimate the Pb^{210} content in the surface layer of the atmosphere above the ocean.

The intensity of Pb^{210} fallout at ground level was determined from radiochemical analyses of fallout samples which were collected monthly from April 1961 to December 1963 in the Moscow area. The samples were collected in two metallic samplers; the area of each sampler was 0.5 m^2 (in April-May 1961, a single sampler with an area of 1 m^2 was used). After January 1962, a lead solution was added to the sampler.

To determine the Pb^{210} concentration in the surface layer of the atmosphere above the oceans, samples of radioactive aerosols were used which were collected by means of FPA-15 filters for 12-48 h periods during trips of Soviet research ships in the Pacific and Indian Oceans.

In samples collected during 1961, Pb^{210} was determined by means of a scheme for separatory analysis of fallout [5], and in samples collected during 1962-1963, it was determined by means of an altered technique.

Declassified and Approved For Release 2013/09/24 : CIA-RDP10-02196R000700010005-2

Declassified and Approved For Release 2013/09/24 : CIA-RDP10-02196R000700010005-2

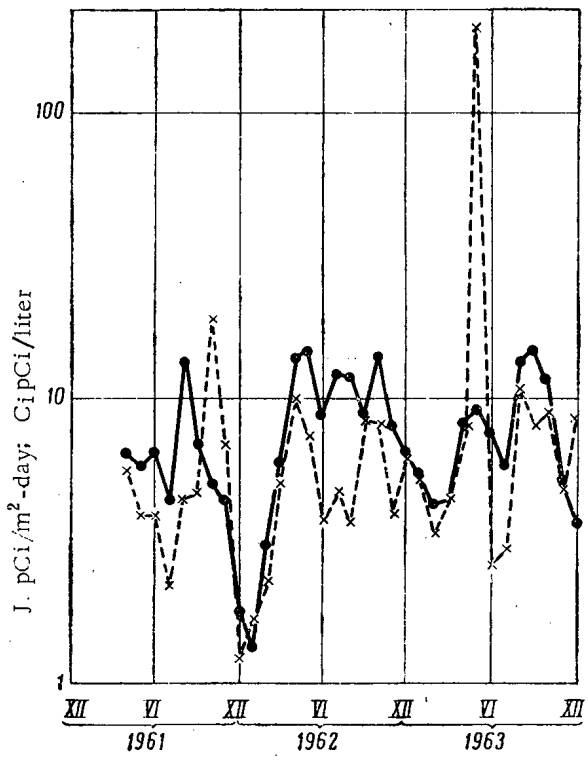

Fig. 1. Intensity of Pb^{210} fallout, J (●) and Pb^{210} concentration in fallout, C(×).

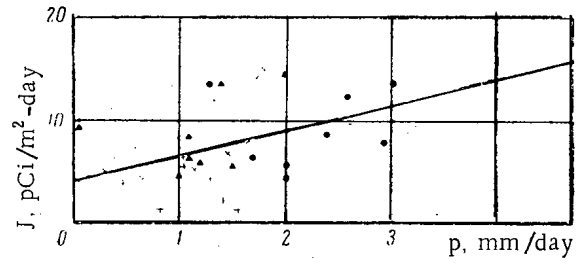

Fig. 2. Dependence of Pb^{210} fallout intensity on amount of precipitation P: +) winter; ▲) spring; ●) summer; ×) fall.

The collected samples, which contained lead carrier, were acidified with nitric acid, evaporated to dryness, and ashed at a temperature around 500°C. The residue was digested with fluoric and hydrochloric acids, and dissolved in 1 N hydrochloric acid. The resulting solution was filtered. Precipitation and purification of the Pb^{210} was carried out as before [5] by passing the hydrochloric acid solution through columns containing the anionite ÉDÉ-10P. The columns were flushed with 1 N hydrochloric acid and the lead washed out with water. Purification of the lead on the anionite was performed two or three times, after which the lead was precipitated in the form of a sulfate. The Pb^{210} content was determined from the Bi^{210} accumulated in a sample prepared for measurement of β activity.

In the samples of radioactive aerosols, the Pb^{210} was determined by a similar technique. After the introduction of a lead carrier, the filters were digested with nitric acid, and in the case of ashed filters, with nitric acid or with fluoric and hydrochloric acids.

Intensity of Pb^{210} fallout in the Moscow Area. Data on the intensity of Pb^{210} fallout during 1961-1963 is shown in Fig. 1. As is clear from the figure, the mean monthly values for the intensity of Pb^{210} fallout vary within wide limits (1.4-17.2 pCi/m²-day), the values for the same months in different years being quite divergent in a number of cases.

An important factor in Pb^{210} fallout from the atmosphere is its deposition on the surface along with precipitation, which is associated with capture by cloud droplets[4]. In this connection, it is of interest to compare the values of mean monthly intensity of Pb^{210} fallout with the mean monthly amounts of precipitation. Data on the amounts of precipitation were obtained from meteorological stations located several kilometers from the fallout sampling point. As a result of the comparison (Fig. 2), a correlation was observed between these quantities. However, a rigorous relationship between intensity of Pb^{210} fallout and the amount of precipitation was not observed because the spread in values was rather large although it was not associated with any kind of seasonal phenomenon.

As a characteristic of Pb^{210} fallout, one can use the value for the average concentration in fallout which, as is usually assumed [6], is proportional to the concentration in the surface layer of the atmosphere. The mean monthly values for this quantity are shown in Fig. 1. The figure shows that, like fallout intensity, the average Pb^{210} concentration in fallout varies within rather broad limits and can be different for the same months in different years. A comparison of the average Pb^{210} concentration in fallout with the mean monthly amounts of precipitation (Fig. 3) indicates that Pb^{210} concentration in fallout is usually independent of the amount of precipitation and of season. Only for very low mean monthly amounts of precipitation (less than 0.4 mm/day) does the Pb^{210} concentration rise sharply. The apparent reason for this is the relative increase in the contribution of "dry" fallout during the arid period. However, such a phenomenon is encountered rather infrequently; for our conditions, it was observed in only two cases out of 33 (in October 1961 and May 1963).

Declassified and Approved For Release 2013/09/24 : CIA-RDP10-02196R000700010005-2

Declassified and Approved For Release 2013/09/24 : CIA-RDP10-02196R000700010005-2

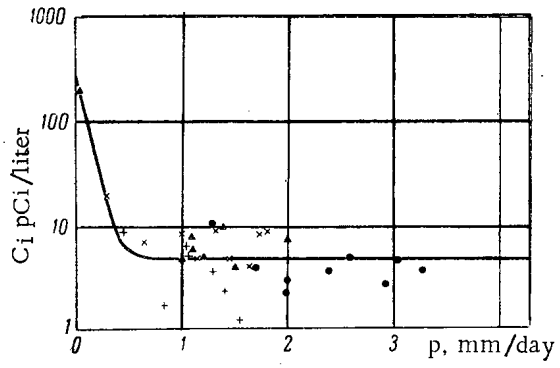

Fig. 3. Dependence of Pb^{210} concentration in fallout on amount of precipitation: +) winter; ▲) spring; ⊙) summer; ×) fall.

TABLE 1. Mean Monthly Values of Pb^{210} Fallout Characteristics in the Moscow Area

Month	P mm/day	J, pCi/m²-day	C, pCi/liter
January	1.0	3.6	3.6
February	1.3	3.8	2.8
March	1.1	5.3	4.8
April	1.1	9.6	8.0
May	1.2	9.7	8.3
June	2.3	7.6	3.3
July	2.2	7.5	3.4
August	2.5	13.1	5.2
September	1.4	10.0	7.2
October	1.1	10.3	9.4
November	1.2	6.0	5.2
December	1.0	3.8	3.9
December-February	1.1	3.7	3.4
March-May	1.2	8.2	7.1
June-August	2.3	9.4	4.0
September-November	1.2	8.8	7.2
Yearly average	1.5	7.5	5.2

Because of the considerable variations in the characteristics of Pb^{210} fallout, the mean monthly values for the entire period of the study (Table 1) may be used to uncover regularities in the seasonal changes of these quantities.

As can be seen from the table, some variations in Pb^{210} fallout characterizes as a function of season are observed. The maximum fallout intensity is observed in April-May and August-October, and the minimum in December-February. The maximum value of the mean concentration of Pb^{210} in fallout is noted in April-May and September-October, the minimum in December-February and June-July.

The lower values of Pb^{210} fallout characteristics in the winter can be explained to a certain extent by snow blowing out of the samplers during the sampling period. However, this factor is apparently not a decisive one since the samples were collected in a spot that was sheltered from strong winds.

Variations in Pb^{210} fallout characteristics can be explained both by fluctuations in its concentration in the tropospheric layers from which it is removed and by variations, in the mode of fallout, i.e., by changes in the meteorological factors which are responsible for the deposition of radioactive isotopes on the ground. At the present time, it is difficult to estimate the effects of these factors. The lack of significant differences in fallout characteristics during the various seasons makes it possible to assume that the average concentration of Pb^{210} in the tropospheric layers from which it comes is practically constant except for seasonal dependence and that fluctuations in fallout characteristics are mainly caused by variations in the mode of fallout.

The averaging that has been done makes it possible to refine the value for the mean annual intensity of Pb^{210} fallout in the Moscow area [4]. This quantity is 2.8 nCi/m²-yr with an average fallout concentration of 5.2 pCi/liter. The actual intensity of Pb^{210} fallout during 1962 was 3.3 nCi/m², and 2.9 nCi/m² during 1963 with corresponding average fallout concentration of 5.3 and 6.3 pCi/liter. The difference in the mean annual values given indicates the possibility of some changes in Pb^{210} fallout characteristics from year to year. The mean annual value arrived at for Pb^{210} fallout intensity is only slightly greater than the average value (2.4 nCi/m²-yr) computed for uniform deposition of Pb^{210} on the entire surface of the northern hemisphere. It follows that the intensity of Pb^{210} fallout on the surface of the oceans must be only slightly less than the fallout intensity on land surfaces.

Pb^{210} in the surface layer of the atmosphere above the oceans. The Pb^{210} content was determined for 40 samples of aerosols from the surface layer of the atmosphere above the Pacific and Indian Oceans (Table 2).

The Pb^{210} concentration in the surface layer of the atmosphere above the oceans varied within wide limits $(0.1\text{-}16.0)\cdot 10^{-3}$ pCi/m³), the average value in the Pacific Ocean from 20°S to 50°N being $2.5\cdot 10^{-3}$ pCi/m³ and in the Indian Ocean from 20°S to 30°N, $8.5\cdot 10^{-3}$ pCi/m³. The reason for such a difference may be both the large separation of sampling points in the Pacific Ocean from the mainland in comparison to the sampling points in the Indian Ocean and the difference in season and meteorological conditions during the sampling periods. The observed spread in values of Pb^{210} concentration points to large fluctuations in the rate of its arrival in the surface layer of the

Declassified and Approved For Release 2013/09/24 : CIA-RDP10-02196R000700010005-2

Declassified and Approved For Release 2013/09/24 : CIA-RDP10-02196R000700010005-2

TABLE 2. Pb^{210} Concentration in the Surface Layer of the Atmosphere Above the Indian and Pacific Oceans

Latitude		Number of samples	Pb^{210} concentration $\times 10^{-3}$ pCi/m^3	
			average	limits
Pacific Ocean				
40°—50° N	III	2	3,2	
20°—40° N	III	5	3,5	1,6—10,0
0°—20° N	III	13	1,4	0,1—5,0
0°—20° S	III	11	2,1	0,8—4,7
Indian Ocean				
20°—30° N	III	1	15,0	—
0°—20° N	III	5	8,1	2,0—16,0
0°—20° S	III	3	2,5	0,5—13,0

atmosphere at different times and in different places in the same latitude range. In this connection, the limited amount of material obtained does not allow one to trace any sort of regularity in the latitudinal variations of Pb^{210} content in the surface layer of the atmosphere above the oceans, and the average values that have been given obviously should be considered as preliminary.

However, it is completely clear that the Pb^{210} concentration in the surface layer of the atmosphere above the oceans is, in many cases, chiefly the result of meteorological factors and is not caused by separation from the mainland. For example, Pb^{210} concentrations in the surface layer of the atmosphere above the Pacific Ocean close to the mainland (20-50°N) turned out to be less than those observed in a number of cases in the tropical portion of the Pacific Ocean (20°S-20°N) far removed from the mainland. The observed concentrations of Pb^{210} in the surface layer of the atmosphere above the oceans is the same as, or slightly less than, that in the surface layer of the atmosphere above dry land (average value $3.0 \cdot 10^{-3}$ pCi/m^2, limits $(1.4\text{-}5.8) \cdot 10^{-3}$ pCi/m^3 [1]).

The data that was obtained makes it possible to conclude that the distribution of Pb^{210} in the troposphere above land and ocean is fairly uniform although the content in the troposphere above the oceans evidently must be somewhat less than above land. However, one can reveal the difference only by extensive and continuing study of Pb^{210} distribution in the troposphere above land and ocean.

On the basis of what has been presented, one can draw the following conclusions:

1. The mean yearly intensity of Pb^{210} fallout is ~ 2.8 nCi/m^2-year from observations in the Moscow area covering a period of 2.5 years (April 1961 to December 1963).

2. The mean monthly intensity of Pb^{210} fallout, from what has been observed, is generally proportional to the amount of precipitation, and changes but little during the spring, summer, and fall while decreasing by a factor of 2-2.5 during the winter. The mean monthly concentration of Pb^{210} in fallout is practically independent of season.

3. The average concentration of Pb^{210} in the tropospheric layers from which it is removed apparently is practically constant and independent of season, while the fluctuations in fallout characteristics are chiefly brought about by changes in the mode of fallout.

4. The concentration of Pb^{210} in the surface layer of the atmosphere above the Pacific and Indian Oceans varies within wide limits $(0.1\text{-}16.0) \cdot 10^{-3}$ nCi/m^3), and, apparently is determined mainly by meteorological factors.

5. The content of Pb^{210} in the troposphere above the oceans is only slightly less than its consideration in the troposphere above land.

LITERATURE CITED

1. I. L. Karol' and S. G. Malakhov, in "Problems in Nuclear Meteorology," Moscow, Gosatomizdat (1962), p. 5.
2. Rama and M. Honda, J. Geophys. Res., 66, 3227 (1961).
3. L. Fry and K. Menon, Science, 137, 994 (1962).
4. V. I. Baranov and V. D. Vilenskii, Radiokhimiya, 4, 493 (1962).
5. V. I. Baranov and V. D. Vilenskii, Radiokhimiya, 4, 493 (1962), p. 486.
6. V. P. Shvedor, L. I. Gedeonov, and Z. G. Gritchenko, in "Radioactive Contamination of the Environment," Moscow, Gosatomizdat (1962), p. 168.

Declassified and Approved For Release 2013/09/24 : CIA-RDP10-02196R000700010005-2

Declassified and Approved For Release 2013/09/24 : CIA-RDP10-02196R000700010005-2

INVESTIGATION OF THE PHONON SPECTRUM IN THE COPPER LATTICE BY USING THE METHOD OF INELASTIC NEUTRON SCATTERING

(UDC 539.171.017)

E. Z. Vintaikin, V. V. Gorbachev, and P. L. Gruzin

Translated from Atomnaya Énergiya, Vol. 18, No. 5,
p. 507, May, 1965
Original article submitted February, 1965 ; abstract submitted March 6, 1965

The method of inelastic scattering of thermal neutrons is widely used at the present time for investigating the spectrum of thermal oscillations of the crystal lattice. Investigations of the spatial and energy distributions of neutrons scattered on monocrystals make it possible to determine the dispersion relationships $\omega(\vec{q})$, from which information can be obtained on the interaction of atomic forces in the crystal lattice. Until recently, the dispersion curves for the copper lattice were plotted by using the x-ray method for high-symmetry orientations and the neutron method for particular orientations. The present article provides the experimental results of a complete determination of the phonon frequencies of copper monocrystals for the basic symmetry orientations [100]; [110]; [111].

The experimental device constituted a combination of a position spectrometer and an analyzer spectrometer. A UNSA device for neutron diffraction analysis [1] served as the position spectrometer. A miniature neutron spectrometer analyzer was used for analyzing scattered neutrons [2]. An ordinary recording circuit was used. The methods of constant ΔE and Q values were used for plotting the dispersion curves. In using the first method, the neutron incidence angle ψ and the scattering angle φ were varied according to a calculated program, which secured the displacement of the Q vector in the assigned direction in the reciprocal lattice. In the other case, ψ, φ, and **k** varied so that the **Q** value was fixed in the space of the reciprocal lattice. In both cases $k_0 > k$. The dispersion curves obtained were in good agreement with the results of other neutron-spectrometric measurements [3, 4], but they deviated from x-ray data [5]. The interplanar interaction constants were calculated on the basis of the obtained dispersion curves (see table).

Interplanar Constants

Order of proximity	[100]		[110]			[111]	
	$\pi_l^{(n)}\times$ $\times 10^{-3}$	$\pi_t^{(n)}\times$ $\times 10^{-3}$	$\rho_l^{(n)}\times$ $\times 10^{-3}$	$\rho_t^{(n)}\times$ $\times 10^{-3}$	$\rho_{t_2}^{(n)}\times$ $\times 10^{-3}$	$\sigma_l^{(n)}\times$ $\times 10^{-3}$	$\sigma_t^{(n)}\times$ $\times 10^{-3}$
0	—55.3	—26.1	—53.1	—52.1	—24.7	—51.2	—11.1
1	53.6	26.0	23.0	50.0	26.5	46.1	10.4
2	2.7	0.3	25.8	0.5	—1.6	5.5	0.8
3	—1.8	0.4	3.2	1.6	—0.2	—0.3	—0.2
4	1.4	0.2	1.3	0.0	0.0	—0.4	—0.2

The symbols π, Q and σ denote the constants pertaining to atomic planes which are perpendicular to the orientations [100]; [110] and [111], respectively. The upper index denotes the order of proximity, while the lower index determines the polarization. The π_l^1 value represents the force per single atom in a certain zero plane in the [100] direction resulting from a shift of the neighboring atomic plane in the [100] direction through a distance of unit length. The other constants have a similar significance.

LITERATURE CITED

1. P. D. Abesadze, et al., Pribory i Tekhnika Éksperimenta, No. 2, 43 (1964).
2. E. Z. Vintaikin and V. V. Gorbachev, Pribory i Tekhnika Éksperimenta (in preparation).
3. D. Cribier, B. Jacrot, and D. Saint-James, J. Phys. et radium, 21, 67 (1960).
4. J. Sosnowski and J. Kozubowski, Phys. Chem. Solids, 23, 1021 (1962).
5. E. Jacobsen, Phys. Rev., 97, 654 (1955).

Declassified and Approved For Release 2013/09/24 : CIA-RDP10-02196R000700010005-2

Declassified and Approved For Release 2013/09/24 : CIA-RDP10-02196R000700010005-2

TURBULENT COUETTE FLOW

(UDC 621.039.51)

V. D. Vilenskii and V. P. Smirnov

Translated from Atomnaya Énergiya, Vol. 18, No. 5,
pp. 508-509, May, 1965
Original article submitted September 14, 1964 ; abstract submitted March 15, 1965

Couette flow in a flat narrow channel in the presence of a longitudinal pressure gradient is investigated. Four types of flow are possible in dependence on the relationship between the wall speed V and the magnitude and direction of the pressure gradient dp/dx.

We shall denote friction at the moving wall by τ_1 and friction at the fixed wall by τ_2. We shall assume that V > 0. The above types of flow are characterized by the following relationships:

$$\text{I. } \frac{dp}{dx}<0,\ \tau_1<0,\ \tau_2<0;\quad \text{II. } \frac{dp}{dx}<0,\ \tau_1>0,\ \tau_2<0;$$

$$\text{III. } \frac{dp}{dx}>0,\ \tau_1>0,\ \tau_2<0;$$

$$\text{IV. } \frac{dp}{dx}>0,\ \tau_1>0,\ \tau_2>0.$$

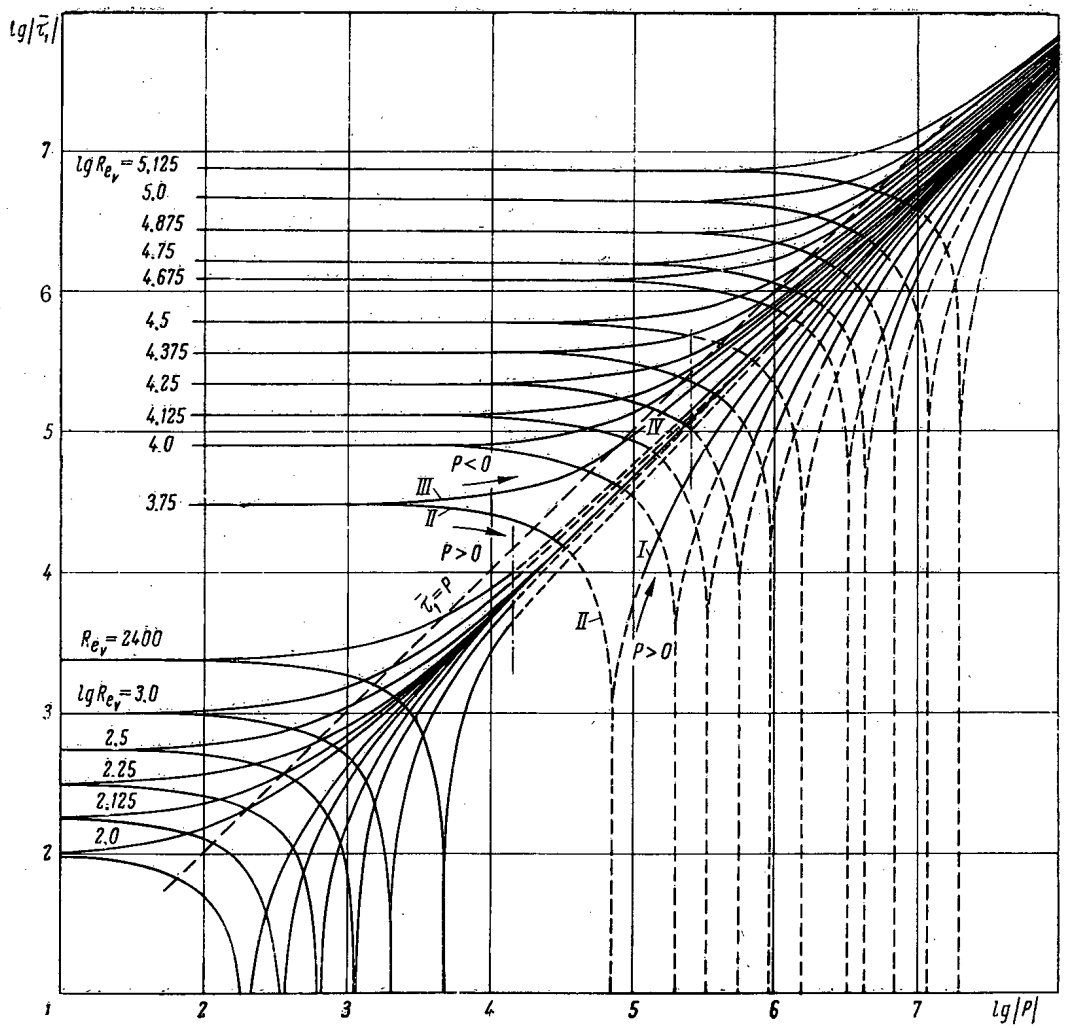

Fig. 1. Dependence of log $|\tau_1|$ on log $|P|$ for a constant Re_V value.

Declassified and Approved For Release 2013/09/24 : CIA-RDP10-02196R000700010005-2

Declassified and Approved For Release 2013/09/24 : CIA-RDP10-02196R000700010005-2

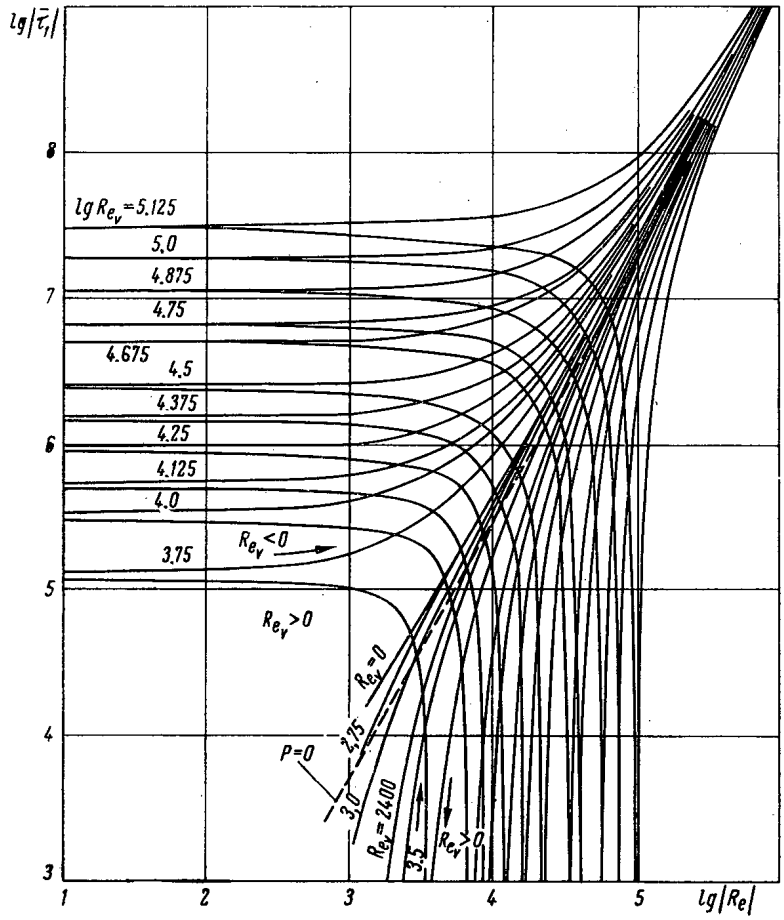

Fig. 2. Dependence on log $|\tau_1|$ on log $|Re_V|$ for a constant Re_V value.

By using the Boussinesq hypothesis and expressing the turbulent viscosity by means of the relationship

$$\frac{\varepsilon}{v^*} = \varkappa \frac{y(h-y)}{h},$$

where $v^* = \sqrt{\frac{|\tau_1|}{\varrho}}$, we obtain the equation for determining the velocity profile:

$$v^* = \frac{v^* h}{\nu} = \pm \varkappa Y (1-Y) \frac{d\bar{u}}{dY}. \qquad (1)$$

here, u = uh/ν and Y = y/h, where u is the present velocity in the narrow channel, and h is the spacing between the walls; the coordinate y is measured from the fixed wall; $\varkappa$ is an empirical constant.

We shall assume that friction in the narrow channel changes linearly. If it is different from zero at the wall, we can consider with a sufficiently high degree of accuracy that the velocity profile is linear within the limits of the laminar sublayer at this wall. By integrating Eq. (1) under these assumptions, we obtain the velocity profile and the resistance equation for each type of flow. The relationships derived contain two empirical constants, α and $\varkappa$, which are determined from particular cases of Couette flow – flow in a straight flat channel with fixed walls and the simple Couette flow (p = 0).

Declassified and Approved For Release 2013/09/24 : CIA-RDP10-02196R000700010005-2

Declassified and Approved For Release 2013/09/24 : CIA-RDP10-02196R000700010005-2

If τ is close to zero, the linear velocity distribution in the laminar sublayer is disturbed. In this case, we shall use the quadratic velocity profile in the sublayer which is determined from the Navier–Stokes equations.

The relationship between the P and Re_V values corresponding to $\tau_1 = 0$ is determined by the expression

$$\frac{\sqrt{P}}{\varkappa}\left(\ln\frac{1-\sqrt{1-\frac{\alpha}{\sqrt{P}}}}{1+\sqrt{1-\frac{\alpha}{\sqrt{P}}}}-\ln\frac{1-\sqrt[6]{\frac{2\alpha^2}{P}}}{1+\sqrt[6]{\frac{2\alpha^2}{P}}}\right)+Re_V-\sqrt[3]{\frac{\alpha^4 P}{2}}-\alpha\sqrt{P}=0.$$

The P and Re_V criteria are defined in the following manner:

$$P=-\frac{dp}{dx}\frac{h^3}{\mu\nu};\quad Re_V=\frac{Vh}{\nu}.$$

A similar relationship is obtained for $\tau_2 = 0$.

The dependence of $\tau_1 = \tau_1 h^2/\mu\nu$ on Re_V and P was obtained by numerically solving the resistance equation for each type of flow. The results are given in Fig. 1. Figure 2 provides the results obtained in converting the characteristics of Couette flow to the parameters Re_V and $Re = u_{me}h/\nu$, where u_{me} is the mean velocity in the narrow channel.

Declassified and Approved For Release 2013/09/24 : CIA-RDP10-02196R000700010005-2

Declassified and Approved For Release 2013/09/24 : CIA-RDP10-02196R000700010005-2

NUCLEAR POWER PLANTS FOR CIVILIAN MARITIME USE

N. S. Khlopkin

Translated from Atomnaya Énergiya, Vol. 18, No. 5,
pp. 510-511, May, 1965

Two papers were presented by the USSR (313, 367)* on maritime propulsion plants at the Geneva 1964 conference†; other papers were presented by delegations of Belgium and Great Britain (515, 565), West Germany (540, the Netherlands (588), and Norway (801)†.

The only paper dealing with actual experience in the operation of nuclear maritime facilities was one presented by the USSR delegation. This paper reported data on the performance of the nuclear propulsion plant in five years of operation of the icebreaker LENIN in Arctic service: in piloting convoys of ships through ice packs, in scientific expedition cruises at high polar latitudes (with the drift station "North Pole-10"), and in sailing on ice-free water in stormy weather. Details were made available on the design of the nuclear plant, which was adequate for reliable operation and energizing of the icebreaker under conditions which are considered the most hazardous and difficult in maritime practice. The report also provided data on the physical and heat transfer characteristics of the plant and on changes made during the reactor campaign, which slightly surpassed the design campaign. These characteristics are of considerable interest. On the whole, the operating experience revealed a promising outlook for the use of nuclear propulsion plants on icebreakers.

A report on the decision taken by the Soviet Government to build two more nuclear-powered icebreakers made a deep impression on the conference participants.

The USA did not present any papers on maritime nuclear power applications at the conference: neither on new developments or projects nor on the operating experience of the passenger-cargo nuclear vessel SAVANNAH. This vessel has completed several demonstration cruises and is still virtually unused in the capacity for which it was built.

Several USA firms presented some design considerations on maritime power plants rated at 20,000 to 30,000 hp and being studied for future work, at the exhibit. The Babcock and Wilcox firm, which had the contract for the SAVANNAH power plant, presented a description of the modularized CNSG-3 facility using a pressurized water reactor. Except for the main circulating pumps mounted on the reactor pressure vessel, the entire primary loop and related equipment, including the straight-flow steam generator and the pressurizer, are enclosed within the reactor pressure vessel. This achieves a compact facility and simplifies the primary loop. Ancillary systems are greatly reduced and simplified in the process. The containment shell joins to the lead-water shielding tank; water fulfills the function of radiation shield and vapor condenser in the event of leaks in the primary loop.

The firm Combustion Engineering presented a mock-up of the UNIMOD facility which is reminiscent in many ways of the CNSG-3. This facility uses a pressurized water reactor, with all the primary-loop equipment installed within the pressure vessel. One distinguishing feature of the UNIMOD facility is the comparatively high temperature of steam superheat (about 100°C) and the higher primary-loop pressure (almost twice that of the CNSG-3). This opens up new opportunities for compensating reactivity changes in reactor transients solely through temperature effects. As a consequence, the reactor power level may be varied in accordance with the turbine load, thereby simplifying the plant control system.

General Electric presented a description of the 630A plant, using low-pressure water as moderator in the reactor, and helium or air as coolant; the steam parameters achieved in this plant are close to the steam parameters achieved in conventional maritime steam turbine power plants (59 atmos, 510°C). Subassemblies are designed for

* The serial numbers of the Geneva 1964 conference papers are parenthesized.

† A list of the reports presented by Soviet scientists has been published in Atomnaya Énergiya, 17, No. 3, 235 (1964), and the list of papers by foreign scientists was published in Atomnaya tekhnika za rubezhom, No. 9, 27 (1964).

Declassified and Approved For Release 2013/09/24 : CIA-RDP10-02196R000700010005-2

Declassified and Approved For Release 2013/09/24 : CIA-RDP10-02196R000700010005-2

removal and replacement in preference to overhaul. The modularized 630A plant is of lesser dimensions than a reactor of equal power rating, but the same in weight.

In June 1964, the ore cargo ship OTTO HAHN, rebuilt into a research vessel, was launched in West Germany. The choice of power plant for the propulsion was preceded by a rather detailed study of maritime power plants of different types. The most prominent firms were contracted to take part in this study: Interatom (an organic-moderated and organic-cooled reactor); Krupp and Weser (helium-cooled reactor with pelletized fuel elements); AEG (boiling-water reactor); Siemens-Schukkert; MAN Babcock and Wilcox (pressurized-water reactor). The Babcock and Wicox pressurized-water reactor plant got the green light from this preliminary study. This power plant was developed around the CNSG-1 project, data on which were furnished by the American Babcock and Wilcox Co. at the October 1962 Turina international symposium on nuclear plants. As a result of the improvements introduced, the power plant of the refitted ore cargo ship now approximates the American CNSG-3 plant in design features.

Great Britain presented, jointly with Belgium, material on the VULCAIN reactor designed to impart 20,000 to 25,000 shaft horse power to a vessel. The main problem posed in the development of this reactor was to achieve costs comparable to those of conventional inland plants by improved utilization of the fuel (raising burnups to 40,000–50,000 MWd/ton) and by simplifying plant design. One interesting feature of this plant is the compensation of reactivity change during the reactor campaign by varying the composition of the moderator through gradual dilution of the heavy water by ordinary water. Modularization of the VULCAIN reactor is carried out pretty much completely. This is of particular importance in the case of heavy-water reactors: a reduction in loop volume leads to a decrease in the amount of heavy water present. Initial core tests are scheduled in the Belgian BR-3 reactor from 1965 through 1968.

The Netherlands presented some design plants on the NERO propulsion plant for a tanker shipping 65,000 tons deadweight and driven by 22,000 shaft hp. A pressurized-water reactor is envisaged; water flowrate through the core is to be increased and conditions for developing natural circulation in the event of pump outage are to be improved by the use of water-water ejectors placed around the core bottom. The dynamic head in these ejectors will be created by the two main circulating pumps of 260 kW rating each.

Japan presented a mock-up of the nuclear-powered oceanographic vessel at the science and engineering exhibit; this vessel is to be driven by 10,000 shaft hp and tests are scheduled for 1969.

The discussion of the materials submitted to the conference lead to the following basic inferences:

1. Most of the maritime power plants now in the design stage call for the use of pressurized-water reactors as the best tested and de-bugged variant;

2. Maritime plants offer significant opportunities for improvement in weight reduction, size reduction, and costs reduction. This may be achieved by simplifying both the basic and the ancillary systems, by placing most of the equipment inside the reactor vessel, and by increasing the core campaigns.

3. Interest has been manifested in lowering the primary-loop pressure. Reductions in pressure vessel weight and thickness will make up for any deficiency associated with the need for developing the heat transfer surfaces of the steam generator.

4. The coolant passages are being designed for low hydraulic drag and high natural circulation levels. This will greatly reduce required pump ratings and will enhance the reliability of the plane in the event of a complete shutdown of all the pumps.

5. The cores are being developed for campaigns of 10,000 hours or longer. Reactivity changes are being compensated, as a rule, by means of burnable poisons installed in rods similar to fuel elements. A mixture of light and heavy water is used in a high-burnup core.

6. The strength of fuel elements is a crucial factor. Every effort is being made to reduce stresses in the cladding; almost in every case, designers consistently shy away from the variant of welding on distance pieces to assure free expansion of fuel elements.

7. Uranium dioxide capable of 60,000 MWd/ton burnup with no substantial deformation of the fuel-element meat is being used as fuel.

8. Fuel element cans are being fabricated either of stainless steel or of zirconium alloys.

Declassified and Approved For Release 2013/09/24 : CIA-RDP10-02196R000700010005-2

Declassified and Approved For Release 2013/09/24 : CIA-RDP10-02196R000700010005-2

9. Slightly superheated steam is being used in almost all nuclear maritime propulsion plants.

10. Steam generators are of the straight-through type, as a rule. The material selected for the heat transfer surfaces is most often high-nickel alloy (inconel). Steam generators are designed in sectionalized format to allow a given section to be shut off, to allow access to the individual tubes from the secondary-loop side in order to remove malfunctioning tubes, have a replaceable tubesheet so that heat transfer surfaces can be removed without major overhaul operations.

On the whole, the materials presented at the Third Geneva conference demonstrate the close attention being paid around the world to the development of civilian-use nuclear maritime industry.

Declassified and Approved For Release 2013/09/24 : CIA-RDP10-02196R000700010005-2

Declassified and Approved For Release 2013/09/24 : CIA-RDP10-02196R000700010005-2

SCIENCE AND ENGINEERING EXHIBITS AT THE THIRD GENEVA CONFERENCE

B. A. Kuvshinnikov and V. V. Frolov

Translated from Atomnaya Énergiya, Vol. 18, No. 5,
pp. 511-514, May, 1965

While the Third International Conference on the Peaceful Uses of Atomic Energy was in session, eighteen of the participating nations set up their own national science and engineering exhibits at Geneva. These exhibits were organized for the purpose of illustrating the reports presented and to display the achievements of the several nations in the field of reactor design and nuclear power. Moreover, several nations presented exhibit displays demonstrating applications of nuclear power in various fields.

Two basic divisions were in evidence at the USSR exhibit (Fig. 1), which was quite successful from the architectural standpoint: one division housed displays informing visitors about the advances achieved in the USSR in the field of controlled thermonuclear fusion. Visitors to the Soviet pavilion manifested keen interest in mock-ups of the I. V. Kurchatov Beloyarsk nuclear power station and the Novo-Voronezh nuclear power station, and particular interest was centered on the full-scale fuel channel of the Beloyarsk plant reactor. The center of attention was, as always, the mock-up of the nuclear icebreaker LENIN. (It should be noted that several countries devoted a good deal of attention in their displays to maritime nuclear power. Mock-ups of nuclear-powered ships now afloat, under construction, or in the design stage, in the USA, West Germany, Belgium, Japan, were on display in the exhibits staged by the various countries.)

The USSR presented an example of low-output nuclear power facilities as one of the promising trends in power reactor design in the USSR. A mock-up of the scaled-down organic-cooled organic-moderated ARBUS power plant, rated 750 MW, was a successful attraction at the exhibit. Visitors had the opportunity of familiarizing themselves with a mock-up of the experimental portable nuclear electric power station TÉS-3, of 1500 kW rating, which can be carried on four caterpillar tractors. A pressurized-water reactor is used in this portable power plant.

Conference delegates and the visiting public manifested unusual interest in a model of the ROMAShKA, the world's first operating nuclear power plant using direct conversion of heat energy to electrical energy (Fig. 2). As we know, this plant was started up in August 1964 at the I. V. Kurchatov Institute of Atomic Energy. A high-temperature fast reactor is used in the plant; uranium dicarbide is the fuel and silicon-germanium thermoelectric cells are the direct converters. The plant has a 500 W(e) rating.

A promising trend in power reactor design in the USSR, that of fast reactors, was represented in materials available on the operating BR-5 reactor, the BN-350 reactor, 350 MW(e), designed for a nuclear power station now under construction, and a mock-up of the BN-1000 fast reactor (100 MW electrical power output) of a projected power station.

A series of mock-ups of Soviet research reactors, viz. the IGR, IBR, MR, MIR, SM-2, was displayed. These facilities evoked intense interest in conference delegates from several countries.

The controlled fusion section of the Soviet pavilion was saturated with many mock-ups of operating thermonuclear machines. A mock-up of the famed PR-5 machine with the combined magnetic field increasing from the center outward on all sides was shown. Visitors to the exhibit were able to familiarize themselves with mock-ups of the OBRA-2, DEL'TA, TOKAMAK, and others. Two operating machines were also on display. In one of these (the UN machine), plasma is heated by shock waves generated in the plasma by a magnetic field growing at a prodigious time rate. Using this machine, the Institute of Nuclear Physics of the Siberian Division of the USSR Academy of Sciences managed to achieve a plasma of 10^{13}–10^{14} particles/cm^3 density. Special equipment alongside the machine recorded the neutron flux, and the plasma was shown by instruments to be heated to a hundred million degrees. The second machine illustrated the work on particle confinement in a magnetic trap.

A large number of exhibits and engineering information was furnished at the USA exhibit. In contrast to their 1958 exhibit (at that conference, the USA pavilion showed many life-size exhibits and operating facilities), the

Declassified and Approved For Release 2013/09/24 : CIA-RDP10-02196R000700010005-2

Declassified and Approved For Release 2013/09/24 : CIA-RDP10-02196R000700010005-2

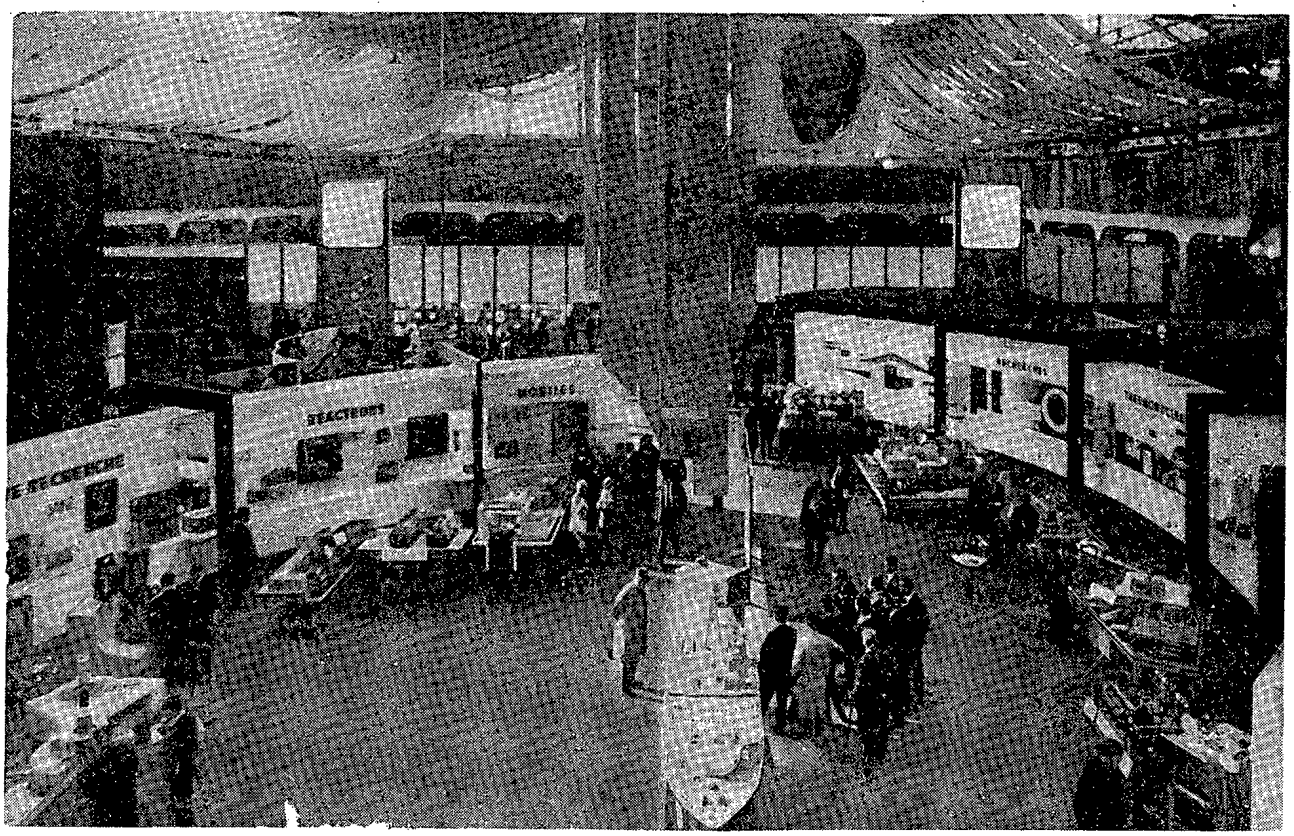

Fig. 1. Scene at the USSR exhibit.

exposition in this case was in the form of colored slides, texts, and diagrams, with some mock-ups and instrumentation on display. Attention was focused on power plants with various reactor types. Mock-ups of a boiling-water reactor (the Oyster Creek [New Jersey] power plant project, about 500 MW output), the 463 MW rating MALIBU power station in California with its water-cooled water-moderated reactor, and the SGR sodium-cooled graphite-moderated reactor (at the 75 MW electric power station at Hallam, Nebraska) were also worthy of note.

Work done in the field of fast reactors was illustrated by data on the operating EBR-2 reactor (in Idaho) and the Enrico Fermi power station reactor.

Data were also presented on reactors for relative low-rating power stations: a steam superheat reactor (BONUS) for a 16.3 MW power station and the high-temperature gas-cooled reactor HTGR for a 40 MW power station.

A special section of the US exhibit was reserved for a demonstration of nuclear power source projects for use in space, and autonomous automatic weather stations (the SNAP line of nuclear power packs). A model of the conversion reactor SNAP-10A featuring a thermoelectric generator of 500 W output, to be ready for service in 1965, was exhibited. The SNAP-10A facility (total weight 450 kg) is designed for space use. An operating automatic marine meteorological station with all systems operated from the isotope generator SNAP-7F (Fig. 3) was also demonstrated. The USA pavilion provided information on nuclear fuel production processes, on equipment for nondestructive testing of materials, and on various components of reactor control and monitoring systems.

A portion of the USA pavilion was reserved for an information center. Here books and bibliographic lists on nuclear science and nuclear engineering published in recent years were made available, as well as a microfilm file. This section of the pavilion scored a hit with visiting delegates.

An appreciable portion of the British pavilion was reserved for a variety of exhibits, demonstrating the achievements in materialization of the so-called one-reactor program (construction of a series of electric power stations based on a single type of standard graphite-moderated gas-cooled reactor). In the pavilion, which contained a large number of interesting displays, information was made available on virtually every research or power reactor in

Declassified and Approved For Release 2013/09/24 : CIA-RDP10-02196R000700010005-2

Declassified and Approved For Release 2013/09/24 : CIA-RDP10-02196R000700010005-2

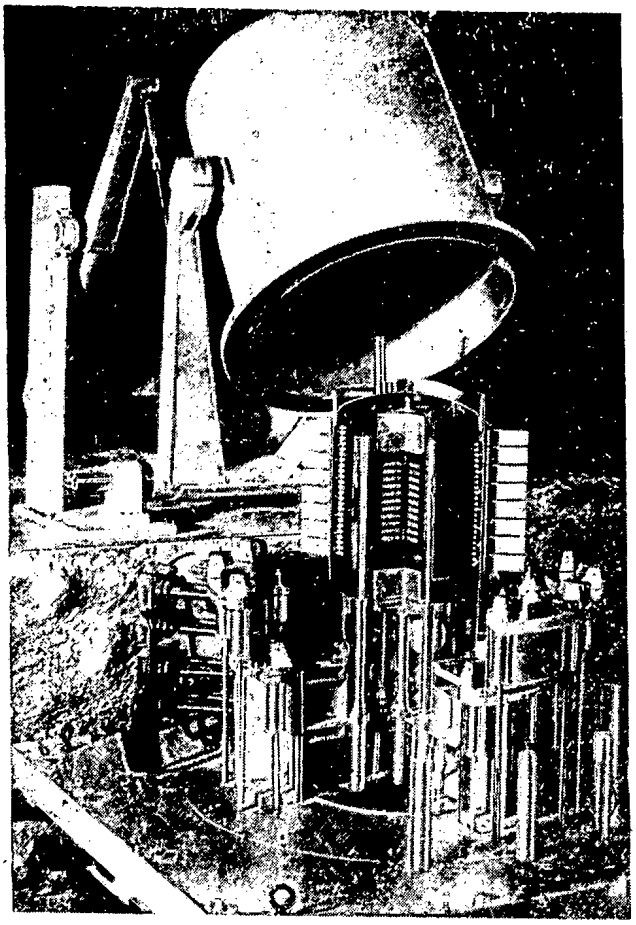

Fig. 2. Mock-up display of the ROMAShKA thermoelectric direct converter.

operation, under construction, or being designed. Mock-ups of reactors and even of electric power stations as a whole, interesting designs of reactor pressure vessels (e. g. a pressure vessel of prestressed reinforcement concrete for the Wylfa reactor), fuel elements and information on fuel element fabrication technology, and seemingly endless specimens of equipment for scientific research work and radioisotope work, were on display.

Models of pool-type research reactors (SILOE, PEGASE) were shown in the French exhibit. A mock-up of the research reactor OSIRIS now under construction at Saclay was also present. Graphite-moderated gas-cooled power reactors such as EDF-1, EDF-2, EDF-3, EDF-4 were represented by mock-ups.

A model of the heavy-water power reactor EL-4 was also demonstrated. Among the large quantity of varied displays in the pavilion we must mention specimens of high-quality graphite moderator blocks, as well as the information on work now underway in France to use concrete for the construction of reactor pressure vessels.

The Canada pavilion anchored its basic exhibits on the achievements in mining and processing of uraniferous ores, and on the building of power stations using natural uranium burners (CANDU type reactors). The first nuclear power station bases on a reactor of that type (the NPD station built at Rolfton in Ontario) has been in operation since 1962, at 22 MW output. This power station is the prototype of the Douglas Point station now being built, and scheduled to feed 200 MW into the power grid. Mock-ups of these power stations and information on them were on display.

The West German exhibit was notable for the volume of information presented. Materials on projects of various types of nuclear power stations, among them the AVR station at Jülich, of 15 MW(el) rating, which has been under construction since 1961, were made available. The high-temperature reactor of this power station is particularly interesting for the fact that its fuel elements will be shaped as pellets or "pebbles" 6 cm in diameter. These pebbles are made of graphite which doubles as moderator, and contain a mixture of uranium carbides (20% U enrichment) and thorium carbides as fuel meat. The coolant used in this reactor will be a helium-neon mixture.

The exposition at the Czechoslovak pavilion was devoted to that country's first nuclear power station, of 150 MW rating, construction of which is being completed at the present time. The basic display item was a life-size mock-up of a portion of the high-pressure vessel. This vessel is about 5 m in diameter and stands 19 m high, with a wall thickness to 300 mm (the vessel wall is made of special carbon steel and weighs about 600 tons). The pressure vessel is designed to sustain a working pressure of 60 atmos.

The Italian exhibit differed from those of other countries in the display of many interesting instruments and auxiliary items along with materials on nuclear power station projects. Among these we noted various types of analyzers and equipment for nuclear reactor control and protection systems. An operating electromechanical manipulator the slave part of which was coupled to the master section by an electrical communications cable and could be moved by command of the operator was popular with visitors. A picture of the work space is projected onto the operator's panel screen by means of a special TV circuit.

India's exhibits reflected in detail the national program for development of research in nuclear science and nucleonics. There was much material on the work of the Trombay research center. The Indian exhibit arrangement met with univeral approval of visitors.

Declassified and Approved For Release 2013/09/24 : CIA-RDP10-02196R000700010005-2

Declassified and Approved For Release 2013/09/24 : CIA-RDP10-02196R000700010005-2

Fig. 3. Radio buoy for ocean service, powered by SNAP-7F isotope power packs.

Exhibits of other countries participating in the show were of smaller volume in terms of information presented. These exhibits told of national nuclear power development programs, of advances achieved in the development of work on peaceful used of atomic energy. Quite a few interesting minor exhibits attracted interest on the part of conference delegates, and met with warm approval.

Science and engineering films were shown to visitors on a regular schedule in many of the national exhibits. The most extensive film showing programs were those of the USSR and USA. The Soviet Union showed 22 wide-screen educational films. These films rendered accounts of the construction and operation of nuclear electric power generating stations and various reactor types, plus work at research centers in the USSR. The USA films (24 narrow-gage films dubbed in four languages) dealt with various research projects and with the work in reactor design achieved in the USA.

Declassified and Approved For Release 2013/09/24 : CIA-RDP10-02196R000700010005-2

Declassified and Approved For Release 2013/09/24 : CIA-RDP10-02196R000700010005-2

LETTERS TO THE EDITOR

MULTIBEAM RADIO-INTERFEROMETER DETERMINES PLASMA PARAMETERS

(UDC 533.9)

V. Ya. Balakhanov, V. D. Rusanov, and A. R. Striganov

Translated from Atomnaya Énergiya, Vol. 18, No. 5,
pp. 515-516, May, 1965
Original article submitted August 13, 1964

The possibility of utilizing an open resonator of the Fabry-Perot interferometer type in the microwave and submillimeter-wavelength region of the spectrum to determine the concentration of electrons and the frequency of occurrence of electron collisions with heavy particles has been discussed in [1]. This method to a certain extent bears a similarity to the "classical" resonator method. But the application of an interferometer enables us to avert certain difficulties encountered in the use of a resonator cavity (the need to "adapt" the dimensions of the plasma to the resonator parameters, the boundedness from above of the range of electron concentrations [2]). The problem dealt with in this article is that of ascertaining the electron concentration in a plasma by means of a multibeam Fabry-Perot radio-frequency interferometer.

Several variants are available in the use of an interferometer in plasma diagnostics. An interferometer with plane reflectors (Fig. 1a) lends itself to use in the case of a plasma of large dimensions. If the curvature of the plasma boundary is sufficiently great, either cylindrical reflectors with coinciding centers of curvature (Fig. 1b) or a confocal resonator with combined foci (Fig. 1c) may be employed. In the case depicted in Fig. 1b, the electromagnetic field is concentrated on the axis and the size of the "focal spot" is equal to the wavelength in order of magnitude. The figure of merit of a multibeam interferometer of any of these types may be several thousand. A confocal resonator was employed to determine the plasma parameters. An arrangement with a stationary plasma of cylindrical geometry consisting of a glass vacuum chamber filled with hydrogen to a pressure of 10^{-3} torr was used. The plasma was created by a high-frequency discharge in a longitudinal magnetic field of 700 oe. intensity. The diameter of the plasma column attained 3.5 cm under these conditions.

Figure 2 shows the experimental arrangement in diagrammatic layout. The electromagnetic wave ($\lambda = 8$ mm) emerging from the klystron oscillator 1 is directed by a horn feed 2 and a polystyrene lens into the resonator cavity. The signal passed by the interferometer is picked up by a detector 3 and is recorded by an amplifier connected to a pointer instrument 4. The interferometer reflectors 5 are positioned in the interior of the glass tube 6, since the glass exhibits high absorptivity in the millimeter region of the spectrum, thereby leading to an appreciable loss in resonator Q. The plasma pinch 7 compressed by the magnetic field does not contact the surfaces of the reflectors. The interferometer employed has cylindrical reflectors sized 5 by 8 cm with a 7.2 cm radius of curvature. A silver layer 20 mμ thick was vacuum-sprayed onto these plates, Mica 50μ thick served as substrate backing on the reflectors.

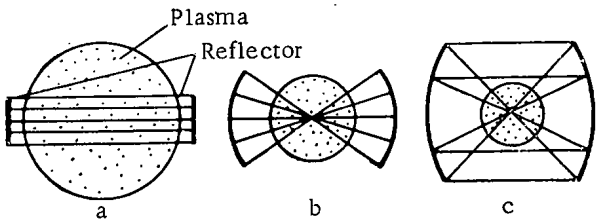

Fig. 1. Variants in use of interferometer in plasma diagnostics.

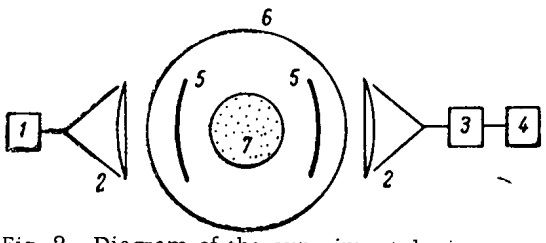

Fig. 2. Diagram of the experimental arrangement.

Declassified and Approved For Release 2013/09/24 : CIA-RDP10-02196R000700010005-2

Declassified and Approved For Release 2013/09/24 : CIA-RDP10-02196R000700010005-2

Transparent marks were cut on the reflector layer to provide transmissivity [3]. The interferometer Q was 1000 under these conditions. The electromagnetic energy was concentrated on the axis of the plasma pinch, and the size of the focal spot did not exceed 1.8 cm.

In the absence of plasma, the interferometer was tuned to one of the characteristic frequencies. The introduction of a plasma brought about a change in the phase difference between two interfering beams of magnitude [1]:

$$\Delta\varphi = \frac{2\omega}{c} d\,(1-N),$$

where $\omega = 2\pi c/\lambda$ is the operating frequency; c is the speed of light; N is the plasma refractive index; d is the thickness of the plasma layer. From this formula we may find the electron concentration

$$n = \frac{mc^2}{e^2} \cdot \frac{\delta\varphi}{2\lambda d},$$

where m is the electron mass. The phase shift was measured by retuning the oscillator frequency, which was recorded by a standard wavemeter. At a spacing h between reflectors, the phase difference is related to the frequency change $\delta\omega$ be the formula $\delta\varphi = 2h/c\ \delta\omega$. From these formulas, we may find the computation formula

$$n = \frac{m\omega^2}{4\pi e^2} \cdot \frac{2h}{d} \cdot \frac{\delta\omega}{\omega}.$$

The interference method can be checked by taking probe measurements. A double electrical probe of 0.2 mm electrode diameter was placed inside the plasma column near the interferometer. Voltage-current characteristics of the probe were taken in each experiment, and (n_{F-P}) and the electron temperature were ascertained therefrom.

Below, the results of measurements taken with the multibeam Fabry-Perot interferometer (n_{F-P}) and with the probe (n_p) are tabulated:

n_{F-P}	$7\cdot10^9$	$2.5\cdot10^{10}$	$4.5\cdot10^{10}$	$5.5\cdot10^{10}$	$1.9\cdot10^{11}$	$2.5\cdot10^{11}$	$3\cdot10^{11}$
n_p	10^{10}	$3.5\cdot10^{10}$	$8\cdot10^{10}$	$8.5\cdot10^{10}$	$2.7\cdot10^{11}$	$3.5\cdot10^{11}$	$4.4\cdot10^{11}$
$\bar{n}_p$	$8\cdot10^9$	$3\cdot10^{10}$	$6.5\cdot10^{10}$	$7\cdot10^{10}$	$2.2\cdot10^{11}$	$3\cdot10^{11}$	$3.5\cdot10^{11}$

The third row in this table lists averaged probe-measured values $\bar{n}_p$ with the distribution of electron concentration across the plasma pinch taken into account. The reader will note that $n_p > n_{F-P}$ consistently. The reason is that the electron concentration is distributed unevenly over the plasma column radius. The averaged value $\bar{n}_p$, as we might well expect, is closer to the n_{F-P} value. The range of electron concentrations measured in our experiments was bounded above by the maximum concentration typical of this mode of discharge. The minimum concentration was determined by the sensitivity of the equipment (and, particularly by the precision in determinations of frequency shift by the wavemeter). The precision in concentration determinations by the Fabry-Perot interferometer was ±10%. The principal contribution to this error is made by the error in determining the plasma diameter as measured by the probe. The precision in electron concentration measurements by the probe method was ±25%.

The width of the resonance curve could not be held accountable to dissipation via collisions in our case, for the experimental value exceeded this level by almost two orders of magnitude. One explanation could be that dissipation of the energy associated with the electromagnetic waves by diffraction on the plasma pinch is possible in this instrument; the same effect would be produced by distortion of the plasma-vacuum interface relative to the interferometer reflectors.

Declassified and Approved For Release 2013/09/24 : CIA-RDP10-02196R000700010005-2

Declassified and Approved For Release 2013/09/24 : CIA-RDP10-02196R000700010005-2

On the basis of the experiment, we concluded that the sensitivity of the Fabry-Perot interferometer is superior to the sensitivity of the conventional dual-beam interferometer. It should also be noted that this approach to measurements may work well in pulsed operation, if the oscillator makes it possible to receive a frequency-modulated signal with a low characteristic time of frequency change.

In conclusion, the authors express their acknowledgements to E. K. Zavoiskii for his kind interest in the progress of the work, their sincere thanks to V. L. Vdovin for his invaluable assistance in testing the performance of the instrument on the plasma arrangement which he devised, and to F. A. Korolev and V.I. Gridnev for their helpful counsel.

LITERATURE CITED

1. V. Ya. Balakhanov, V. D. Rusanov, and A. R. Striganov, Zhur. tekhn. fiz., 35, 127 (1965).
2. V. D. Rusanov, Modern techniques in plasma research [in Russian], Moscow, State atom press (1962).
3. F. A. Korolev and V. I. Gridnev, Radiotekhnika i élektronika, 8, 1480 (1963).

All abbreviations of periodicals in the above bibliography are letter-by-letter transliterations of the abbreviations as given in the original Russian journal. *Some or all of this periodical literature may well be available in English translation.* A complete list of the cover-to-cover English translations appears at the back of this issue.

Declassified and Approved For Release 2013/09/24 : CIA-RDP10-02196R000700010005-2

Declassified and Approved For Release 2013/09/24 : CIA-RDP10-02196R000700010005-2

BREMSSTRAHLUNG AND CHARACTERISTIC RADIATION SPECTRA OF ZIRCONIUM-TRITIUM SOURCES

(UDC 539.121.75)

Yu. P. Betin

Translated from Atomnaya Énergiya, Vol. 18, No. 5,
pp. 516-518, May, 1965
Original article submitted May 20, 1964

There are two known types of tritium radiation sources: titanium-tritium and zirconium-tritium sources. Continuous-spectrum bremsstrahlung and the characteristic radiations of elements in the composition of the source's active layer and the base-layer material arise in the source under the action of beta particles emitted by tritium (E_{max} = 18 keV).

Secondary radiation spectra of tritium sources, which were measured by means of a proportional counter with beryllium windows with thicknesses of 0.2 and 0.5 mm, were described in [1, 2]. Such a thickness of the counter's entrance window unavoidably causes distortions in the long-wave portion of the spectrum as a result of the absorption of the radiation in the window material; moreover, absorption in the air layer separating the source from the counter exerts a considerable influence in the soft region.

We measured the spectral composition of the radiation of a zirconium-tritium source by means of an unsealed proportional soft x-ray radiation counter with a lateral window consisting of a Terylene film with a thickness of

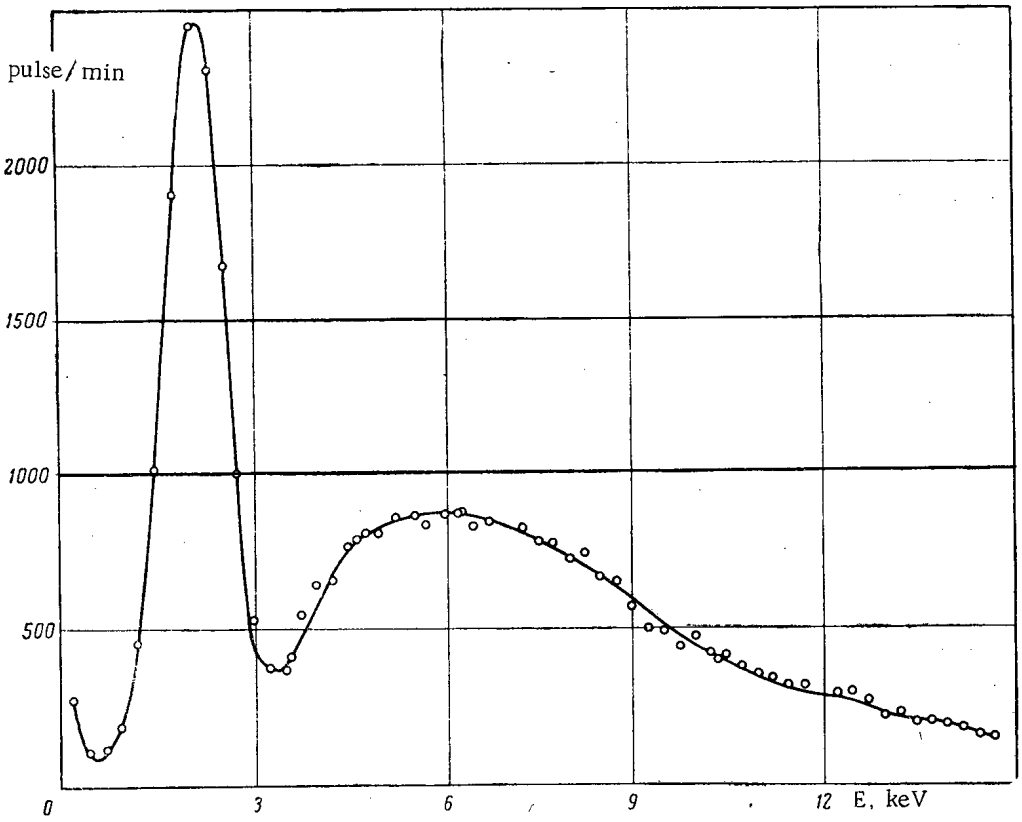

Radiation spectrum of the zirconium-tritium source.

Declassified and Approved For Release 2013/09/24 : CIA-RDP10-02196R000700010005-2

Declassified and Approved For Release 2013/09/24 : CIA-RDP10-02196R000700010005-2

about 20μ [3]. The counter's entrance window consisted of a slit with a width of 1.5 mm and a length of 20 mm. The inside diameter of the counter was 18 mm. The filling consisted of a mixture of argon and isopentane; the total pressure was approximately equal to 600 mm Hg. The spectrum of pulses from the proportional counter was recorded by means of a 100-channel amplitude analyzer.

The figure shows the amplitude spectrum of pulses from the proportional counter that was obtained in measurements with a thick zirconium-tritium source and a tungsten base-layer (the thickness of the active zirconium layer was 16 mg/cm^2, while the diameter of the source's active part was 14 mm). The source activity was approximately equal to 12 Ci. The source was placed at a distance of 1 cm from the proportional counter's entrance window; a lead diaphragm which had an opening with a diameter of 0.5 mm was installed between them.

The energy calibration of the spectrometer was performed by using an Fe^{55} source (the energy of the radiation accompanying the electron capture was E_k = 5.9 keV).

It is obvious from the figure that the secondary radiation spectrum of the zirconium-tritium source contains a continuous portion corresponding to bremsstrahlung with an intensity maximum in the 6-keV region and a sharply pronounced line of the characteristic L-radiation of zirconium with an energy of about 2.0 keV. This line is absent in the radiation spectra given in [1, 2], which can be explained by its virtually total absorption in the material of the counter window and in the air layer.

The actual curve of the electromagnetic radiation spectrum of the zirconium-tritium source must differ from the curve shown in the figure, since the L-radiation of zirconium is attenuated in the Terylene film of the counter's entrance window (a reduction by a factor of 3 according to our measurements) and in the air layer (a reduction by about one half for a thickness of 1 cm). Measurements of the transmission of a beryllium layer with a thickness of 0.22 mm indicated that the 2.0 keV radiation was attenuated by a factor of at least 30.

The above data on the electromagnetic radiation spectrum of zirconium-tritium sources indicate that such sources can be successfully used for exciting the characteristic x-ray K-radiation of light elements and elements with medium atomic numbers from aluminum (E_k = 1.5 keV) to germanium (E_k = 9.9 keV) as well as the L-series of heavier elements from niobium (E_L = 2.3 keV) to tungsten (E_L = 9 keV).

LITERATURE CITED

1. W. Kühn, Nukleonik, 4, 30 (1962).
2. J. Cameron and J. Roads, in the book: Transactions of the Internation Conference on the Uses of Radioisotopes in Physical Sciences and Industry (Copenhagen, 1960). Selected articles by foreign scientists [Russian translation], Moscow, Atomizdat (1962).
3. V. N. Baronin et al., Zavodsk. Laboritoriya, No. 4, 498 (1964).

All abbreviations of periodicals in the above bibliography are letter-by-letter transliterations of the abbreviations as given in the original Russian journal. *Some or all of this periodical literature may well be available in English translation.* A complete list of the cover-to-cover English translations appears at the back of this issue.

Declassified and Approved For Release 2013/09/24 : CIA-RDP10-02196R000700010005-2

Declassified and Approved For Release 2013/09/24 : CIA-RDP10-02196R000700010005-2

DETERMINATION OF THE RELATIVE FISSION REACTION RATES FOR DIFFERENT ISOTOPES BY RECORDING THE γ-RADIATION OF La^{140} FISSION FRAGMENTS

(UDC 539.173.4)

L. N. Yurova and A. V. Bushuev

Translated from Atomnaya Énergiya, Vol. 18, No. 5,
pp. 518-519, May, 1965
Original article submitted October 1, 1964

The problem of determining the ratio of the cross sections of two isotopies, for instance, U^{238} and U^{235} or Th^{232} and Pu^{239}, etc., arises in investigating certain characteristics of nuclear reactors.

Although such measurements are usually performed by means of fission chambers, this problem can also be solved by using the method of scintillation γ-spectrometry. Numerous measurements [1] have shown that, in the fission of various isotopes from Th^{232} to Pu^{239}, certain fragments are formed with almost the same probability, while some of them intensively emit γ-rays and decay with periods suitable for measurements.

After a foil made of the isotope under investigation is irradiated in a reactor, the intensity of the γ-radiation of one of these fragments can be used for estimating the fission reaction rate for the isotope in question, and, if parallel measurements with two isotopes are performed, the ratio of their fission cross sections can be determined. If fission chambers are used for measurements, the chambers must be calibrated in a converter or a thermal column. The basic advantage of measurements by means of γ-spectrometers is that no additional calibration measurements are necessary, as a result of which the measurement process is simplified, while the accuracy is improved.

Such a measurement method was first described in [2], where it was used for determining the ratio of the fission cross sections of U^{235} and U^{238} in a thermal reactor. It was found that the measurements can be conveniently performed by using the radiation of La^{140}, which is located at the top of the right-hand hump in the mass distribution of fission fragments. Therefore, in fission by neutrons with energies from the thermal energy to 10 MeV, the yield of a fragment with a mass of 140 does not change [1]. The information available in the literature on the La^{140} yield in the fission of various isotopes is given below:

Isotope	Yield per single fission, %	
U^{235}	6.44	[3]
U^{238}	5.8	[4]
U^{233}	6.1	[3]
Th^{232}	6.2	[3]
Pu^{239}	6.0	[5]

The La^{140} isotope emits hard (E_γ = 1.6 MeV) γ-radiation in an amount of 0.95 quantum per decay [6]. The rate of radioactive decay of La^{140} is determined by the half-life of the parent isotope Ba^{140}, which is equal to 12.8 days.

Our aim was, in the first place, to determine the suitability of the γ-spectrometry method for measurements by means of fast experimental systems and, in the second place, to apply this method to measurements with Th^{232} and Pu^{239} The figure shows the 1.6-MeV La^{140} line in the γ spectra of irradiated U^{238} and Pu^{239} specimens. The measurements were performed by means of a scintillation spectrometer with a 40 × 40 mm NaI(Tl) crystal and a

Declassified and Approved For Release 2013/09/24 : CIA-RDP10-02196R000700010005-2

Declassified and Approved For Release 2013/09/24 : CIA-RDP10-02196R000700010005-2

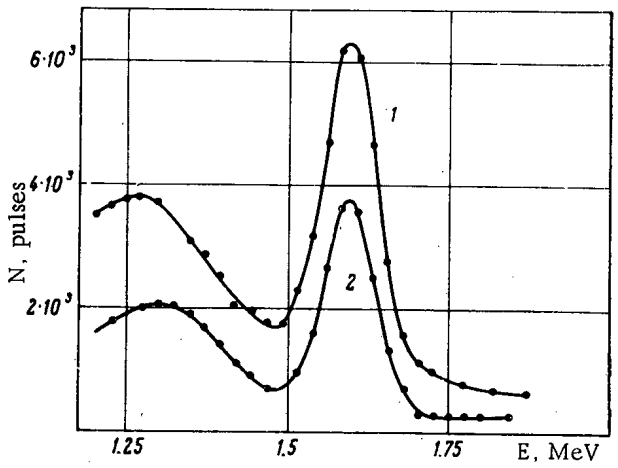

γ-Radiation spectrum of Pu^{239} (1) and U^{238} (2) fission fragments in the 1.2-2-MeV range four days after irradiation over a period of 10 h.

Ratios of U^{238} and U^{235} Fission Cross Sections, Measured by Means of a γ-Spectrometer and a Fission Chamber

Reactor	γ-spectrometer	Fission chambers	calc.
BR-1	$\frac{\sigma_{nf}(U^{238})}{\sigma_{nf}(U^{235})} = 0.164 \pm 0.03$	0.167±0.03	0.164
Experimental assembly	$\frac{\sigma_{nf}(U^{238})}{\sigma_{nf}(U^{235})} = 0.089 \pm 0.03$	0.091±0.02	0.090

100-channel amplitude analyzer. As a result of the investigations performed, it was found that, five to six days after irradiation lasting tens of hours, no extraneous activity under the 1.6-MeV La^{140} photopeak was observed in the γ-spectrum of fission fragments of any of the above-mentioned isotopes. The area under the photopeak of the γ-line serves as a measure of its intensity. Therefore, the measurement of the ratio of the fission cross sections of two isotopes consisted in determining the ratio of areas under the 1.6-MeV photopeaks in the spectra of reactor-irradiated specimens of these isotopes. The weights and the chemical and isotope compositions of the specimens were determined first. The specimens were irradiated simultaneously at the same location in the reactor. The measurements based on La^{140} radiation lasted two to three weeks; the results of these measurements were used for plotting the decay curves and determining the initial areas under the 1.6-MeV photopeaks and their ratio.

The effects investigated by means of fast experimental systems are weak, since the reaction cross sections and the neutron fluxes in such systems are small. Therefore, some of the measurements methods successfully used on thermal reactors cannot be used on fast assemblies. The suitability of the described method was checked experimentally in investigations of the BR-1 reactor and a fast experimental assembly. Foils of natural and enriched uranium and thorium were used. The results obtained in measuring the ratios of the fission cross sections U^{238} and U^{235} by means of a γ-spectrometer and fission chambers as well as the calculation data are given in the table.

It was found that the γ-spectrometry method can be used in measurements if the integral influx of fast neutrons is equal to or larger than 10^{13} fast neutrons/cm^2.

The possibility of using the method of recording La^{140} γ-radiation in measurements with thorium and plutonium was investigated in experiments performed on a fast reactor with thorium specimens and a thermal reactor with plutonium specimens. The experimental values of the $\frac{\sigma_{nf}(Th^{232})}{\sigma_{nf}(U^{235})}$ and $\frac{\sigma_{nf}(Pu^{239})}{\sigma_{nf}(U^{235})}$ ratios were close to the theoretical values.

The investigations have shown that the above-described method can be used for measurements in various nuclear reactors. The accuracy of the thus obtained data is to a large extent determined by the available information on the La^{140} yield in the fission of various isotopes. For instance, the ratio of yields of this fragment in U^{238} and U^{235} fission is known with an accuracy to ±5% [4]. The accuracy of the described method will improve as new data on the La^{140} yield become available.

LITERATURE CITED

1. Yu. A. Zysin et al., Yields of Fission Products and Their Mass Distributions [in Russian], Moscow, Gosatomizdat (1963).
2. J. Wolberg et al., Report SM-42/46, Symposium on exponential and critical experiments. Netherlands, Amsterdam (1963).
3. S. Katcoff, Nucleonics, 18, 201 (1960).
4. S. Levy et al., Phys. Rev., 124, 544 (1961).
5. F. Walter et al., Phys. Rev., 133, B1500 (1964).
6. O. Khol'nova, Izv. AN SSSR, Phys. Sect., 22, 848 (1958).

Declassified and Approved For Release 2013/09/24 : CIA-RDP10-02196R000700010005-2

Declassified and Approved For Release 2013/09/24 : CIA-RDP10-02196R000700010005-2

ENERGY DISTRIBUTION OF α PARTICLES EMERGING FROM A THICK SOURCE

(UDC 539.12 39.121.64)

É. B. Ershov, A. A. Karan, and V. P. Shamov

Translated from Atomnaya Énergiya, Vol. 18, No. 5,
pp. 519-520, May, 1965
Original article submitted March 18, 1964

As is known, the experimental determination of the stopping power and the relationship between the range and the energy of α particles in the material under investigation is based on counting the particles that have passed through stopping screens with different thicknesses. However, it is difficult or entirely impossible to prepare thin absorbing foils or films from most materials, especially those with a complex molecular structure. Therefore, we shall consider here the possibility of determining the range–energy relationship for a thick plane-parallel radiator by analyzing the shape of its spectrum of α particles.

The spectrum was measured by means of an α ionization chamber and a 100-channel amplitude analyzer. The integral background of the chamber was 3 pulses/min. The operating pressed specimen (area: ~3 cm^2; thickness: 2 mm), which was mounted in a holder, contained Pu^{239} atoms which were uniformly distributed in talc.

In order to determine the empirical form of the N(E) spectrum for $E \leq E_{max}$, the measured spectrum was divided into four sections with respect to energy: 0.1-0.8; 0.8-2.0; 2-4 and 4-5 MeV.

By using the equalization method, the following dependences of the spectral form on the energy ($E_{max} = 4.9$ MeV), normalized to the distribution maximum, were obtained for each energy interval:

$$\left.\begin{aligned} N_1(E) &= 0.202e^{0.78E} + 0.704e^{-3.5E}; \\ N_2(E) &= 0.027E^{2.31} + 0.40; \\ N_3(E) &= 1.125E + 0.28; \\ N_4(E) &= 0.23(E-4)^{1.1} + 0.79. \end{aligned}\right\} \quad (1)$$

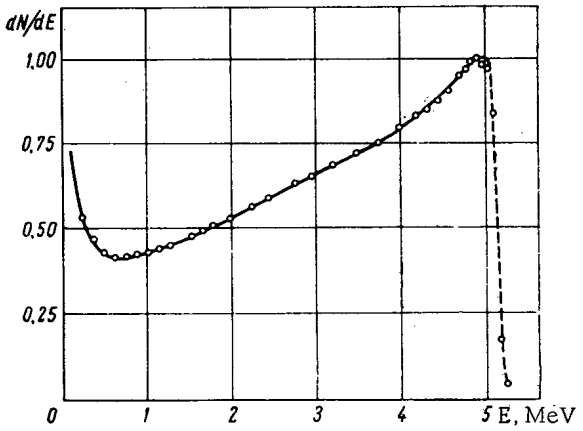

Normalized empirical form of the Pu^{239} spectrum.

The analytical form of the spectrum (1) with the marked normalized experimental values is shown in the figure (the root-mean-square errors in the experimental data do not exceed 0.5%). It is seen from the figure that relationships (1) describe the gentle decline of the experimental spectrum with satisfactory accuracy (the discrepancies do not exceed 1%).

From an estimate of the effective atomic number values ($Z \approx 13$) and of the excitation potential ($I \approx 0.180$ keV) obtained on the basis of [1] for talc ($3MgO \cdot H_2O \cdot 4SiO_2$), it follows that talc is close to aluminum with respect to its stopping proportional to the derivative of the range with respect to energy. Therefore, for comparison with our results, we calculated the range vs energy curves on the basis of theoretical calculations [3] and on the basis of the empirical expression [4], which makes it possible to determine the range of α particles in the material if their range in air is known [3].

Declassified and Approved For Release 2013/09/24 : CIA-RDP10-02196R000700010005-2

Declassified and Approved For Release 2013/09/24 : CIA-RDP10-02196R000700010005-2

It was found that the range vs energy curve obtained on the basis of relationships (1) agrees well with the curve obtained by means of the empirical expression [4] for all energy intervals.

Thus, as was shown on the example with talc, the proposed method makes it possible to determine with a sufficiently high degree of accuracy the stopping characteristics of any complex material to be used as the base mass of a thick α source.

LITERATURE CITED

1. M. Z. Maksimov, ZhÉTF, 37, 127 (1959).
2. N. K. Abrosimov and G. E. Kocharov, Izv. AN SSSR, Phys. Sect., 26, 237 (1962).
3. G. A. Bete and Yu. Ashkin, In the book: Experimental Nuclear Physics, Edited by E. Segré [Russian translation], Moscow, Izd. Inostr. Lit., 1, (1955), p. 190, 154.
4. V. Price, Recording of Nuclear Radiation [Russian translation], Moscow, Izd. Inostr. Lit., (1960).

All abbreviations of periodicals in the above bibliography are letter-by-letter transliterations of the abbreviations as given in the original Russian journal. *Some or all of this periodical literature may well be available in English translation.* A complete list of the cover-to-cover English translations appears at the back of this issue.

Declassified and Approved For Release 2013/09/24 : CIA-RDP10-02196R000700010005-2

Declassified and Approved For Release 2013/09/24 : CIA-RDP10-02196R000700010005-2

PARABOLIC APPROXIMATION OF THE TOTAL ATTENUATION COEFFICIENTS OF γ-QUANTA IN THE ENERGY RANGE FROM 0.03 TO 10 MeV

(UDC 539.172.3)

O. S. Marenkov and R. S. Derzhimanov

Translated from Atomnaya Énergiya, Vol. 18, No. 5, pp. 520-521, May, 1965
Original article submitted May 25, 1964

As is known, the total coefficients of the attenuation of γ-quanta in a material constitute complex functions of the energy ε. In order to solve particular problems in the theory of transport of γ-quanta by means of various analytical and approximate methods, it is necessary to represent the dependence $\mu(\varepsilon)$ of the total linear attenuation coefficient in analytical form. Simplified analytical expressions for this function can be obtained only for a limited range of changes in the argument.

The present communication is concerned with a possible variant of analytical presentation of the dependence of μ on λ the wavelength in Compton units) in the energy range from 0.03 to 10 MeV. In its general form, the $\mu(\lambda)$ dependence can be represented as a polynomial of the nth degree:

$$\mu(\lambda)=\varrho\sum_{k=0}^{n}c_k\lambda^k, \tag{1}$$

where p is the density of the material, and c_k are undetermined coefficients. In cases of practical interest, it is obvious that μ can be conveniently approximated by means of expression (1) with a small n value in order to avoid exceedingly complicated calculations. We shall consider the parabolic approximation of the total mass attenuation coefficient:

$$\frac{\mu}{\varrho}=c_0+c_1\lambda+c_2\lambda^2. \tag{2}$$*

By using expression (2) and the data from [1, 2], the μ/p coefficients were approximated (without an allowance for coherent scattering) in the energy ranges 0.03-0.08; 0.08-0.3; 0.3-10.0 MeV for beryllium, carbon, oxygen, sodium, magnesium, aluminum, silicon, phosphorus, sulfur, potassium, calcium, iron, copper, water, sand, calcium phosphate, and concrete.

Article [1] contains a detailed analysis of the theoretical and experimental data, and it provides the values of the total mass attenuation coefficients μ/p as well as the partial coefficients of photoelectric absorption, scattering (with an without an allowance for coherent scattering), and formation of electron-positron pairs. It is assumed that the errors in the above coefficients attain 10% for energies below 50 keV and that they do not exceed 3-5% for energies above 100 keV. The experimental data obtained after [1] was published made it possible to revise the values of the coefficients for low energies and to determine them with the same degree of accuracy (i.e., 3-5%) as in the case of higher energies [2]. A larger part of the tables given in [2] is intended for replacement of

*Equation (2) can be written in a form that is more convenient for practical calculations:

$$\frac{\mu}{\varrho}=b_0+\frac{b_1}{\varepsilon}+\frac{b_2}{\varepsilon^2},$$

where ε is the energy of γ quanta (MeV), while the coefficients b_k and c_k are related by the following expressions $b_0 = c_0$; $b_1 = 0.511c_1$; $b_2 = 0.261\ c_2$.

Declassified and Approved For Release 2013/09/24 : CIA-RDP10-02196R000700010005-2

Declassified and Approved For Release 2013/09/24 : CIA-RDP10-02196R000700010005-2

Parabolic Appoximation Coefficients

Element, material	$\varepsilon = 0.03 \div 0.08$ MeV			$\varepsilon = 0.08 \div 0.3$ MeV			$\varepsilon = 0.3 \div 10$ MeV		
	c_0	c_1	c_2	c_0	c_1	c_2	c_0	c_1	c_2
Beryllium	110	4.89	—0.0889	62.9	21.5	—1.54	12.1	105	—36.0
Carbon	135	2.07	0.201	71.5	23.3	—1.56	14.9	113	—37.7
Oxygen	174	—8.65	1.04	75.4	21.1	—1.20	16.3	108	—34.5
Sodium	246	—33.0	3.24	70.4	20.2	—0.808	17.2	99.3	—30.7
Magnesium	319	—53.5	4.95	76.1	18.4	—0.381	18.3	100	—30.4
Aluminum	353	—65.3	6.10	69.8	20.3	—0.430	18.4	96.9	—29.1
Silicon	411	—83.2	7.92	73.9	19.5	0.0400	19.7	98.2	—28.9
Phosphorus	476	—104	9.78	73.3	17.2	0.550	19.6	93.9	—27.3
Sulfur	564	—131	12.3	78.2	15.5	1.27	20.8	94.8	—26.7
Potassium	866	—227	21.4	86.4	4.75	4.12	22.0	86.9	—22.8
Calcium	999	—269	25.7	90.3	2.14	5.34	23.1	87.8	—22.6
Iron	1730	—512	51.2	103	—21.7	13.8	24.8	72.1	—14.4
Copper	2110	—646	66.6	118	—40.4	20.1	25.9	65.1	—9.85
Water	182	—6.27	0.891	75.4	28.5	—2.0	17.0	124	—40.5
Sand	289	—44.6	4.32	67.2	25.6	—1.34	17.8	104	—32.1
Calcium phosphate	567	—132	12.5	73.3	18.1	0.979	19.5	96.8	—27.8
Concrete	365	—68.2	6.59	67.9	24.2	—0.739	18.2	103	—31.6

Remark. All the c_k values must be multiplied by 10^{-3}

those parts of the tables in [1] which pertain to the energy range from 0.01 to 0.1 MeV, while the data on the scattering cross section with and without an allowance for coherent scattering remain unchanged. With certain subsequent corrections [2], paper [1] contains the latest and most complete data on a large number of elements and certain materials in the energy range of α quanta from 0.01 to 100 MeV.

We composed a program for the BÉSM-2M computer for the purpose of calculating the coefficients c_k in the above-indicated energy ranges. The coefficients were determined from the condition for the minimum of the expression

$$S(c_k) = \sum_{l=1}^{m} \frac{\left[\left(\frac{\mu}{\varrho}\right)_l^{\mathrm{T}} - \frac{\mu}{\varrho}(\lambda_l)\right]^2}{\lambda_l^p},$$

where $\left(\frac{\mu}{\varrho}\right)_l^{\mathrm{T}}$ — are the tabular values μ/ρ [1, 2], λ_l are the tabular wavelength values, $\frac{\mu}{\varrho}(\lambda_l)$ — is the total mass attenuation coefficient defined by means of (2), and m is the number of tabular μ/ρ values in the interval chosen for approximation.

The optimum value of the exponent of the weighting function is $p = 2\alpha$, where α is the mean index of increase in μ/ρ in the range under consideration. By varying p, the maximum error can be moved along the $\mu/\rho\ (\lambda)$.

The results of the calculations performed are given in the table. The maximum relative error of approximation did not exceed 4% in the 0.03-0.08 MeV range, 3% in the 0.08-0.3 MeV range, and 5% in the 0.3-10.00 MeV range. In the latter case, the errors for beryllium, carbon, and oxygen were equal to 8, 7, and 6%, respectively.

Thus, the parabolic approximation of μ/ρ can be effected not only for individual elements, but also for multicomponent media (concrete) and chemical compounds (water, sand, calcium phosphate). However, it can be shown that, in the latter case, the $\mu/\rho\ (\lambda)$ coefficients can be obtained on the basis of the well-known dependences $\mu_i/\rho_i\ (\lambda)$ for individual elements:

$$\frac{\mu}{\varrho} = \sum_l \frac{\mu_i}{\varrho_i}(\lambda)\, a_i, \qquad (3)$$

Declassified and Approved For Release 2013/09/24 : CIA-RDP10-02196R000700010005-2

Declassified and Approved For Release 2013/09/24 : CIA-RDP10-02196R000700010005-2

where a_i is the percentage by weight of the i-th element in a mixture or a chemical compound.

The calculations performed by means of expression (3) for sand, calcium phosphate, and concrete showed that the maximum relative approximation error did not exceed 5%.

The authors hereby extend their thanks to Yu. P. Shcherbin for his assistance in performing the calculations.

LITERATURE CITED

1. G. White-Grodstein. X-ray Attenuation Coefficients from 10 keV to 100 MeV, NBS, Circular No 538 (1957).
2. R. McGinnies. X-ray Attenuation Coefficients from 10 keV to 100 MeV, NBS, suppl. to Circular No 583 (1959).

Declassified and Approved For Release 2013/09/24 : CIA-RDP10-02196R000700010005-2

Declassified and Approved For Release 2013/09/24 : CIA-RDP10-02196R000700010005-2

THE EFFECT OF BORON-CONTAINING BLOCKING ON THE YIELD OF CAPTURE γ-RADIATION

(UDC 539.122 : 539.121.73)

S. A. Kozlovskii, V. S. Kyz'yurov, K. K. Popkov and D. N. Lebedev

Translated from Atomnaya Énergiya, Vol. 18, No. 5, pp. 522-525, May, 1965
Original article submitted May 22, 1964

This letter investigates the effect of various boron-containing blockings on the yield of capture γ-radiation from the composition of the primary shielding of a water-moderated water-cooled reactor. The reactor vessel, thermal screens and the water layers between the screens were modeled by sheets of steel (Grade 3) and Plexiglas, respectively, of size 800 x 800 mm. The blocking layers were placed between the steel vessel and the water tank,

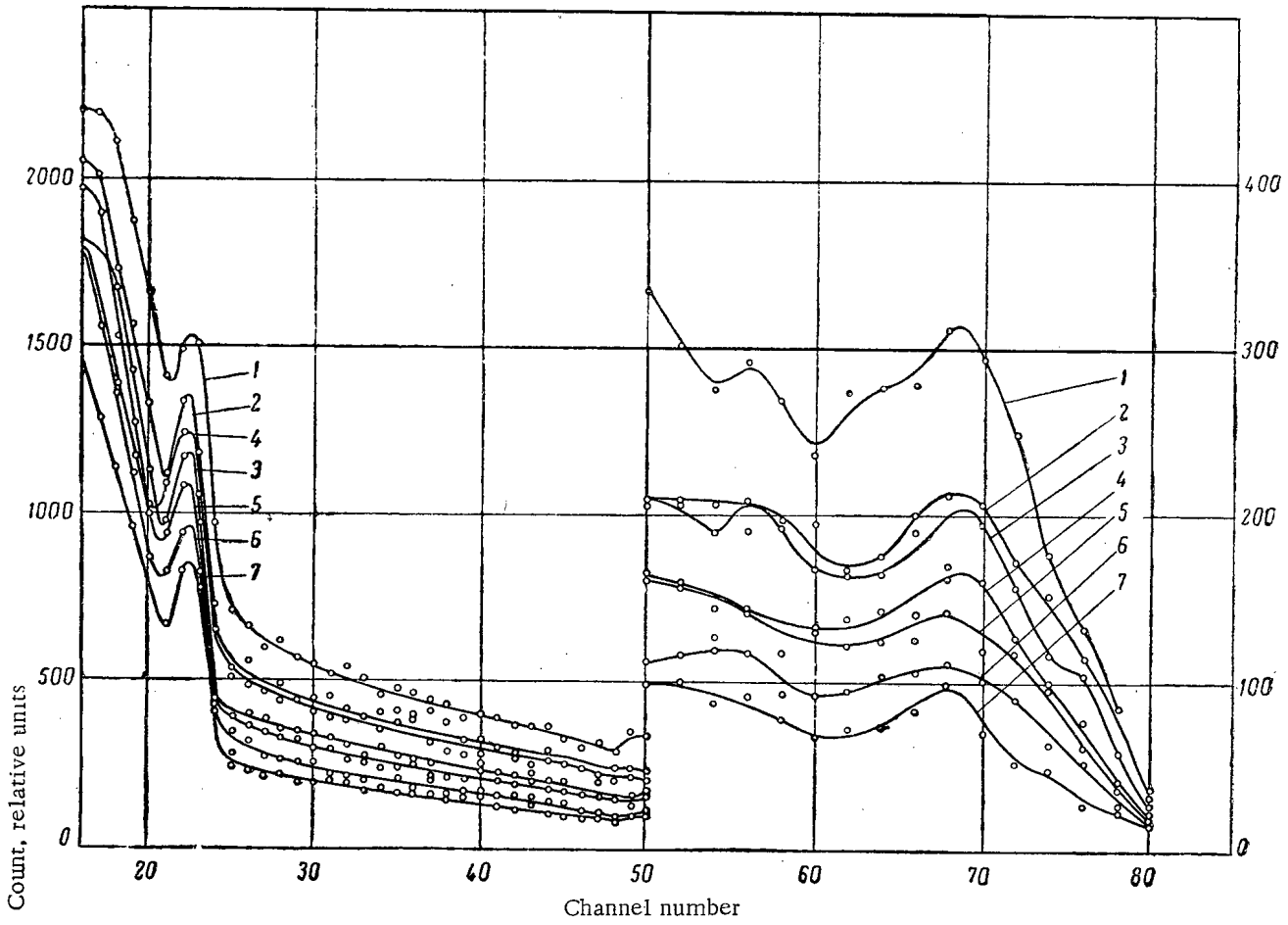

Fig. 1. Spectrum of capture α-radiation from shielding. 1) Without blocking layer; 2, 3) With blocking layer of B_4C of thickness, d, equal to 1.5 and 3.5 cm, respectively; 4, 5, 6, 7) with blocking layer of borated lead, thickness 1.5, 2.5, 3.5, 5,5, cm, respectively.

Declassified and Approved For Release 2013/09/24 : CIA-RDP10-02196R000700010005-2

Declassified and Approved For Release 2013/09/24 : CIA-RDP10-02196R000700010005-2

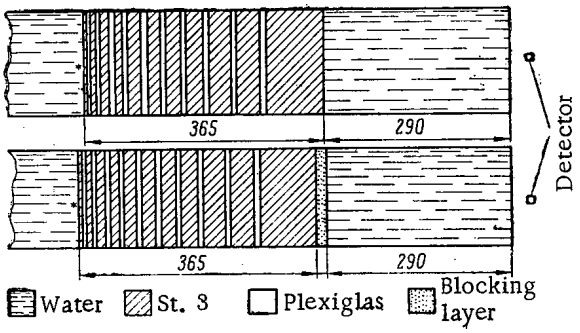

Fig. 2. Geometry of experiment.

modeling the water of the primary shielding. They were made of boron carbide (covering to a density of 1.1 g/cm^3) and borated lead, i.e., a mixture of red lead and boric anhydride in the proportion 9 : 1 by weight. The mixture density was ~5.5 g/cm^3, containing about 3 wt. % boron.

The scheme of composition studied is shown in Fig. 2. The radiation was from a Po-Be source of power 10^8 neutron/sec.

We measured the spatial distribution of fluxes of thermal and epithermal neutrons. The measurements were

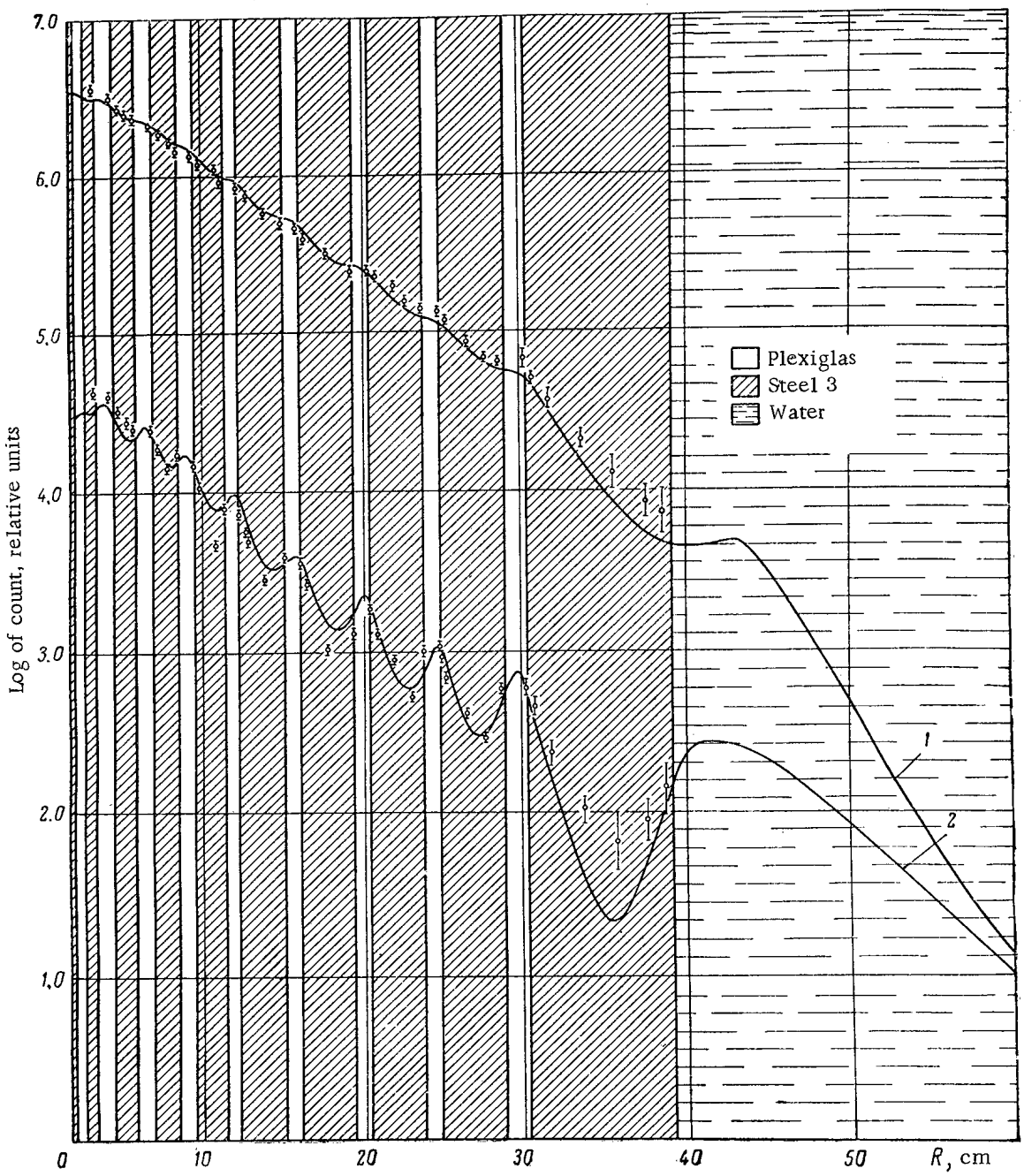

Fig. 3. Spatial distribution of neutrons in shielding without blocking layer. 1, 2) Epithermal and thermal neutron fluxes, respectively ———— Calculated results. ○ Results measured with indium indicators.

Declassified and Approved For Release 2013/09/24 : CIA-RDP10-02196R000700010005-2

Declassified and Approved For Release 2013/09/24 : CIA-RDP10-02196R000700010005-2

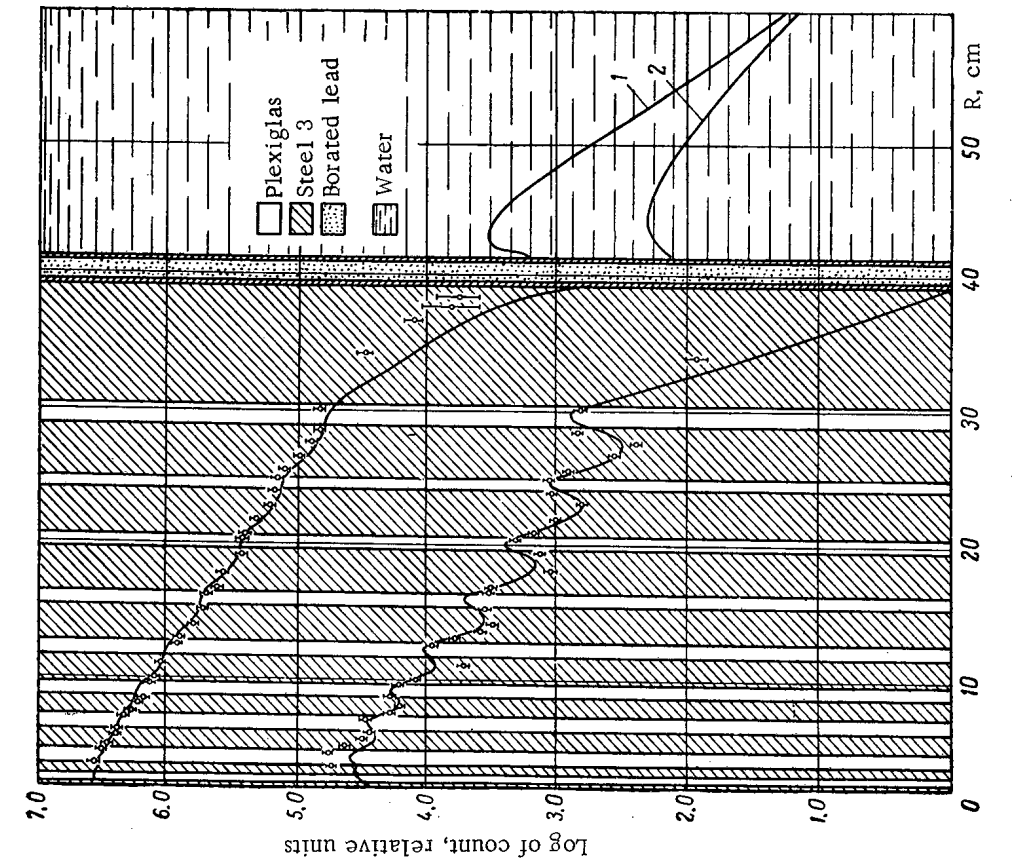

Fig. 5. Spatial distribution of neutrons in shielding with blocking layer of borated lead of thickness 1.5 cm (for meanings of symbols see under Fig. 3).

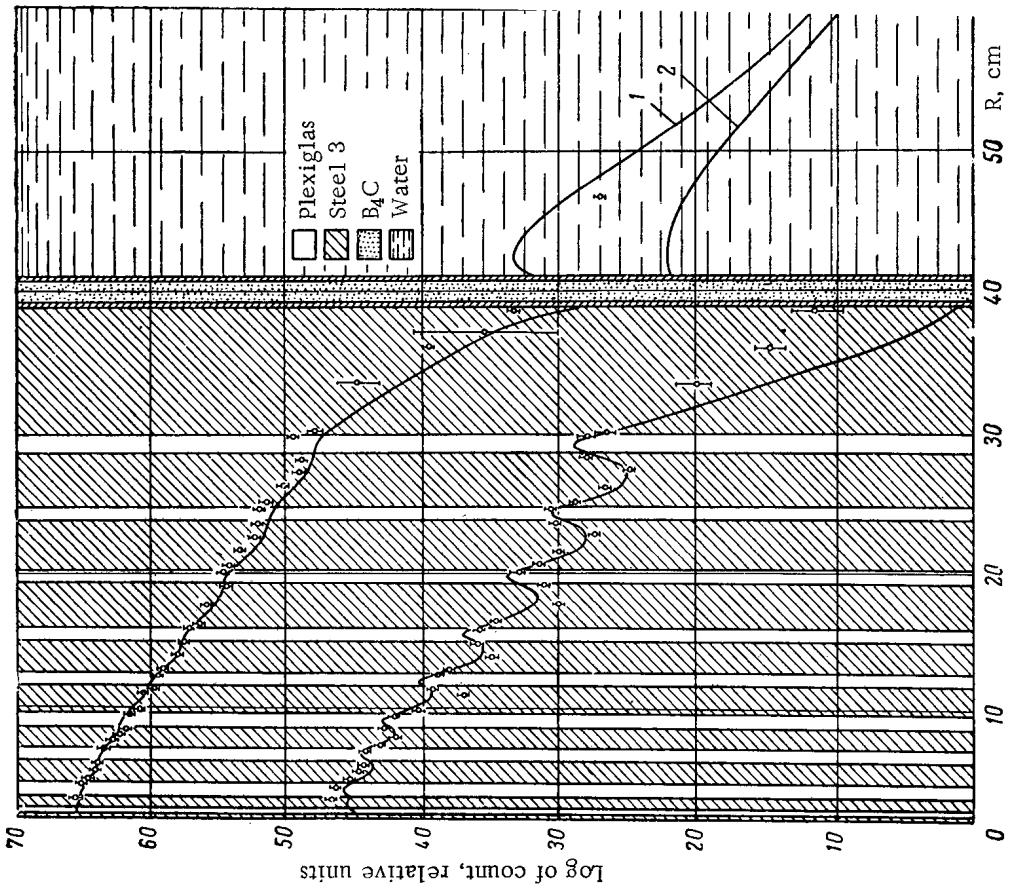

Fig. 4. Spatial distribution of neutrons in shielding with blocking layer of B_4C of thickness 1.5 cm (for meanings of symbols see under Fig. 3).

Declassified and Approved For Release 2013/09/24 : CIA-RDP10-02196R000700010005-2

Declassified and Approved For Release 2013/09/24 : CIA-RDP10-02196R000700010005-2

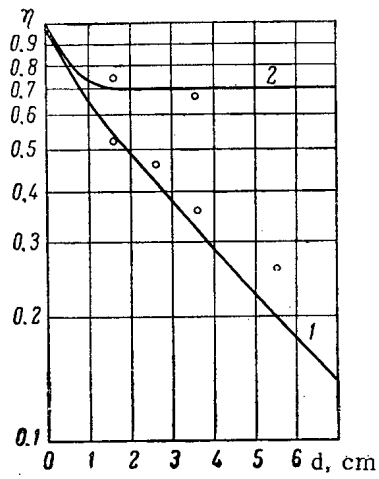

Fig. 6. Relative reduction of yield, η, of capture γ-radiation with energy 7.64 Mev, plotted versus thickness of blocking screen. 1, 2) Blocking by borated lead and boron carbide, respectively. ——— Theoretical results. ● Experimental results.

made with an indium foil of diameter 21 mm and thickness 100 mg/cm^2, stuck on to an aluminum substrate of thickness 0.5 mm. When measuring the fluxes of epithermal neutrons, the foils were placed in a cadmium box with sides of thickness 1 mm. The indicators were "suspended" in the neutron flux, and the scatter of the readings was 5% or less.

The yields of capture γ-radiation from the experimental compositions were measured by a scintillation γ-spectrometer with NaI crystal 40 × 40 mm in size and FÉU-13B photomultiplier. The pulses were analyzed with an AI-100-1 amplitude analyzer. The resolution on Co^{60} was 11%. The scale linearity was checked with Cs^{137}, Co^{60} and Po-Be sources.

The relative yield of capture γ-radiation was determined from the area under the peak of the 7.64 Mev line. The spectra of capture γ-radiation, shown in Fig. 1, have two lines corresponding to absorption of neutrons by hydrogen nuclei (2.23 Mev) and iron nuclei (7.64 Mev).

In addition, a computer was used to calculate the spatial and energetic distributions of the neutron fluxes for the compositions under examination, using the diffusion-age approximation and the semi-grouped scheme suggested in [1].

Figs. 3-5 give the spatial distribution curves of the fluxes of thermal and epithermal neutrons, as calculated theoretically; the experimental points are superimposed.

Using the method described in [2], we calculated the yields of capture γ-radiation from the experimental assemblies. Fig. 6 gives the experimental and theoretical values of the relative yields of capture γ-radiation, η, as functions of the blocking screen thickness. The discrepancies with the results in [3] are explained by the differing thickness of the steel monoliths and the different composition of the assemblies. In [3] the experiment was performed with a single layer of iron of thickness 25 cm, screened on both sides by boron carbide; the present authors used compositions containing a fairly large number of hydrogen-containing layers. The presence of hydrogen reduces the effect of blocking.

In conclusion, the authors wish to thank D. L. Broder for valuable advice, and also V. N. Dorofeikov, V. G. Komov, L. G. Kocherova, V. A. Lazukov and Yu. K. Spivak for assistance in the work.

LITERATURE CITED

1. D. L. Broder et al. Atomnaya Énergiya , 12, 129 (1962).
2. L. P. Bokacheva, K. K. Popkov, and L. N. Tabolina. Inzh.-fiz. zh. , 6, No. 11, 85 (1963).
3. D. L. Broder et al., Atomnaya Énergiya , 8, 49 (1960).

Declassified and Approved For Release 2013/09/24 : CIA-RDP10-02196R000700010005-2

Declassified and Approved For Release 2013/09/24 : CIA-RDP10-02196R000700010005-2

PULSATIONS OF THE PIPE WALL TEMPERATURE UNDER CONDITIONS OF INTENSIVE CONVECTIVE HEAT EXCHANGE

(UDC 539.122;539.121.73)

V. I. Subbotin, M. Kh. Ibragimov, V. I. Merkulov, E. V. Nomofilov, and N. A. Tychinskii

Translated from Atomnaya Énergiya, Vol. 18, No. 5, pp. 525-527, May, 1965
Original article submitted August 20, 1964

Temperature pulsations in the heat-transfer wall under steady-state heat exchange conditions were detected as a result of our investigations. These pulsations, however, are due to different causes.

In transverse flow around bunches of heat-releasing rods, temperature pulsations in the wall are caused by the hydrodynamic instability of the flux washing the rods [1]. In the case of longitudinal flow along bunches of rods, the characteristics of which are given in [2], temperature pulsations are caused by random redistributions of the liquid discharge and, consequently, by the heating of the liquid in individual cells. Meanwhile, the liquid discharge through the bunch remains constant. The magnitude of temperature pulsations depends on the length of the heating section (the greater the length, the larger the pulsation amplitude). The hydrodynamic instability of the liquid flow is caused by external factors (the channel geometry, the inlet conditions, separation of large vortices, etc.). Therefore, the frequency of temperature pulsations in the wall is very low, while the amplitude is large. The temperature pulsations caused by such flow instability can be considerably reduced. Thus, the pulsation amplitude can be greatly reduced by using smaller spacing in the bunch (in transverse flow) or by increasing the hydraulic resistance at the inlet (in longitudinal flow). In the case of turbulent flow of the coolant in a straight round pipe, temperature pulsations in the heat-releasing wall are obviously connected with the internal structure of the flow [3].

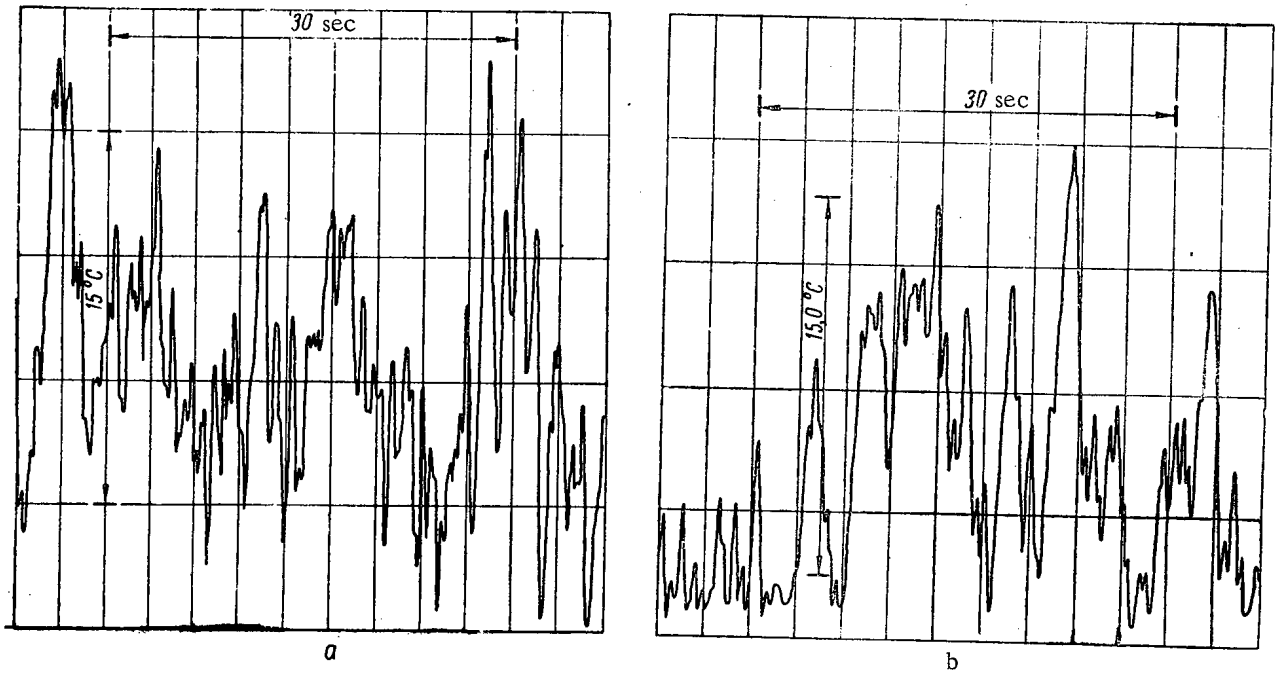

Fig. 1. Temperature pulsations in the wall. a) q = const, $Re = 6 \cdot 10^4$; b) t ≈ const, in the pipe and Re = $= 2.7 \cdot 10^4$, in the annular clearance $Re = 3.2 \cdot 10^5$.

Declassified and Approved For Release 2013/09/24 : CIA-RDP10-02196R000700010005-2

Declassified and Approved For Release 2013/09/24 : CIA-RDP10-02196R000700010005-2

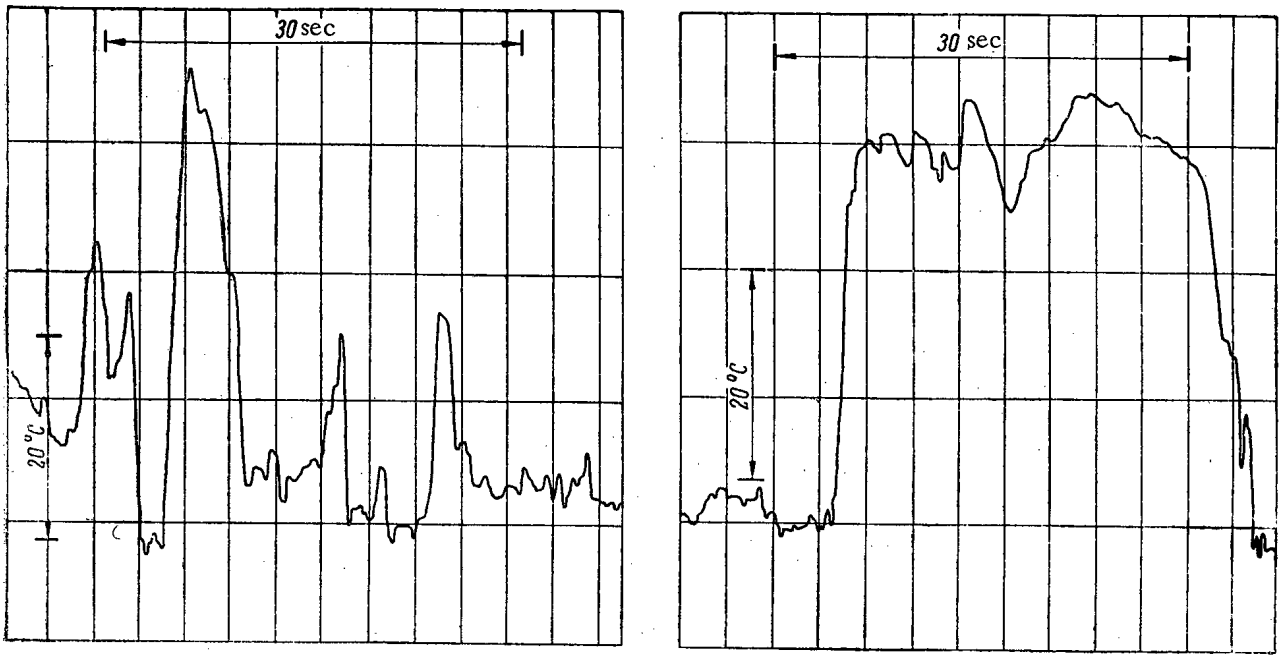

a b

Fig. 2. Splashes of the wall temperature (a) and changes in the temperature conditions of the wall (b) for $Re = 1.5 \cdot 10^4$.

In nonisothermic flow, where a temperature gradient exists along the pipe radius, the migration of an individual particle (mole) from one layer to another causes temperature pulsations in this layer. It is possible that certain most intensively moving moles reach the pipe wall, causing rapid temperature changes in it. Most of the moles, however do not reach the heat-releasing wall. They disintegrate in the "viscous" sublayer near the wall and produce temperature fluctuations in it. As a result of the thermal conductivity of the liquid, these fluctuations are also transmitted to the heat-releasing wall. Temperature pulsations caused by the turbulence of the flow itself are also possible in transverse flow as well as in longitudinal flow. However, the role of such pulsations is relatively limited. The damping of the temperature pulsation amplitudes in the viscous sublayer and in the solid wall obeys the exponential law, while the degree of the attenuation of pulsations depends on their frequency. Consequently, the intensity and the spectral composition of temperature pulsations in the wall will be determined by the intensity and the spectrum of pulsation in the layer near the wall. In the case of small thermal fluxes [4], when even the maximum pulsation magnitude amounts to a few degrees, pulsations of considerable magnitude penetrate the pipe wall only at low frequencies (about 0.2-1 cps), while high-frequency pulsations have negligibly low intensity. The intensity of temperature pulsations in the coolant flow increases in direct proportion to the thermal flux. Therefore, in the case of large thermal fluxes, even high-frequency (~8-10 cps) temperature pulsations have large amplitudes and may penetrate the pipe wall while retaining a rather high intensity. Consequently, with an increase in the thermal flux, we can expect not only an increase in the intensity of temperature pulsations, but also a change in their spectral composition and a greater role of high-frequency pulsations.

Statistical investigations of wall temperature pulsations in the case of large thermal fluxes under different conditions of flow around the heat-releasing surface are of great importance for highly stressed heat-exchange devices.

The experiments on temperature pulsation measurements were performed in a heat exchanger of the "pipe-in-pipe" type, where the inside pipe had a diameter of 24 mm and a wall thickness of 2 mm, while the outside pipe had a diameter of 41 mm and a wall thickness of 3 mm. The length of the heat exchange section was equal to 900 mm. Coolants at different temperatures were pumped through the two passages of the heat exchanger. The arrangement used for connecting the heat exchanger to the device made it possible to perform the experiments under conditions close to constant-flux conditions or constant-wall temperature conditions. The thermal flux varied $1.3 \cdot 10^5$ to $6 \cdot 10^5$ W/m^2 in the experiments. The wall temperature of the inside pipe was measured by means of Chromel-Alumel microthermocouples, which had an outside diameter of 0.8 mm (the method used for preparing and installing the thermocouples was described in [5]).

Declassified and Approved For Release 2013/09/24 : CIA-RDP10-02196R000700010005-2

Declassified and Approved For Release 2013/09/24 : CIA-RDP10-02196R000700010005-2

The microthermocouple readings were recorded by means of an ÉPP-09 automatic potentiometer with 0-1 and 0-2.5-mV measurement ranges; the time of travel over the scale was equal to 1 sec. Larger thermo-emf values were compensated by means of a PPTN-1 potentiometer. The speed of the strip chart was 21,600 mm/h.

The experiments were performed in the range of Re number values from $65 \cdot 10^3$ to $180 \cdot 10^3$. The thermocouples recorded the superposition of two random processes: turbulent temperature pulsations in the liquid which penetrated the wall from the side of the pipe and from the side of the annular clearance.

An analysis of the recorded temperature pulsations in the pipe wall showed the following:

1. Temperature pulsations in the wall constitute a steady-state random process with a wide frequency spectrum (0.01-5 cps). Consequently, pulsations should be studied by using the correlation theory of random functions [6].

2. For a constant thermal flux, an increase in the mean frequency of temperature pulsations is observed with an increase in the velocity in the range of Re numbers under investigation.

3. The character of temperature pulsations in the wall is virtually independent of the boundary conditions at the heat-releasing wall. The temperature pulsations in the case of a constant thermal flux (Fig. 1a) are almost equal to pulsations in the case of a constant wall temperature (Fig. 1b).

4. The intensity $\sigma = \sqrt{\frac{\Sigma t'^2}{n-1}}$ of temperature pulsations in the wall is proportional to the thermal flux.

In the investigated range of Re numbers, the relative intensity $\sigma/(t_{wa}-t_l)$ of temperature pulsations increases with an increase in the velocity.

5. The state of the heat-exchange surface may affect considerably the character of temperature pulsations in the wall. In certain experiments, the character of wall temperature pulsations differed considerably from the pulsations show in Figs. 1, a and b. In these experiments, low-frequency small-amplitude pulsations were observed most of the time. Along with this, there were large temperature splashes of up to 60°C (Fig. 2a) and changes in the operating temperature conditions of the wall (Fig. 2b). It can be assumed that the cause of changes in the character of temperature pulsations is the unstable thermal contact resistance at the wall-liquid interface. If there is contact resistance, it is necessary to check experimentally whether the random function describing the temperature pulsations in the wall is a steady-state function.

The results of our experiments indicate that, even under conditions of steady-state turbulent flow of the liquid, temperature pulsations arise in the pipe wall as a result of the disordered nature of turbulent flow. These pulsations are the cause of rapidly changing thermal stresses. The effect of the additional stresses on the operating efficiency of structures can apparently be considerable and must be taken into account in strength calculations. Such stresses are especially critical if there are microcracks, deep grooves, etc., which form stress raisers in the heat-releasing wall. Thus, in one of the experiments, a heat-exchanger pipe with thermocouples fitted in rectangular grooves failed after a short time (about 10 h). The temperature pulsations in this experiment attained values of ± 12-15°C. In the case of small temperature pulsations (± 1-2°C), such pipes remained in operation for a long period of time.

The results given in the present article are provisional. It is necessary to perform additional thorough investigations of the statistical characteristics of temperature pulsations in the walls of channels with different geometries for the cases of inside and outside flow over heat-releasing surfaces and for different states of these surfaces. Along with this, it is necessary to develop methods for calculating the thermal stresses arising under the action of temperature pulsations.

The authors hereby express their gratitude to A. I. Leipunskii for the discussion and useful advice.

LITERATURE CITED

1. V. I. Subbotin, V. E. Minashin, and E. I. Deniskin, Teplofizika Vysokikh Temperatur, 1, 238 (1963).
2. V. I. Subbotin et al. Report No. 378, submitted by the USSR at the Third International Conference on the Peaceful Uses of Atomic Energy, Geneva (1964).
3. V. I. Subbotin, M. Kh. Ibragimov, and M. N. Ivanovskii, Atomnaya Énergiya, 8, (1960), p. 254.
4. V. I. Subbotin, M. Kh. Ibragimov, and E. V. Nomofilov, Teploénergetika, No. 3 (1962), p. 64.
5. V. I. Subbotin et al., Teploenergetika, No. 2, (1965).
6. V. S. Pugachev, Theory of Random Functions and its Application to Automatic Control Problems [in Russian], Moscow, Gostekhizdat (1957).

Declassified and Approved For Release 2013/09/24 : CIA-RDP10-02196R000700010005-2

Declassified and Approved For Release 2013/09/24 : CIA-RDP10-02196R000700010005-2

EXPERIMENTAL INVESTIGATION OF THE THERMAL CONDITIONS OF FUEL ELEMENTS IN THE VVR-M REACTOR

I. F. Barchuk, M. M. Nazarchuk, S. S. Ogorodnik,
D. T. Pilipets, and S. O. Slesarevskii

Translated from Atomnaya Énergiya, Vol. 18, No. 5,
pp. 528-529, May, 1965
Original article submitted March 24, 1964

The surface temperature of fuel elements was measured for determining the optimum cooling conditions for the core of the VVR-M reactor [1] in operation at different power levels and also for determining the capacity margin of the existing cooling system.

Its known that the neutron distribution in the core of the VVR-M reactor is not uniform [2]. Consequently, the thermal stresses state of fuel elements is not the same at various locations in the core. The determination of the optimum cooling conditions is of great importance for assessing the possibility of forcing the reactor power [3].

The aims of our measurements were the following:

1) Investigation of the distribution of the surface temperature of fuel elements along the height and the radius of the core;

2) determination of the effect of control rods on this distribution;

3) determination of the optimum values of the coolant discharge.

In order to perform the above complex of measurements, Chromel-Alumel or Chromel-Copel thermocouples with a diameter of 0.5-0.1 mm were fixed on the fuel element surfaces along the generatrices of all the tubes. The small thickness of the fuel element jackets (0.7 mm) caused certain difficulties in fastening the hot junction of thermocouples. The well-known

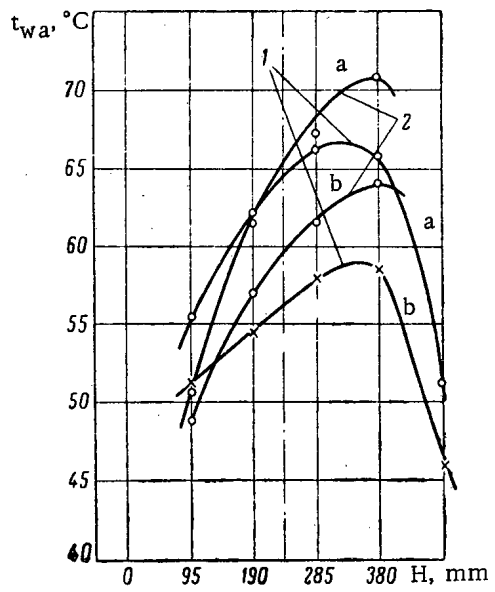

Fig. 1. Distribution along the height of the surface temperature t_{wa} of fuel elements in dependence on the position of the control rod in the neighboring cell for a reactor power level of 2 MW. 1) Temperature of the fuel element's surface facing the control rod; 2) temperature of the fuel element's surface farthest removed from the rod: a) with the rod removed from the core; b) with the rod introduced in the core.

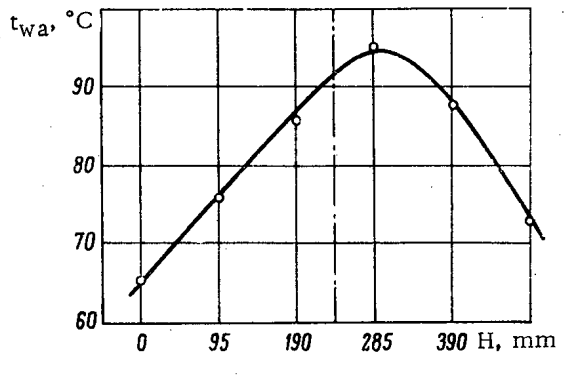

Fig. 2. Distribution along the height of the surface temperature t_{wa} of fuel elements at a reactor power level of 12 MW for a coolant discharge of 1300 m^3/h.

Declassified and Approved For Release 2013/09/24 : CIA-RDP10-02196R000700010005-2

Declassified and Approved For Release 2013/09/24 : CIA-RDP10-02196R000700010005-2

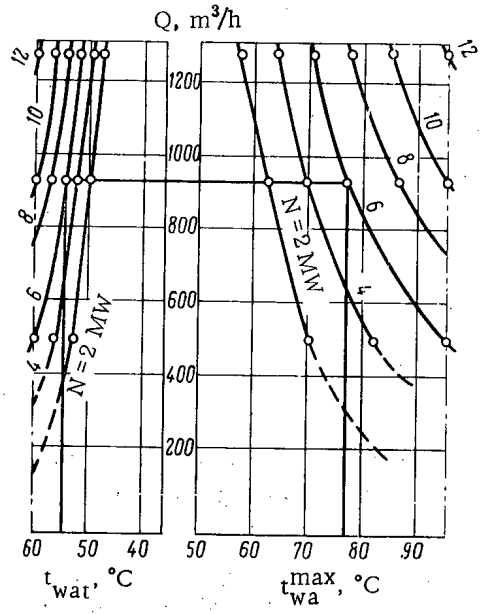

Fig. 3. Dependence of the maximum surface temperature (t_{wa}^{max}) of fuel elements and of the water temperature (t_{wat}) at the outlet from the channels on the coolant discharge Q and the reactor power level N.

method of wedging in could not be used as there was danger of damaging the fuel element. Therefore aluminum cover plates with a thickness of 0.15 mm, which were fastened on the surfaces of the fuel elements by spotwelding or by means of a condenser welding machine, were used for fastening the thermocouples. This method of fastening secured reliable contact between the thermocouple and the element's surface, while the good thermal conductivity and the small thickness of the aluminum cover plates prevented any noticeable effect of this arrangement on the measured temperature. Before they were installed in the reactor, the thermocouples were calibrated in the range from 20 to 100°C. This operation was necessitated by the fact that the technological process used for preparing the thermocouples was not uniform.

The object of the first series of measurements was a investigation of the temperature conditions of fuel elements which are located in the reactor core near the water-filled cavity, the beryllium reflector, and the control rods. Experiments have shown that the difference between the surface temperatures of the elements on the side of the cavity and on the side of the core is negligible. The position of the control rods exerts a considerable influence on the fuel element temperature (Fig. 1). It has been found that the fuel element temperature on the side of the control rod is lower than the temperature of the element's opposite surface even when the rod has been withdrawn.

Measurements have shown that the core region under the greatest thermal stress is located at the core periphery near the beryllium reflector. In connection with this, in choosing the optimum coolant discharge values and determining the maximum reactor power, the measurements were performed in the peripheral layer of the core. The aim of the measurements was to raise the reactor power to a level corresponding to the maximum surface temperature of the fuel elements (95°C) for the assigned coolant discharge through the core. For coolant discharges of 530, 960, and 1300 m^3/h, the maximum reactor power was equal to 6, 10, and 12 MW, respectively. In this, the temperature of the cooling water at the outlet from the core was equal to 60-62°C. Fig. 2 shows the distribution along the height of the surface temperature of fuel elements for a reactor power level of 12 MW and a coolant discharge of 1300 m^3/h.

A nomogram of the reactor's optimum operating conditions (Fig. 3) was plotted on the basis of the result obtained in measuring the temperature conditions of fuel elements. As a result of the investigations performed, it was found that the cooling system of the VVR-M reactor has a sufficiently large margin for reliable reactor operation at a power level of 12 MW.

LITERATURE CITED

1. V. V. Goncharov et al, In the book: Transactions of the Second International Conference on the Peaceful Uses of Atomic Energy. Reports by Soviet Scientists [in Russian], 2, Moscow, Atomizdat, (1959), p. 243.
2. M. V. Pasechnik, I. F. Barchuk, and V. B. Klimentov, Ukr. Fiz. Zh., 7, 3 (1962).
3. V. Byshevski, E. Aleksandrovich, and L. Lablo. Nukleonika, 5, 727 (1960).

Declassified and Approved For Release 2013/09/24 : CIA-RDP10-02196R000700010005-2

Declassified and Approved For Release 2013/09/24 : CIA-RDP10-02196R000700010005-2

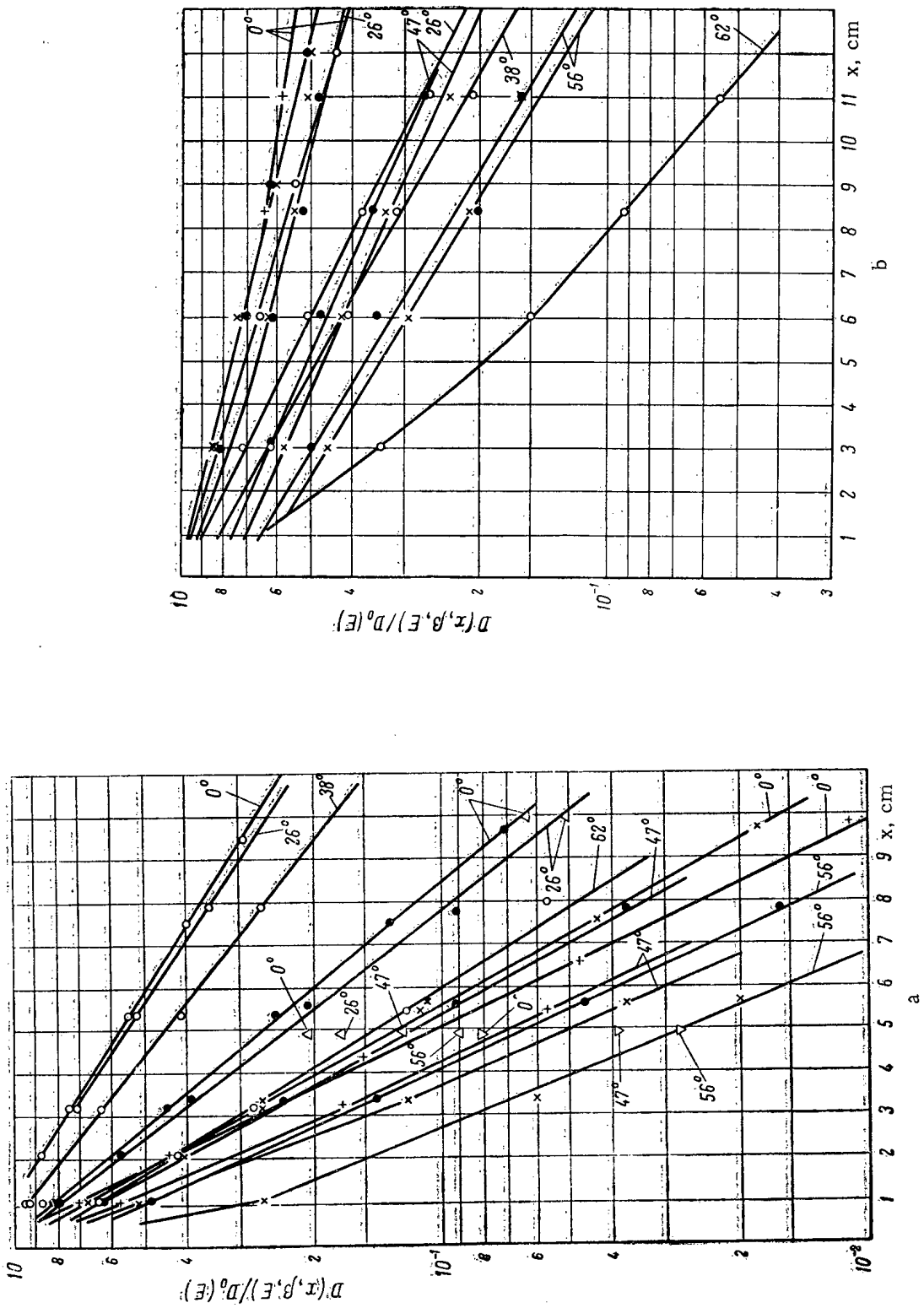

Attenuation of tissue dose rate, $\frac{D(x, \beta, E)}{D_0(E)}$, by (a) polyethylene and (b) iron, plotted versus the normal layer thickness x, for various angles of incidence of monoenergetic neutrons at an obstacle, the energies being: ○ 3 MeV; ● 0.83 MeV; × 0.22 MeV; + 24 keV; △ 1 MeV [5]; ▽ 0.3 MeV [5].

Declassified and Approved For Release 2013/09/24 : CIA-RDP10-02196R000700010005-2

Declassified and Approved For Release 2013/09/24 : CIA-RDP10-02196R000700010005-2

Dose Relaxation Length L_g and Coefficients C_g for Iron and Polyethylene for Various Angles of Incidence and Neutron Energies

Angle of incidence, deg	Iron							
	3 MeV			0.83 MeV			0.22 MeV	
	C_g (experiment)	C_g (calculated)	L_g, cm (experiment)	C_g, (experiment)	C_g (calculated)	L_g, cm (experiment)	C_g (experiment)	L_g, cm (experiment)
0	1.00±0.03	1.0	14.2±0.3	1.00±0.05	1.0	19.0±0.4	1.00±0.05	19.0±0.3
26	1.00±0.03	0.90	8.4±0.2	0.88±0.06	0.90	18.0±0.3	0.88±0.05	18.0±0.3
38	0.93±0.04	0.79	7.4±0.3	—	0.79	—	—	—
47	—	0.68	—	0.85±0.06	0.68	9.3±0.5	0.80±0.04	9.3±0.5
56	—	0.56	—	0.73±0.04	0.56	7.3±0.4	0.69±0.04	7.3±0.4
62	0.47±0.03	0.47	5.1±0.3	—	0.47	—	—	—

Angle of incidence, deg	Iron			Polyethylene								
	24 keV			3 MeV				0.83 MeV				
	C_g (experiment)	C_g (experiment)	L_g, cm (experiment)	C_g (experiment)	C_g (calculated)	L_g, cm (experiment)	L_g, cm (calculated)	C_g, cm (experiment)	C_g (calculated)	L_g, cm (experiment)	L_g, cm (calculated)	
0	0.83±0.03	0.83	27±1	1.30±0.04	1.30	6.4±0.2	6.4	1.10±0.04	1.10	3.4±0.1	3.4	
26	—	0.75	—	1.25±0.04	1.17	6.3±0.2	5.8	1.10±0.06	0.99	3.15±0.07	3.06	
38	—	0.66	—	1.17±0.05	1.03	5.2±0.3	5.1	—	0.87	—	2.7	
47	0.75±0.05	0.56	11.0±0.5	—	0.88	—	4.4	1.00±0.05	0.75	2.3±0.07	2.3	
56	—	0.47	—	—	0.73	—	3.6	0.83±0.05	0.62	2.0±0.1	1.9	
62	—	0.39	—	0.85±0.04	0.61	2.9±0.15	3.0	—	0.52	—	1.6	

Angle of incidence, deg	Polyethylene					
	0.22 MeV			24 keV		
	C_g (experiment)	C_g (calculated)	L_g, cm (experiment)	C_g (experiment)	C_g (calculated)	L_g, cm (experiment)
0	1.1±0.04	1.1	2.3±0.05	1.33±0.06	1.33	2.0±0.1
26	1.1±0.1	0.99	2.2±0.12	—	1.2	—
38	—	0.87	—	—	1.05	—
47	0.78±0.08	0.75	1.9±0.1	0.89±0.05	0.91	2.0±0.15
56	0.49±0.05	0.62	1.8±0.1	—	0.74	—
62	—	0.52	—	—	0.62	—

Consequently, if in the above formula we measure the layer thickness x along the direction of the ray joining the source and detector (instead of along the normal), then the relaxation length will be independent of β. This shows that neutron reflection has only a small effect on L_{g0}, as reflection depends markedly on the angle of incidence [6]. We note that the albedo will fail to affect L_{g0} only in the case when it depends weakly on the layer thickness. In fact, with water (polyethylene) thicknesses more than 2-3 cm, the albedo scarcely changes for neutron energies ~ 0.9 MeV [6].

With polyethylene thicknesses more than 30-40 cm, the dose relaxation length will evidently not depend on β, provided that the layer thickness is taken along the normal, since the neutron spectrum is constant. In the intermediate thickness region ($\sim 10 \leq x \leq 30$-40 cm), the relaxation lengths for monoenergetic neutrons with energy 3-0.8 MeV should depend much more weakly on β than the cosine law. This confirms the data on the passage of 0.22 MeV and 24 keV neutrons through a polyethylene layer. For thicknesses 1-2 $\leq x \leq$ 6-10 cm, the relaxation length for $E_n = 0.22$ MeV depends only very weakly on β (intermediate thicknesses). For $E_n = 24$ keV and thicknesses more than about 4 cm, the dose relaxation length is independent of β, i.e., the spectrum is constant; the main process is neutron diffusion (diffusion length ~ 2 cm). For the distribution of neutrons in iron, L_g depends on β more strongly than the cosine law. This may be explained by the marked increase in neutron albedo with increase in iron layer thickness throughout the thickness range examined.

Declassified and Approved For Release 2013/09/24 : CIA-RDP10-02196R000700010005-2

Declassified and Approved For Release 2013/09/24 : CIA-RDP10-02196R000700010005-2

LITERATURE CITED

1. G. G. Gol'dshtein, Principles of Reactor Shielding [in Russian], Moscow., Gosatomizdat, (1961).
2. D. L. Broder, A. A. Kutuzov, and V. V. Levin. Inzh.-fiz. zh. , V, No. 47, (1962).
3. V. N. Avaev et al., Atomnaya énergiya , 15, 17 (1963).
4. I. B. Keirim-Marjus et al., Ibid., p. 386.
5. S. M. Ermakov, V. G. Zolotukhin, and É. E. Petrov, Ibid., p. 253.
6. T. Rockwell (ed.). Nuclear Reactor Shielding [in Russian translation], Moscow., Izd-vo inostr. Lit., (1958).

All abbreviations of periodicals in the above bibliography are letter-by-letter transliterations of the abbreviations as given in the original Russian journal. *Some or all of this periodical literature may well be available in English translation.* A complete list of the cover-to-cover English translations appears at the back of this issue.

Declassified and Approved For Release 2013/09/24 : CIA-RDP10-02196R000700010005-2

Declassified and Approved For Release 2013/09/24 : CIA-RDP10-02196R000700010005-2

ATTENUATION OF NEUTRON TISSUE DOSE BY THIN LAYERS OF HYDROGENOUS MATERIALS

(UDC 539.125.52)

G. V. Miroshnikov

Translated from Atomnaya Energiya, Vol. 18, No. 5,
pp. 532-535, May, 1965
Original article submitted May 4, 1964

At the present time a semi-empirical method involving removal cross sections Σ_r is in wide use for calculating neutron shielding. The applicability of this method is restricted to the case of thick shielding layers, where a certain dynamical equilibrium in the energy distribution of neutrons can be effected. For example, in dosimeter measurements of neutron tissue dose between a metal–water shield, the thickness of the water at which the dose relaxation length will begin to coincide with the value of $1/\Sigma_r$ is not below 25-30 cm [1]. At lesser thicknesses, the use of Σ_r will lead to significant error. In that case we have to resort to the device of decreasing the removal cross section values, as we see from Table 1, where values of $1/\Sigma_r$ are listed [2, 3], and dose relaxation lengths L_{dose} based on experimental findings by the authors are included.

The shielding properties of these materials were studied with the aid of monoenergetic neutrons produced by the reactions

$$D^2(d, n)He^3\ (E_n = 3\ \ Mэв);\quad T^3(d, n)He^4\ (E_n = 15\ \ Mэв),$$

and by the photoneutron sources:

$$Sb^{124}(\gamma) + Be^9\ (E_n = 24\ \ кэв);\quad Na^{24}(\gamma) + D^2\ (E_n = 0{,}22\ \ Mэв);\quad Na^{24}(\gamma) + Be^9\ (E_n = 0{,}83\ \ Mэв).$$

The neutron tissue dose was measured by the following types of dosimeters: a dosimeter using an ionization chamber with polyethylene walls and ethylene filling [4], the RUS-5 dosimeter, and the all-wavelength radiometer [5].

The neutron ionization dosimeter consisted of two chambers (one of which had graphite walls and was argon-filled, the other polythene walls and was ethylene-filled), and were both compensated for γ radiation. The RUS-5 dosimeter was a paraffin sphere 30 cm in diameter with a concentrically placed cadmium sphere 15 cm in diameter enclosed within it. The all-wavelength radiometer was a polyethylene sphere 21 cm in diameter. Slow-neutron detectors were placed at the centers of the spherical moderator blocks in both instruments of spherical design.

TABLE 1. Tables of Dose Relaxation Length L_{dose} and of $1/\Sigma_r$ [2, 3]

Neutron energy, MeV	3	4	15	
Data source	This article	[2, 3]	[2, 3]	This article
Shield thickness, cm:				
water	7.6	5 29	13.2	18.4
polythene	6.4	5.5	13.9	18.4

The ionization dosimeter was employed to measure the maximum tissue dose of neutrons beyond the shielding, where the initial neutron energy was 15 MeV. The maximum and tissue-average neutron doses for neutrons of energies 3 MeV, 0.83 MeV, 0.22 MeV, were measured by the RUS-5 dosimeter. In that case the effectiveness curves of the instruments fit well on the "dose" curve plotted from the data in [6]. The all-wavelength radiometer was used for measurements of maximum and tissue-average doses of neutrons of initial energy 24 keV which had penetrated beyond the shielding (below this

Declassified and Approved For Release 2013/09/24 : CIA-RDP10-02196R000700010005-2

Declassified and Approved For Release 2013/09/24 : CIA-RDP10-02196R000700010005-2

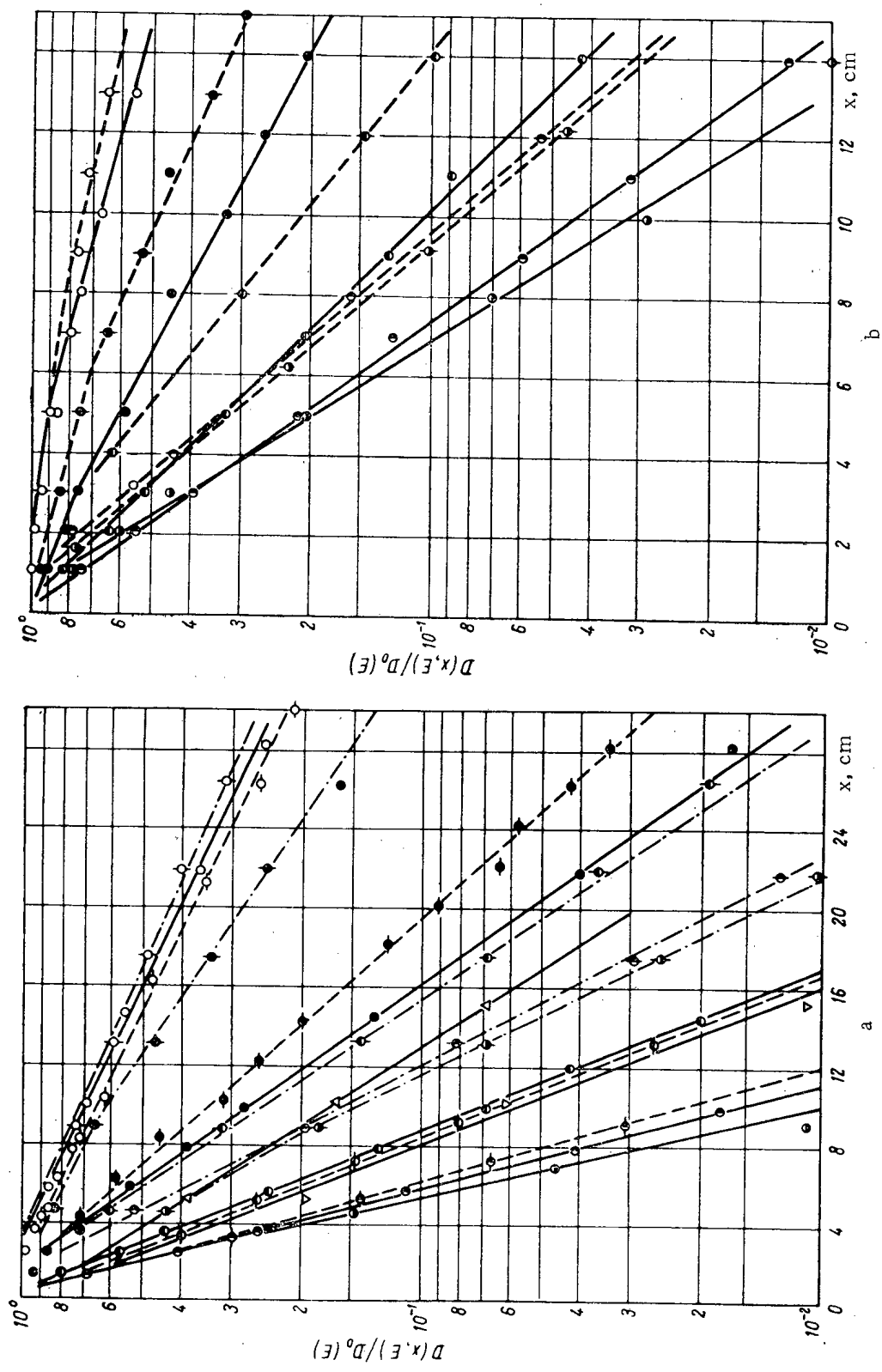

Attenuation of tissue does rate for neutrons (D(x, E) /D_0 (E) for neutrons of various media as a function of layer thickness x measured along the normal; a) ——— polyethylene; – – – – – water; –·–·–·– glass-reinforced plastic; b) ——— plexiglas; – – – – polychlorovinyl; ◑ – 24 keV; ◑ – 0.22 MeV; ● – 0.83 MeV; ▽ – 1 MeV [7]; △ – 2 MeV [7]; ⊘ – 3 MeV; ○ – 15 MeV.

Declassified and Approved For Release 2013/09/24 : CIA-RDP10-02196R000700010005-2

Declassified and Approved For Release 2013/09/24 : CIA-RDP10-02196R000700010005-2

TABLE 2. Ultimate analysis of epoxy-base glass-fiber reinforced plastics

Element	H	C	O	Si	B	Ca	Al	Mg	Na
Number atoms per cm^3, $\times 10^{-22}$	2.95	2.29	2.54	0.55	0.171	0.175	0.169	0.061	0.04

TABLE 3. Experimental Values of L_{dose} (cm) and c_{dose} for Various Elements

Neutron energy, MeV	Polyethylene		Glass-reinforced plastic		Water		Polychlorovinyl		Plexiglas	
	L_{dose}	c_{dose}	L_{dose}	c_{dose}	L_{dose}	c_{dose}	L_{dose}	c_{dose}	L_{dose}	c_{dose}
15	18.4±0.4	1.18±0.02	20.0±0.4	1.18±0.02	18.4±0.4	1.10±0.03	19.2±0.4	1.30±0.03	17.5±0.3	1.15±0.03
3	6.4±0.2	1.30±0.04	13.0±0.4	1.30±0.05	7.6±0.15	1.20±0.04	9.7±0.2	1.35±0.04	8.3±0.16	1.10±0.02
0.83	3.4±0.1	1.10±0.04	6.0±0.1	1.25±0.04	3.40±0.07	1.00±0.05	5.5±0.1	1.30±0.04	4.20±0.1	1.05±0.03
0.22	2.30±0.05	1.10±0.04	4.60±0.1	1.3±0.05	2.61±0.07	1.00±0.05	3.85±0.07	1.28±0.03	3.20±0.06	1.00±0.3
0.24	2.00±0.10	1.33±0.06	4.40±0.16	1.3±0.04	—	—	3.80±0.08	1.20±0.04	2.80±0.05	1.25±0.04

energy, the dose per single neutron and the radiometer effectiveness depend only slightly on energy and are similar to each other in slope plotted).

Measurements were performed in barrier geometry. The materials investigated (slabs dimensioned 1000 by 1000 by 10 mm) were placed at distances of 2 meters from the neutron sources. Close-to-normal neutron drops took place across the barrier. The dosimeters were placed on the far side of the slabs and flush up to them. The following hydrogenous materials were investigated: water (H_2O) d = 1 g/cm³; polyethylene $(CH_2)_n$ d = 0.0.93 g/cm³; plexiglas $(C_5H_8O_2)$ d = 1.2 g/cm³; polychlorovinyl laminates (C_2H_3Cl) d = 1.6 g/cm³; epoxy-base glass-fiber reinforced plastic d = 1.7 g/cm³ (Table 2). The statistical error in the attenuation measurements remained with ~3%.

The results of these measurements are depicted in the diagram, and results of calculations (by the Monte Carlo method [7]) of neutron-dose attenuation by polyethylene layers are plotted in the same diagram. Experimental and theoretically predicted dose attentuation curves display an approximately exponential slope and fit will both in slope and in the relative positions of the curves. As we see from the diagram, the dose attenuation curves may be presented, after a small interval is skipped, in the form

$$\frac{D(x, E)}{D_0(E)} = c_{dose} e^{-\left(\frac{x}{L_{dose}(E)}\right)}$$

where D(x, E) and $D_0(E)$ are the neutron dose rates beyond a shield of thickness x and in the absence of shielding, respectively, c_{dose} is a quantity close to unity; $L_{dose}(E)$ is the relaxation length of the neutron dose. Experimental values of L_{dose} and c_{dose} for all the materials investigated as a function of neutron energy are listed in Table 3.

As we know, the spectrum for neutrons of energies 3 MeV and 15 MeV is a nonequilibrium spectrum at low shield thicknesses (less than 30 to 40 cm), so that the dose relaxation length must decline monotonically with increased thickness, the former tending to the value of $1/\Sigma_r$ at great thicknesses.

From the Monte Carlo finding [7, 8], however, as well as from experimental data (see diagram), the dose relaxation length in the range of thicknesses from 4-8 cm to 20-30 cm will depend only slightly on thickness and may be assumed constant to an error

Declassified and Approved For Release 2013/09/24 : CIA-RDP10-02196R000700010005-2

Declassified and Approved For Release 2013/09/24 : CIA-RDP10-02196R000700010005-2

TABLE 4. Relaxation Lengths L_{dose} (E_n = 24 keV) and Diffusion Lengths L of Thermal Neutrons

Medium.....	Polyethylene	Plexiglas	Water	Polychlorovinyl	Glass-fiber reinforced plastics
L, cm	2.12±0.07	2.9±0.15	2.86±0.06	0.67±0.07	$\frac{1}{\Sigma_a}$=0.75 *
L_{dose}, cm ...	2.00±0.06	2.80±0.05	2.61±0.07 (E_n=0.22 MeV)	3.80±0.08	4.40±0.16

*Σ_a is the macroscopic absorption cross section for thermal neutrons.

not exceeding 3 to 5% (cf. Table 3). As we realize from Table 1, the dose relaxation length is roughly 40% greater than $1/\Sigma_r$ for E_n = 15 MeV, and 15-20% greater than $1/\Sigma_r$ for E_n = 3 MeV. In the latter case, consequently, the spectrum is closer to the equilibrium spectrum over the thickness range in question.

In the case of neutrons of 0.8 MeV energy, the difference in dose relaxation length deviating from the value of $1/\Sigma_r$ will probably be less, since the neutron spectrum in this instance leads to an equilibrium state at lesser thicknesses.

Experimentally derived dose relaxation lengths for neutrons of initial energies 0.22 and 0.024 MeV are not commensurate with values of $1/\Sigma_r$, since the semi-empirical method of removal cross sections is applicable only to the case of fast neutrons [9].

A comparison of the dose relaxation length at E_n = 24 keV and diffusion lengths (Table 4) is in order.

Values of the transport cross section for hydrogen (32.7 ± 1.0 barn) in hydrogenous substances [10] were used in the diffusion length calculations.

Excellent agreement between dose relaxation lengths and diffusion lengths was observed in the case of water, polyethylene, and plexiglas. Neutron-dose attenuation in these materials is therefore primarily due to neutron diffusion. This is to be expected therefore, considering $\tau \ll L^2$ (τ is the neutron age), and after a certain small thickness the thermal flux (Φ_T) satisfies the solution of the diffusion equation

$$\Phi_T = ce^{-\frac{x}{L}}$$

In the case of polychlorovinyl and glass-fiber reinforced plastic laminates $\tau \gg L^2$, so that the thermal flux will satisfy the solution of the age equation. The dose relaxation length will depend mostly, in this case, on the moderating properties of the medium, and will not coincide with diffusion length in this instance.

LITERATURE CITED

1. B. I. Sinitsyn and S. G. Tsypin, In the collection "Advances in reactor shielding physics," edited by D. L. Broder et al., Moscow, State atom press, [in Russian], (1963), p. 75.
2. D. L. Broder, Proc. of the Geneva 1958 conference on the peaceful uses of atomic energy.
3. D. L. Broder, A. A. Kutuzov, and V. V. Levin, Inzhener.-fiz. zhur., 5, No. 2, 47 (1962).
4. G. Hurst. Brit. J. Radiol., 27, 353 (1954).
5. I. B. Keirim-Markus et al. Atomnaya énergiya, 15, 386 (1963).
6. W. Snayder and J. Neufeld, Brit. J. Radiol., 28, 342 (1955).
7. S. M. Ermakov, V. G. Zolotukhin, and E. E. Petrov, Atomnaya énergiya, 15, 253 (1963).
8. Nuclear reactor shielding. [Russian translation of "Reactor shielding design manual]. Moscow, Foreign lit. press, (1958), p. 112.
9. B. Price, C. Horton, and K. Spinney, Radiation shielding. edited by S. G. Tsypin. Moscow, Foreign lit. press, [Russian translation], (1959), p. 262.
10. L. N. Yurova et al. In symposium "Neutron physics," edited by P. A. Krupchitskii, Moscow, State atom press, [in Russian], (1961), p. 193.

Declassified and Approved For Release 2013/09/24 : CIA-RDP10-02196R000700010005-2

Declassified and Approved For Release 2013/09/24 : CIA-RDP10-02196R000700010005-2

FRACTIONATION OF RADIOACTIVE ISOTOPES IN HOT PARTICLES

(UDC 551.577.7)

Ya. I. Gaziev, S. G. Malakhov, and L. E. Nazarov

Translated from Atomnaya Énergiya, Vol. 18, No. 5,
pp. 535-537, May, 1965
Original article submitted April 20, 1964

The fission products formed as a result of nuclear explosions are distributed nonuniformly in radioactive particles, depending on their dimensions [1, 2]. This phenomenon produces the so-called fractionation. The hypothesis has been expressed [3] that the activity of refractory isotopes is distributed proportionally to the cube of the radius of the radioactive particles, and for volatile isotopes proportionally to the square of the radius.* It has also been shown that the β-activity of hot aerosol particles with identical growth depends on their dimensions [4]. Hence, it would be expected that there is a relationship between fractionation of radioactive isotopes in hot particles and their β-activity

From September to December 1962 we carried out investigations at Podmoskova into the special features of the distribution of Ce^{141}, Ru^{103} and $Zr^{95} + Nb^{95}$ in hot particles of different activity. Samples of radioactive aerosols were collected from near the earth's surface by means of air-sampling filter equipment and at an altitude of 5000 m by means of FPP-15 filters in an airplane. After autoradiography the samples were stripped from the filter and the magnitude of their β-activity A was determined by means of an end-window counter with an error not exceeding 25%. All the hot particles which were removed were grouped according to their β-activity, after which the $Ce^{141} + Ce^{144}$, Ru^{103} and $Zr^{95} + Nb^{95}$ contents were determined in each group of particles by the γ-spectrometer method. The error in measuring the Ru^{103} content in the aerosol samples and particles did not exceed ± 20%, and that for Ce^{141}, Ce^{144}, and $Zr^{95} + Nb^{95}$ did not exceed ± 10%. The maximum errors in determining the activity ratios, the results of which are given in the table, were ± 15% for $\frac{A(Zr^{95} + Nb^{95})}{A(Ce^{141} + Ce^{144})}$, ± 25% for $\frac{A(Zr^{95} + Nb^{95}}{A\ (Ru^{103})}$ and $\frac{A(Ru^{103})}{A(Ce^{141})}$. For comparison, the table also shows the corresponding ratios for all the aerosol samples from which the hot particles were removed.

*More correctly, one should say here isotopes having high and low oxide condensation temperatures.

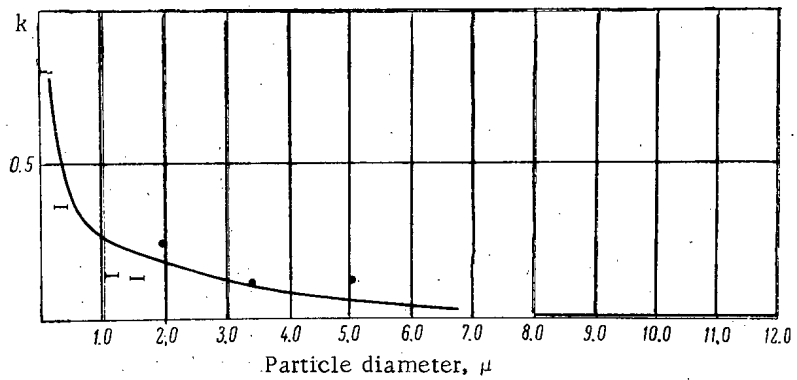

Fractionation of Ru^{103} relative to Ce^{141} in hot particles (according to data from [1, 2]): ●) Data for a single particle; ⊢⊣) Average data for an aggregate of particles.

Declassified and Approved For Release 2013/09/24 : CIA-RDP10-02196R000700010005-2

Declassified and Approved For Release 2013/09/24 : CIA-RDP10-02196R000700010005-2

No. of particle	Activity of particle, 10^{-11} Ci	Hot particles			Integral aerosol sample			$\Phi\left(\frac{Zr^{95}+Nb^{95}}{Ce^{141}+Ce^{144}}\right)$	$\Phi\left(\frac{Zr^{95}+Nb^{95}}{Ru^{103}}\right)$
		$\frac{A(Zr^{95}+Nb^{95})}{A(Ce^{141}+Ce^{144})}$	$\frac{A(Ru^{103})}{A(Ce^{141})}$	$\frac{A(Zr^{95}+Nb^{95})}{A(Ru^{103})}$	$\frac{A(Zr^{95}+Nb^{95})}{A(Ce^{141}+Ce^{144})}$	$\frac{A(Ru^{103})}{A(Ce^{141})}$	$\frac{A(Zr^{95}+Nb^{95})}{A(Ru^{103})}$		
32	1—5	1	0.6	2	0.7	1.1	1.1	1.4	1.3
32	2—10	1.3	0.7	2.6	0.8	1.3	0.9	1.6	2.9
8	5—20	0.9	0.3	4.7	0.7	1.1	1.1	1.3	4.3
10	5—20	1.3	Not detected*	Not detected*	1.3	1.1	1.5	1	Not detected*
4	10—40	Not determined**	Not detected*	2.7	0.7	1	0.8	Not determined**	3.3
44	10—50	1	0.2	5	1.1	0.6	1.2	0.9	4.2
7	10—80	1.6	0.3	6	0.8	1.3	0.9	2	5.5
4	500—1600	2.5	0.1	10	2	0.7	1.5	1.2	6.7

*Ru^{103} not detected.

†Ce^{141} + Ce^{144} not determined.

The normal degree of fractionation of single isotopes retalive to others (for example, Ru^{103} relative to Zr^{95} + Nb^{95}) is defined by the coefficient f [1], which is defined as the product

$$f(\mathrm{Ru/Zr}) = \left[\frac{N(\mathrm{Ru^{103}})}{N(\mathrm{Zr^{95}+Nb^{95}})}\right]_{\mathrm{exp.}} \times \left[\frac{N(\mathrm{Zr^{95}+Nb^{95}})}{N(\mathrm{Ru^{103}})}\right]_{\mathrm{theor.}}$$

where N is the number of atoms, whose value is reduced to a fixed instant of the time (date of explosion, sample collection or measurement) of growth of the particles being considered. Since the determination of the particle growth is associated with considerable difficulties, we compared the ratio of the activities of isotope pairs in the hot particles and in the whole sample (filter), reduced to the date of their collection.

In this case the relative Ru^{103} fractionation relative to Zr^{95} + Nb^{95} is determined by the relationship

$$f'(\mathrm{Ru/Zr}) = \left[\frac{A(\mathrm{Ru^{103}})}{A(\mathrm{Zr^{95}+Nb^{95}})}\right]_{\mathrm{particle}} \times \left[\frac{A(\mathrm{Zr^{95}+Nb^{95}})}{A(\mathrm{Ru^{103}})}\right]_{\mathrm{filler}}$$

Under conditions of measuring global radioactive contamination, when the aerosol represents mixtures of the products from many explosions, f' differs from f. However, to a first approximation for the isotope pairs considered, this difference can be neglected, since their ratios are only slightly sensitive to a difference in their growths even over several weeks (f'(Zr/Ce) varies by a factor of two for a change of growth of two months).

Together with f', the reciprocal of its value Φ can be taken as a fractionation characteristic, and in certain cases it is more convenient in practice.

Data concerning fractionation in hot particles for Ru^{103} and Ce^{141} + Ce^{144} relative to Zr^{95} + Nb^{95} as a function of the β-activity of the particles is shown in the table in the form of values for the parameter Φ.

It can seen from the table that in particles is of order 10^{-10} Ci and above in many cases a deficiency of Ru^{103} and Ce^{141} + Ce^{144} relative to Zr^{95} + Nb^{95} is detected. There is particularly large deficiency of Ru^{103}. In particles with a higher level of β-activity the content of this isotope is insignificant in comparison with the Zr^{95} + Nb^{95}. For studying the fractionation of Ru^{103}, in addition to the

Declassified and Approved For Release 2013/09/24 : CIA-RDP10-02196R000700010005-2

Declassified and Approved For Release 2013/09/24 : CIA-RDP10-02196R000700010005-2

two methods discussed above for determining the coefficients of fractionation (f and f'), it is convenient to use the expression $k = \frac{A(Ru^{103})}{A(Ce^{141})}$ for hot particles as well as for integral samples of radioactive aerosols collected on the filter. In the initial period after fission of Pu^{239} and U^{238}, the values of $k = 1$; moreover, because of the closeness of the half-lives of Ru^{103} and Ce^{141}, k depends weakly on the growth of the radioactive aerosols. Thus, for example, an increase in k by a factor of two occurs only over 170 days after the formation or Ru^{103} and Ce^{141}. The latter fact is very important, since under conditions of fractionation of radioactive isotopes in hot particles and the intensive mixing of aerosols from different explosions and the separation of hot particles, it is extremely difficult to determine their growth reliably. This growth may also be different from the effective growth of the radioactive aerosols collected on a filter. We note also that Ce^{141} and Ru^{103} are measured relatively simply by γ-spectrometry methods.

The data obtained indicates that for filters $0.7 \leq k \leq 1.3$ and for hot particles $0 \leq k \leq 0.7$. These data refer to the period of frequent appearance of hot particles in the atmosphere, i.e., to the period when the nuclear tests were carried out. The diameter of the most active particles found is about 16-17 μ. It is interesting to note that f' (Ru/Zr) ≈ 0.15 and k (Ru/Ce) ≈ 0.1 represents as yet the maximum values among the literature data for particles with diameter $\geq 10\ \mu$ [2, 5]. By way of an additional illustration of the feasibility of the method, the dependence of the ratio A (Ru^{103})/A (Ce^{141}) on the diameter of the aerosol particles is shown in the figure, which we obtained by averaging the data from [1, 2]. The first portion of the graph relates to the 1959 measurements and the second portion to the 1961 measurements.

Fractionation of $Ce^{141} + Ce^{144}$ relative to $Zr^{95} + Nb^{95}$ in the majority of samples which we investigated was found to be insignificant. This is in accordance with [5], which is related to the tests carried out in 1962. In this paper it is shown that significant fractionation of $Ce^{141} + Ce^{144}$ relative to $Zr^{95} + Nb^{95}$ takes place only for high-activity coarse particles with a diameter of more than 8-10 μ (f = 0.6-0.3). With a reduction of the particle dimensions the value of f was reduced, and even for particles with a diameter of 7-8μ it was equal to 0.8-0.9. (The overwhelming portion of the particles which we investigated had dimensions of less than 5μ.)

LITERATURE CITED

1. K. Edvarson, K. Low, and J. Sisefsky, Nature, 184, 1771 (1959).
2. T. Mamuro et al. Nature, 197, 964 (1963).
3. E. Freiling, Radioactive fallout from nuclear weapons tests. 1 TiD-7632. Washington, (1962), p. 47.
4. Collection, "Radioactive particles in the atmosphere". Pod red. G. A. Sered. Moscow, Gosatomizdat, (1963).
5. T. Mamuro et al. Fractionation phenomena in highly fallout particles. Ann. Rept. Radiat. Center. Osaka, Prefect, No. 4, (1963), p. 9.

Declassified and Approved For Release 2013/09/24 : CIA-RDP10-02196R000700010005-2

Declassified and Approved For Release 2013/09/24 : CIA-RDP10-02196R000700010005-2

SCIENCE AND ENGINEERING NEWS

DUBNA AUGUST 1964 INTERNATIONAL CONFERENCE ON HIGH ENERGY PHYSICS

Translated from Atomnaya Énergiya, Vol. 18, No. 5,
pp. 538-543, May, 1965

The XII international conference on high-energy physics convened in August 1964 at the Joint Institute for Nuclear Research (in Dubna) to hear reports from delegations representing 30 nations throughout the world before an audience of over 500 physicists. Scientists from 120 or so physics institutes, universities, and from two of the world's largest scientific research center (JINR and CERN) submitted some 300-odd original papers on experimental and theoretical research in the physics of elementary particles and on the development of experimental research tecniques in high-energy physics. The main purpose of the conference was to discuss the latest results in the study of weak, electromagnetic, and strong interactions. A summary of the work accomplished in these domains may be found in the various tutorial survey papers presented.*

Weak Interactions. An intensive exchange of scientific information had been arranged which virtually excluded any possibility of unheralded or unexpected disclosures on the conference floor. Just the same, information on an extremely interesting research project by physicists at Princeton University (J. Cronin et al., USA) on the discovery of the decay mode $K_2^0 \rightarrow \pi^+ + \pi^-$ was made public for the first time at this conference. The existence of this mode of decay of the K_2^0-meson may be interpreted as an indication of nonconservation of CP-parity in weak interactions. It was established that the $K_2^0 \rightarrow \pi^+ + \pi^-$ decay takes place in $(2.0 \pm 0.4) \cdot 10^{-3}$ fraction of all decays by these mesons.

Some rather interesting experiments conducted by V. S. Evseev and associates (JINR) yielded a surprisingly high ($\approx 100\%$) asymmetry in the flight of high-energy neutrons appearing as a result of the capture of polarized μ^--mesons by Ca^{40} and S^{32} nuclei. This asymmetry might be explained in terms of a violation of CP-invariance. But the interpretation of this effect is obscured by the effect of nuclear forces in the reactions.

Work has progressed on the decay of μ- and π-mesons, on the capture of μ-mesons by nuclei, on leptonic decay of strange particles, and so forth, in laboratories throughout the world in the two years since the XI international conference, and the axial-vector variant in the theory of weak interactions as well as the hypothesis of $e = \mu$-universality in weak interactions have been confirmed. Further confirmation has been obtained for the hypothesis of conserved vector current; work on the decay $\pi^+ \rightarrow \pi^0 + e^+ + \nu$ was specifically described at the conference in a paper (CERN) reporting the relative rate of this process, $R_{exp} = (1.17 \pm 0.12) \cdot 10^{-8}$. The value fits closely predictions based on the hypothesis $R_{theor} = (1.00 \pm 0.02) \cdot 10^{-8}$.

An important stage in weak interactions research was reached in the discovery (Inst. Theoret. Exp. Physics, USSR) of the parity-changing internucleon potential as predicted by the theory of weak interactions. The asymmetry in the emission of gammas accompanying the capture of slow polarized neutrons by the nuclide Cd^{113}, measured by Yu. G. Abov, P. A. Krupchitskii, and Yu. I. Oratovskii, showed that the admixture of parity-nonconserving internucleon potential to the parity-conserving potential was $\approx 10^{-7}$; this value is in agreement with predictions based on universal weak interaction theory. A search is in order for the $(e\nu)$ $(e\nu)$-interaction predicted by this theory, using high-intensity neutrino flux from pulsed reactors as a tool.

New results of a neutrino experiment carried out on the CERN 30 GeV proton accelerator presented copious statistical material to confirm the existence of two types of neutrino: ν_e and ν_μ. The findings support the view that the muon leptonic charge is a good quantum number, along with negative results of searches for the decay modes $\mu \rightarrow e + \gamma$ and $\mu \rightarrow 3e$. Analysis of the neutrino experiment data in the context of the quest for the intermediate vector meson W have led to the conclusion that no such meson exists in the mass range $m_W < 1.6$ GeV.

*These will be published as JINR preprints.

Declassified and Approved For Release 2013/09/24 : CIA-RDP10-02196R000700010005-2

Declassified and Approved For Release 2013/09/24 : CIA-RDP10-02196R000700010005-2

Table of Fundamental Particles (Resonances Included)

Particle classification	Letter symbol	Rest mass, MeV/c^2	Lifetime (sec) or width (MeV)	Basic decay modes (relative probability, %)	Quantum numbers: spin J	space parity P	charge conjunction parity C	isotopic spin T	G-parity	strangeness S	baryon charge B	SU_3-group classification of hadrons
Photon	γ	0	Stable		1	−	−					
Leptons	$e^{\mp}$	0.511006±0.000002	Stable		1/2							
	ν_e	0 (<0.2 keV)	Stable		1/2							
	$\mu^{\pm}$	105.659±0.002	$(2.2001\pm0.0008)\cdot10^{-6}$ sec	$e^{\pm}+\nu_\mu+\nu_e$ (~100)	1/2							
	ν_μ	0 (<2.5 MeV)	Stable		1/2							
Hadrons / Mesons	π^0	135.01±0.05	$(1.80\pm0.29)\cdot10^{-16}$ sec	$\gamma+\gamma$ (98.7)	0	−	+	1/2	−	0	0	Unitary mesonic octet $J^P=0^-$.
	π^+, π^-	139.60±0.05	$(2.551\pm0.026)\cdot10^{-8}$ sec	$\mu^{\pm}+\nu_\mu$ (~100)	0	−		1	−	0	0	
	K^+	493.8±0.2	$(1.229\pm0.008)\cdot10^{-8}$ sec	$\mu^{+}+\nu$ (63), $\pi^{+}+\pi^0$ (21)	0	−		1/2		1	0	
	K^0	498.0±0.5	$\tau(K_1^0)=(0.92\pm0.02)\times10^{-10}$ sec	$K_1^0\to\pi^+\pi^-$ (69)	0	−		1/2		1	0	
	$\widetilde{K}^0$	498.0±0.5	$\tau(K_2^0)=(5.00\pm0.45)\times10^{-8}$ sec	$K_1^0\to\pi^0+\pi^0$ (31) $K_2^0\to\pi+e+\nu$ (34) $K_2^0\to\pi^0+\pi^0+\pi^0$ (27) $K_2^0\to\pi+\mu+\nu$ (27)	0	−		1/2		−1	0	
	K^-	493.8±0.2	$(1.229\pm0.008)\cdot10^{-8}$ sec	$\mu^{-}+\nu$ (63), $\pi^{-}+\pi^0$ (21)	0	−		1/2		−1	0	
	η	548.7±0.5	<10 MeV	$\gamma+\gamma$ (35), $\pi^{+}+\pi^0+\pi^-$ (27) $3\,\pi^0$, $\pi^0\gamma\gamma$ (32)	0	−	+	0	+	0	0	
	ϱ^0	763±4	106±5 MeV	$\pi+\pi$ (~100)	1	−	−	1	+	0	0	Unitary mesonic octet $J^P=1^-$ with admixture of unitary single $J^P=1^-$
	ϱ^+, ϱ^-	763±4	106±5 MeV	$\pi+\pi$ (~100)	1	−		1	+	0	0	
	K^{*+}	891±1	50±2 MeV	$\pi+K$ (~100)	1	−		1/2		1	0	
	K^{*0}	891±1	50±2 MeV	$\pi+K$ (~100)	1	−		1/2		1	0	
	$\widetilde{K}^{*0}$	891±1	50±2 MeV	$\pi+\widetilde{K}$ (~100)	1	−		1/2		−1	0	
	K^{*-}	891±1	50±2 MeV	$\pi+\widetilde{K}$ (~100)	1	−		1/2		−1	0	
	ω	782.8±0.5	9.4±1.7 MeV	$\pi^{+}+\pi^0+\pi^-$ (86), $\pi^0+\gamma$ (11)	1	−	−	0	−	0	0	
	φ	1019.5±0.3	3.1±0.6 MeV	$K_1^0+K_2^0$ (41), $K^{+}+K^-$ (59)	1	−	−	0	−	0	0	
	$(\eta 2\pi)^0$	957.5±2.5	<4 MeV	$\pi+\pi+\eta$ (~100)	0	−	+	0	+	0	0	?
	$A_1^{+,0,-}$	1090	125±25 MeV	$\pi+\varrho$ (~100)	2?	−?	A_1^{0}?	1	−	0	0	
	$A_2^{+,0,-}$	1310	80 MeV	$\pi+\varrho$ (~70), $K+\widetilde{K}$ (~30)	2	+	A_2^{0}+	1	−	0	0	
	$B^{+,\,-}$	1215±18	122±17 MeV	$\pi+\omega$ (~100)	1?	+?	B^{0}−	1	+	0	0	
	f^0	1253±20	100±25 MeV	$\pi+\pi$ (~100)	2	+	+	0	+	0	0	

Declassified and Approved For Release 2013/09/24 : CIA-RDP10-02196R000700010005-2

Declassified and Approved For Release 2013/09/24 : CIA-RDP10-02196R000700010005-2

(Cont.)

Particle classification	Letter symbol	Rest mass, MeV/c²	Lifetime (sec) or width (MeV)	Basic decay modes (relative probability, %)	Quantum numbers: spin J	space parity P	charge conjuction parity C	isotopic spin T	G-parity	strangeness S	baryon charge B	SU₃-group classification of hadrons
Hadrons												
Baryons **	p	988.256±0.005	Stable		1/2	+		1/2		0	1	Unitary baryonic octet $J^P = 1/2^+$.
	n	939.550±0.005	(1.01±0.3)·10³ sec	$p+e^-+\nu$ (100)	1/2	+		1/2		0	1	
	Λ	1115.40+0.11	(2.62±0.02)·10⁻¹⁰ sec	π^-+p (68), π^0+n (31)	1/2	+		0		−1	1	
	Σ^+	1189.41±0.14	(0.788±0.027)·10⁻¹⁰ sec	π^0+p (51), $\pi^+ + n$ (49)	1/2	+		1		−1	1	
	Σ^0	1192.4±0.3	<1.0·20⁻¹⁴ sec	$\gamma+\Lambda$ (100)	1/2	+		1		−1	1	
	Σ^-	1197.08±0.19	(1.58±0.05)·10⁻¹⁰ sec	π^-+n (~100)	1/2	+		1		−1	1	
	Ξ^0	1314.3±1.0	(3.06±0.40)·10⁻¹⁰ sec	$\pi^0+\Lambda$ (100)	1/2	+		1/2		−2	1	
	Ξ^-	1320.8±0.2	(1.74±0.05)·10⁻¹⁰ sec	$\pi^-+\Lambda$ (100)	1/2	+		1/2		−2	1	
	$N^*_{3/2}$	1236±2	125 MeV	$\pi+N$ (100)	3/2	+		3/2		0	1	Unitary baryonic decuplet $J^P = 3/2^+$ (N^{*++}, N^{*+}, N^{*0}, N^{*-}, Y^{*+}, Y^{*0}, Y^{*-}, Ξ^{*0}, Ξ^{*-}, Ω^-)
	Y^*_1	1382±1	53±3 MeV	$\pi+\Lambda$ (96)	3/2	+		1		−1	1	
	Ξ^*	1529±1	7.5±1.7 MeV	$\pi+\Xi$ (100)	3/2	+		1/2		−2	1	
	Ω^-	1675±3	0.7·10⁻¹⁰ sec	$\pi+\Xi$ (?), $K+\Lambda$ (?)	3/2?	+?		0		−3	1	
	$N^*_{1/2}$	1518±10	125±12 MeV	$\pi+N$ (80)	3/2	−		1/2		0	1	?
	$N^*_{1/2}$	1688	100 MeV	$\pi+N$ (80)	5/2	+		1/2		0	1	
	$N^*_{1/2}$	2190	200 MeV	$\pi+N$ (30), $K+\Lambda$ (?)	9/2?	+?		1/2		0	1	
	$N^*_{3/2}$	1924	170 MeV	$\pi+N$ (34), $K+\Sigma$ (?)	7/2	+		3/2		0	1	
	$N^*_{3/2}$	2360	200 MeV	$\pi+N$ (10)	11/2?	+?		3/2		0	1	
	Y^*_0	1405	50 MeV	$\pi+\Sigma$ (~100)	1/2?	−?		0		−1	1	
	Y^*_0	1519±1.5	16±2 MeV	$\pi+\Sigma$ (55), $\widetilde{K}+N$ (29)	3/2	−		0		−1	1	
	Y^*_0	1815	70 MeV	$\widetilde{K}+N$ (80)	5/2	+?		0		−1	1	
	Y^*_1	1660±10	44±5 MeV	$\pi+\Sigma$ (31), $\pi+\pi+\Sigma$ (27), $\pi+\Lambda$ (21)	3/2	−		1		−1	1	

* $K_1^0 = \frac{1}{\sqrt{2}}\left(K^0 + \widetilde{K}^0\right)$, $K_2^0 = \frac{1}{\sqrt{2}}\left(K^0 - \widetilde{K}^0\right)$; here K is the symbol of the K – meson wave function.

** For antibaryons, the quantum number B is −1, and the strangeness, electric charge, and magnetic moment are opposite to the strangeness, charge, and magnetic moment of baryons.

Declassified and Approved For Release 2013/09/24 : CIA-RDP10-02196R000700010005-2

Declassified and Approved For Release 2013/09/24 : CIA-RDP10-02196R000700010005-2

Experiments designed to study the reactions $\nu_\mu + n \rightarrow p + \mu^-$ yielded the axial and vectorial form factors of weak interactions F_A and F_V. The F_V values obtained are in satisfactory agreement with the values of nucleon electromagnetic form factors, thereby confirming the hypothesis of conserved vector current. New calculations of the spectrum of nuonic neutrinos (CERN) have eliminated the problem of a disquietingly intense increase, with energy, in the cross sections of inelastic processes of the type $\nu_\mu + N \rightarrow N + \mu + \pi$, etc. in response to neutrinos.

A wealth of experimental data was presented at the conference on decays of strange particles, particularly Kaons (see table). The investigation of three-particle leptonic decays of K-mesons (and particularly the K_{e3}-decays studied by Soviet physicists) clearly indicated that these decays are described by the vector variant of the interaction. The selection rules: $\Delta S = 1$ and $|\Delta T| = 1/2$ for nonleptonic decays, and $\Delta S = 1$, $|\Delta T| = 1/2$, $\Delta Q = \Delta S$ for leptonic decays of strange particles were established with a reasonable degree of certainty in some papers. The $\Delta Q = \Delta S$ selection rule had been seriously questioned by papers submitted to the previous conference. Any such doubts have put aside by now, since the amplitude ratio $\frac{A(\Delta Q = -\Delta S)}{A(\Delta Q = \Delta S)} < 0.1$ has been demonstrated (USA, France, CERN). The $|\Delta T| = 1/2$ selection rule has been arrived at with approximately the same level of precision.

These selection rules found a natural explanation in the propagation of the unitary symmetry concept in weak interactions (N. Cabibbo, Italy). A paper by M. Ademollo and R. Gatto (Italy) showed that the relationships for vector current of singularly interacting particles inferred from this symmetry are not distorted by medium-strong interactions breaking this symmetry.

Strong Interactions. Close attention was paid to the systematics of strongly interacting particles (hadrons) in the light of the SU_3 group. A Salam (Britain) summarized this research in a tutorial review paper demonstrating a successful application of the SU_3 group concept in predicting the recently discovered hyperon Ω^-, in the derivation of relationships between particle masses, in predictions of resonance widths, and so forth. The report reviewed composite models of elementary particles, dynamical approaches to SU_3 symmetry fundamentals, and problems in extending this symmetry. These questions are of cardinal significance in view of the prediction by the SU_3 group concept of particles of fractional electric and baryonic charge ("quarks"), searches for which have been futile to date in the mass range to 4 GeV. The enlargement of the SU_3 group to the SU_4 group would get around the difficulty of fractional charges at the cost of introducing a new additive quantum number, the supercharge* C (or "charm") quantum number, which is assigned the value zero for the elementary particles currently known to us. A report by M. Gell-Mann (USA) discussed the properties of hypothetical particles possessing supercharge. If C is an absolutely conserved quantum number, then there must exist some new form of stable matter unknown to us which may be present in the constituent matter of the nuclei of galaxies, quasars, etc.

There are at the present time 53 known hadrons—particles and antiparticles—accounted for within the framework of SU_3 symmetry (see table). But the list of elementary particles is being added to continually. Information on new resonances became known at the conference. Physicists working at the Berkeley, Brookhaven, and University of California laboratories (USA) detected and investigated a resonance in the $\pi\pi\eta$-system in their work on interactions between k^--mesons and protons. The mass, width, and quantum numbers of this resonance were defined more precisely as a result of a study of the modes and characteristics of the decay of this resonance. Confirmation of cascade and multiparticle decays of resonances [e.g. the decays $N^*_{1/2}(1688) \rightarrow N^*_{3/2}(1238) + \pi$, $N^*_{3/2}(1238) \rightarrow N + \pi$] was important to an understanding of the nature of these resonances. These modes of decay (in cases allowed by conservation laws) are typical of almost all existing resonances. Fresh evidence of the existence of $\widetilde{K}K\pi$ resonances (USA, CERN, France) was also reported for $\Lambda\eta$ (JINR), and many other resonances as well.

A conclusion has been reached on the nonexistence of the so-called ABC-resonance in some laboratories (JINR, CERN, Berkeley). Papers by B. N. Valuev, V. V. Anisovich, and L. G. Dakhno (USSR) showed that the ABC-anomaly in the $p + d \rightarrow He^3 + \pi^+ + \pi^0$ reaction seems to be due to a logarithmic singularity in the amplitude of that reaction.

Unfortunately, hopes for achieving relative simplicity in phenomena involving strongly interacting particles at high energies by invoking the Regge pole hypothesis were not sustained in the period elapsed since the 1962 conference. Theoretical investigations (USA, Italy) reveales that in addition to the poles, branch points in the plane of

*Supercharge, a term adopted by Zel'dovich, Okun, and Pikel'ner, should not be confused with hypercharge, Y—Publisher's note.

Declassified and Approved For Release 2013/09/24 : CIA-RDP10-02196R000700010005-2

Declassified and Approved For Release 2013/09/24 : CIA-RDP10-02196R000700010005-2

complex angular momenta figure in the amplitudes. An experimental study of scattering of π^-, K-mesons and antinucleons on nucleons at Brookhaven (USA) revealed no narrowing of the diffraction cone as predicted by the Regge pole hypothesis, and the absence of asymptotic confluence of total scattering cross sections of particles and antiparticles in the energy range to 30 GeV. Nonetheless, the method of complex angular momenta yields interesting predictions in some cases (notably where inelastic processes are involved).

Research on high-energy phenomena opens up some interesting possibilities for verifying such fundamental principles in quantum field theory as microcausality and locality. Proof of the asymptotic relationships between the characteristics of processes (cross sections, etc.) in the high-energy region rests on those principles. A substantial number of these relations were established by A. A. Logunov et al. (JINR), N. N. Meiman (Inst. Theoret. Exp. Phys., USSR), L. Van Hove (CERN). Asymptotic relations were derived not only for total cross sections of elastic processes, but also for differential cross sections (including cross sections for polarization characteristics), inelastic cross sections, and form factors.

Results of experiments on elastic and total cross sections of p-p-,p-$\tilde{p}$-, $\pi^{\pm}$-p-interactions in the energy range from 10 to 30 GeV, reported in the tutorial review by S. J. Lindenbaum (Brookhaven), were not in agreement with relationships derived theoretically. This stood out conspicuously in the case of scattering of K^+- and K^--mesons on nucleons, cross sections of which run parallel to each other, plotted as functions of energy. But a tendency of the cross sections to approach with increasing energy was noted in other particle-antiparticle systems. It would be premature, therefore, to view the discrepancies as a violation of the causality principle: the energies attained are evidently still not high enough to be truly asymptotic.

Cross section measurements for nucleon and pion scattering on nucleons at vanishingly small angles, performed first at Dubna (JINR) and later at other laboratories (in Britain, USA, at CERN) should be examined for possible verification of the causality principle. Measurements revealed a real part in the scattering amplitude up to 10-20 GeV, and thereby simplify verification of dispersion relations in that energy range. This attempt at vertification yielded positive results. But errors in the experimental data are still large. Improved exactness in the experimental data will make for a more conclusive verification of causality in those experiments. This principle constitutes, with Lorentz invariance and spectral character, the basis of the axiomatic approach to quantum field theory. Some progress in the derivation of field equations in this approach, plus some propositions, were presented by V. Ya. Fainberg (Lebedev Inst. Phys., USSR), B. V. Medvedev, and M. K. Polivanov (JINR).

An imposing number of papers on the results of measurements of differential characteristcs (cross sections, polarizations, etc). of elastic and inelastic π-N- and N-N-interaction processes over a broad range of angles and energies was presented at the conference. A phenomenological analysis of data on elastic scattering reactions was made in the range of particle kinetic energies up to 500 MeV, and sets of phase shifts of π-N- and N-N-interactions were determined. Experimental data in the high-energy region were analyzed within the framework of the optical and statistical models, and the model of peripheral collisions.

The study of inelastic interaction processes at very high energies (on the order of 10^{10} and 10^{12} eV) yielded new arguments in support of the mechanism of pion production via the creation of pion clusters (known as fire-balls) decaying into 8 to 10 pions. Emulsion studies of inelastic $\tilde{N}$-N-interaction events at energies in the neighborhood of 10,000 GeV in cosmic radiation (Poland, USA) showed a preferential formation of two fire-balls in that energy range.

Electromagnetic Interactions. Information on these interactions between elementary particles has been supplemented heavily since the 1962 conference. The main impetus for this has been the substantial broadening (by about a factor of five) of the range of electron energies available after the commissioning of the 6 GeV synchrotron at Cambridge, USA, and the production of reasonably clean and high-intensity secondary muon beams of high energy, and on antiproton beams in proton accelerators. New experimental opportunities were exploited in this area primarily to verify electrodynamics at short range. Experiments on photoproduction of muon and electron pairs in the coulombic field of the carbon nucleus at large angles (F. Pipkin et al., G. Friedman, Cambridge, USA), and on muon scattering on protons (G. Tinlot et al., Brookhaven) narrowed the range to distances of $\approx 10^{-14}$ cm, where deviations from predictions based on quantum electrodynamics are yet to be observed. Some experiments involving the participation of muons demonstrated the complete identity of these particles with electrons. This e-μ-universality, which is also observed in weak interaction processes (e.g. in decays of λ- and Σ-hyperons to $N + \nu + e$ and to $N + \nu + \mu$), together with the riddle of the large muon mass, are today one of the most intriguing problems in the physics of elementary particles.

Declassified and Approved For Release 2013/09/24 : CIA-RDP10-02196R000700010005-2

Declassified and Approved For Release 2013/09/24 : CIA-RDP10-02196R000700010005-2

A large batch of experimental papers dealt with recent research on the electrical form factor $G_{Ep,n}$ and magnetic form factor $G_{Mp,n}$ of the proton and neutron. Impressive improvements in the values of the form factors in experiments involving scattering of electrons and muons on hydrogen and deuterium (USA, France) confirmed the following remarkable relationships for the form factors over the entire range of transferred momenta q investigated: $G_{En} = 0$, $G_{Ep} = \frac{1}{1 + \mu_p} G_{Mp} = \frac{1}{\mu_p} GM_n$, where $\mu p,n$ are the anomalous magnetic moments of the proton and neutron. In a paper by R. Wilson (USA), information was communicated on the results of a measurement of form factors of proton and neutron up to $q^2 = 175\ f^{-2}$ and $q^2 = 100\ f^{-2}$ respectively. These results, in addition to all the data on e-N- and μ-N-scattering, showed that when $q^2 > 2.5\ (GeV/c)^2$ the form factors decrease with increasing q as $1/q^2$. Keen interest was manifested at the conference in a report by N. Zikiki et al. (CERN) on the first results of a study of the $\tilde{p} + p \rightarrow \mu^+ + \mu^-$ reaction which yielded information on the structure of the nucleon in the time-like momentum transfer region where $q^2 < 0$. It was found that in the region $q^2 = -6.8\ (GeV/c)^2$ the proton form factor is much less than unity. Refinements in the value of the magnetic moment μ_Λ of the Λ-hyperon (CERN) are highly important from the standpoint of verifying corollaries of SU_3-symmetry. As a result of this and earlier experiments, we have for μ_Λ the average $\mu_\Lambda = (-0.8 + 0.3)$ nuclear magneton, which is not too far at variance with the SU_3 group prediction: $\mu_\Lambda = \frac{1}{2} = -0.95$ nuclear magneton.

In a review paper, N. Ramsay cited new data on measurements of the hyperfine structure of muonium, reporting the value $\alpha^{-1} = 137.0388 \pm 0.0012$ for the fine structure constant. This value of α is in accord with the results of Lamb's measurement of the fine splitting of levels of the deuterium atom.

Several laboratories (in the USSR, USA, also CERN and JINR) presented new data to the conference on investigations of π- and μ-mesoatomic processes. An imposing number of papers was presented on single and pair photoproduction of mesons over a wide range of gamma-photon energies.

One of the conference sessions was devoted to a discussion of fresh attempts, new in principle, at constructing a theory of the elementary particles. Participants of the conference laid great stress on these questions because of the unsatisfactory state of the theory explaining the phenomena of the micro-universe, and called on theoretical physicists to seek out a solution to the problem in a radical break from the basic principles of contemporary theory. Reports were heard at this session on the quantizing of space-time (I. E. Tamm, Lebedev Inst. Physics, V. G. Kadyshevskii of JINR), on problems of nonlocal theories in which the principle of causality breaks down at short distances (D. I. Blokhintsev, G. I. Kolerov, JINR; D. A. Kirzhnits, Lebedev Inst. of Physics), on investigations of equations in field theory with nonlinear Lagrangians (E. S. Fradkin, Lebedev Inst. Physics), etc. A lively discussion was provoked at this session by a report submitted by K. Johnson et al. (USA) on an attempt at constructing quantum electrodynamics free of divergences.

Experimental Method. In the last two days of the conference, problems concerning experimental research methods in the physics of high and ultrahigh energies were discussed. The use of secondary "clean" beams of particles from accelerators, the widespread use of large-volume spark chambers and bubble chambers for the detection of particles, the acquisition of information from particle detection chambers of these types, and processing of this information by electronic digital computers, have become a specific feature of this research. In addition to processing data from detecting instruments, digital computers are also being used to monitor and control equipment and accelerators during the experiments, to introduce corrections where required, etc. The use of increasingly larger and speedier digital computers (with an operating memory volume ranging to $2 \cdot 10^5$ bits, capability of handling as many as 10^6 operations in one second, with devices for converting from computer control) has become a typical feature of modern experimental practice in high-energy physics.

Another characteristic feature is the automated scanning of plates from bubble chambers, spark chambers, diffusion chambers, and other equipment of that type. Some of the papers reported on the development of new systems for automatic scanning of chamber plates. Cathode-ray tubes of high resolution are being employed on a broad scale to pick up and process information acquired by those systems.

The steadily increasing use of bubble chambers, both hydrogen bubble chambers and chambers filled with heavier liquids, in experimental research work, is notable. A report was made on a contruction project underway at Brookhaven National Laboratory, and another at Argonne National Laboratory (USA) involving the installation of enormous hydrogen bubble chambers (~25,000 liters in volume). These bubble chambers may be used in neutrino experiments. A cylindrical propane chamber 1.65 meter in diameter and 4 meters long will be built at CERN.

Declassified and Approved For Release 2013/09/24 : CIA-RDP10-02196R000700010005-2

Declassified and Approved For Release 2013/09/24 : CIA-RDP10-02196R000700010005-2

An important engineering innovation promising to facilitate the work of illuminating such a large-volume bubble chamber will be the use of a special reflecting material (known as scotchlite) coating the interior walls of the chamber. At the present time, successful work is underway in the design of new high-speed bubble chambers and in the creation of ultra-strength magnetic fields (in tens of thousands of gauss) for bubble chambers of up to 1 m^3 vol.

Spark chambers, which are controlled-track devices capable of high spatial and time resolution, have undergone extensive improvements in technique in recent years. The development of this technology has been crowned by the development of isotropic (streamer) discharge chambers (USSR) rich in experimental possibilities.

Several colloquia, seminars, and workshops were held during the conference for a more detailed discussion of the latest results and newest plans in research on the physics of high-energy particles. The success of the conference as a whole was aided mightily by scientific collaboration and the exacting demands for research findings. The next XIII international conference on high-energy physics is scheduled for 1966, to be held in Berkeley (USA).

Declassified and Approved For Release 2013/09/24 : CIA-RDP10-02196R000700010005-2

Declassified and Approved For Release 2013/09/24 : CIA-RDP10-02196R000700010005-2

SECOND COLLOQUIUM ON INELASTIC SCATTERING OF SLOW NEUTRONS IN CRYSTALS AND LIQUIDS

Translated from Atomnaya Énergiya, Vol. 18, No. 5,
pp. 543-545, May, 1965

In June 1964, the second colloquium on inelastic scattering of slow neutrons in crystals and liquids met in Dubna under the auspices of the Joint Institute for Nuclear Research (JINR); representatives from various institutes throughout the USSR participated in the deliberations. 4 tutorial review papers were read along with 33 original contributions, including 15 papers by delegates representing participating nations in the JINR, 14 papers by delegates representating institutes in the Soviet Union, and 8 papers from the Neutron Physics Laboratory of the Joint Institute for Nuclear Research. 86 scientists, 22 of them from institutes of member-nations of the JINR, took part in the colloquium.

Two reviews papers were read at sessions devoted to scattering of slow neutrons in crystals: A. Afanas'ev and Yu. Kagan (Kurchatov Inst. of Atomic Energy) "The effect of the electron-phonon interaction on the phonon spectrum of a crystal," E. Brovman (Kurchatov Inst. of Atomic Energy): "The present state of the dynamical theory of the crystal lattice in relation to neutron experiments."

The first report took up specific features observed in the phonon spectrum and attributed to phonon-electron coupling. (The position of these spectral features is generally determined by the geometry of the Fermi surface.) Topics discussed included the effect of the Fermi surface configuration, spin-flip processes, electron-phonon interaction constants, and the effect of temperature on the nature of these spectral details, and also ways in which these details show up in the frequency distribution function of phonons.

The second review report surveyed work done on the dynamics of crystals with ionic, covalent, and metallic bonds. Theoretical models of vibrations of crystals of this type and opportunities for neutron diffraction research were discussed.

Slow neutron scattering on anharmonic crystals was the subject of a paper by A. Zhernov and Yu. Kagan (Kurchatov Inst. of Atomic Energy). They determined the Debye-Waller factor for crystals of arbitrary symmetry over an entire temperature range. The effect of several anharmonic processes on the coherent and incoherent neutron scattering cross sections was treated.

E. Brovman and Yu. Kagan (both of the Kurchatov Inst. of Atomic Energy) proposed a model describing the coupling of forces in the white tin lattice. The model takes the coupling of each atom to the four coordination spheres into account. The force constants of the dynamical matrix required for the calculations were found from experimentally derived elastic moduli. Various dynamical lattice characteristics were calculated on a computer on the basis of the proposed model. The resulting dispersion curves demonstrate a great deal of "mixing" of the optical and acoustical branches of the vibrations. The specific heat of the tin lattice was determined. The high sensitivity with which the specific heat of a complex lattice of this type responds to which model is selected was demonstrated, as fairly conclusive evidence of the validity of any particular model.

A. Czachor et al. (Poland) employed a triaxial crystal spectrometer in determining the phonon dispersion law for the three crystallographic directions in a zinc single crystal. Utilizing Born–von Karman theory, these workers derived some general formulas for the dispersion curves, with five-nearest-neighbor taken into account.

M. Zemlyanov et al. (Kurchatov Inst. of Atomic Energy) cited their research findings on inelastic scattering of cold neutrons by lithium hydride and lithium deuteride. The authors used model representations of the energy dependence of the polarization vectors in attempting to secure quantitative information on the phonon spectrum from the experimental data. The polarization vectors were determined in the proposed models by applying the Born–von Karman equations. The point ion model was selected in the calculations. It was demonstrated that peaks observed in the experimentally measured cross section do not correspond consistently to the maxima in the phonon distribution, and vice versa. It was reported that the entire phonon spectrum of lattices such as those of lithium hydride and

Declassified and Approved For Release 2013/09/24 : CIA-RDP10-02196R000700010005-2

Declassified and Approved For Release 2013/09/24 : CIA-RDP10-02196R000700010005-2

lithium deuteride can be reliably investigated in cold-neutron experiments, even though the acoustic region is depressed considerably. But it is impossible to extend the features in the inelastic scattering cross section onto the phonon spectrum of the substance under investigation when we lack knowledge of the energy dependence of the polarization vectors. Other finding were that theoretical calculations in the incoherent approximation yield excellent agreement with experiment, despite the fact that the contribution from coherent scattering on lithium deuteride is quite substantial in the true cross section.

I. Dzyub (Institute of Physics, Academy of Sciences of the Ukrainian SSR) calculated the broadening of the one-pronon peak in the spectrum of neutrons scattered coherently by disordered binary solid solutions. These calculations neglected differences in the coupling constants of the impurity atoms and the host crystal atom. The broadening of the one-pronon peak by scattering of phonons on impurity atoms was demonstrated to be of a resonance nature, and to be capable of reaching a higher value than line broadening in the anharmonic case.

Some opportunities for studying the lifetime and the laws of motion of local degrees of freedom of atomic systems in experiments on quasielastic incoherent scattering of slow neutrons were discussed in a paper by M. Kazarnovskii and A. Stepanov (Lebedev Institute of Physics).

Several papers (E. Janik et al., Poland; A. Bajorek, JINR; K. Mikke and L. Dobrzynski, Poland) reported investigations of the dynamics of the NH_4, CH_3, H_3O groups in a variety of molecular crystals and liquid over a wide temperature range, with the aid of different experimental techniques (scattering of cold neutrons, total neutron cross section measurements, placing a filter in front of the detector). It was shown that these groups rotate freely in some substances (NH_4ClO_4, NH_4PF_6, NH_4I at room temperature, etc.). At the same time, hindered rotation of molecular groups is observed in some cases (NH_4Br, NH_4F, NH_4Cl, H_3OCl_4, etc.); the value of the hindered rotation barrier was determined in certain cases. Temperature variations of the width and intensity of individual peaks were discussed. The authors noted the inapplicability of Krieger-Nelkin theory to calculations of neutron scattering by molecular groups in condensed media.

At the session devoted to scattering of slow neutrons by molecules and liquids, the delegates heard a review paper by G. Ivanov and Yu. Sayasov (Institute of Chemical Physics), entitled "Theory of neutron-molecule interactions at energies on the order of the chemical binding energy." A consistent theory dealing with neutron interactions with molecules and taking the energy dependence of the cross sections for neutron-nucleus scattering and molecular transformations into account was developed. The results were obtained on the basis of the momentum approximation, i.e., the assumption that the neutron-nucleus collision time is less than the vibrational periods of the molecule and that the rotation of the molecule is describable in classical terms. Measuring double differential cross sections yielded valuable information on the vibrational characteristics of the molecule, on the magnitude of the amplitude vectors and the related force constants of molecules, for which experimental methods of determination (applicable in all cases) are still lacking at this writing.

G. Kosaly and G. Solt (Hungary) performed an investigation of the applicability of the mass tensor approximation is calculations of doubly differential cross section. They found that the mass tensor approximation improves with increase in the momentum transferred for a given energy transfer and a reasonably high temperature.

D. Balli et al. (Rumania) reported on measurements of scattering of thermal neutrons of ethylene, methane, and other assorted mixtures of hydrocarbons. The findings demonstrated that, at low initial neutron energies and scattering angles below 30°, the half-widths of the experimental curves in the case of ethylene and methane are less than the half-widths of the curves computed on the basis of Krieger-Nelkin theory. Modulations of the curve describing the doubly differential cross section as a function of the energy of the scattered neutron were observed in the high-energy region, as predicted from Griffing's theory. In the case of neutrons scattered on hydrocarbon mixtures, the diffusion coefficient and the lifetime of a molecule in the equilibrium position can be determined from the width of the quasielastic peak.

M. Zemlyanov and N. Chernoplekov (Kurchatov Inst. Atomic Energy) carried out measurement of scattering of cold neutrons on various polyphenyls (benzene, monoisopropyldiphenyl, diphenyl). They found that the spectrum of neutrons scattered on diphenyl varies substantially in the transition through the melting point, particularly in the low-energy portion of the spectrum. The energy dependence of the differential cross section for inelastic scattering on polyphenyls cannot be described satisfactorily in terms of the monatomic gas model. Satisfactory agreement between theory and experiment is obtained only in the model which takes internal vibrational degrees of freedom partially into account.

Declassified and Approved For Release 2013/09/24 : CIA-RDP10-02196R000700010005-2

Declassified and Approved For Release 2013/09/24 : CIA-RDP10-02196R000700010005-2

V. Vertebnyi et al. (Inst. of Physics of the Academy of Sciences of the Ukrainian SSR) reported their findings of an investigation of total neutron cross sections of liquid oxygen and liquid nitrogen in the 4-12 A wavelength range. The energy dependences of the total neutron cross sections of liquefied nitrogen and liquefied oxygen differ from the energy dependence of cross sections for the gases of those same substances. Instead of a smooth rise with increase in wavelength, as in the case of the gas, what we see in the total cross sections of the liquids is a maximum at 5.5 A wavelength, followed by a rather precipitous decline. The dependence of the total cross section on energy seems to be associated with short-range ordering in the liquids.

H. Teici et al. (Rumania) measured cold neutron scattering by ordinary water and heavy water. Their findings point to a jump diffusion mechanism in water. The generalized frequency spectrum function was computed by the method suggested by Egelstaff.

V. Golikov and associates (JINR) presented papers reporting measurements of scattering of cold neutrons in water, ethylene glycol, acetic acid, benzene, naphthalene, and dioxane over a broad temperature range. They showed that the jump diffusion mechanism is more explicit in substances forming intermolecular hydrogen linkages. They noted that the transition through the melting point is accompanied by a notable decrease in effective Debye temperature in the case of benzene, naphthalene, and dioxane. Of greatest interest were the results of measurements of cold neutron scattering in highly viscous liquids (ethylene glycol), where the self-diffusion coefficient measured with the aid of neutrons turned out to be at least 10 times greater than the diffusion coefficient computed from the viscosity data.

Z. Rogalska (Poland) performed investigations of the dynamics of methane molecules in the liquid and solid states with the aid of total neutron cross sections measurements. Results indicated that rotation of molecules is virtually unhindered near the melting point in solid methane.

At the session dealing with magnetic scattering of neutrons, delegates heard a review tutorial paper delivered by F. Shapiro (JINR) entitled "Neutron scattering in semiconductors." He pointed out that superconductors of group II, which includes niobium and most superconducting alloys, are typified by the fact that the magnetic field penetrates in these superconductors in the form of filaments of dimensions on the order of 10^{-5} cm, forming a regular lattice. The uneven distribution of the magnetic field may lead to neutron scattering at angles on the order of minutes of arc, and this can be exploited in studies of magnetic field structure in superconductors. Neutron scattering can also be used for information on current distribution in superconductors. He reported an experiment set up at the Neutron Physics Laboratory of JINR and cited the first results of Jacquereau's work (France) on magnetic scattering of neutrons in niobium.

K. Blinowski (Poland) reported the findings of his investigation of critical magnetic scattering of neutrons in iron chromium. He reported a large discrepancy between experiment and theory in the temperature variation of the length of the spin correlation region.

A paper by S. Krasnicki (Poland) reported an investigation of spin dynamics in pyrrhotines and magnetite, carried out by inelastic magnetic neutron scatterin. The experimental law of magnon dispersion derived is in agreement with theory. An anisotropy was discovered on the acoustical branch of the dispersion law. The lifetime of magnons of different energies was estimated for various temperatures.

At the session devoted to experimental procedures, interest was stimulated by a report by A. Chicherin (Kurchatov Inst. Atomic Energy) " The problem of inversion of experimental data in the case of resolution function of arbitrary form."

A paper by V. Somenkov (Kurchatov Inst. Atomic Energy) discussed focusing neutron crystal monochromators of iron silicide. He reported that iron single crystals are not inferior to melt-grown single crystals in their reflectivity. Since they ben easily, they can be utilized in various focusing systems, thereby increasing the intensity of the neutron beam several times with no loss in resolution.

Papers by B. Buras et al. (Poland), and W. Nietzsche et al. (JINR) described a method of neutron structural research on powders using time-of-flight techniques. Among the advances of the technique may be counted the absence of second-order reflections and the short exposure time. The method allows the use of external stimuli pulsed at the same frequency as the neutron beam. This opens the way for investigating such time effects as relaxation phenomena.

The papers submitted at the conference demonstrated that slow-neutron spectroscopy is playing an increasingly prominent role in research on the molecules of liquids and solids.

At the concluding session, a decision was adopted to schedule similar colloquia on neutron diffraction investigations of condensed media once every two years. The next colloquium is to be convened sometimes in 1966.

V. V. Golikov

Declassified and Approved For Release 2013/09/24 : CIA-RDP10-02196R000700010005-2

Declassified and Approved For Release 2013/09/24 : CIA-RDP10-02196R000700010005-2

NEWS

THE BETA-2: NEW ISOTOPE ELECTRIC POWER SOURCE

Translated from Atomnaya Énergiya, Vol. 18, No. 5,
pp. 545-546, May, 1965

Several types of isotope electric power supply packs have been developed in the Soviet Union, and may be used in various branches of the national economy, e.g. hydrometeorological service.

At the present time, the principal source of information in the compilation of weather forecasts are hydrometeorological stations and posts situated in various remote and difficulty accessible parts of our country. The necessary data are collected and transmitted by automatically operated radiometeorological stations which are battery-supplied with recharging from a wind-powered generator. These power sources are beset with certain drawbacks which interfere with the functioning of the automatic weather stations, and which stand in the way of reliable interruption-free performance. For example, these wind-power units are of low reliability and cannot render service at all in regions deprived of high wind loads over long periods (Yakutia, the Krasnoyarsk region, etc.). Reliance on unrecharged batteries is paid for in greatly increased total weright of batteries and concomitant unreliability. Severe climatic conditions also exert as adverse effect on their performance to a considerable extent. The deficiencies enumerated are absent in the new BETA-2 isotopic electric power package (see figure) developed and fabricated by the All-Union Scientific Research Institute for Radiation Techniques of the State Committee on the Uses of Atomic Energy of the USSR, co-opting the services of several specialized organizations.

The BETA-2, now in experimental service, is designed as a power-supplies source for the unattended automatically operated radiometeorological ARMS type weather station, to provide trouble-free service for 10 years, to meet the 150-to 200-W power demand of station when the transmitter is on. The station periodically monitors air pressure and temperature, wind velocity and directions, the amount of radioactive fallout, and the presence of sunshine, and transmits the information by radio over distances up to 600 km.

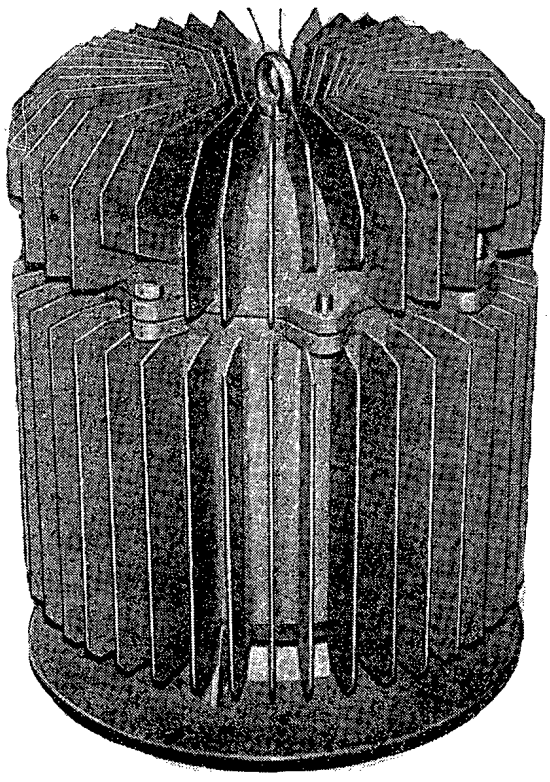

The BETA-2 isotope electric power pack.

The BETA-2 is capable of producing an electrical power output from 5 up to 7 W, at an output voltage of 3.5 to 4.5 V; this means a power demand of 500 to 600 kWh calculated over a 10-year service period, or a specific energy capacity of 3 to 4 kWh/kg. A special system for converting voltage to electric power accumulation makes it possible to achieve output voltage as high as 32 V and to supply various systems of radiometeorological stations with pulsed power, with as much as 1000 W per pulse delivered.

The conversion of the heat energy liberated by the decay of the radioactive material to electric power in the BETA-2 power package is carried out by low-temperature thermoelectric cells. Sr^{90} was selected as the radioactive material, and the thermoelectric cell module is designed as a gastight enclosure. The package is made up of two parts: the operational package and the carrying case. The operational package is shaped as a cylinder (350 mm diameter, 400 mm height). This package weighs 150 kg, the dose rate at a distance of one meter from the surface does not exceed 1 r/h. The

Declassified and Approved For Release 2013/09/24 : CIA-RDP10-02196R000700010005-2

Declassified and Approved For Release 2013/09/24 : CIA-RDP10-02196R000700010005-2

carrying case reduces the dose rate to 10 mr/h at one meter distance, so that the device can be transported on any means of transportation with no special restrictions applying, and the total weight in transit will be about 500 kg. The design of the over-all power package and the use of Sr^{90} in the form of special chemical compounds excludes any possibility of radioactive material gaining access to the environment and becoming a source of contamination.

The BETA-2 is distinguished by high reliability, the system is unaffected by changes in climate or weather, and will withstand short circuits for an unlimited time; individual components of the BETA-2 are under static load and will retain their properties practically unchanged over a long time span.

The BETA-2 won wide acclaim at the Leipzig industrial fair (February—March 1965), where it was awarded a gold metal.

This device may find application as a source of electric power in various systems intended for long-term unattended service, in places where constant sources of electric power are otherwise absent, and in systems where high reliability and stability of output parameters are required.

G. M. Fradkin, V. M. Kodyukov, and A. I. Rogozinskii

Declassified and Approved For Release 2013/09/24 : CIA-RDP10-02196R000700010005-2

Declassified and Approved For Release 2013/09/24 : CIA-RDP10-02196R000700010005-2

GENERAL-PURPOSE GAMMA-RAY DEVICE DESIGNED FOR PILOT-PLANT RADIATION-CHEMICAL PROCESSES WITH DISPLACEMENT OF RADIOACTIVE Co^{60} PREPARATIONS BY COMPRESSED AIR

Translated from Atomnaya Énergiya, Vol. 18, No. 5, pp. 546-548, May, 1965

A multichannel arrangement in which boxes are suspended on cables with electromagnets is described in [1]. In view of the large number of cables in the operating area, the current-carrying wires as sources of sparking, and the inadequate heat removal from the γ-ray sources, these arrangements have achieved widespread use as laboratory items.

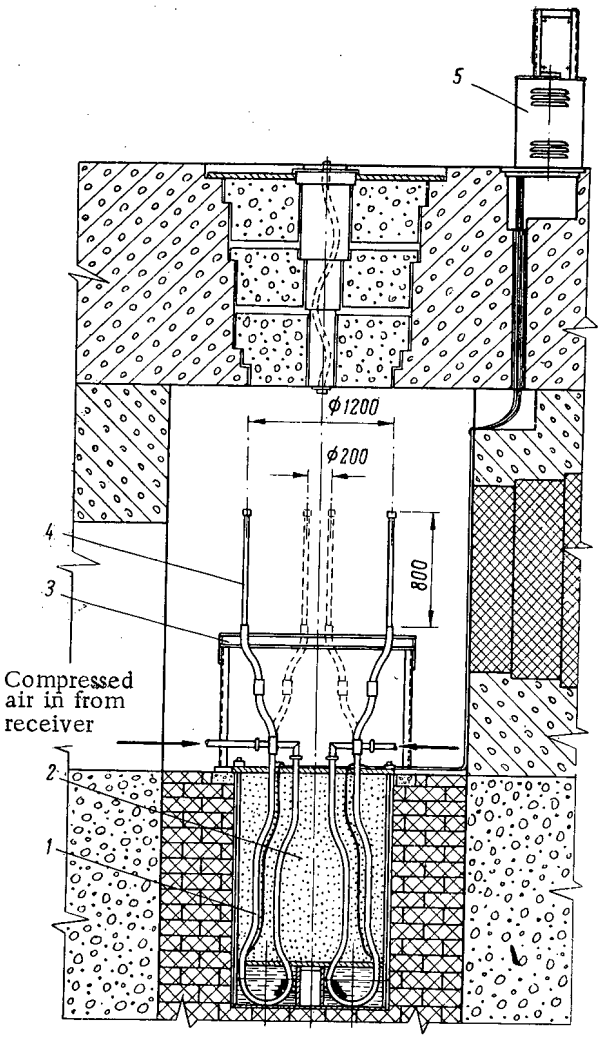

Fig. 1. Operational chamber: 1) storage unit channels; 2) iron shot filling; 3) worktable; 4) irradiator; 5) control panel.

The KP-140 γ-irradiator with Co^{60} sources of $2 \cdot 10^5$ gram equivalents of Ra total activity has been designed, fabricated, and adapted for general use in work done at a branch of the L. Ya. Karpov Physical Chemistry Research Institute. In contrast to the γ-ray facilities described earlier in the literature [1-2], the design of this KP-140 arrangement calls for empressed air to move the sources, locate them at their operating positions, and cool them.

A method for storing the radioactive sources while simultaneously using them to cool a liquid and a gas [3, 4] lies at the basis of the KP-140 facility.

The operating chamber of the device (Fig. 1) combines the functions of source storage chamber and irradiator.

The storage chamber for the γ-ray sources is made of 20 isolated U-shaped channel tubes with iron shot filling the spaces between them. The bottoms of these tubes are welded into a leaktight enclosure. This enclosure is fitted with channels for the admission and removal of the water or air cooling the operating channels. There is also a tubular coil of stainless steel for cooling the water in the enclosure.

The irradiator proper (Fig. 2) consists of 20 separate tubes communicating with the corresponding channels of the source storage unit via tube bends making it possible to situate the radiation sources on the generatrices of a cylinder whose base diameter may be anywhere from 200 to 1200 mm. The height of the irradiator tubes is 800 mm.

Seven standard Co^{60} sources (11 by 81 mm diameter) are placed in each irradiator tube in stainless steel ampules with a self-locking threaded cover. The sources may be in either of two positions: storage

Declassified and Approved For Release 2013/09/24 : CIA-RDP10-02196R000700010005-2

Declassified and Approved For Release 2013/09/24 : CIA-RDP10-02196R000700010005-2

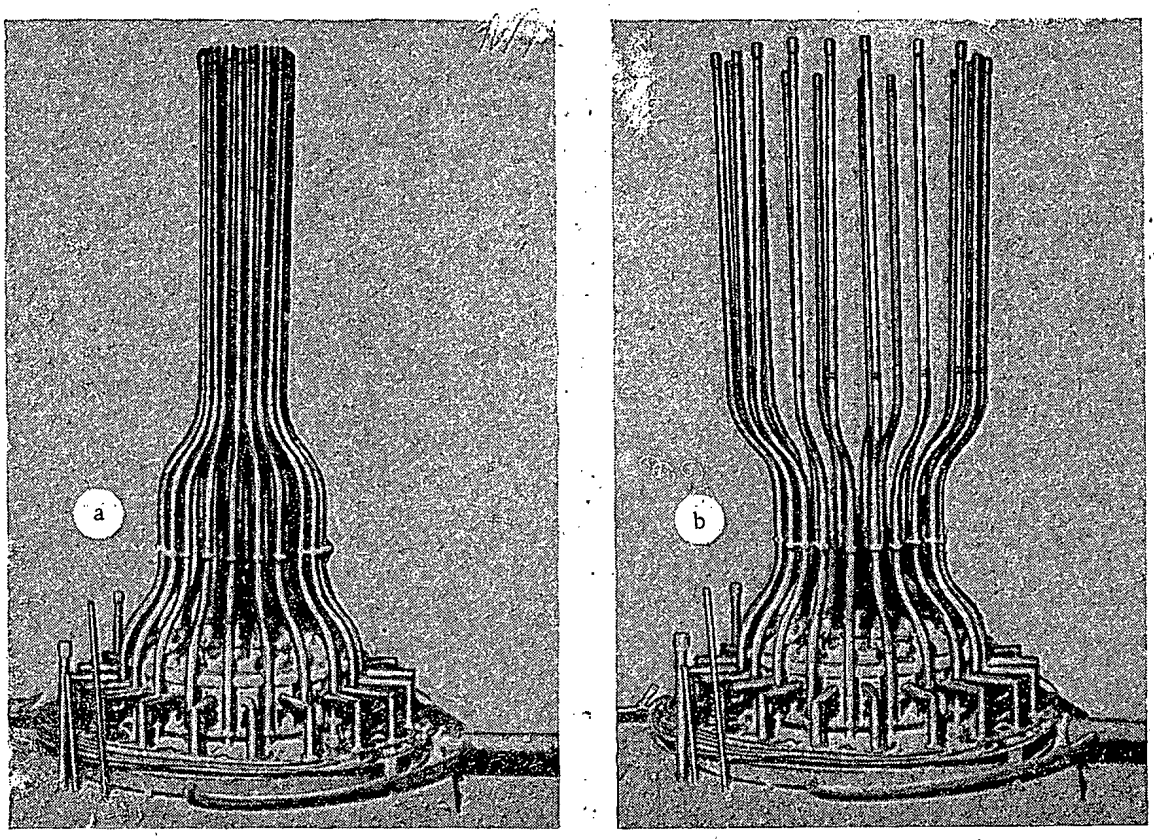

Fig. 2. Irradiator: a) smallest irradiator diameter; b) average diameter (only upper tube bends released)

or operational. In the operational position, the columns containing the sources are forced into the irradiator tubes by compressed air. The sources are lifted from the storage unit into the irradiator tubes either channel by channel, or all simultaneously, depending on the requirements of the specific radiation-chemical process. Air for controlling the setting is supplied either from a centralized network or from autonomously operated gas blowers on standby. The compressed air from the centralized network is fed through a water-oil separator unit prior to being supplied into the channels, and through a pressure relief valve and receiver tank, and, when air blowers are used, through a heat exchanger and receiver tank.

The subsequent lifting of the sources into place is accomplished in the following manner. The receiver is filled with air to a pressure of 0.44 kg /cm^2. The valve of the corresponding channel, in which the air is to force a piston with the column of sources into the irradiator tube, where it will subsequently remain for the entire time it takes to establish the necessary pressure behind the piston, is opened from the control panel. This operation is repeated in order to life the sources in all the channels, and takes a total of 1 to 1.5 min.

It is sufficient to cover the corresponding channel (selectively) in order to drop the sources back into the storage position. The feed of compressed air from the receiver is cut off if all the sources are to be returned to storage simultaneously. The pressure in the channels then drops and the piston with sources falls back into storage position under gravity action. The sources are brought to a gentle stop without shock impact at the bottom of the storage well by braking action in the U-shaped channel.

A pressure on the order of 1 atmos is set up in the receiver if the sources in all or in several channels are to be raised simultaneously, and then the valves of the several or of all channels, as the case may be, are opened and the general air line valve is opened up.

The position of sources in the irradiator tube or in the storage channel is monitored by pneumatic sensors. Monitoring tubes are brought from the bottoms and tops of each storage channel to bellows devices in the sensor control panel. The bellows energize or de-energize the appropriate electrical switches depending on the pressure drop in the tubes. Signal bulbs on the control panel light up when the electrical switches are closed.

Declassified and Approved For Release 2013/09/24 : CIA-RDP10-02196R000700010005-2

Declassified and Approved For Release 2013/09/24 : CIA-RDP10-02196R000700010005-2

The doors leading into the chamber are interlocked with the aid of dosimetric monitors backed up by a specially designed air lock.

The absence of any parts in the working space of the chamber other than the irradiator tubes themselves allows for unhindered movement and repositioning of any equipment used.

A large number of experiments were run on various mock-ups and test stands to check out the pneumatic system used to deliver the radiation sources into place or into storage. Radiation sources were run through 20,000 cycles of lifting and dropping, with a cycle time of 5 sec, on an automatic pneumatic test stand. The dimensions and weight of the mock-ups, of the piston and channel were all set in accordance with working conditions. Thermal fluctuations were simulated by supplying air at 75°C. It was found that, after the indicated number of cycles had been carried out under operating conditions and matching no less than 15-20 years of actual operating wear and tear, the ampules were still satisfactorily pressuretight, and wear on them was negligible.

The arrangement was loaded with radiation sources and put into experimental operation in September 1964. At the present time, scaled-up radiation-chemical processes are underway on the arrangement. The irradiator arrangement has been operated dependably without any substantial changes in the time elapsed. All experiments conducted have fully confirmed the design specifications. Especially noteworthy is the convenient reloading of ampules, since contamination of the operating channels, air, and operating chamber remain within the limits of the radiation background.

LITERATURE CITED

1. A. Kh. Breger, V. B. Osipov, and V. A. Gol'din, Atomnaya énergiya, 8, 441 (1960).
2. C. Murray and R. Roberts, D. Dool. 3rd international UNESCO conference on applications of radioactive isotopes in scientific research. Paris 1957. London Pergamon Press, (1958).
3. S. S. Gurvits, É. M. Krisik, A. N. Liberman, and E. D. Chistov, Public health rules and regulations for the design and operation of high-level γ-ray isotope facilities, No. 482-64. Ministry of Public Health of the USSR, [in Russian], (1964).
4. Patent No. 161438, Byulleten' izobretennii, No. 7, April 1964.

V. I. Volgin, V. E. Drozdov, M. E. Eroshov,
G. I. Lisov, A. N. Neprokin, and Yu. S. Ryabukhin

Declassified and Approved For Release 2013/09/24 : CIA-RDP10-02196R000700010005-2

Declassified and Approved For Release 2013/09/24 : CIA-RDP10-02196R000700010005-2

SOVIET JOURNALS AVAILABLE IN COVER-TO-COVER TRANSLATION

This list includes all Russian journals which—to the publisher's knowledge—were available in cover-to-cover translation on June 30, 1965, or for which definite and immediate plans for cover-to-cover translation had been announced by that date. The list reflects only *current* publication arrangements, but the date and issue listed for first publication refer to translations available from any source. Thus, earlier volumes of a translation journal may have been published by an organization other than that listed as the current publisher, and possibly under a different title (and, for *Doklady Akademii Nauk SSSR*, in a different arrangement of sections).

Five bits of information are furnished, separated by bullets:

1. The abbreviation(s) by which the journals are most frequently referred to in Russian bibliographies (if the name of the journal is customarily spelled out, no abbreviation is given).
2. The transliterated full name of the journal.
3. The full name of the translation journal (in bold type).
4. The year, volume (in parentheses), and issue of first publication of the translation (parentheses are empty if the Russian journal does not use volume numbers).
5. The current publisher of the translation [AGI—American Geological Institute, AGU—American Geophysical Union, AIP—American Institute of Physics, CB—Consultants Bureau, CH—Clearing House for Federal Scientific and Technical Information, CS—The Chemical Society (London), FP—Faraday Press, IEEE— Institute of Electrical and Electronic Engineers, ISA—Instrument Society of America, PP—Pergamon Press].

For convenience in locating bibliographic references the journals are listed in alphabetical order of the *abbreviated* titles.

AÉ • Atomnaya énergiya • **Soviet Journal of Atomic Energy** • 1956(1)1 • CB

Akust. zh. • Akusticheskii zhurnal • **Soviet Physics—Acoustics** • 1955(1)1 • AIP

Astrofiz. • Astrofizika • **Astrophysics** • 1965(1)1 • FP

Astr(on). zh(urn). • Astronomicheskii zhurnal • **Soviet Astronomy—AJ** • 1957(34)1 • AIP

Avtomat. i telemekh. • Avtomatika i telemekhanika • **Automation and Remote Control** • 1956(27)1 • ISA

Avto(mat). svarka • Avtomaticheskaya svarka • **Automatic Welding** • 1959(12)1 • British Welding Research Association

Avtometriya • **Autometry** • 1965(1)1 • CB

Biokhim. • Biokhimiya • **Biochemistry** • 1956(21)1 • CB

Byul. éksp(erim). biol. (i med.) • Byulleten' éksperimental'noi biologii i meditsiny • **Bulletin of Experimental Biology and Medicine** • 1959(41)1 • CB

DAN (SSSR) • *see* Doklady AN SSSR

Defektoskopiya • **Soviet Defectoscopy** • 1965(1)1 • CB

Diff. urav. • Differentsial'nye uravneniya • **Differential Equations** • 1965(1)1 • FP

Dokl(ady) AN SSSR; DAN (SSSR) • Doklady Akademii Nauk SSSR • The translation of Doklady is published in various journals, according to subject matter. The sections of Doklady contained in each of the translation journals are listed in parentheses.

Doklady Biochemistry (biochemistry) • 1957(112)1 • CB

Doklady Biological Sciences Sections (anatomy, cytology, ecology, embryology, endocrinology, evolutionary morphology, parasitology, physiology, zoology) • 1957(112)1 • CB

Doklady Biophysics (biophysics) • 1957(112)1 • CB

Doklady Botany (botany, phytopathology, plant anatomy, plant ecology, plant embryology, plant physiology, plant morphology) • 1957(112)1 • CB

Doklady Chemical Technology (chemical technology) • 1956(106)1 • CB

Doklady Chemistry (chemistry) • 1956(106)1 • CB

Doklady Earth Sciences Sections (geochemistry, geology, geophysics, hydrogeology, lithology, mineralogy, paleontology, permafrost, petrography) • 1959(124)1 • AGI

Doklady Physical Chemistry (physical chemistry) • 1957(112)1 • CB

Doklady Soil Science (soil science) • 1964(154)1 • Soil Science Society of America

Soviet Mathematics—Doklady (mathematics) • 1960(130)1 • American Mathematical Society

Soviet Oceanography (oceanology) • 1959(124)1 • AGU

Soviet Physics—Doklady (aerodynamics, astronomy, crystallography, cybernetics and control theory, electrical engineering, energetics, fluid mechanics, heat engineering, hydraulics, mathematical physics, mechanics, physics, technical physics, theory of elasticity • 1956(106)1 • AIP

Élektrokhimiya • **Soviet Electrochemistry** • 1965(1)1 • CB

Élektrosvyaz' • combined with Radiotekhnika in **Telecommunications and Radio Engineering** • 1957(16)1 • IEEE

Élektrotekh. • Élektrotekhnika • **Soviet Electrical Engineering** • 1965(36)1 • FP

Éntom(ol). oboz(r). • Éntomologicheskoe obozrenie • **Entomological Review** • 1958(37)1 • Entomological Society of America

Fiz. goreniya i vzryva • Fizika goreniya i vzryva • **Combustion, Explosion, and Shock Waves** • 1965(1) • FP

Fiziol(ogiya) rast. • Fiziologiya rastenii • **Soviet Plant Physiology** • 1957(4)1 • CB

Fiz.-khim. mekh(anika) mater(ialov); FKhMM • Fizikokhimicheskaya mekhanika materialov • **Soviet Materials Science** • 1965(1)1 • FP

Fiz. met. i metallov.; FMM • Fizika metallov i metallovedenie • **Physics of Metals and Metallography** • 1957(5)1 • Acta Metallurgica

Fiz.-tekhn. probl. razr. polezn. iskopaem. • Fizikotekhnicheskie problemy razrabotki poleznykh iskopaemykh • **Soviet Mining Science** • 1965(1)1 • CB

Fiz. tv(erd). tela; FTT • Fizika tverdogo tela • **Soviet Physics—Solid State** • 1959(1)1 • AIP

FKhMM • *see* Fiz.-khim. mekhanika materialov

FMM • *see* Fiz. met. i metallov.

FTT • *see* Fiz. tverd. tela

Geliotekh. • Geliotekhnika • **Applied Solar Energy** • 1965(1)1 • FP

Geol. nefti i gaza • Geologiya nefti i gaza • **Petroleum Geology** • 1958(2)1 • Petroleum Geology, Box 171, McLean, Va.

Geomagnet. i aéronom. • Geomagnetizm i aéronomiya • **Geomagnetism and Aeronomy** • 1961(1)1 • AGU

Inzh.-fiz. zh. • Inzhenerno-fizicheskii zhurnal • **Journal of Engineering Physics** • 1965(8)1 • FP

Inzh. zh. • Inzhenernyi zhurnal • **Soviet Engineering Journal** • 1965(5)1 • FP

Iskusstv. sputniki Zemli • Iskusstvennye sputniki Zemli • **Artificial Earth Satellites** • 1958(1)1 • CB [superseded by Kosmich. issled.]

Izmerit. tekhn(ika) • Izmeritel'naya tekhnika • **Measurement Techniques** • 1958(7)1 • ISA

Izv. AN SSSR, o(td.) kh(im.) n(auk) (*or* ser. khim.) • Izvestiya Akademii Nauk SSSR: Otdelenie khimicheskikh nauk (*or* Seriya khimicheskaya) • **Bulletin of the Academy of Sciences of the USSR: Division of Chemical Science** • 1952(16)1 • CB

Izv. AN SSSR, ser. fiz(ich). • Izvestiya Akademii Nauk SSSR: Seriya fizicheskaya • **Bulletin of the Academy of Sciences of the USSR: Physical Series** • 1954(18)3 • Columbia Technical Translations

Izv. AN SSSR, ser. fiz. atm. i okeana • Izvestiya Akademii Nauk SSSR: Seriya fiziki atmosfery i okeana • **Izvestiya, Atmospheric and Oceanic Physics** • 1965( )1 • AGU

Izv. AN SSSR, ser. fiz. zemli • Izvestiya Akademii Nauk SSSR: Seriya fiziki zemli • **Izvestiya, Physics of the Solid Earth** • 1965( )1 • AGU

Izv. AN SSSR, ser. geofiz. • Izvestiya Akademii Nauk SSSR: Seriya geofizicheskaya • **Bulletin of the Academy of Sciences of the USSR: Geophysics Series** • 1957(7)1 • AGU [superseded by Izv. AN SSSR, ser. fiz. atm. i okeana and Izv. AN SSSR, ser. fiz. zemli]

Izv. AN SSSR, ser. geol. • Izvestiya Akademii Nauk SSSR: Seriya geologicheskaya • **Bulletin of the Academy of Sciences of the USSR: Geologic Series** • 1958(23)1 • AGI

Izv. AN SSSR, ser. neorgan. mat(er). • Izvestiya Akademii Nauk SSSR: Seriya neorganicheskie materialy • **Inorganic Materials** • 1965(1)1 • CB

Declassified and Approved For Release 2013/09/24 : CIA-RDP10-02196R000700010005-2

Declassified and Approved For Release 2013/09/24 : CIA-RDP10-02196R000700010005-2

Izv. AN SSSR, tekhn. kiber(netika) • Izvestiya Akademii Nauk SSSR: Tekhnicheskaya kibernetika • **Engineering Cybernetics** • 1963(1)1 • IEEE

Izv. v(yssh.) u(ch.) z(av.) aviats. tekh. • Izvestiya vysshikh uchebnykh zavedenii. Aviatsionnaya tekhnika • **Aviation Engineering** • 1963(6)1 • CH

Izv. v(yssh.) u(ch.) z(av.) fiz. • Izvestiya vysshikh uchebnykh zavedenii. Fizika • **Soviet Physics Journal** • 1965(8)1 • FP

Izv. v(yssh.) u(ch.) z(av.) geodez. i aérofot. • Izvestiya vysshikh uchebnykh zavedenii. Geodeziya i aérofotos"emka • **Geodesy and Aerophotography** • 1959(4)1 • AGU

Izv. v(yssh.) u(ch.) z(av.) priborostr. • Izvestiya vysshikh uchebnykh zavedenii. Priborostroenie • **Izvestiya VUZOV. Instrument Building** • 1962(5)1 • CH

Izv. v(yssh.) u(ch.) z(av.) radiofiz. • Izvestiya vysshikh uchebnykh zavedenii. Radiofizika • **Izvestiya VUZOV. Radiophysics** • 1958(1)1 • CH

Izv. v(yssh.) u(ch.) z(av.) radiotekhn(ika) • Izvestiya vysshikh uchebnykh zavedenii. Radiotekhnika • **Izvestiya VUZOV. Radio Engineering** • 1959(2)1 • CH

Izv. v(yssh.) u(ch). z(av.) tekh. teks. prom. • Izvestiya vysshikh uchebnykh zavedenii. Tekhnologiya tekstilnoi promyshlennosti • **Technology of the Textile Industry, USSR** • 1960(4)1 • The Textile Institute (Manchester)

Kauch. i rez. • Kauchuk i rezina • **Soviet Rubber Technology** • 1959 (18)3 • Maclaren and Sons Ltd.

Khim. getero(tsik). soed. • Khimiya geterotsiklicheskikh soedinenii • **Chemistry of Heterocyclic Compounds** • 1965(1)1 • FP

Khim. i neft. mash(inostr). • Khimicheskoe i neftyanoe mashinostroenie • **Chemical and Petroleum Engineering** • 1965( )1 • CB

Khim. i tekhnol. topliv i masel • Khimiya i tekhnologiya topliv i masel • **Chemistry and Technology of Fuels and Oils** • 1965( )1 • CB

Khim. prirod. soed. • Khimiya prirodnykh soedinenii • **Chemistry of Natural Compounds** • 1965(1)1 • FP

Kib. • Kibernetika • **Cybernetics** • 1965(1)1 • FP

Kinet. i katal. • Kinetika i kataliz • **Kinetics and Catalysis** • 1960(1)1 • CB

Koks i khim. • Koks i khimiya • **Coke and Chemistry, USSR** • 1959( )8 • Coal Tar Research Assn. (Leeds, England)

Kolloidn. zh(urn). • Kolloidnyi zhurnal • **Colloid Journal** • 1952(14)1 • CB

Kosmich. issled. • Kosmicheskie issledovaniya • **Cosmic Research** • 1963(1)1 • CB

Kristallog. • Kristallografiya • **Soviet Physics—Crystallography** • 1957 (2)1 • AIP

Liteinoe proiz(-vo). • Liteinoe proizvodstvo • **Russian Castings Production** • 1961(12)1 • British Cast Iron Research Association

Mag. gidrodin. • Magnitnaya gidrodinamika • **Magnetohydrodynamics** • 1965(1)1 • FP

Mekh. polim. • Mekhnika polimerov • **Polymer Mechanics** • 1965(1)1 • FP

Metalloved. i term. obrabotka metal.; MiTOM • Metallovedenie i termicheskaya obrabotka metallov • **Metal Science and Heat Treatment** • 1958(6)1 • CB

Metallurg • **Metallurgist** • 1957( )1 • CB

Mikrobiol. • Mikrobiologiya • **Microbiology** • 1957(26)1 • CB

MiTOM • *see* Metalloved. i term. obrabotka metal.

Ogneupory • **Refractories** • 1960(25)1 • CB

Opt. i spektr.; OS • Optika i spektroskopiya • **Optics and Spectroscopy** • 1959(6)1 • AIP

Osnovan. fund. i mekh. gruntov • Osnovaniya fundamenty i mekhanika gruntov • **Soil Mechanics and Foundation Engineering** • 1964 ( )1 • CB

Paleon. zh(urn). • Paleontologicheskii zhurnal • **Journal of Paleontology** • 1962( )1 • AGI

Plast. massy • Plasticheskie massy • **Soviet Plastics** • 1960(8)7 • Rubber and Technical Press, Ltd.

PMM • *see* Prikl. matem. i mekhan.

PMTF • *see* Zhur. prikl. mekhan. i tekhn. fiz.

Pochvovedenie • **Soviet Soil Science** • 1958(53)1 • Soil Science Society of America

Poroshk. met. • Poroshkovaya metallurgiya • **Soviet Powder Metallurgy and Metal Ceramics** • 1962(2)1 • CB

Priborostroenie • **Instrument Construction** • 1959(4)1 • Taylor and Francis, Ltd.

Pribory i tekhn. éksp(erimenta); PTÉ • Pribory i tekhnika éksperimenta • **Instruments and Experimental Techniques** • 1958(3)1 • ISA

Prikl. biokhim. i mikrobiol. • Prikladnaya biokhimiya i mikrobiologiya • **Applied Biochemistry and Microbiology** • 1965(1)1 • FP

Prikl. matem. i mekh(an).; PMM • Prikladnaya matematika i mekhanika • **Applied Mathematics and Mechanics** • 1958(22)1 • PP

Probl. pered. inform. • Problemy peredachi informatsii • **Problems of Information Transmission** • 1965(1)1 • FP

Probl. severa • Problemy severa • **Problems of the North** • 1958( )1 • National Research Council of Canada

PTÉ • *see* Pribory i tekhn. éksperimenta

Radiokhim. • Radiokhimiya • **Soviet Radiochemistry** • 1962(4)1 • CB

Radiotekh. • Radiotekhnika • combined with Élektrosvyaz' in **Telecommunications and Radio Engineering** • 1961(16)1 • IEEE

Radiotekhn. i élektron(ika) • Radiotekhnika i élektronika • **Radio Engineering and Electronic Physics** • 1961(6)1 • IEEE

Stal' • **Stal' in English** • 1959(19)1 • The Iron and Steel Institute

Stanki i instr. • Stanki i instrument • **Machines and Tooling** • 1959 (30)1 • Production Engineering Research Association

Stek. i keram. • Steklo i keramika • **Glass and Ceramics** • 1956(13)1 • CB

Svaroch. proiz(-vo). • Svarochnoe proizvodstvo • **Welding Production** • 1959(5)4 • British Welding Research Association (London)

Teor. i éksperim. khim. • Teoreticheskaya i éksperimental'naya khimiya • **Theoretical and Experimental Chemistry** • 1965(1)1 • FP

Teor. veroyat. i prim. • Teoriya veroyatnostei i ee primenenie • **Theory of Probability and Its Application** • 1956(1)1 • Society for Industrial and Applied Mathematics

Teploénergetika • **Thermal Engineering** • 1964(11)1 • PP

Teplofiz. vys(ok). temp. • Teplofizika vysokikh temperatur • **High Temperature** • 1963(1)1 • CB

Tsvet. metally • Tsvetnye metally • **The Soviet Journal of Nonferrous Metals** • 1960(33)1 • Primary Sources

Usp. fiz. nauk; UFN • Uspekhi fizicheskikh nauk • **Soviet Physics—Uspekhi** • 1958(66)1 • AIP

Usp. khim.; UKh • Uspekhi khimii • **Russian Chemical Reviews** • 1960(29)1 • CS

Usp. mat. nauk; UMN • Uspekhi matematicheskaya nauk • **Russian Mathematical Surveys** • 1960(15)1 • Cleaver-Hume Press, Ltd.

Vest. Akad. med. nauk SSSR • Vestnik Akademii meditsinskikh nauk SSSR • **Vestnik of USSR Academy of Medical Sciences** • 1962(17)1 • CH

Vest. mashinostroeniya • Vestnik mashinostroeniya • **Russian Engineering Journal** • 1959(39)4 • Production Engineering Research Association

Vest. svyazi • Vestnik svyazi • **Herald of Communications** • 1954(14)1 • CH

Vysoko(molek). soed(ineniya) • Vysokomolekulyarnye soedineniya (SSSR) • **Polymer Science (USSR)** • 1959(1)1 • PP

Yadernaya fizika • **Soviet Journal of Nuclear Physics** • 1965(1)1 • AIP

Zashch(ita) met(allov) • Zashchita metallov • **Protection of Metals** • 1965(1)1 • CB

Zav(odsk). lab(oratoriya); ZL • Zavodskaya laboratoriya • **Industrial Laboratory** • 1958(24)1 • ISA

ZhÉTF pis'ma redaktsiyu • **JETP Letters** • 1965(1)1 • AIP

Zh(ur). anal(it). khim(ii); ZhAKh • Zhurnal analiticheskoi khimii • **Journal of Analytical Chemistry** • 1952(7)1 • CB

Zh(ur). éks(perim). i teor. fiz.; ZhÉTF • Zhurnal éksperimental'noi i teoreticheskoi fiziki • **Soviet Physics—JETP** • 1955(28)1 • AIP

Zh(ur). fiz. khimii; ZhFKh • Zhurnal fizicheskoi khimii • **Russian Journal of Physical Chemistry** • 1959(33)7 • CS

Zh(ur). neorg(an). khim.; ZhNKh • Zhurnal neorganicheskoi khimii • **Russian Journal of Inorganic Chemistry** • 1959(4)1 • CS

Zh(ur). obshch. khim.; ZhOKh • Zhurnal obshchei khimii • **Journal of General Chemistry of the USSR** • 1949(19)1 • CB

Zh(ur). org. khim.; ZhOrKh(im) • Zhurnal organicheskoi khimii • **Journal of Organic Chemistry of the USSR** • 1965(1)1 • CB

Zh(ur). prikl. khim.; ZhPKh • Zhurnal prikladnoi khimii • **Journal of Applied Chemistry of the USSR** • 1950(23)1 • CB

Zh(ur). prikl. mekhan. i tekhn. fiz. • Zhurnal prikladnoi mekhaniki i tekhnicheskoi fiziki • **Journal of Applied Mechanics and Technical Physics** • 1965( )1 • FP

Zh(ur). prikl. spektr. • Zhurnal prikladnoi spektroskopii • **Journal of Applied Spectroscopy** • 1965(2)1 • FP

Zh(ur). strukt(urnoi) khim.; ZhSKh • Zhurnal strukturnoi khimii • **Journal of Structural Chemistry** • 1960(1)1 • CB

Zh(ur). tekhn. fiz.; ZhTF • Zhurnal tekhnicheskoi fiziki • **Soviet Physics—Technical Physics** • 1956(26)1 • AIP

Zh(ur). vses. khim. ob-va im. Mendeleeva • Zhurnal vsesoyuznogo khimicheskogo obshchestva im. Mendeleeva • **Mendeleev Chemistry Journal** • 1965(10)1 • FP

Zh(ur). vychis. mat. i mat. fiz. • Zhurnal vychislitel'noi matematika i matematicheskoi fiziki • **USSR Computational Mathematics and Mathematical Physics** • 1962(1)1 • PP

ZL • *see* Zavodsk. laboratoriya

Declassified and Approved For Release 2013/09/24 : CIA-RDP10-02196R000700010005-2

Declassified and Approved For Release 2013/09/24 : CIA-RDP10-02196R000700010005-2

RUSSIAN TO ENGLISH

scientist-translators wanted

You can keep abreast of the latest Soviet research in your field while supplementing your **income** by translating **in your own home** on a part-time basis. In the expanding Consultants Bureau publishing program, we **guarantee a continuous flow of translation** in your specialty. If you have a native command of English, a good knowledge of Russian, and experience and academic training in a scientific discipline, you may be qualified for our program. Immediate openings are available in the following fields: physics, chemistry, engineering, biology, geology, and instrumentation. Call or write now for additional information: TRANSLATIONS EDITOR

CONSULTANTS BUREAU
227 West 17 Street, New York, N. Y. 10011 • (Area Code: 212) AL-5-0713

Declassified and Approved For Release 2013/09/24 : CIA-RDP10-02196R000700010005-2

Declassified and Approved For Release 2013/09/24 : CIA-RDP10-02196R000700010005-2

REVIEWS OF PLASMA PHYSICS
VOLUME 1

A comprehensive introduction to "classical" plasma physics, containing the following four important papers:

MOTION OF CHARGED PARTICLES IN ELECTROMAGNETIC FIELDS IN THE DRIFT APPROXIMATION

By D. V. Sivukhin

A development of the first-order approximation for the motion of a charged particle in strong magnetic fields with weak spatial inhomogeneities or in strong magnetic fields when weak electric fields are present. The solution of the equations of motion for the problem of a constant, uniform magnetic field provides the zero-th approximation to these special cases. Using this zero-th approximation as a basis, the first approximation is obtained, representing an estimate of the particles' motion in these electromagnetic fields which does not, however, account for small rapid oscillations of the particle about the trajectory characteristic of the smooth motion.

CONTENTS: Motion of a charged particle in a constant uniform magnetic field • Motion of the guiding center • Origin of the drifts • Smoothing and averaging of quantities containing rapidly varying terms • Complete system of equations of motion in the drift approximation • More exact system of equations of motion in the drift approximation • Derivation of certain auxiliary relations • Derivation of a compatible system of equations of motion in the drift approximation • Another approach to the equation of motion of the guiding center • Examples • Drift integrals of the motion in constant electric and magnetic fields • Liouville theorem in the drift approximation • Extension of drift theory to the case of strong transverse electric fields • References.

PARTICLE INTERACTIONS IN A FULLY IONIZED PLASMA

By B. A. Trubnikov

Reviews the kinetic effects associated with particle interactions in a fully ionized homogeneous gas. Special potential functions and electrostatic analogies are employed in the analysis. The motion of test particles in a plasma is considered, and a non-rigorous derivation of the kinetic equations is presented. Kinetic effects in high-temperature plasmas are also investigated.

CONTENTS: Test Particles in a Plasma: Force of friction due to scattering in a Coulomb field • Coulomb logarithm and the role of remote interactions • Average force acting on a particle in a plasma • Test particles in a plasma • Rate of change of the moments • Characteristic features of the Coulomb interaction: The potential functions ψ and φ • Use of the scattering cross sections • **Kinetic Equation for Coulomb Particles:** Motion of particles in phase space • Expression for the flux • Force of dynamical friction and the diffusion tensor • Kinetic equation for the Coulomb interaction • Kinetic equation taking account of polarization of the medium • **Kinetic Effects in High-Temperature Plasmas:** Test particle in a medium of infinitely heavy field particles at rest • Solution of the kinetic equation for the preceding case: "basic" relaxation time • Spherically symmetric distribution of field particles • Runaway electrons • Maxwellian distribution of field particles: relaxation time • Plane flux in an equilibrium plasma • Energy transfer • Approach to equilibrium in a two-component plasma • References.

TRANSPORT PROCESSES IN A PLASMA

By S. I. Braginskii

Discusses transport processes in a fully ionized gas having a single species (simple plasma). The transport coefficients for a simple plasma are presented and given qualitative physical interpretations. They are then computed numerically from the kinetic equation. Some of the problems arising from the use of the transport equations to describe a plasma in a strong field are investigated. The application of the transport equations for particles of different species in analyses which assume a plasma model based on a single complex gas is also studied.

CONTENTS: Transport equations • Transport equations for a simple plasma (summary of results) • Kinetics of a simple plasma (qualitative description) • Kinetics of a simple plasma (quantitative analysis) • Certain paradoxes • Hydrodynamic description of a plasma • Multicomponent plasma • Examples • Appendix • References.

THERMODYNAMICS OF A PLASMA

By A. A. Vedenov

Examines the statistical thermodynamics of a system of particles characterized by Coulomb interactions. The difficulty of determing the thermodynamic quantities of nonideal systems when there is no small physical parameter in terms of which the quantities of interest can be expanded is noted, and for this reason, only weakly nonideal Coulomb gases are studied. In this case, the small parameter is the ratio of the mean Coulomb scattering amplitude to the mean distance between particles. The thermodynamic potential of the plasma is expanded in terms of this small parameter, and the leading terms of the virial expansions for both classical and quantum Coulomb systems are studied.

CONTENTS: Classical Coulomb system • Quantum Coulomb system • Degree of ionization of a plasma.

326 pages 1965 $12.50

(c/b) CONSULTANTS BUREAU 227 West 17th Street, New York, New York 10011

Declassified and Approved For Release 2013/09/24 : CIA-RDP10-02196R000700010005-2